



**HAL**  
open science

# Micro-macro approach of dilatancy phenomenon in remoulded clays - Study of the behaviour under saturated and unsaturated conditions

Qian-Feng Gao

► **To cite this version:**

Qian-Feng Gao. Micro-macro approach of dilatancy phenomenon in remoulded clays - Study of the behaviour under saturated and unsaturated conditions. Géotechnique. Université de Lorraine, 2018. English. NNT: 2018LORR0257 . tel-02127042

**HAL Id: tel-02127042**

**<https://hal.univ-lorraine.fr/tel-02127042>**

Submitted on 14 Jan 2020

**HAL** is a multi-disciplinary open access archive for the deposit and dissemination of scientific research documents, whether they are published or not. The documents may come from teaching and research institutions in France or abroad, or from public or private research centers.

L'archive ouverte pluridisciplinaire **HAL**, est destinée au dépôt et à la diffusion de documents scientifiques de niveau recherche, publiés ou non, émanant des établissements d'enseignement et de recherche français ou étrangers, des laboratoires publics ou privés.



## AVERTISSEMENT

Ce document est le fruit d'un long travail approuvé par le jury de soutenance et mis à disposition de l'ensemble de la communauté universitaire élargie.

Il est soumis à la propriété intellectuelle de l'auteur. Ceci implique une obligation de citation et de référencement lors de l'utilisation de ce document.

D'autre part, toute contrefaçon, plagiat, reproduction illicite encourt une poursuite pénale.

Contact : [ddoc-theses-contact@univ-lorraine.fr](mailto:ddoc-theses-contact@univ-lorraine.fr)

## LIENS

Code de la Propriété Intellectuelle. articles L 122. 4

Code de la Propriété Intellectuelle. articles L 335.2- L 335.10

[http://www.cfcopies.com/V2/leg/leg\\_droi.php](http://www.cfcopies.com/V2/leg/leg_droi.php)

<http://www.culture.gouv.fr/culture/infos-pratiques/droits/protection.htm>



Dissertation presented to obtain the doctor's degree of:

**Université de Lorraine**

by:

**Qian-Feng GAO**

Speciality: **Geotechnical Engineering**

**Micro-macro approach of dilatancy phenomenon in remoulded clays - Study of the behaviour under saturated and unsaturated conditions**

Defended on December 13, 2018

In front of the jury:

Philippe Cosenza	Professor	Université de Poitiers	Reviewer
Pierre Delage	Professor	Ecole des Ponts ParisTech	Reviewer
Cristina Jommi	Professor	Delft University of Technology	Examiner
Zhenyu Yin	MCF-HDR	Ecole Centrale de Nantes	Examiner
Mohamad Jrad	MCF	Université de Lorraine	Examiner
Lamine Ighil Ameer	Doctor	Cerema de Blois	Examiner
Mahdia Hattab	Professor	Université de Lorraine	Supervisor
Jean-Marie Fleureau	Professor	Université Paris Saclay CentraleSupélec	Co-supervisor

Laboratoire d'Étude des Microstructures et de Mécanique des Matériaux

LEM3 UMR CNRS 7239 - Université de Lorraine

7 rue Félix Savart - F-57070 Metz - France





Thèse pour l'obtention du Grade de:

**Docteur de l'Université de Lorraine**

Présentée par:

**Qian-Feng GAO**

Spécialité: **Géotechnique**

**Approche micro-macro du phénomène de dilatance dans  
les argiles remaniées - Etude du comportement en  
condition saturé et non saturé**

Soutenue le 13 décembre 2018

Devant le jury composé de :

Philippe Cosenza	Professeur	Université de Poitiers	Rapporteur
Pierre Delage	Professeur	Ecole des Ponts ParisTech	Rapporteur
Cristina Jommi	Professeur	Delft University of Technology	Examineur
Zhenyu Yin	MCF-HDR	Ecole Centrale de Nantes	Examineur
Mohamad Jrad	MCF	Université de Lorraine	Examineur
Lamine Ighil Ameer	Docteur	Cerema de Blois	Examineur
Mahdia Hattab	Professeur	Université de Lorraine	Directeur de thèse
Jean-Marie Fleureau	Professeur	Université Paris Saclay CentraleSupélec	Co-directeur de thèse

Laboratoire d'Étude des Microstructures et de Mécanique des Matériaux

LEM3 UMR CNRS 7239 - Université de Lorraine

7 rue Félix Savart - F-57070 Metz - France



## Acknowledgements

This dissertation was carried out at the laboratory of LEM3 of the University of Lorraine, in Metz, France, from 2015 to 2018. It was financed by the China Scholarship Council (CSC) (No. 201508430168). I have received great help from many people during the preparation and writing of the dissertation. I would like to take this opportunity to thank them.

First of all, I would like to sincerely thank my supervisor Prof. Mahdia Hattab for her valuable expertise and patient guidance. I am extremely grateful for her enthusiastic encouragement and help, which enable me to overcome all the problems I faced during the course of experiments and the preparation of the dissertation.

I would like to express my deepest thanks to my co-supervisor Prof. Jean-Marie Fleureau at CentraleSupélec, whose excellent guidance, precious ideas and useful advice have greatly contributed to the accomplishment of my doctoral research.

Besides my supervisors, I am very grateful to the jury members Prof. Philippe Cosenza at Université de Poitiers, Prof. Pierre Delage at Ecole des Ponts ParisTech, Prof. Cristina Jommi at Delft University of Technology, Prof. Zhenyu Yin at Ecole Centrale de Nantes, Dr. Mohamad Jrad at Université de Lorraine and Dr. Lamine Ighil Ameer at Cerema de Blois for their insightful comments and constructive suggestions to improve my dissertation.

I am very grateful for the technical assistance provided by Dr. Mohamad Jrad in unsaturated triaxial tests and X-ray microtomography scans. The results and specimens of saturated triaxial tests offered by Dr. Lamine Ighil Ameer are also highly appreciated.

I would like to thank Prof. Zhenyu Yin for his recommendation, otherwise I would not have the opportunity to meet with my current excellent supervisors. My special thanks are also extended to Prof. Pierre-Yves Hicher at Ecole Centrale de Nantes for his invaluable advice in interpreting the macro-micro results of saturated clays.

I would like to express my great appreciation to my Master's supervisors, Prof. Hui Dong at Xiangtan University and Prof. Zongwei Deng at Hunan City University, who encouraged me to start the doctoral research and have given me continued support.

I take this opportunity to express my sincere gratitude to all the faculty members of the LEM3 laboratory, particularly, Mr. Hanbing Bian, Ms. Wen Chen, Mr. Guillaume Robin, Ms. Yudong Zhang, Mr. Olivier Perroud, Mr. Jean-Sébastien Lecomte and Mr. Jérôme Slowensky, for their kind help and technical assistance.

I would like to express my sincere gratitude to my colleagues and friends especially Dr. Dan Zhao, Mr. Zhengtian Yang, Mr. Wenqing Cheng, Dr. Yajun Zhao, Dr. Jing Wen and Mr. Lizhao Dai for their helps in performing unsaturated triaxial tests, soil-water characteristic tests and scanning electron microscopy observations.

Last but not least, I must extend my warmest and most sincere thanks to my family and my girlfriend for providing me with continued support and encouragement throughout the three years of my study in France.

Qian-Feng GAO

Metz, France

September 15, 2018

## Abstract

Clay is extensively distributed on the Earth's surface. It is widely used in the field of Civil Engineering, for example, as a building material. Furthermore, clay can be used as not only a natural barrier in the dam cores but also a matrix for the storage of radioactive wastes because of its desired retention properties. The complex nature of clay has aroused great interest of researchers in its mechanical behaviour under saturated and unsaturated conditions. The microscopic observation is a necessary complement for a better understanding of this behaviour.

The objective of this research is to examine the influence of triaxial stress paths on the mechanical behaviour of remoulded clay and the mechanisms that occur at the microstructural level. The dilatancy phenomenon is particularly investigated considering a given stress level reached by following different stress paths. In the second part, this research focuses on the influence of suctions on the mechanical behaviour.

For the saturated remoulded clay, the dilative behaviour at a given stress level, reached by following two different stress paths (i.e., the constant  $\sigma'_3$  stress path and the purely deviatoric stress path), was analysed in detail. The influence of stress levels was also examined in this research. The microstructural analysis was conducted at different scales by means of different methods: scanning electron microscopy (SEM), mercury intrusion porosimetry (MIP) and X-ray microtomography (XR- $\mu$ CT).

The macroscopic results of saturated clay show that, at a given stress level, the volumetric behaviour greatly depends on the stress path. In the case of overconsolidated clay, the dilatancy is activated especially when triaxial shearing is performed following the purely deviatoric stress path. At the microscopic level, the results highlight five modes of particle orientation that could be activated under triaxial loading. The results also reveal that the appearance of dilatancy phenomenon in highly overconsolidated remoulded clay may be attributed to the tortuous arrangement of clay particles, the opening of micropores, and the formation and opening of mesocracks.

For the unsaturated remoulded clay, the studies were performed through many macroscopic and mesoscopic tests on Kaolin K13 clay (the same material as that for saturated tests) and a

kaolinite-montmorillonite mixture termed M35 (to show the influence of mineralogy). The evolution of suctions was measured using hygrometers placed near the upper and lower ends of clay specimens. The results show that, at a high suction level, the deviatoric stress of unsaturated clay increases to a peak and then decreases down to a residual value. The shear strength of unsaturated clay generally increases with increasing mean stress and suction. However, in the high suction tests, the development of cracks during drying led to the inhomogeneity of the specimens and thus resulted in relatively small shear strengths.

**Keywords:** Remoulded Clay; Triaxial Test; Dilatancy; Microstructure; Suction; Shear Strength

## Résumé

L'argile est abondamment distribuée à la surface de la Terre, c'est un matériau très largement utilisé dans la domaine Génie Civil, comme matériaux de construction par exemple. L'argile est également utilisée comme des barrières naturelles dans les cœurs de barrages, mais aussi comme matrice pour le stockage des déchets radioactifs à cause de ses propriétés de rétention. La nature complexe de l'argile a amené les chercheurs à s'intéresser à son comportement mécanique en condition saturée et non-saturée. L'observation microscopique est un plus pour une meilleur compréhension de ce comportement.

L'objectif de cette recherche est d'étudier l'influence des chemins de contrainte triaxiaux sur le comportement mécanique et sur les mécanismes qui se produisent au niveau microstructural. L'étude est réalisée en considérant à un niveau de contrainte donné, le phénomène de dilatance est approché suivant des chemins de contraintes différents. Dans un deuxième temps, l'étude se porte sur l'influence de la succion sur le comportement.

Pour les argiles remaniées saturées, le comportement dilatant à un niveau de contrainte donné, atteint par deux chemins de contrainte différents (le chemin de constant  $\sigma'_3$  et le chemins de contrainte purement déviatorique), a été finement analysé. L'influence du niveau de contrainte a été également abordée dans le cadre de cette étude. L'analyse microstructurale a été analysée à différentes échelles au moyen de différentes méthodes : la microscopie électronique à balayage, la porosimétrie par intrusion de mercure et la micro tomographie à rayons X.

Au niveau macroscopique, les résultats ont montré que, pour un niveau de contrainte donné, le comportement volumétrique est fonction du chemin de contrainte. La dilatance est activée dans le cas d'argiles surconsolidées principalement lorsque le chargement est purement déviatorique. Au niveau microscopique, les résultats mettent en évidence cinq modes d'orientation des particules qui pourraient être activés sous chargement triaxial. Les résultats révèlent que l'apparition de la dilatance dans les argiles remaniées fortement surconsolidées peut être attribuée à l'arrangement tortueux des particules d'argile, l'ouverture des micropores ainsi que la formation et l'ouverture de fissures mésoscopiques.

Pour les argiles remaniés non saturées, les études sont réalisés par les essais

macroscopiques et mésoscopiques sur l'argile Kaolin K13 (même matériau que pour les essais en condition saturée) et un mélange kaolinite-montmorillonite M35 (pour montrer l'influence de la minéralogie). L'évolution des succions a été mesurée au moyen d'hygromètres placés dans les extrémités supérieure et inférieure d'échantillon. Les résultats démontrent que la contrainte déviatorique d'argile non saturée, lorsque la succion est forte, commence par augmenter jusqu'à un sommet puis diminue pour rejoindre une valeur résiduelle. La résistance au cisaillement d'argile non saturée augmente généralement avec la contrainte moyenne et la succion. Cependant, dans nos essais à succion très élevée le développement d'une fissuration lors du séchage a conduit à perdre l'homogénéité du matériau et à réduire la résistance au cisaillement de l'éprouvette.

**Mots-clefs:** Argile Remaniée; Essai Triaxial; Dilatance; Microstructure; Succion; Résistance au Cisaillement

---

## Table of Contents

<b>List of Symbols and Abbreviations.....</b>	<b>XI</b>
<b>List of Tables.....</b>	<b>XV</b>
<b>List of Figures.....</b>	<b>XVII</b>
<b>General introduction.....</b>	<b>1</b>
Background.....	1
Research objectives.....	1
organisation of the dissertation.....	2
<b>Chapter 1 Literature review.....</b>	<b>5</b>
1. Dilatancy phenomenon.....	7
1.1 Definition of dilatancy.....	7
1.2 Dilatancy of granular materials.....	8
1.3 Dilatancy of remoulded clay.....	12
2. Macro-micro relationship of remoulded clay.....	17
2.1 Characterisation of particle organisation.....	17
2.2 Characterisation of micropore structure.....	24
2.3 Characterisation of local cracks.....	28
3. Mechanical behaviour of unsaturated clay affected by suction.....	29
3.1 Basic concepts regarding unsaturated clay.....	30
3.2 Shear strength and volume change of unsaturated clay.....	33
4. Summary.....	43
<b>Chapter 2 Material properties and experimental methods.....</b>	<b>45</b>
1. Material properties and specimen preparations.....	47
1.1 Mineralogy analyses.....	47
1.2 Grain size distribution.....	49
1.3 Physical properties and compressibility.....	50
1.4 Specimen preparations.....	51
2. Experimental programme.....	52
2.1 Experiments on saturated clay.....	52
2.2 Experiments on unsaturated clay.....	53

3. Mechanical experimental procedures.....	55
3.1 Triaxial tests on saturated clay.....	55
3.2 Triaxial tests on unsaturated clay.....	60
4. Microscale experimental procedures.....	65
4.1 Scanning electron microscopy (SEM) observations.....	66
4.2 Mercury intrusion porosimetry (MIP) tests.....	78
4.3 X-ray microtomography (XR- $\mu$ CT) scans.....	81
5. Summary.....	86
<b>Chapter 3 Multiscale behaviour of saturated remoulded clays.....</b>	<b>89</b>
1. Experimental approach.....	91
2. Macromechanical results.....	93
2.1 Determination of plastic volumetric strains.....	93
2.2 Mechanical behaviour under triaxial loading.....	94
2.3 Discussion on volumetric strain mechanisms.....	98
3. Microstructural results.....	100
3.1 Global orientation of clay particles and pores.....	100
3.2 Pore morphology and pore size distribution.....	108
3.3 Microscopic and mesoscopic cracks.....	118
4. Mechanism of dilatancy phenomenon.....	121
4.1 Conceptual modes of particle orientation.....	121
4.2 Discussion on dilatancy mechanisms.....	126
5. Summary.....	129
<b>Chapter 4 Hydromechanical behaviour of unsaturated remoulded clays.....</b>	<b>131</b>
1. Experimental approach.....	133
2. Soil-water characteristics of unsaturated clay.....	135
2.1 Unsaturated remoulded Kaolin K13 clay.....	135
2.2 Unsaturated remoulded M35 clay.....	141
3. Mechanical behaviour of remoulded Kaolin K13 clay.....	145
3.1 Saturated test results affected by mean effective stress.....	145
3.2 Unsaturated test results affected by mean stress.....	147
3.3 Unsaturated test results affected by suction.....	159
4. Mechanical behaviour of remoulded M35 clay.....	166
4.1 Saturated test results affected by mean effective stress.....	166

---

4.2 Unsaturated test results affected by mean stress.....	169
5. Theoretical calculation of apparent cohesions.....	173
5.1 Theoretical equations.....	174
5.2 Comparison between calculated and measured cohesions.....	175
6. Summary.....	176
<b>Chapter 5 Conclusions and perspectives.....</b>	<b>179</b>
1. Conclusions.....	181
1.1 Investigations of saturated remoulded clay.....	181
1.2 Investigations of unsaturated remoulded clay.....	183
2. Future perspectives.....	185
<b>References.....</b>	<b>187</b>



## List of Symbols and Abbreviations

### Greek letters:

$\alpha$	Direction of plastic strain increment vector
$\alpha^*$	Constant in the van Genuchten model
$\gamma$	Surface tension of mercury
$\Delta V$	Volume change
$\bar{\varepsilon}, d\bar{\varepsilon}$	Deviatoric strain and deviatoric strain increment
$\bar{\varepsilon}^p, d\bar{\varepsilon}^p$	Plastic deviatoric strain and plastic deviatoric strain increment
$\varepsilon_f$	Axial strain at failure
$\varepsilon_v, d\varepsilon_v$	Total volumetric strain and total volumetric strain increment
$\varepsilon_v^p, d\varepsilon_v^p$	Plastic volumetric strain and plastic volumetric strain increment
$\varepsilon_1, d\varepsilon_1$	Axial strain and axial strain increment
$\eta$	Stress ratio
$\Theta$	Contact angle
$\theta, \theta_i$	Particle or pore orientation and $i$ th orientation range
$\rho_s$	Mass density of soil solids
$\sigma, \sigma'$	Total stress and effective stress
$\sigma'_c$	Preconsolidation effective pressure
$\sigma^c, \sigma^s$	Capillary stress and suction stress
$\sigma_{t,iso}$	Isotropic tensile strength
$\sigma_1, \sigma'_1$	Axial stress and axial effective stress
$\sigma_3, \sigma'_3$	Confining stress and confining effective stress
$\tau_f$	Shear strength
$\varphi, \varphi'$	Internal friction angle and effective internal friction angle
$\varphi^*$	Internal friction angle defined in $(p, q)$ plane
$\varphi', \varphi^b$	Internal friction angles related to $(\sigma - u_a)$ and $(u_a - u_w)$
$\chi$	Material variable related to degree of saturation
$\psi, \psi_{max}$	Angle of dilation and maximum angle of dilation
$\psi_m, \psi_o$	Matric suction and osmotic suction
$\omega_v$	Molecular mass of water vapour

### Latin letters:

$A, A_T, A_P$	Pore area, total image area and total pore area
$a, b$	Major axis length and minor axis length of pores
$a_0, b_0, c_0$	Constants in the shrinkage curve model
$\bar{a}$	Parameter related to the drainage condition
$C$	Constant for calculating fractal dimension
$C_c, C_s$	Compression index and swelling index
$c, c'$	Cohesion and effective cohesion
$c^*$	Cohesion defined in $(p, q)$ plane

$D, D_i$	Pore diameter and median diameter of $i$ th pore class
$D_f$	Fractal dimension of pore structure
$d_e$	Equivalent size of a 2D pore
$d\varepsilon_v^{(p)}, d\varepsilon_v^{(q)}$	Volumetric strain increments induced by $dp'$ and $dq$
$e, e_{\min}$	Void ratio and minimum void ratio
$e_{\text{MIP}}, e_{\text{SEM}}$	Microvoid ratios determined by MIP and SEM-stereology methods
$e_{00}, e_0, e_f$	Void ratios after one-dimensional compression, isotropic loading and triaxial shearing
$e_{2D}$	2D microvoid ratio
$G_s$	Specific gravity of soil
$H_0$	Specimen height before triaxial shearing
$I_{or}$	Orientation index
$I_p$	Plastic index
$K_0$	Coefficient of lateral earth pressure at rest
$L$	Pore perimeter
$M$	Slope of critical state line (critical stress ratio)
$m_s$	Soil solid mass
$N$	Total number of clay particles or pores
$N_{\theta_i}$	Number of clay particles or pores with orientation towards $\theta_i$
$n^*$	Constant in the van Genuchten model
$P$	Purely deviatoric stress path
$P_m$	Applied intrusion pressure of mercury
$P(\theta_i)$	Percentage of clay particles or pores with orientation towards $\theta_i$
$p, p', p'_f$	Mean stress, mean effective stress and final mean effective stress
$p'_0$	Effective consolidation stress
$q, q_f$	Deviatoric stress and final deviatoric stress
$R$	Representative radius of soil grains
$R_s$	Pore roundness
$R^*$	Universal gas constant
$S$	Conventional constant $\sigma'_3$ stress path
$S_r, S_{r0}, S_r^e, S_{re}$	Degree of saturation, initial degree of saturation, effective degree of saturation and residual degree of saturation
$S_s$	Specific surface area
$s, s_0, s_{AE}, s_{SL}$	Suction, initial suction, air entry suction and shrinkage limit suction
$T$	Absolute temperature
$T_s$	Surface tension of water
$t_{100}$	Time of primary consolidation
$u, u_w, u_a$	Pore pressure, pore water pressure and pore air pressure
$\bar{u}_v$	Partial pressure of pore water vapour
$\bar{u}_{v0}$	Saturation pressure of water vapour over a flat surface of pure water
$V_{\text{diff},i}$	Differential volume of the intruded mercury

$V_{\text{Hg}}$	Cumulative volume of the intruded mercury
$V_i$	Volume of the intruded mercury
$V_v, V_s$	Void volume and soil solid volume
$V_{00}$	Initial volume of specimen
$v_{\text{max}}$	Maximum loading velocity
$v_{w0}$	Specific volume of water
$w, w_s$	Water content and saturated water content
$w_L, w_P, w_{SL}$	Liquid limit, plastic limit and shrinkage limit

**Abbreviations:**

BP	Back pressure
CD	Consolidated drained triaxial test
CSL	Critical state line
CT	Computerized tomography
CU	Consolidated undrained triaxial test
CW	Constant water content test
MIP	Mercury intrusion porosimetry
NC	Normally consolidated
OC	Overconsolidated
OCR	Overconsolidation ratio
PSD	Pore size distribution
RH	Relative humidity
SEM	Scanning electron microscopy
TEM	Transmission electron microscopy
UC	Unconfined compression test
UU	Unconsolidated undrained triaxial test
XR-CT	X-ray computerized tomography
XR- $\mu$ CT	X-ray microtomography



## List of Tables

### Tables in Chapter 1:

Table 1.1 Average pore shape factor and fractal dimension (Wen et al., 2011).....	26
Table 1.2 Various triaxial tests for unsaturated soil (Fredlund and Rahardjo, 1993).....	33

### Tables in Chapter 2:

Table 2.1 Physical properties of studied materials (Hammad, 2010; Zhao, 2017).....	50
Table 2.2 Compressibility (Hammad, 2010; Ighil Ameer, 2016; Zhao, 2017).....	51
Table 2.3 Specifications of mechanical tests on saturated Kaolin K13 clay.....	59
Table 2.4 Saturated salt solutions used for controlling suctions.....	60
Table 2.5 Specifications of triaxial tests on Kaolin K13 clay.....	63
Table 2.6 Specifications of triaxial tests on M35 clay.....	64
Table 2.7 Test results of clay sample with two metal fibres.....	85
Table 2.8 Test results of clay sample with an organic fibre.....	85

### Tables in Chapter 3:

Table 3.1 Overview of the experimental programme.....	92
Table 3.2 Values and directions of plastic strain increment vectors.....	99
Table 3.3 Pore orientation indexes of different clay specimens.....	102
Table 3.4 Identified modes of clay particle orientation.....	124

### Tables in Chapter 4:

Table 4.1 Shear strength parameters of remoulded Kaolin K13 clay.....	162
Table 4.2 Summary of parameters for cohesion calculation.....	175
Table 4.3 Comparison between calculated and measured apparent cohesions.....	176



## List of Figures

### Figures in Chapter 1:

Figure 1.1 Dilatancy phenomenon in sand during shearing.....	8
Figure 1.2 Triaxial test results of different sands (Lancelot et al., 2006).....	9
Figure 1.3 Triaxial test results of a Pleistocene age sand (Esposito III and Andrus, 2016).....	10
Figure 1.4 Triaxial test results of a rounded material (Varadarajan et al., 2003).....	11
Figure 1.5 Triaxial test results of an angular material (Varadarajan et al., 2003).....	11
Figure 1.6 Sawtooth model for granular materials (Revuzhenko, 2007).....	12
Figure 1.7 Microscale interpretation of dilatancy of granular materials (Chi et al., 2009).....	12
Figure 1.8 Typical results of triaxial tests on a remoulded clay.....	13
Figure 1.9 Triaxial test results of remoulded Kaolin P300 clay (Hattab and Hicher, 2004)....	14
Figure 1.10 CD triaxial test results of remoulded Kaolin K13 clay (Zhao et al., 2018).....	15
Figure 1.11 Three volume change domains of remoulded clay (Hattab and Hicher, 2004).....	16
Figure 1.12 Influence of Lode angles on dilatancy of a remoulded clay (Ye et al., 2013).....	17
Figure 1.13 Image sequence of clay specimens sheared normal to original fabric (Morgenstern and Tchalenko, 1967c).....	18
Figure 1.14 Fabric of the shear zone after direct shear test (Takizawa et al., 2005).....	19
Figure 1.15 Fabric of remoulded M35 clay after oedometer tests (Hammad, 2010).....	20
Figure 1.16 Particle orientation of a remoulded kaolinite clay (Anandarajah et al., 1996).....	20
Figure 1.17 Influence of microfabrics on the mechanical behaviour of kaolin clay (Sachan and Penumadu, 2007).....	22
Figure 1.18 Rose diagrams of particle orientation of M35 clay (Hammad, 2010).....	23
Figure 1.19 Particle orientation of remoulded clay specimens under triaxial loading (Hattab and Fleureau, 2010).....	24
Figure 1.20 Pore orientation of M35 clay under triaxial loading (Hammad, 2010).....	25
Figure 1.21 Sketch of the multiscale pore structure of clay.....	27
Figure 1.22 MIP test results of kaolin clay after compaction (Tarantino and De Col, 2008)....	27
Figure 1.23 Microcracks observed in remoulded clays after CD triaxial tests (Hattab and Fleureau, 2010; Hattab et al., 2015).....	28
Figure 1.24 Local cracks development in sedimentary soil specimen (Viggiani et al., 2004).	29
Figure 1.25 Extended Mohr-Coulomb failure surface (Lu and Likos, 2004).....	32
Figure 1.26 Oedometer results of compacted smectites (Al-Mukhtar et al., 1999).....	34

Figure 1.27 Void ratio and equivalent effective stress of clay during drying(Vesga, 2008)....	35
Figure 1.28 Compression behaviour of clay specimens (Mun and McCartney, 2015).....	35
Figure 1.29 Stress-strain relationships of unsaturated silt (Cui and Delage, 1996).....	36
Figure 1.30 Triaxial test results of unsaturated sand-bentonite mixtures (Blatz et al., 2002)..	37
Figure 1.31 Triaxial tests on compacted unsaturated kaolin clay (Oh et al., 2008).....	39
Figure 1.32 Effect of suctions on shear strength of clay (I <sub>c</sub> U-f test) (Oh et al., 2008).....	39
Figure 1.33 Critical state lines of unsaturated kaolinite clay.....	40
Figure 1.34 CW triaxial test results on unsaturated silty clay (Jotisankasa et al., 2009).....	41
Figure 1.35 Volumetric deformations of unsaturated silt (Cui and Delage, 1996).....	42
Figure 1.36 Triaxial test results of clay affected by preparation methods (Gao et al., 2015)...	43

### Figures in Chapter 2:

Figure 2.1 X-ray diffraction analysis of Kaolin K13 clay.....	48
Figure 2.2 X-ray diffraction analysis of Ca-montmorillonite.....	49
Figure 2.3 SEM images of the raw Kaolin K13 clay powder.....	49
Figure 2.4 Particle size distributions of the studied materials.....	50
Figure 2.5 Preparation of pre-consolidated clay material.....	51
Figure 2.6 Extraction of triaxial test specimens.....	52
Figure 2.7 Experimental programme on saturated remoulded clay.....	53
Figure 2.8 Loading paths used in saturated triaxial tests.....	53
Figure 2.9 Experimental programme on unsaturated remoulded clay.....	54
Figure 2.10 Loading paths used in unsaturated triaxial tests.....	55
Figure 2.11 Photo of the GDS Triaxial Testing System.....	55
Figure 2.12 Anti-frictional device for reducing end restraints.....	56
Figure 2.13 Specimen saturation stage.....	57
Figure 2.14 Isotropic consolidation stage.....	58
Figure 2.15 Triaxial shearing stage.....	59
Figure 2.16 Imposition of suctions to clay specimens in desiccators.....	60
Figure 2.17 Calibration of hygrobutton using saturated NaCl solution.....	61
Figure 2.18 Triaxial testing setup with suction measurement.....	62
Figure 2.19 Stress path used for unsaturated triaxial testing.....	63
Figure 2.20 Limitations of digital photography for volume change measurement.....	65
Figure 2.21 Sample preparation for microstructural observations.....	65
Figure 2.22 Lyophilisation (freeze-drying) technique.....	67

Figure 2.23 SEM setup and metallised samples.....	68
Figure 2.24 Acquisition of SEM images from the vertical observation surface.....	68
Figure 2.25 Analysis methods of particle orientation.....	69
Figure 2.26 Relationship between global particle orientation and image numbers.....	70
Figure 2.27 Quantitative characterisation of clay particle orientation.....	71
Figure 2.28 Principle of image segmentation.....	72
Figure 2.29 Image processing procedures for pore structure identification.....	73
Figure 2.30 2D characterisation of micropore structure.....	74
Figure 2.31 Quantitative characterisation of pore orientation.....	75
Figure 2.32 Problems with 2D pore size characterisation.....	76
Figure 2.33 Principle of stereology (after Sahagian and Prousevitich, 1998).....	77
Figure 2.34 Examples of SEM-based 2D PSD and SEM-stereology-based 3D PSD.....	78
Figure 2.35 MIP test setup for pore structure quantification.....	79
Figure 2.36 Example of PSD deduced from MIP test.....	81
Figure 2.37 Sample preparation for XR- $\mu$ CT scans.....	82
Figure 2.38 Schematic illustration of XR- $\mu$ CT scans (after Landis and Keane, 2010).....	83
Figure 2.39 Calibration of sample preparation methods.....	84
Figure 2.40 Image processing method for identification of mesocracks.....	86

### Figures in Chapter 3:

Figure 3.1 Triaxial test results at a given stress level reached along different stress paths.....	95
Figure 3.2 Triaxial test results at different stress levels following a given stress path.....	97
Figure 3.3 Volumetric strain mechanisms during triaxial loading.....	99
Figure 3.4 Global particle orientation of clay specimens under isotropic loading.....	101
Figure 3.5 Global pore orientation of clay specimens under isotropic loading.....	102
Figure 3.6 Global particle orientation of clay specimens on different triaxial stress paths....	104
Figure 3.7 Global pore orientation of clay specimens on different triaxial stress paths.....	105
Figure 3.8 Global particle orientation of clay specimens at different triaxial stress levels....	107
Figure 3.9 Global pore orientation of clay specimens at different triaxial stress levels.....	108
Figure 3.10 Fractal dimensions of different clay specimens under triaxial loading.....	110
Figure 3.11 Pore roundness of clay specimens under isotropic loading.....	111
Figure 3.12 Pore roundness of specimens at a given stress level on different stress paths....	112
Figure 3.13 Micropore system (black areas) identified in different specimens.....	113
Figure 3.14 Pore roundness of specimens at different stress levels on a given stress path....	114

Figure 3.15 Relationship between pore roundness and pore diameter.....	115
Figure 3.16 PSD of clay specimens at a given stress level on different stress paths.....	116
Figure 3.17 PSD of clay specimens at different stress levels on a given stress path.....	117
Figure 3.18 Relationship between microvoid ratios and macrovoid ratios.....	117
Figure 3.19 Microcracks within clay specimens observed by SEM .....	119
Figure 3.20 XR- $\mu$ CT projections and slices of remoulded clay specimens.....	120
Figure 3.21 A typical mesocrack within the specimen OCR3.3_P300_P2.....	121
Figure 3.22 Different features of clay particle orientation affected by stress paths.....	122
Figure 3.23 Representative SEM images observed in the vertical plane of specimens.....	125
Figure 3.24 Evolution of particle orientation of remoulded clay under triaxial loading.....	126
Figure 3.25 Microstructural evolution of remoulded clay under triaxial loading.....	128
Figure 3.26 Dilatancy model for strongly overconsolidated remoulded clay.....	128

#### Figures in Chapter 4:

Figure 4.1 Experimental programme for unsaturated clays.....	134
Figure 4.2 Water content evolution of remoulded Kaolin K13 clay.....	135
Figure 4.3 Open crack on a cylindrical specimen ( $s_0 = 38$ MPa, NaCl solution).....	137
Figure 4.4 Sketch of a typical shrinkage curve.....	138
Figure 4.5 Soil-water characteristic curves of remoulded kaolinite clays.....	140
Figure 4.6 Water content evolution of remoulded M35 clay ( $s_0 = 38$ MPa, NaCl solution)..	142
Figure 4.7 Soil-water characteristic curves of remoulded M35 clays.....	144
Figure 4.8 Behaviour of saturated Kaolin K13 clay under various mean effective stresses..	146
Figure 4.9 Failure modes of saturated remoulded Kaolin K13 clay.....	147
Figure 4.10 Relative humidity and total suction (Kaolin K13, NaCl) before triaxial tests....	148
Figure 4.11 Mechanical behaviour of unsaturated Kaolin K13 clay under $s_0 = 38$ MPa.....	149
Figure 4.12 Photographs and XR- $\mu$ CT images of specimen K13_S38_P200.....	153
Figure 4.13 Photographs and XR- $\mu$ CT images of specimen K13_S38_P600.....	153
Figure 4.14 Photographs and XR- $\mu$ CT images of specimen K13_S38_P1000.....	154
Figure 4.15 Relative humidity and total suction (Kaolin K13, Na <sub>2</sub> SO <sub>4</sub> ) before triaxial tests	155
Figure 4.16 Mechanical behaviour of unsaturated Kaolin K13 clay under $s_0 = 10$ MPa.....	156
Figure 4.17 Photographs and XR- $\mu$ CT images of specimen K13_S10_P200.....	159
Figure 4.18 Photographs and XR- $\mu$ CT images of specimen K13_S10_P600.....	159
Figure 4.19 Photographs and XR- $\mu$ CT images of specimen K13_S10_P1000.....	160
Figure 4.20 Behaviour of Kaolin K13 clay under $p = 200$ kPa affected by total suctions....	161

---

Figure 4.21 Behaviour of Kaolin K13 clay under $p = 600$ kPa affected by total suctions.....	163
Figure 4.22 Behaviour of Kaolin K13 clay under $p = 1000$ kPa affected by total suctions...	165
Figure 4.23 Behaviour of saturated M35 clay under various mean effective stresses.....	167
Figure 4.24 Failure mode of saturated remoulded M35 clay under $p' = 1000$ kPa.....	168
Figure 4.25 Relative humidity and total suction (M35, NaCl) before triaxial tests.....	169
Figure 4.26 Mechanical behaviour of unsaturated M35 clay under $s_0 = 38$ MPa.....	170
Figure 4.27 Photographs and XR- $\mu$ CT images of specimen M35_S38_unconfined.....	173
Figure 4.28 Photographs and XR- $\mu$ CT images of specimen M35_S38_P1000.....	173



# General introduction

## Background

Clay is a fine-grained geomaterial composed of one or more clay minerals (e.g., kaolinite, illite and montmorillonite) with possible traces of quartz, metal oxides and organic matter. It is extensively distributed on the Earth's surface. Natural clay usually comes from the weathering, decomposition and transportation of rocks and soils (Velde and Meunier, 2008). Clay is very plastic due to fine grain sizes and high water contents, and it becomes hard, brittle and non-plastic after drying. As a fraction, clay influences the plasticity, viscosity, permeability and chemical properties of soil.

Because it is cheap and readily available, clay has been widely used as an engineering material for a very long history. For instance, clay is directly used to construct buildings and structures or serves as roadbeds and foundations in the field of Civil Engineering (Ward-Harvey, 2009). Another example is, in Environmental Engineering, clay is adopted as natural barriers in landfills and nuclear waste storages against the seepage of toxic liquids (Delage et al., 2010). The complex nature of clay, however, has challenged engineers to understand how remoulded clays mechanically behave and what the microscopic mechanisms are under various loading conditions.

It is commonly accepted that the microstructure of clay is significantly affected by the macroscopic loading and deformation. On the other hand, many previous studies have provided sufficient evidences that the physical and mechanical properties of clay such as the shear strength, compressibility, permeability and water-retention ability are highly related to the microstructure. Therefore, it is feasible to give new insight into the mechanical behaviour of remoulded clay through a multiscale investigation.

## Research objectives

This dissertation involves a multiscale experimental investigation of the mechanical behaviour of both saturated and unsaturated remoulded clays. The overall goal of this work is

to increase the understanding of the volumetric deformation of saturated remoulded clays on different triaxial stress paths and the shear strength of unsaturated remoulded clays on various high suction-stress paths. The main objectives can be divided into the following three parts.

The first objective is to examine the influence of triaxial stress paths on the mechanical behaviour and microstructural evolution of saturated remoulded clays at a stress level below the critical state line. This is achieved through four consolidated drained triaxial compression tests and a series of microscopic investigations (i.e., scanning electron microscopy observations, mercury intrusion porosimetry tests and X-ray microtomography scans) on the fully saturated remoulded Kaolin K13 clay. The triaxial tests are performed considering a given stress level in the  $(p', q)$  plane reached by following two different stress paths (i.e., the conventional constant  $\sigma'_3$  stress path and the purely deviatoric stress path).

The second objective is to identify the microscopic mechanism of dilatancy phenomenon in strongly overconsolidated saturated remoulded clays. To this end, additional consolidated drained triaxial compression tests are performed on a normally consolidated clay specimen and an overconsolidated clay specimen at a second stress level near the estimated critical state following the purely deviatoric stress path. Microscopic investigations are also carried out on these additional specimens using scanning electron microscopy and mercury intrusion porosimetry. The obtained results combined with the previous findings are used to interpret the dilatancy phenomenon from both macroscopic and microscopic points of view.

The third objective is to investigate the hydromechanical behaviour, in particular, the shear strength and volume change of unsaturated remoulded clays on different high suction-stress paths. This is achieved through a series of unconsolidated undrained triaxial tests on two remoulded clays (i.e., Kalin K13 and M35). The clay specimens are pre-imposed with two levels of suction (i.e., 10 MPa and 38 MPa) using the vapour equilibrium method. The specimens with initial suctions are then sheared under different mean stresses (i.e., 200 kPa, 600 kPa and 1000 kPa) using a conventional triaxial testing system. The suction changes around the specimen ends are measured by hygrometers during triaxial loading.

## **Organisation of the dissertation**

This dissertation is organised into five chapters in addition to the current general introduction, each of them has a separate and distinct function, as given below.

Chapter 1 presents a general review on the published works related to the topics of this research. The state of the art is presented from the mechanical behaviour of saturated clays to that of unsaturated clays and from macroscopic phenomena to microstructural characteristics.

Chapter 2 provides the mineralogical, chemical and physical properties of two clay materials (i.e., Kaolin K13 and M35) and then presents a detailed description of both macroscopic and microscopic experimental methodologies applied in this research.

Chapter 3 examines the multiscale behaviour of a saturated remoulded clay (i.e., Kaolin K13) under triaxial loading. Specific emphases are placed on the influence of stress paths on both macro and micro behaviour as well as the microscale mechanism of dilatancy.

Chapter 4 presents an experimental study on the hydromechanical behaviour especially the shear strengths and volume changes of two unsaturated remoulded clays (i.e., Kaolin K13 and M35) under triaxial loading considering different initial suctions and mean stresses.

Finally, a chapter is presented to summarise the main conclusions that can be drawn from this research and provide recommendations for future study.



## Chapter 1

# Literature review

<b>1. Dilatancy phenomenon.....</b>	<b>7</b>
1.1 Definition of dilatancy.....	7
1.2 Dilatancy of granular materials.....	8
1.2.1 General behaviour.....	8
1.2.2 Dilatancy interpretation.....	11
1.3 Dilatancy of remoulded clay.....	12
1.3.1 General behaviour.....	12
1.3.2 Literature review.....	14
<b>2. Macro-micro relationship of remoulded clay.....</b>	<b>17</b>
2.1 characterisation of particle organisation.....	17
2.1.1 Under simple or direct shear.....	17
2.1.2 Under one-dimensional consolidation.....	19
2.1.3 Under isotropic and triaxial loading.....	21
2.2 characterisation of micropore structure.....	24
2.2.1 Pore morphology.....	24
2.2.2 Pore size distribution and porosity.....	26
2.3 characterisation of local cracks.....	28
<b>3. Mechanical behaviour of unsaturated clay affected by suction.....</b>	<b>29</b>
3.1 Basic concepts regarding unsaturated clay.....	30
3.1.1 Definition of soil suction.....	30
3.1.2 Effective stress and shear strength of unsaturated soil.....	31
3.1.3 Triaxial testing types for unsaturated soil.....	32
3.2 Shear strength and volume change of unsaturated clay.....	33
3.2.1 Volume change of unsaturated clay during consolidation.....	33
3.2.2 Shear strength of unsaturated clay under triaxial loading.....	36
3.2.3 Volume change of unsaturated clay under triaxial loading.....	40
<b>4. Summary.....</b>	<b>43</b>



This chapter presents a review of the published works that relate to the topics of this research. Section 1 introduces the definition of dilatancy and presents the dilatancy phenomenon in granular materials and remoulded clay. Section 2 presents the microstructural evolution of remoulded clay and its relation to macromechanical behaviour under various loading conditions. Section 3 introduces some basic concepts regarding unsaturated soil and presents some previous experimental results on the shear strength and volume change of clay affected by suction. Finally, a conclusion section is presented.

## **1. Dilatancy phenomenon**

Dilatancy is an important phenomenon of soil, which clearly distinguishes soil from other engineering materials. A good understanding of the influence factors and mechanisms of dilatancy is of great significance for the development of constitutive models and the determination of shear strength parameters of soil.

### **1.1 Definition of dilatancy**

Dilatancy has been known for more than one century since the work of Reynolds (1885). Osborne Reynolds explained the existence of dilatancy in sand by the phenomenon of colour change when walking on seashore sand. He noticed that the sand whitens or appears momentarily to dry around the foot as one walks over it after the tide ebbs. As the foot imposes a normal pressure on the sand, the sand distorts by letting grains ride up over each other. This leads to the expansion of sand, sucking water to fill the induced void space. When the foot is removed, the water rises to the surface again because of the elimination of distorting forces and the contraction of sand.

Two different definitions of dilatancy can be found in the literature. The first definition is a classical one, which defines dilatancy as the change in the volume of pore space of soil during shearing. Typically, as illustrated in Figure 1.1, if the soil volume decreases or  $\varepsilon_v > 0$  ( $\varepsilon_v$  is the volumetric strain) under shear, the phenomenon is termed contraction (negative dilatancy). On the other hand, if the soil increases in volume or  $\varepsilon_v < 0$  under shear, the phenomenon is termed dilation (positive dilatancy). In general, subjected to a shear stress, loose sands, soft clays and normally consolidated or slightly overconsolidated clays contract, while medium to dense sands and highly overconsolidated clays dilate.

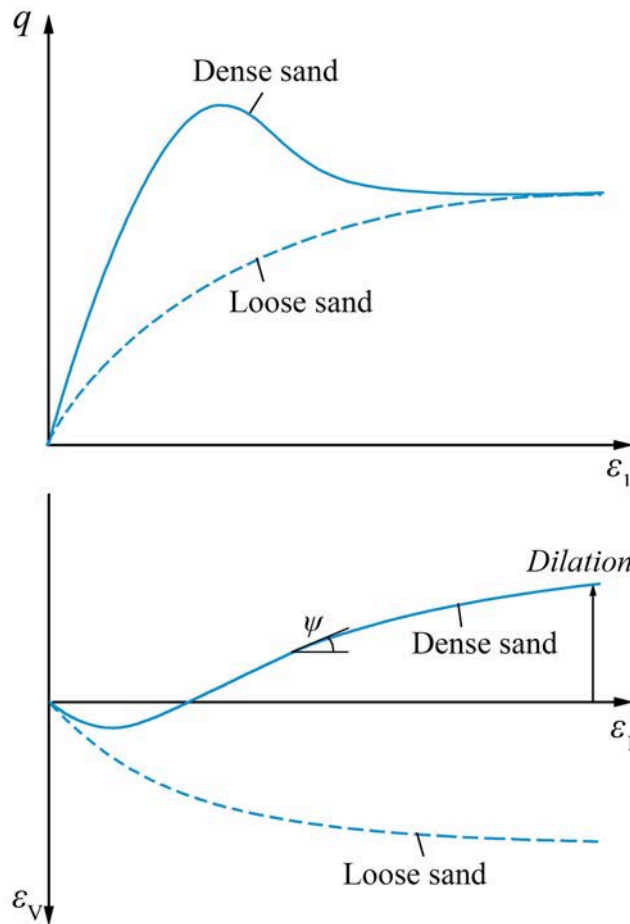


Figure 1.1 Dilatancy phenomenon in sand during shearing

The second one defines dilatancy as the ratio of the volumetric strain increment ( $d\varepsilon_v$ ) to the shear strain increment ( $d\varepsilon_1$ ):  $\tan(\psi) = - (d\varepsilon_v/d\varepsilon_1)$ ,  $\psi$  is the angle of dilation. Generally,  $\psi_{\max} < 0$  ( $\psi_{\max}$  is the maximum angle of dilation) represents contractive behaviour and  $\psi_{\max} > 0$  represents dilative behaviour. The second definition is used for example by Rowe (1962) and others to investigate the stress-dilatancy relationship of soil. The above two definitions of dilatancy are related, in that the first one is simply the integral of the second over the stress path imposed on the soil (Jefferies and Been, 2015).

## 1.2 Dilatancy of granular materials

### 1.2.1 General behaviour

After the work of Reynolds (1885), the dilatancy phenomenon especially that in granular materials such as sand and gravel has received great attention. Plenty of experimental studies of granular materials have indicated that the dilatancy phenomenon significantly depends on the soil density (or porosity) and confining stress (Schanz and Vermeer, 1996; Been and

Jefferies, 2004; Guo and Su, 2007; Esposito III and Andrus, 2016). Generally, the denser the granular material or the smaller the confining stress, the more evident the dilatancy phenomenon. The work of Verdugo and Ishihara (1996) and Lancelot et al. (2006) indicated that the dense sand may exhibit behaviour similar to that of a loose sand when it is sheared under a high cell pressure, while a loose sand may behave like a dense sand when it is sheared under a low cell pressure (Figure 1.2).

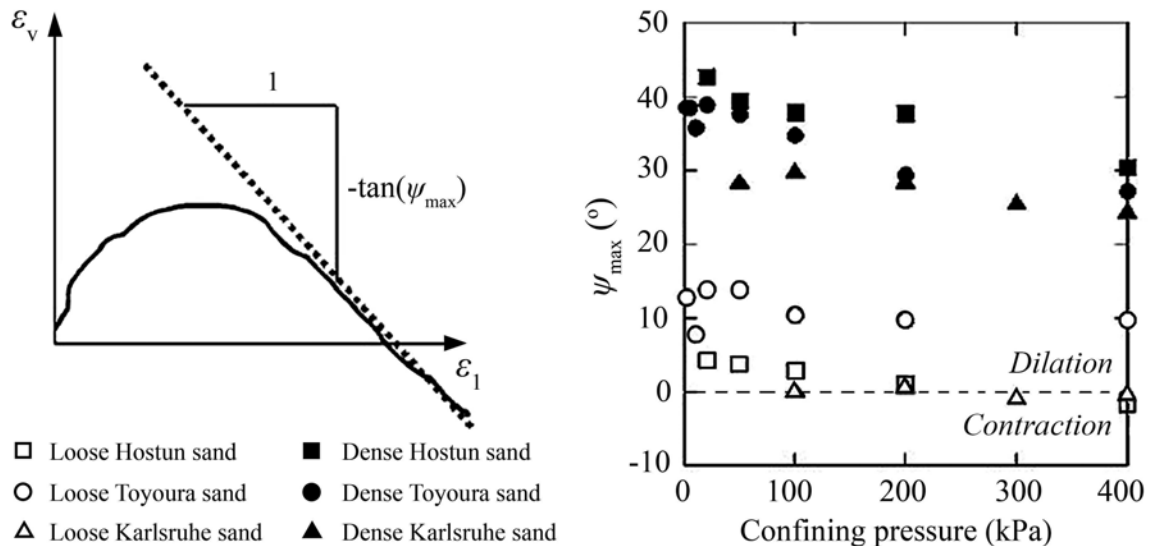


Figure 1.2 Triaxial test results of different sands (Lancelot et al., 2006)

It is also noted by many researchers such as Wan and Guo (2001) and Esposito III and Andrus (2016) that the dilatancy of granular materials is closely related to the soil fabric. Esposito III and Andrus (2016) performed drained triaxial compression tests on intact and remoulded specimens of a Pleistocene age sand. The authors observed completely different volumetric behaviour with respect to the intact specimens and remoulded specimens. Under a confining effective stress of 138 kPa, they noticed that the intact specimen shows positive dilatancy while the remoulded one shows negative dilatancy, as shown in Figure 1.3.

Moreover, the dilatancy phenomenon of granular materials also depends on the particle shape (Rothenburg and Bathurst, 1992; Ng, 2001; Liu and Matsuoka, 2003; Powrie et al., 2005; Alshibli and Cil, 2017) and grain size distribution (Kokusho et al., 2004; Simoni and Houlsby, 2006; Alshibli and Cil, 2017). For example, Varadarajan et al. (2003) carried out consolidated drained triaxial tests on a rounded granular material and an angular granular material considering different grain sizes and confining pressures. Their results showed that the volume change behaviour of the two materials is significantly different from each other

(see Figures 1.4-1.5). During triaxial shearing, particle rearrangements take place in the rounded material due to the sliding of the rounded particles. The breakage of the rounded particles further enhances the volume compression. Therefore, this material exhibits continuous contraction throughout the test (Figure 1.4). By contrast, in the angular material, volume compression first takes place due to the movement and breakage of particles. As the shear strain increases, the dilative behaviour gradually develops due to the high degree of interlocking among the angular particles (Figure 1.5).

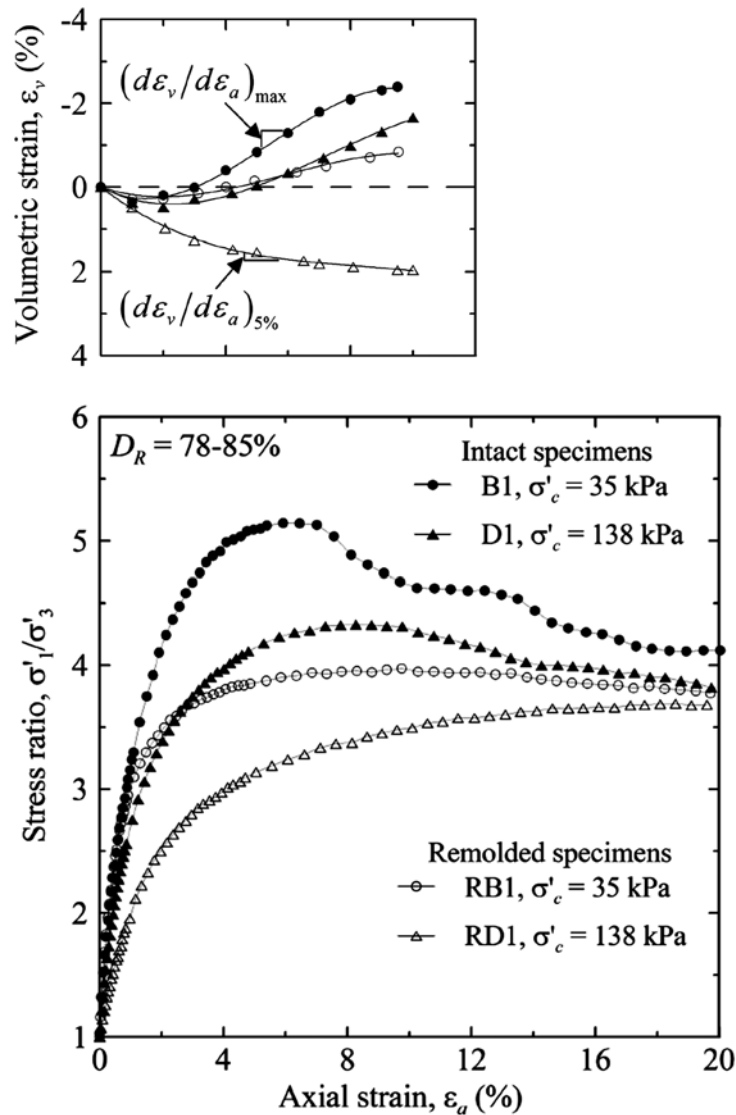


Figure 1.3 Triaxial test results of a Pleistocene age sand (Esposito III and Andrus, 2016)

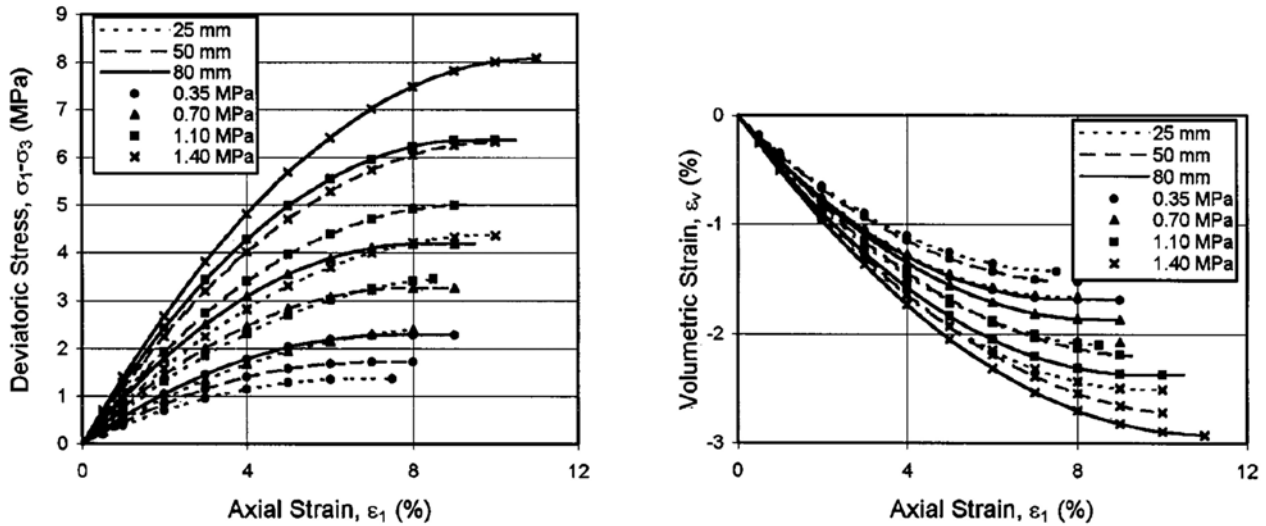


Figure 1.4 Triaxial test results of a rounded material (Varadarajan et al., 2003)

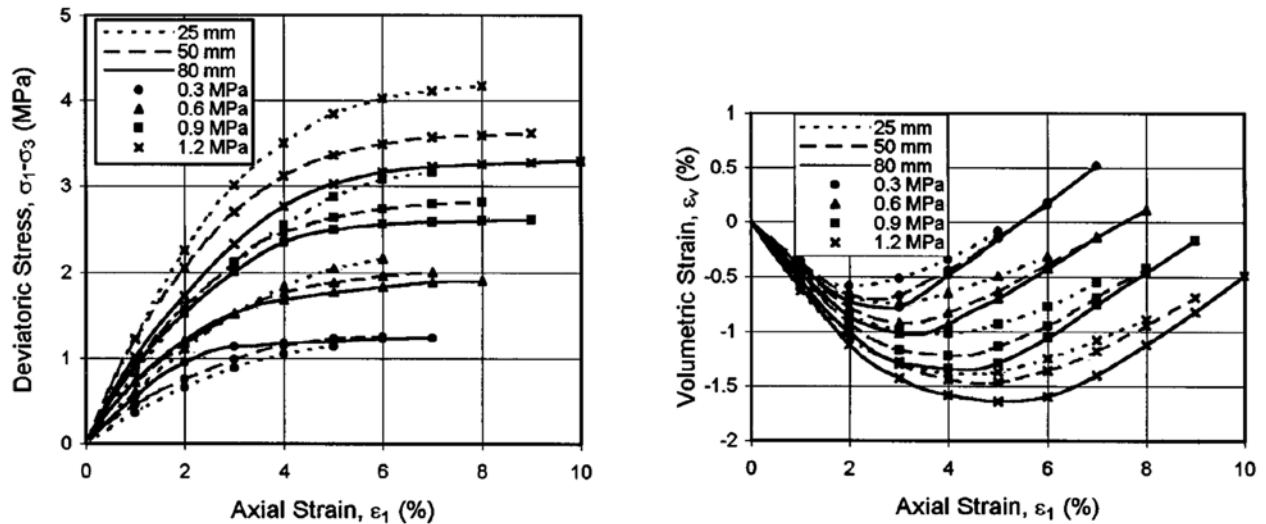


Figure 1.5 Triaxial test results of an angular material (Varadarajan et al., 2003)

### 1.2.2 Dilatancy interpretation

The dilatancy mechanism of granular materials may be explained using the sawtooth model (Newland and Allely, 1957; Revuzhenko, 2007), as shown in Figure 1.6. During shearing, the particles may interlock, translate, and/or rotate as they interact with each other. When the granular material is loose, the shear stress makes the particles fall into large voids. Thus, the apparent height of the material decreases. By contrast, when the material is dense, the particles climb up the neighbouring particles due to the interlocking, and thus the overall volume increases. After shearing, the particles that have not completely climbed up drop to the initial position, leading to recoverable volumetric deformation; the particles have completely climbed up the adjacent particles and become stable, leading to unrecoverable

volumetric deformation.

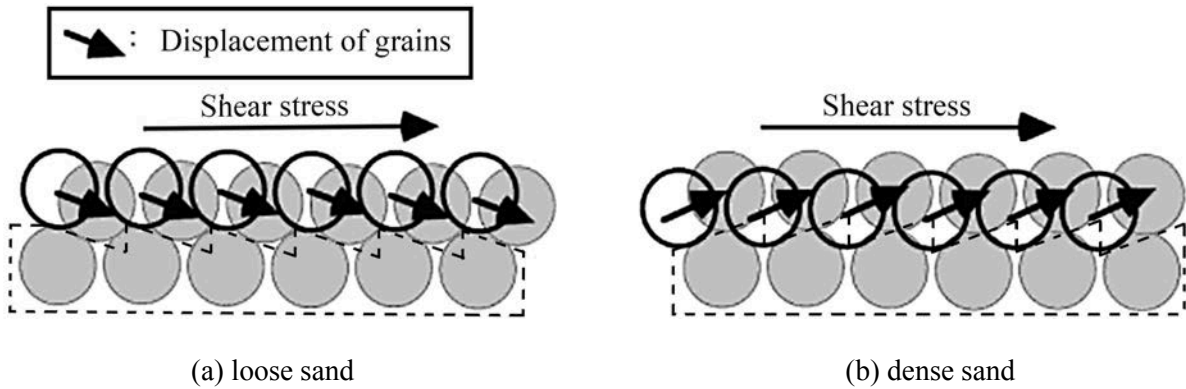


Figure 1.6 Sawtooth model for granular materials (Revuzhenko, 2007)

The local mechanism of dilatancy phenomenon in granular materials under triaxial loading may also be interpreted with the sketch shown in Figure 1.7 (Rowe, 1962; Chi et al., 2009). When the granular material is in a dense state (state I) under a confining pressure of  $\sigma'_3$ , the increase in axial stress  $\sigma'_1$  (or deviatoric stress  $q = \sigma'_1 - \sigma'_3$ ) makes it be compressed in the axial direction and expanded in the lateral direction (state II), causing the development of volumetric dilation. Nevertheless, when the granular material is loose (state II) under a confining pressure of  $\sigma'_3$ , the increase in axial stress  $\sigma'_1$  (or deviatoric stress  $q = \sigma'_1 - \sigma'_3$ ) also makes it be compressed in the axial direction and expanded in the lateral direction (state III), but in this case the material shows contraction.

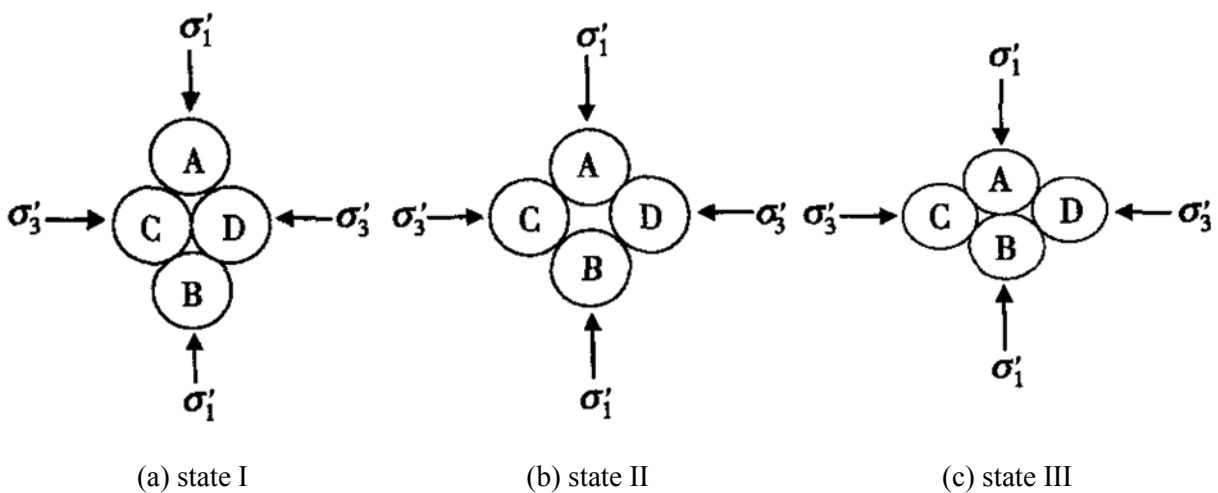


Figure 1.7 Microscale interpretation of dilatancy of granular materials (Chi et al., 2009)

### 1.3 Dilatancy of remoulded clay

#### 1.3.1 General behaviour

In the case of clay materials, numerous experimental results have shown that the dilatancy phenomenon is closely dependent on the loading history. The loading history may be described by the overconsolidation ratio (OCR), which is defined as:

$$\text{OCR} = \frac{\sigma'_c}{\sigma'} \quad (1.1)$$

where  $\sigma'_c$  is the pre-consolidation effective pressure;  $\sigma'$  is the actual effective pressure.

According to the loading history (i.e., overconsolidation ratio), the clay can be divided into two types: (i) the normally consolidated clay, whose actual effective overburden pressure is the maximum pressure over the history, namely  $\text{OCR} = 1.0$ ; (ii) the overconsolidated clay, whose actual effective overburden pressure is less than the maximum pressure that the soil experienced in the past, namely  $\text{OCR} > 1.0$ .

Figure 1.8 shows the typical relationship between the volumetric strain and the axial strain of a remoulded clay during conventional consolidated drained triaxial tests. One can notice that a highly overconsolidated clay usually shows similar behaviour as a dense sand and a normally consolidated clay exhibits similar behaviour as a loose sand. In other words, the volumetric strain of a normally consolidated clay is always positive showing contractive behaviour (negative dilatancy); however, the volumetric strain of a highly overconsolidated clay is negative showing dilative behaviour (positive dilatancy) except for the beginning at which the volumetric strain is slightly positive.

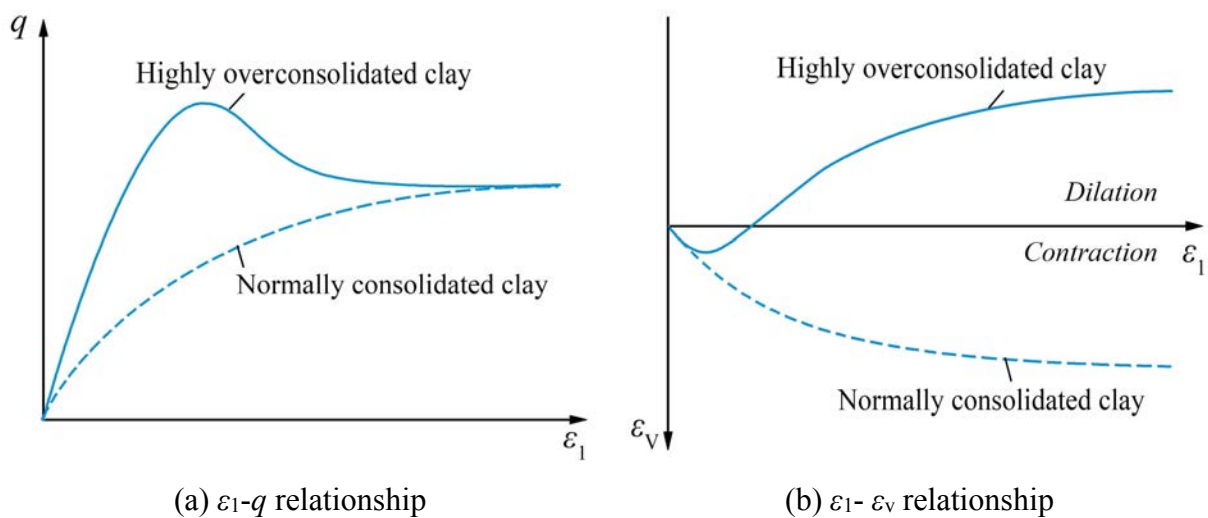


Figure 1.8 Typical results of triaxial tests on a remoulded clay

1.3.2 Literature review

The overconsolidation ratio is a generally recognised factor affecting the dilatancy behaviour of clay (Henkel, 1956; Hattab and Hicher, 2004; Ighil Ameer, 2016; Gao et al., 2016; Gu et al., 2016; Zhao et al., 2018). The triaxial tests performed by Henkel (1956) on the remoulded London clay and Weald clay indicated that the volume changes occurred during shearing are profoundly altered by the consolidation history of the clay material. The author noted that the normally consolidated clay specimens contract throughout the test, while the heavily overconsolidated clay specimens with an overconsolidation ratio of 24 are initially contractive and then dilative, and the dilative behaviour persists until the failure of specimens. Hattab and Hicher (2004) carried out consolidated drained triaxial tests on remoulded Kaolin P300 clay on the purely deviatoric stress path (i.e.,  $p' = \text{constant}$ ). They demonstrated that a clay specimen with an overconsolidation ratio less than 2.5 contracts while a clay specimen with an overconsolidation ratio larger than 2.5 dilates during triaxial loading (see Figure 1.9). Similar results were also obtained for example by Zhao et al. (2018) on the remoulded Kaolin K13 clay (see Figure 1.10).

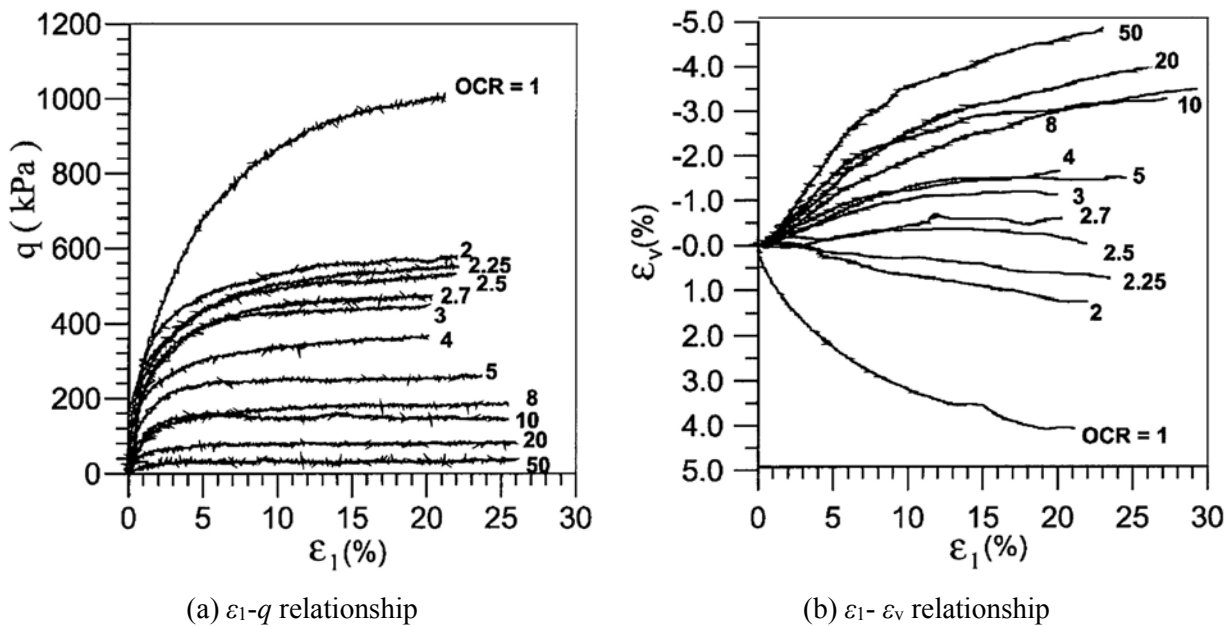


Figure 1.9 Triaxial test results of remoulded Kaolin P300 clay (Hattab and Hicher, 2004)

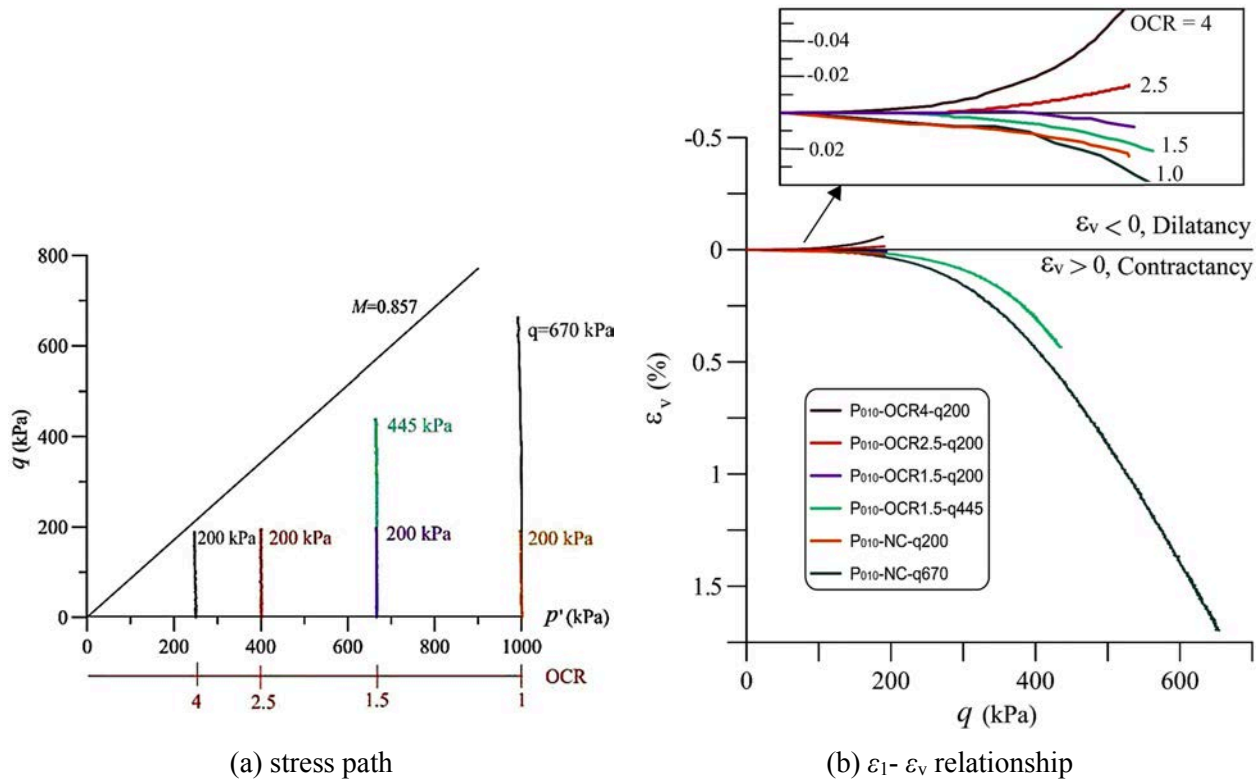


Figure 1.10 CD triaxial test results of remoulded Kaolin K13 clay (Zhao et al., 2018)

However, the overconsolidation ratio is not the only factor that influences the dilatancy phenomenon of remoulded clays. In fact, many previous experimental works have shown that the dilative behaviour of clay is also related to the stress ratio ( $\eta = q/p'$ ) (Shimizu, 1982; Biarez and Hicher, 1994), the stress path (Mofiz and Islam, 2010), the Lode angle (Ye et al., 2013) and the intermediate principal stress (Dai et al., 2017).

Shimizu (1982) performed triaxial tests on Fujinanori clay of different overconsolidation ratios along the constant mean effective stress path. He showed that the  $(p', q)$  plane could be divided into several regions of contractive and dilative behaviour according to the stress ratio ( $\eta = q/p'$ ) and the overconsolidation ratio. The triaxial test results of Hattab and Hicher (2004) further highlighted three domains (i.e., no volume change domain, dilatancy domain and contraction domain) in the  $(p', q)$  plane (Figure 1.11). The no volume change domain corresponds to the volumetric pseudo-elastic domain proposed by Biarez and Hicher (1994). According to the three-domain concept, a remoulded clay specimen exhibits dilatancy if the stress state falls in the dilatancy domain; it exhibits contraction if the stress state is in the contraction domain; and it shows little volumetric deformation if the stress state locates in the no volume change domain. Notice that in the last case (in the no volume change domain), only the mechanism of the isotropic part of the stress tensor is activated (Hattab and Hicher,

2004).

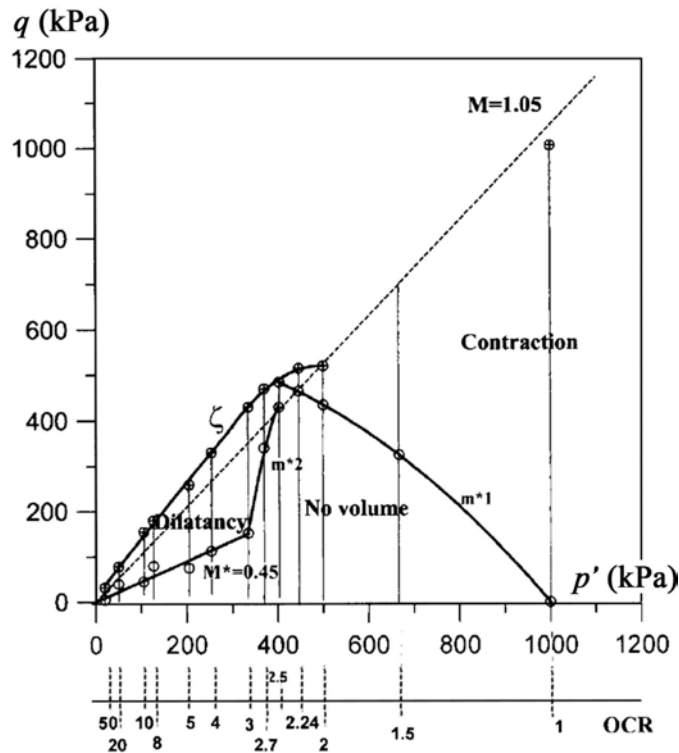


Figure 1.11 Three volume change domains of remoulded clay (Hattab and Hicher, 2004)

Ye et al. (2013) investigated the influence of Lode angles on the shear strength and dilatancy of a remoulded clay on the purely deviatoric stress path ( $p' = 196$  kPa) using a true triaxial cell. Their results showed that the normally consolidated clay exhibits contractive behaviour (i.e., negative dilatancy) at various Lode angles (see Figure 1.12). However, the overconsolidated clay ( $OCR = 3.5$ ) at a small Lode angle initially exhibits contractive behaviour (i.e., negative dilatancy) but then shows dilative behaviour (i.e., positive dilatancy) just before the deviatoric stress reaches the peak value. At a large Lode angle, the overconsolidated clay shows dilative behaviour (i.e., positive dilatancy) from the beginning of the test. Their results indicated that an increase in the Lode angle restrains the volumetric contraction and enhances the volumetric dilation of remoulded clays.

The dilatancy phenomenon of sand has been well known, and several models have been proposed in the literature to interpret the dilatancy mechanism of granular materials. However, clay is a complicated multiscale geomaterial that differs greatly from sand, its dilatancy mechanism remains to be further explored.

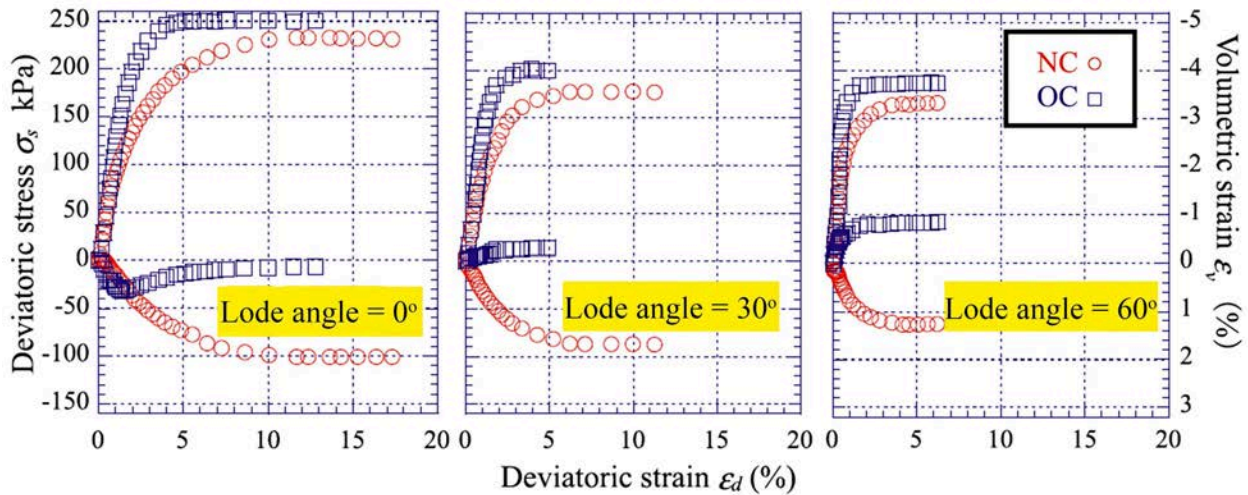


Figure 1.12 Influence of Lode angles on dilatancy of a remoulded clay (Ye et al., 2013)

## 2. Macro-micro relationship of remoulded clay

It is generally accepted that the mechanical behaviour of clay such as shear strength and deformation highly depends on the microstructure. On this basis, a multiscale investigation may help establish the relationship between the macroscopic behaviour and the microstructural change of remoulded clay and reveal the local mechanisms of some macroscopic phenomena. A variety of microscopic techniques such as X-ray diffraction, optical microscopy, mercury intrusion porosimetry (MIP), scanning electron microscopy (SEM), transmission electron microscopy (TEM), X-ray computerized tomography (XR-CT) and X-ray microtomography (XR- $\mu$ CT) are available for this purpose.

### 2.1 Characterisation of particle organisation

#### 2.1.1 Under simple or direct shear

The microstructure of clay subjected to simple or direct shear has been investigated by many researchers using optical microscopy and the SEM technique (Morgenstern and Tchalenko, 1967c; Ramiah and Purushothamaraj, 1971; Czurda and Hohmann, 1997; Takizawa et al., 2005; Hue et al., 2010).

Morgenstern and Tchalenko (1967c) studied the microstructural evolution of a remoulded kaolin with original horizontal fabrics under direct shear using an optical microscope. During the shear tests, an initial rotation of kaolin particles associated with a non-homogeneous discontinuity are first exhibited, and then a shear failure is observed with the increase in

relative shear displacement (see Figure 1.13). However, they noted that different shear directions lead to no significant difference in the drained strength of the material. Similar results were also obtained by other researchers such as Ramiah and Purushothamaraj (1971), who investigated the effect of initial structures on the residual strength of kaolinite clay. The shear test results of Ramiah and Purushothamaraj (1971) showed that the residual strength of clay under a given effective normal pressure is independent upon the initial structure. This result is also reflected by the formation of a particular pattern of particle orientations in the residual state.

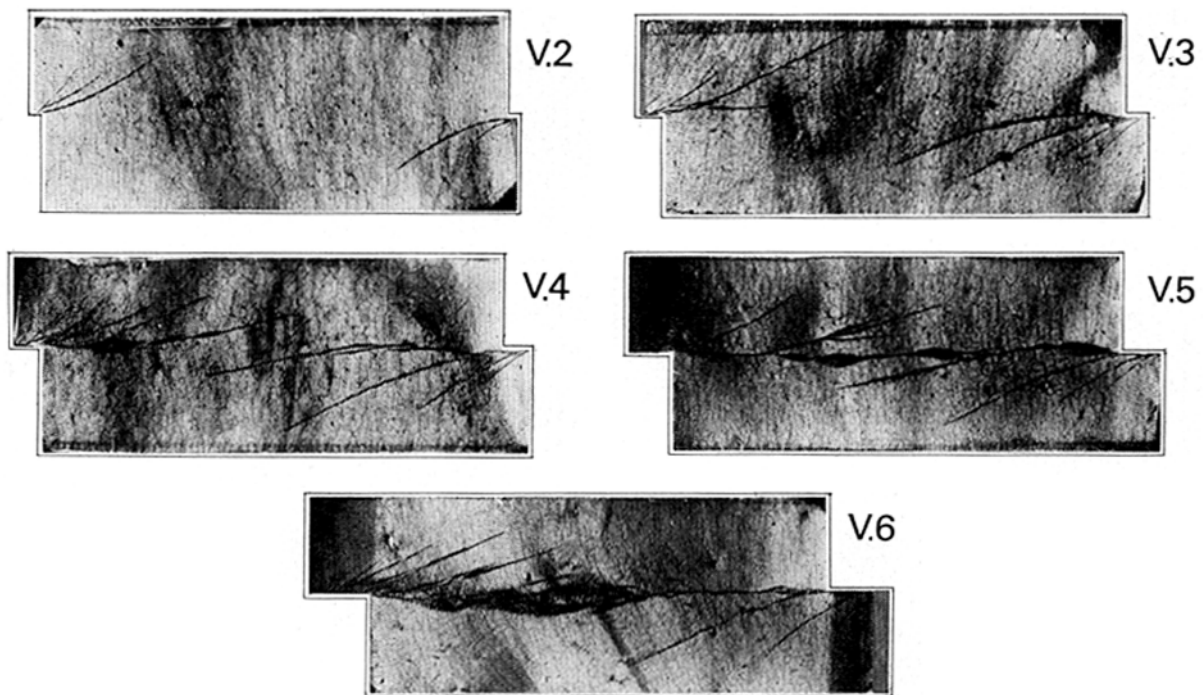
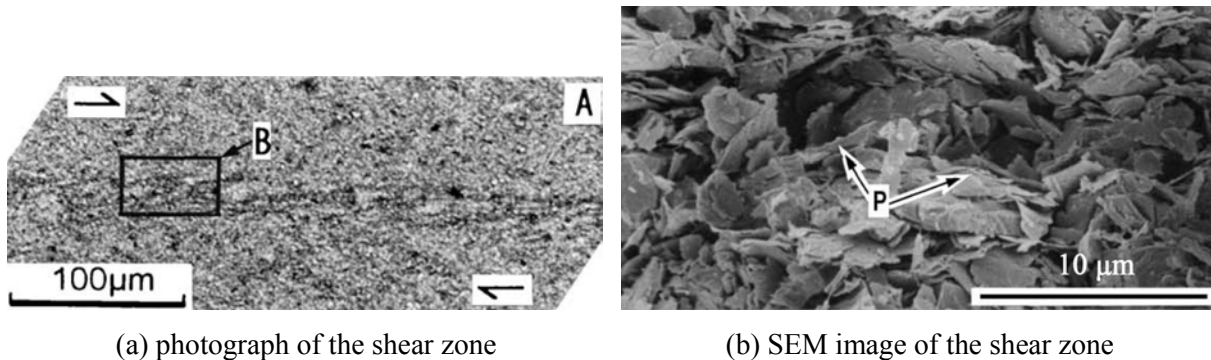


Figure 1.13 Image sequence of clay specimens sheared normal to original fabric  
(Morgenstern and Tchalenko, 1967c)

Czurda and Hohmann (1997) performed direct shear tests and then the SEM observations on frozen clayey soils. Their results indicated that the aggregates of frozen kaolinite are destroyed while those of smectite are compacted and remain practically intact, which leads to the differences in the shear strengths between kaolinite clay and smectite clay. Takizawa et al. (2005) also employed the direct shear tests and the SEM technique to investigate the microstructural change of normally consolidated and overconsolidated kaolin clays. They demonstrated that the microstructure in the shear zone is characterised by an oriented fabric with relatively small voids and large equidimensional pores similar to channels parallel to the shear direction (Figure 1.14). This microstructure appears in both normally consolidated and

overconsolidated specimens. The authors concluded that the dilatancy phenomenon of the kaolin clay is related to the formation of large pore-like channels and the change in packing of the particles. In addition, they reported that large pores are probably caused by the high fluid pressure in the shear zone.



(a) photograph of the shear zone

(b) SEM image of the shear zone

Figure 1.14 Fabric of the shear zone after direct shear test (Takizawa et al., 2005)

### 2.1.2 Under one-dimensional consolidation

The identification of the microstructural change of clay under consolidation has received wide attention in the literature (Morgenstern and Tchalenko, 1967a, b; Martin and Ladd, 1975; Bai and Smart, 1997; Djéran-Maigre et al., 1998; Hicher et al., 2000; Hue et al., 2010; Hammad, 2010; Kong et al., 2011; Sachan et al., 2013; Cotecchia et al., 2016).

Martin and Ladd (1975) used the X-ray diffraction technique to determine the development of induced anisotropy of a kaolinite clay during one-dimensional ( $K_0$ ) consolidation tests. The authors demonstrated that, when the kaolinite slurry is consolidated, the clay particles become oriented with their surface perpendicular to the direction of loading. Similar results of remoulded clays under one-dimensional consolidation were also revealed by other authors including Djéran-Maigre et al. (1998), Hicher et al. (2000), Kong et al. (2011) and Hammad (2010). For example, Hammad (2010) investigated the microstructural change of a remoulded kaolinite-montmorillonite mixture (named M35 by the author) during oedometer tests. He observed that most of the clay particles rotate towards the horizontal direction, developing an induced-anisotropic microstructure; this characteristic is especially pronounced in clay specimens under a high consolidation stress (Figure 1.15).

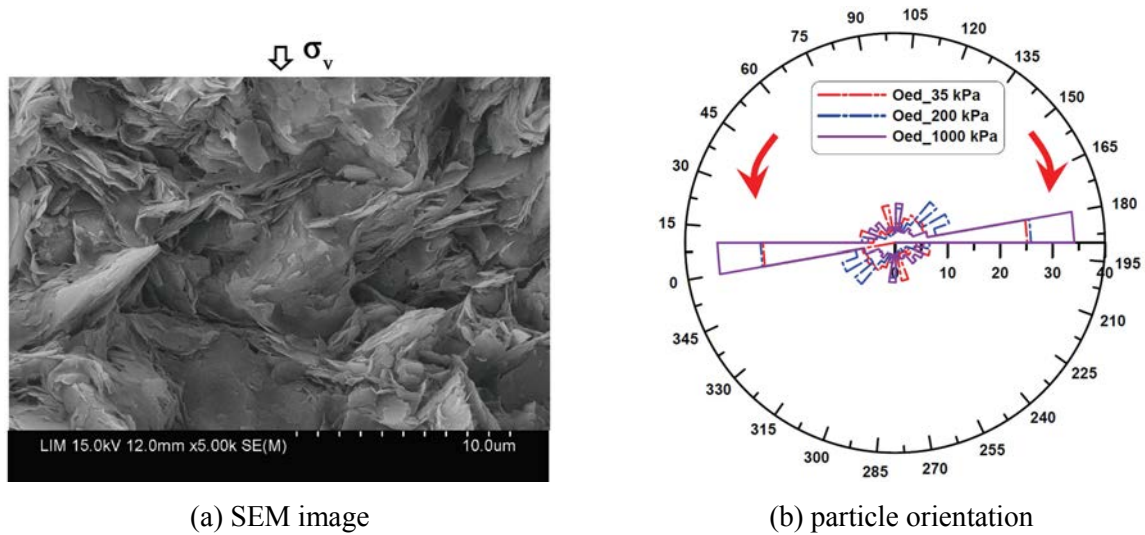


Figure 1.15 Fabric of remoulded M35 clay after oedometer tests (Hammad, 2010)

The experimental work of Martin and Ladd (1975) showed that changing the direction of the one-dimensional consolidation stress appears to vary the clay fabric; however, the stress increment required to completely rotate the original fabric into alignment normal to the new stress direction depends on the initial microstructure. On the other hand, Anandarajah et al. (1996) reported that the initial fabric anisotropy of kaolinite clay can not easily be erased or reversed by mechanical loading. They found that even an isotropic consolidation pressure as high as 10 times the prior  $K_0$ -consolidation pressure is inadequate to fully reorient the clay particles and render the soil completely isotropic with respect to the overall particle orientation, as shown in Figure 1.16 ( $P(\theta)$  is the normalised frequency corresponding to a given orientation  $\theta$ ).

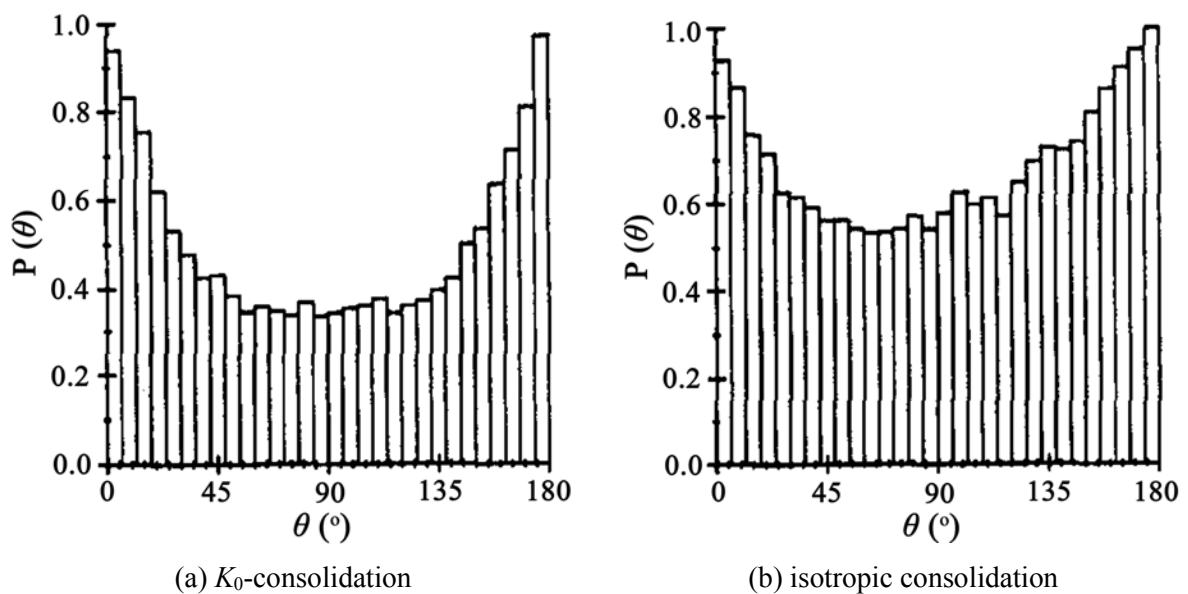
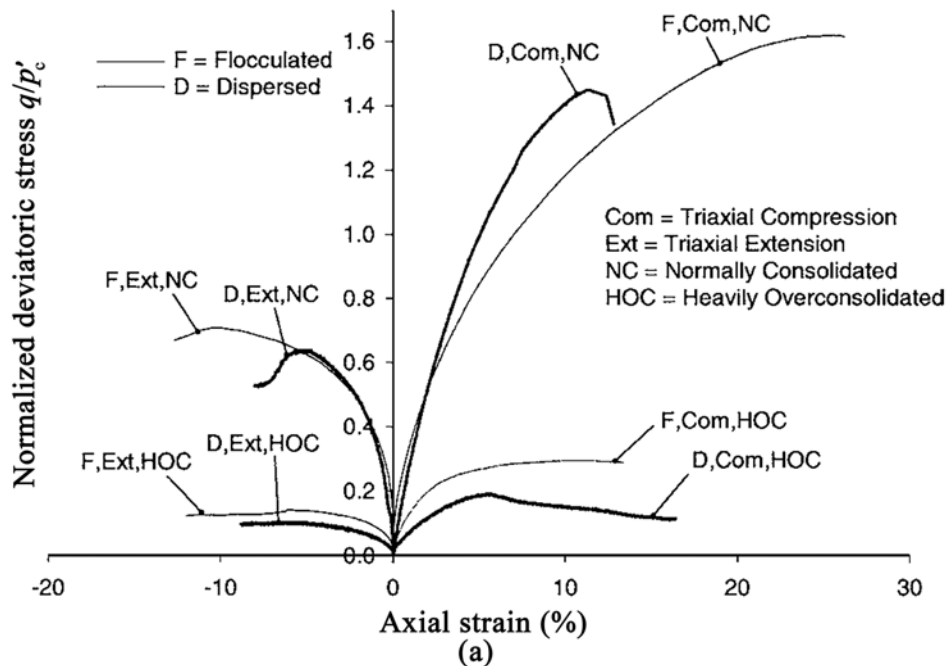


Figure 1.16 Particle orientation of a remoulded kaolinite clay (Anandarajah et al., 1996)

### 2.1.3 Under isotropic and triaxial loading

Over the past decades, many researchers have investigated and confirmed the fact that the initial microfabric of clay strongly affects its mechanical behaviour such as stress–strain relationship, shear strength and volume change (Nagaraj, 1964; Sridharan et al., 1971; Sachan and Penumadu, 2007; Mukherjee and Sachan, 2008; Kochmanová and Tanaka, 2010; Pillai et al., 2010, 2014; Sachan, 2013).

Sachan and Penumadu (2007) carried out a series of triaxial compression and extension tests on kaolin clay specimens with dispersed and flocculated microfabrics. They observed that the dispersed microfabric shows relatively sudden failure responses at low strain levels followed by significant softening compared to the flocculated microfabric (Figure 1.17a). They also noted that concerning both the normally consolidated and heavily overconsolidated specimens, the dispersed microfabric shows significantly less volumetric strains compared to the flocculated microfabric, indicating the dilatative or less contractive nature of the dispersed microfabric (Figure 1.17b). The dispersed microfabric can even lead to the dilation of normally consolidated specimens under drained extension conditions. Similar results were obtained by Pillai et al. (2010 and 2014) regarding the normally consolidated remoulded kaolinite clay.



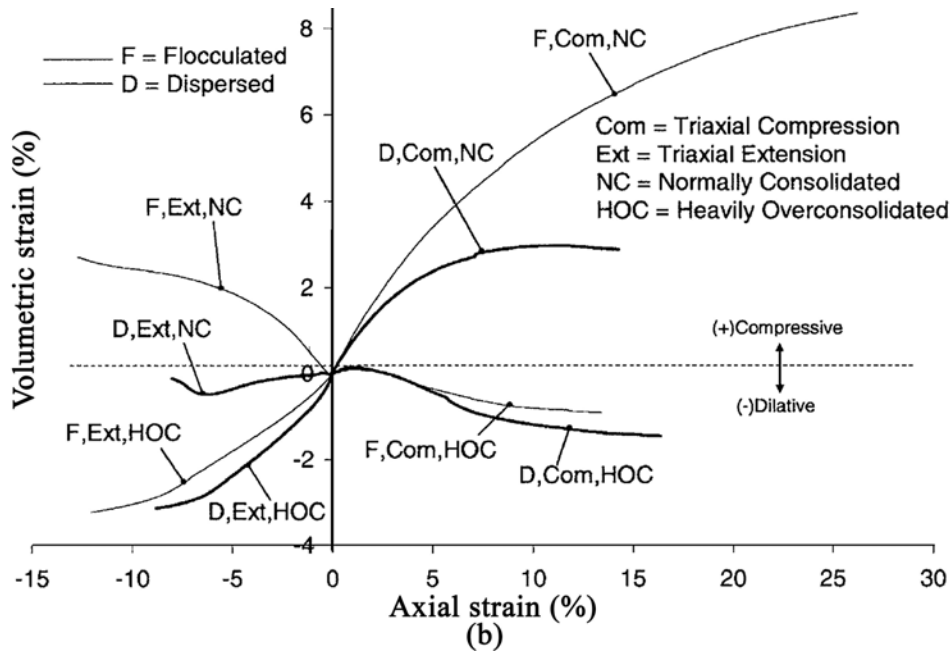


Figure 1.17 Influence of microfibrils on the mechanical behaviour of kaolin clay (Sachan and Penumadu, 2007)

The evolution of clay microstructure is found closely related to the imposed triaxial loading conditions (McKyes and Yong, 1971; Bai and Smart, 1997; Hicher et al., 2000; Sachan, 2007; Hammad, 2010; Raynaud et al., 2010; Hattab and Fleureau, 2010, 2011; Hattab, 2011; Hattab et al., 2015). The experimental work of Bai and Smart (1997) showed that the clay particles rotate and are arranged somewhat randomly during isotropic consolidation; they are preferentially oriented to form an anisotropic fabric during triaxial shearing. When studying the fabric evolution of remoulded clays, Hammad (2010) observed the isotropic organisation of clay particles under isotropic consolidation and the preferred orientation of clay particles under drained triaxial loading, as shown in Figure 1.18. These results are in agreement with those reported by other researchers such as Hicher et al. (2000). Bai and Smart (1997) also noted that the clay particle groups grow in size and rotate parallel to the failure plane at the end of triaxial shearing. This is consistent with the finding of McKyes and Yong (1971) that the clay particles inside the shear bands at failure align themselves along the failure plane. Furthermore, the SEM observation on the shear band of a triaxial test specimen performed by Raynaud et al. (2010) revealed that the macroscopic shear bands are composed of a “sandwich” of micro-shear bands of reoriented and non-reoriented particles. In the reoriented micro-shear bands, the clay particles rotate and tend to be parallel to the macroscopic shear band direction.

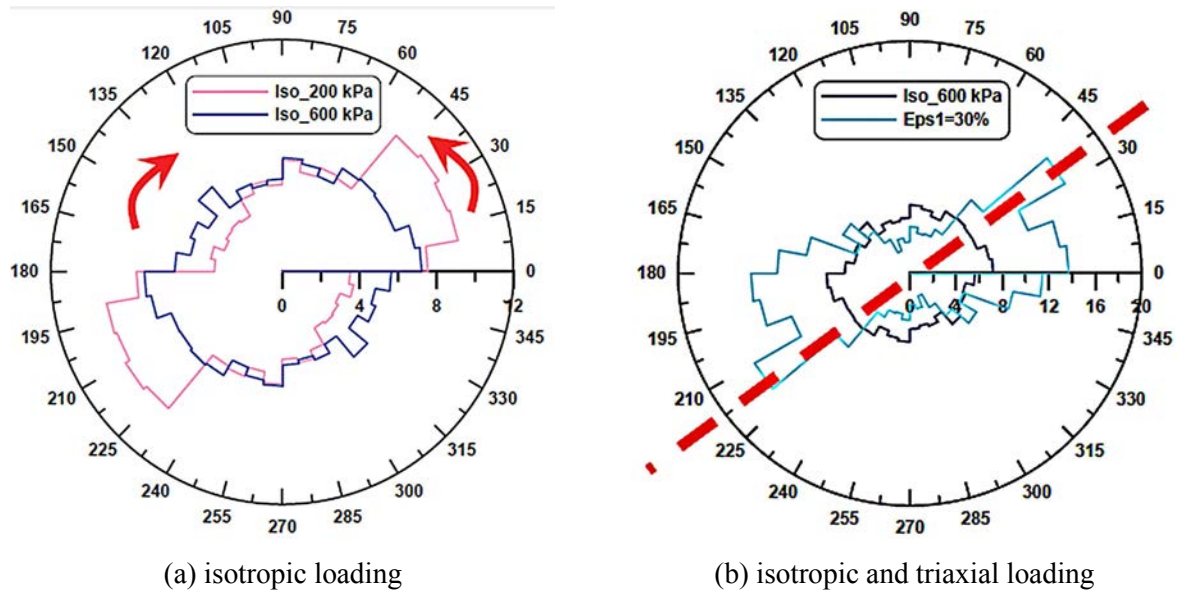


Figure 1.18 Rose diagrams of particle orientation of M35 clay (Hammad, 2010)

Hattab and Fleureau have made great efforts to identify the relationship between the macroscopic behaviour and the microstructural change of remoulded clays (Hattab and Fleureau, 2010 and 2011; Hattab et al., 2010; Hattab, 2011; Hattab et al., 2015). For instance, by performing triaxial tests and subsequently SEM observations on remoulded Kaolin P300 clay, Hattab and Fleureau (2010 and 2011) and Hattab et al. (2010) investigated the link between the phenomenological behaviour and the local mechanisms. They revealed that the structural anisotropy appears and develops itself when the deviatoric mechanism is activated until the ultimate critical state. They also noted that the clay specimen remains a relatively isotropic microstructure under isotropic loading as well as at a low axial strain under triaxial loading (see Figure 1.19). As the axial strain increases, the clay particles gradually show preferred orientation. At the critical state, Hattab (2011) and Hattab et al. (2015) revealed that local slip mechanisms could be activated in various points of the specimens of both kaolinite clay and montmorillonite clay. A marked result was obtained by the authors when the clay specimen is made of kaolinite and montmorillonite mixture. In this case, the slip mechanisms are developed mainly in the montmorillonite fraction even if this fraction constitutes a low percentage of the mixture.

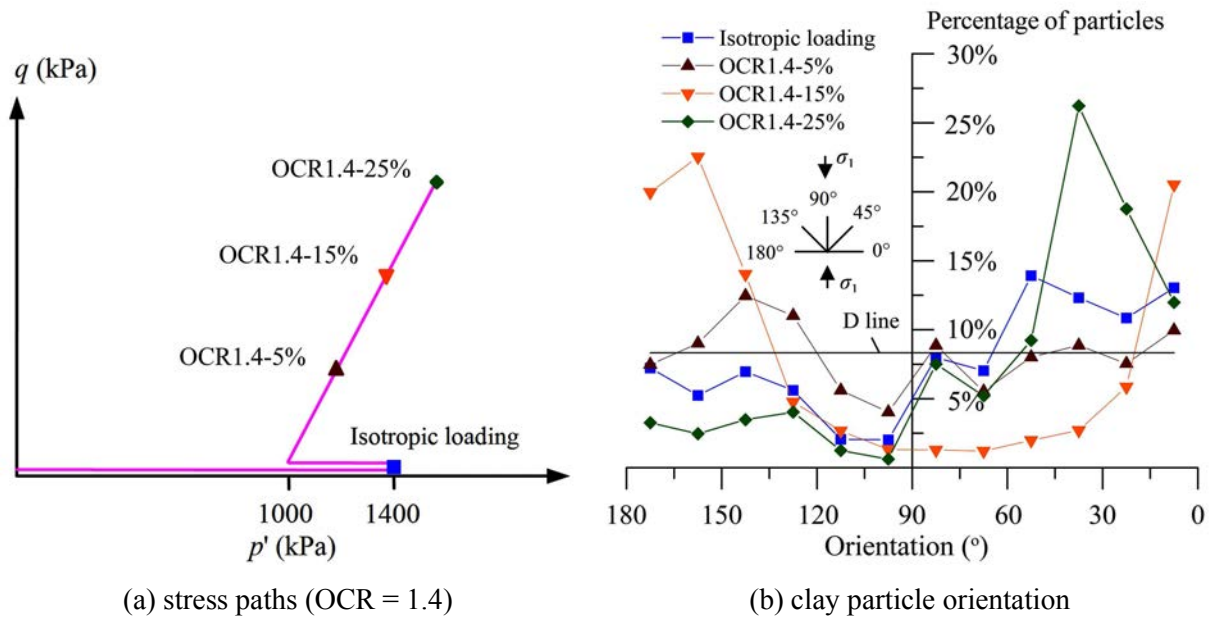


Figure 1.19 Particle orientation of remoulded clay specimens under triaxial loading (Hattab and Fleureau, 2010)

## 2.2 Characterisation of micropore structure

The micropore structure of clay can be described by two groups of parameters. On the one hand, the geometric form of pores is characterised by pore morphological parameters; on the other hand, the pore volume and area are quantified by porosity and pore size distribution (PSD).

### 2.2.1 Pore morphology

During the past several decades, the variation in pore morphology (e.g., pore shape, pore roughness, pore orientation and tortuosity of pore channels) of clay has been extensively studied (Ingles and Lafeber, 1966; Murphy et al., 1977; Vallejo, 1996; Cetin and Söylemez, 2004; Hammad, 2010; Liu et al., 2011; Pires et al., 2008; Tang et al., 2012; Zhao, 2017).

Under the compaction condition, Ingles and Lafeber (1966) and Murphy et al. (1977) investigated the pore morphology of cement-stabilised kaolin and Cavenham soil by means of an optical microscope. They both concluded that the pore shape and pore orientation of soils change considerably under compaction stresses. Based on the SEM technique and image processing method, Vallejo (1996) evaluated the fabric changes of intact Champlain clay subjected to consolidation. He found that the pores not only vary in size but also experience a change in their degree of roughness. Cetin and Söylemez (2004) and Liu et al. (2011)

conducted shear tests on a cohesive sandy silt-clay soil and Guangzhou clay, respectively. Afterwards, they examined the pore structure by analysing digital photos and SEM images of soils. They noticed that after shear tests the average form factors of pores decrease, the fractal dimensions of pores near the shear plane increase, and the orientation of particles and pores tends to the shear plane. The experimental results of Hammad (2010) showed that the pore orientation of a clay mixture (termed M35) composed of 65% kaolinite and 35% montmorillonite exhibits a similar evolution as the particle orientation of the same material: the microstructural anisotropy is induced and enhanced during triaxial shearing (see Figure 1.20, Iso = isotropic loading, Cis = triaxial shearing).

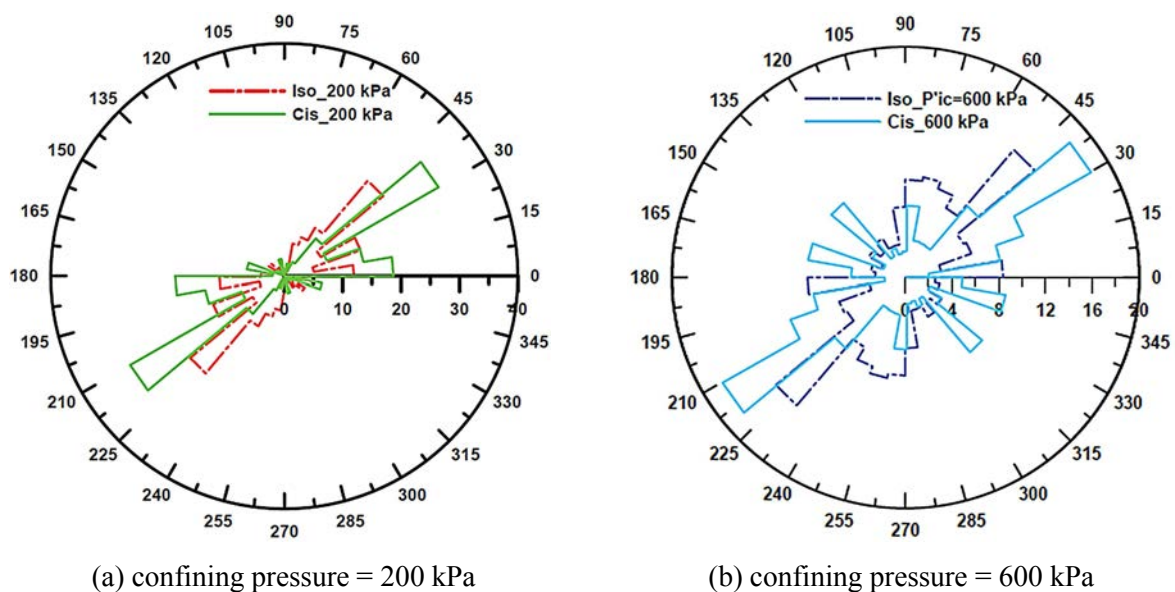


Figure 1.20 Pore orientation of M35 clay under triaxial loading (Hammad, 2010)

Pires et al. (2008) investigated the pore morphology of three natural soils subjected to wetting and drying cycles. They divided the pores into three categories, i.e., round pores, elongated pores and irregular pores. Their results indicated that the increase in pore areas after wetting and drying cycles is mainly due to the increase of large irregular pores. Using a hollow cylinder apparatus and an SEM apparatus, Wen et al. (2011) examined the microstructure of a soft clay before and after shearing on complex stress paths. The authors reported that both the average shape factor (the smaller the average shape factor, the more elongated the pores) and the fractal dimension (the larger the fractal dimension, the more complicated the pore structure) show a trend to decrease after the hollow cylinder torsional shear tests except for individual data (see Table 1.1). Tang et al. (2012) performed freezing tests and the SEM observations on Shanghai muddy clay. They stated that the pore shape and pore orientation change little due to freezing.

Table 1.1 Average pore shape factor and fractal dimension (Wen et al., 2011)

Condition	Coefficient of intermediate principal stress	Direction of major principal stress	Average shape factor	Fractal dimension
Initial state	/	/	0.67	1.23
Hollow cylinder torsional shear tests	0	0°	0.69	1.23
		5°	0.62	1.26
		20°	0.65	1.22
		35°	0.65	1.22
		50°	0.64	1.20
		60°	0.66	1.29
		0°	0.66	1.23
	0.5	5°	0.64	1.22
		20°	0.65	1.20
		35°	0.67	1.20
		50°	0.65	1.19
		60°	0.66	1.22

### 2.2.2 Pore size distribution and porosity

Identification of microporosity and PSD is another matter of great concern (Delage and Lefebvre, 1984; Lloret et al., 2003; Tarantino and De Col, 2008; Monroy et al., 2010; Liu et al., 2012; Hattab et al., 2013; Jiang et al., 2014; Hattab et al., 2015; Yu et al., 2016).

Using the microscopic techniques such as MIP and SEM, many researchers (e.g., Delage and Lefebvre, 1984; Lloret et al., 2003; and Monroy et al., 2010) revealed that the micropores in clay can be divided into two groups, i.e., the inter-aggregate pores and the intra-aggregate pores (Figure 1.21). Delage and Lefebvre (1984) further demonstrated that the inter-aggregate pores decrease in size during consolidation, while the intra-aggregate pores remain almost unchanged. Similar results have been reported by Griffiths and Joshi (1989), Tarantino and De Col (2008), Jiang et al. (2014), Yu et al. (2016) and others with respect to clays under compaction, shear tests, consolidation, triaxial tests and wetting and drying. For example, Tarantino and De Col (2008) performed MIP tests on a kaolin clay, which was previously

subjected to one-dimensional compaction. They stated that an increase in the compaction stress affects only the inter-aggregate porosity with the modal size of the inter-aggregate pores shifting from  $0.8 \mu\text{m}$  to  $0.7 \mu\text{m}$  (Figure 1.22).

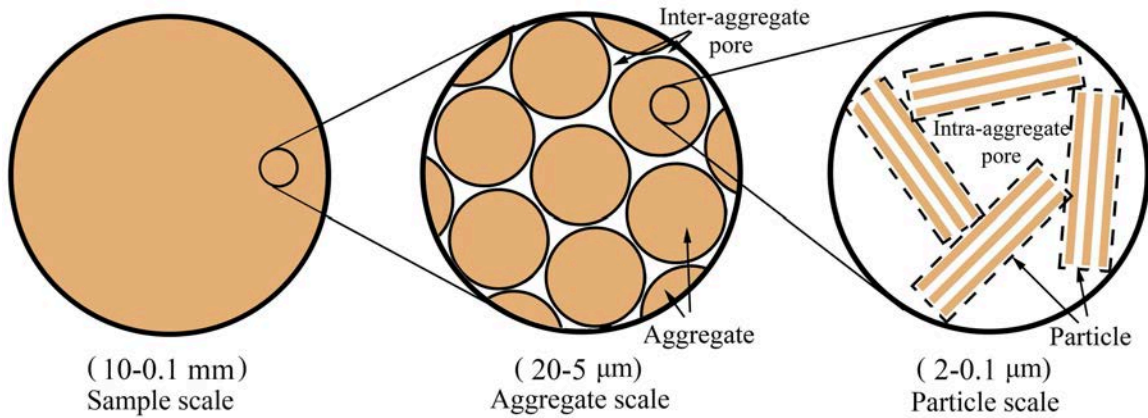


Figure 1.21 Sketch of the multiscale pore structure of clay

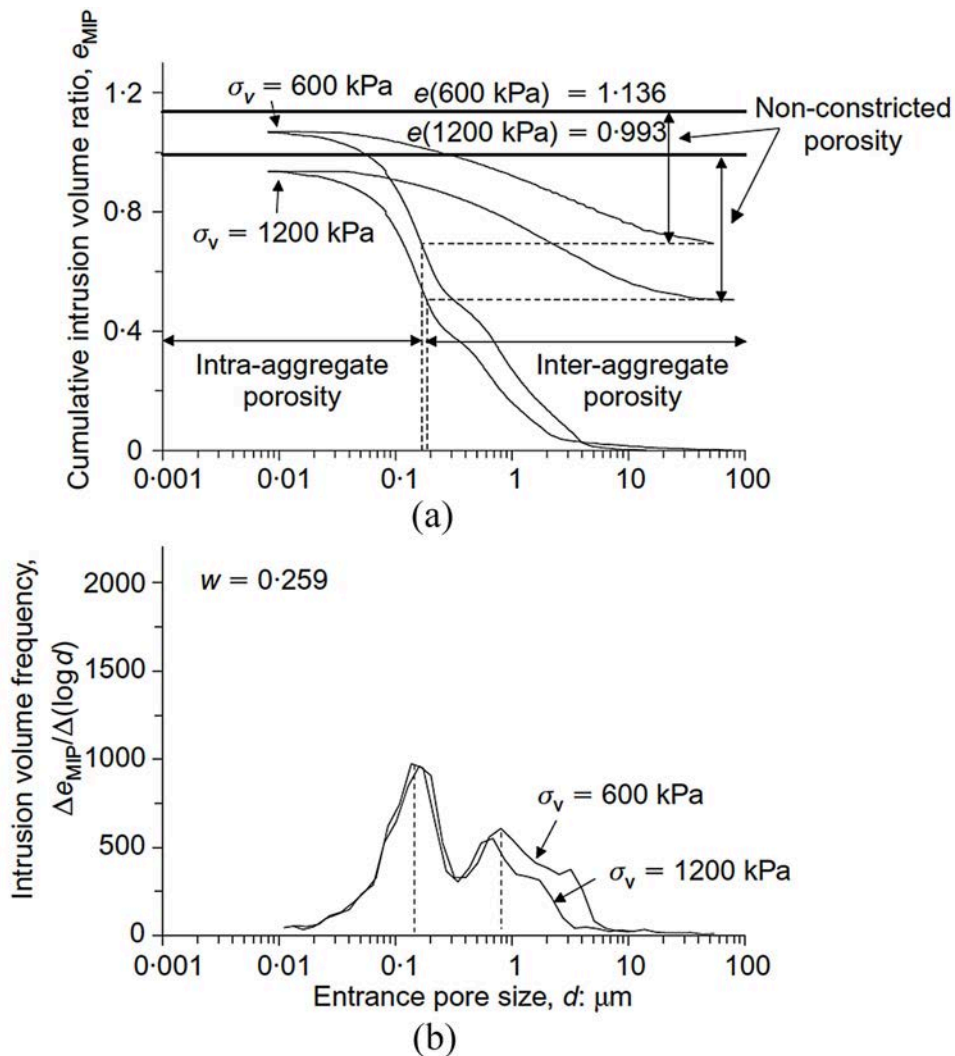


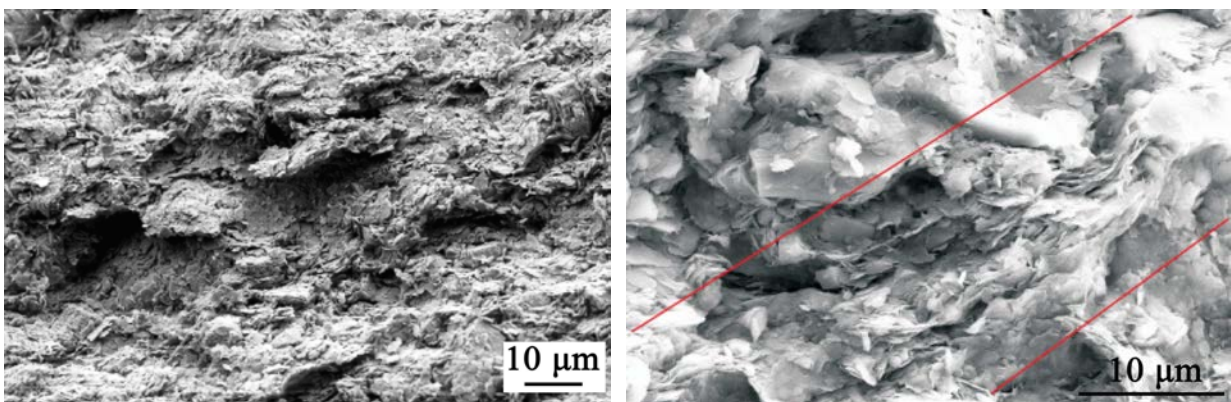
Figure 1.22 MIP test results of kaolin clay after compaction (Tarantino and De Col, 2008)

However, some experimental results such as reported by Li and Zhang (2009) and Monroy et al. (2010) highlighted that the change of intra-aggregate pores in some clay is dominant during wetting and drying. In addition, numerous experimental results have indicated that the PSD curves of many types of clay are in bimodal form (Li and Zhang, 2009; Hattab et al., 2013; Burton et al., 2015). Nevertheless, the double-porosity structure does not necessary exist in all clayey materials. For instance, the results of Liu et al. (2012), Ng and Coe (2015) and Hattab et al. (2015) showed that the PSD curves of some remoulded clays are unimodal.

### 2.3 Characterisation of local cracks

Shear-induced cracks are developed at different scales in remoulded clays under direct shear tests and triaxial tests when the shear stress meets the critical state.

Optical and electron microscopes are commonly used techniques to identify the microcracks within clays. Using an optical microscope, Morgenstern and Tchalenko (1967c) investigated the development of discontinuity in the remoulded kaolin under direct shear tests. They noted an initial local non-homogeneous discontinuity followed by an evident shear plane during the test, as shown in Figure 1.13. When studying the microstructure of remoulded kaolin clay during CD triaxial loading, Hattab and Fleureau (2010) observed some microcracks in SEM images of the slightly overconsolidated specimen ( $OCR = 1.4$ ) at the critical state (Figure 1.23a). They stated that the microcracks appear between parallel-arranged particles, which are associated in face-to-face form in the strongly oriented regions of specimens. Hattab et al. (2015) also noted the appearance of microcracks in the remoulded montmorillonite clay at the end of CD triaxial tests (Figure 1.23b).



(a) kaolin ( $OCR=1.4$ )

(b) montmorillonite ( $OCR=1.0$ )

Figure 1.23 Microcracks observed in remoulded clays after CD triaxial tests

(Hattab and Fleureau, 2010; Hattab et al., 2015)

XR-CT and XR- $\mu$ CT are employed to investigate the macrocracks and mesocracks in clay by many authors. For example, Viggiani et al. (2004) used the XR- $\mu$ CT technique to evaluate the onset and evolution of shear bands in a heavily overconsolidated sedimentary soil subjected to triaxial loading. They observed the activation and propagation of local cracks within the specimen after the deviatoric stress reaches the peak value (Figure 1.24). The authors also pointed out that it is difficult to discriminate the dilation-induced bands from the shear-induced bands. Using an XR-CT triaxial testing setup, Sun et al. (2004a) investigated the development of shear-induced cracks within silty clay specimens under different triaxial loading conditions. Their results showed that the studied silty clay has initial local cracks indicating an originally damaged structure, and new local cracks are gradually induced when the triaxial stress approaches the shear strength of the material.

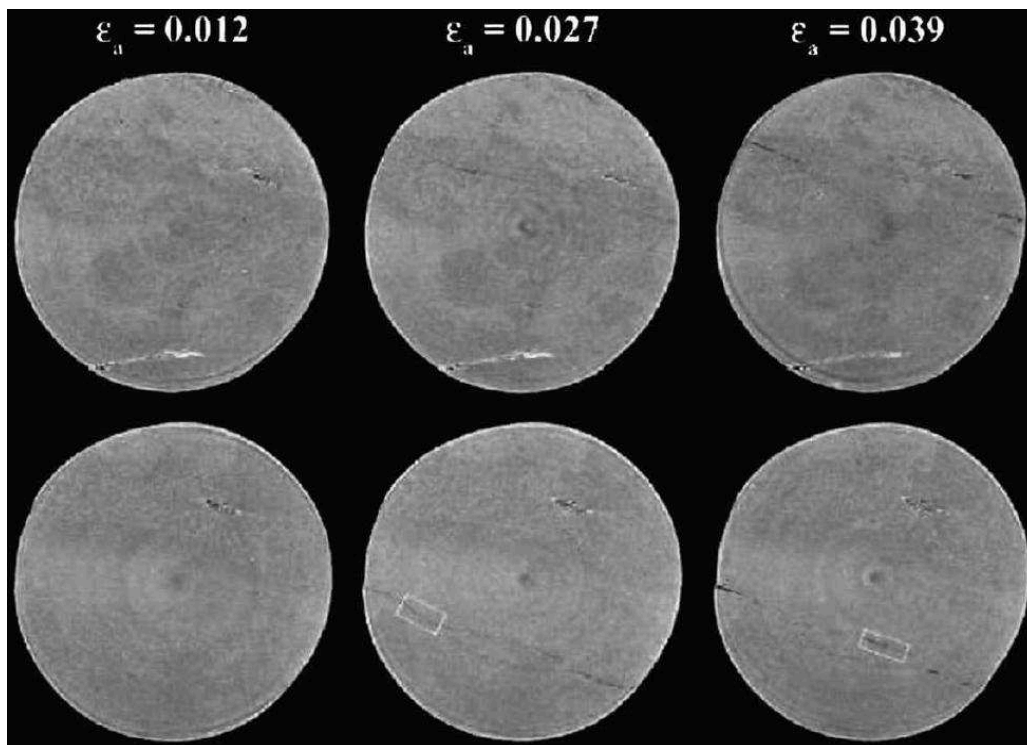


Figure 1.24 Local cracks development in sedimentary soil specimen (Viggiani et al., 2004)

As noted by Viggiani et al. (2004), in addition to shear stress, the dilatancy mechanism may also lead to the development of local cracks. The shear-induced crack in geomaterials is well known. However, there is a lack of studies of the relationship between the appearance of local cracks and the dilatancy phenomenon in strongly overconsolidated remoulded clays.

### 3. Mechanical behaviour of unsaturated clay affected by suction

The clay whose voids are filled with both water and air is referred to as unsaturated clay. Many geotechnical problems such as bearing capacity, lateral earth pressure, slope stability and landfills are related to the shear strength and volume change of unsaturated clay. This leads to the necessity of determining the hydromechanical behaviour of unsaturated clays under various suction conditions.

### 3.1 Basic concepts regarding unsaturated clay

#### 3.1.1 Definition of soil suction

Soil suction represents the water potential in a soil-water system. When suction is high, it can be measured in terms of the partial vapour pressure of the soil water (Fredlund and Rahardjo, 1993). The thermodynamic relationship between soil suction and the partial pressure of pore water vapour can be written as follows:

$$s = -\frac{R^*T}{v_{w0}\omega_v} \ln(RH) \quad (1.2)$$

$$RH = \frac{\bar{u}_v}{\bar{u}_{v0}} \quad (1.3)$$

where  $s$  is the total suction (kPa);  $R^*$  is the universal gas constant (8.314 J/mol·K);  $T$  is the absolute temperature (K);  $v_{w0}$  is the specific volume of water (m<sup>3</sup>/kg);  $\omega_v$  is the molecular mass of water vapour (18.016 kg/kmol);  $RH$  is the relative humidity;  $\bar{u}_v$  is the partial pressure of pore water vapour (kPa);  $\bar{u}_{v0}$  is the saturation pressure of water vapour over a flat surface of pure water at the same temperature (kPa).

The soil suction as quantified in terms of relative humidity is commonly called “total suction”, which has two components, i.e., matric suction and osmotic suction:

$$s = \psi_m + \psi_o \quad (1.4)$$

$$\psi_m = u_a - u_w \quad (1.5)$$

where  $\psi_m$  is the matric suction;  $\psi_o$  is the osmotic suction;  $u_a$  is the pore air pressure;  $u_w$  is the pore water pressure.

Matric suction arises due to capillarity while osmotic suction is produced by pore fluid chemistry and water adsorption (Fredlund and Rahardjo, 1993). Matric suction is generally considered to be the dominant component of total suction in non-plastic cohesionless soils with a relatively pure pore fluid (Blatz et al., 2008). Osmotic suction can be appreciable in highly plastic clays that have high activity due to the clay mineralogy or in cases where the pore fluid activity is high due to the presence of dissolved salts (Blatz et al., 2008).

### 3.1.2 Effective stress and shear strength of unsaturated soil

Effective stress is an important variable for evaluating the mechanical behaviour of saturated soil, and it is defined as the difference between total stress and pore pressure.

For unsaturated soil, the physical meaning of effective stress remains the same. However, its definition is slightly different from that of saturated soil. Bishop's effective stress for unsaturated soil has the following expression:

$$\sigma' = (\sigma - u_a) + \chi(u_a - u_w) \quad (1.6)$$

where  $\sigma'$  is the effective stress;  $\sigma$  is the total stress;  $(\sigma - u_a)$  is referred to as the net normal stress;  $\chi$  is a material variable, which is considered to be dependent on the degree of saturation and varies between zero and unity.

Substituting Equation (1.6) into the traditional Mohr-Coulomb criterion, one can deduce the failure condition of unsaturated soil:

$$\tau_f = c' + [(\sigma - u_a)_f + \chi_f(u_a - u_w)_f] \tan \phi' \quad (1.7)$$

where  $\tau_f$  is the shear strength;  $c'$  and  $\phi'$  are the effective cohesion and internal friction angle, respectively;  $(\sigma - u_a)_f$  is the net normal stress at failure;  $(u_a - u_w)_f$  is the matric suction at failure.

Fredlund et al. (1978) proposed an extended Mohr-Coulomb criterion to describe the shear strength behaviour of unsaturated soil. The failure envelope is a planar surface in the space of two stress state variables  $(\sigma - u_a)$  and  $(u_a - u_w)$  and shear stress  $\tau$  (see Figure 1.25) and may be written as:

$$\tau_f = c' + (\sigma - u_a)_f \tan \phi' + (u_a - u_w)_f \tan \phi^b \quad (1.8)$$

where  $c'$  is the cohesion at zero matric suction and zero net normal stress;  $\phi'$  is the internal friction angle associated with the net normal stress ( $\sigma - u_a$ );  $\phi^b$  is the internal friction angle associated with the matric suction ( $u_a - u_w$ ).

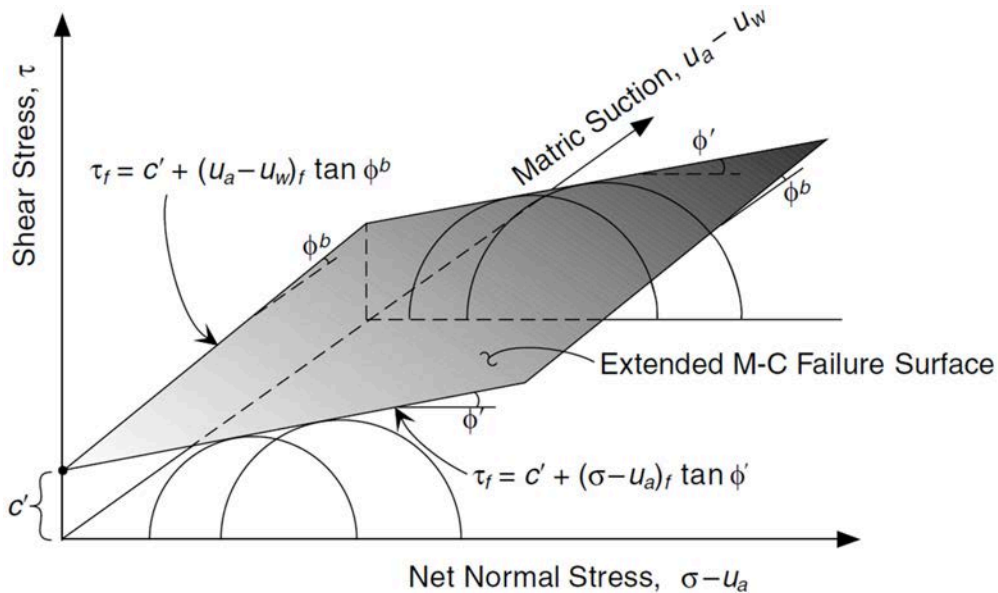


Figure 1.25 Extended Mohr-Coulomb failure surface (Lu and Likos, 2004)

### 3.1.3 Triaxial testing types for unsaturated soil

One of the most common tests used to measure the shear strength of a soil in the laboratory is triaxial test. Various triaxial test procedures are used for unsaturated soil based on the drainage conditions during isotropic loading and triaxial shearing stages. These test types include consolidated drained (CD) test, consolidated undrained (CU) test, unconsolidated undrained (UU) test, constant water content (CW) test and unconfined compression (UC) test, as summarised in Table 1.2.

Particularly, in an unconsolidated undrained test or UU test, the confining pressure is applied to the specimen quickly and then the deviatoric stress is applied. The whole test is performed under the condition that both the pore air and pore water are not allowed to drain. In this type of test, excess pore water and pore air pressures develop and the pore pressures are generally not measured during shearing. Therefore, the shear strength is related to the total stress without a knowledge of the pore pressure at failure. The UU test for unsaturated soil is usually run at a strain rate of 0.017~0.03%/s and no attempt is made to measure the pore air pressure and pore water pressure (Fredlund and Rahardjo, 1993). Conventional triaxial

equipment can be used to perform the UU test on unsaturated soil. The porous disks are usually replaced by metal or plastic disks on the top and bottom of the specimen.

Table 1.2 Various triaxial tests for unsaturated soil (Fredlund and Rahardjo, 1993)

Test type	Consolidation	Triaxial shearing process				
		Drainage		Controlled (C) / measured (M)		
		Pore air	Pore water	$u_a$	$u_w$	Volume change
Consolidated drained (CD) test	Yes	Yes	Yes	C	C	M
Consolidated undrained (CU) test	Yes	No	No	M	M	—
Unconsolidated undrained (UU) test	No	No	No	—	—	—
Constant water content (CW) test	Yes	Yes	No	C	M	M
Unconfined compression (UC) test	No	No	No	—	—	—

### 3.2 Shear strength and volume change of unsaturated clay

#### 3.2.1 Volume change of unsaturated clay during consolidation

The compression of unsaturated clays occurs due to the compression of pore fluids and the rearrangement of clay particles (Mun and McCartney, 2015), and it is quite complicated to describe or predict the result, due to the coupled hydromechanical interplay among the solid, water and air phases (Zou et al., 2018). The compressibility of unsaturated remoulded clay has been investigated by many authors through suction-controlled oedometer tests and isotropic consolidation tests (Delage et al., 1992; Al-Mukhtar et al., 1999; Kato and Kawai, 2000; Romero et al., 2005; Vesga, 2008; Mun and McCartney, 2015 and 2016).

Delage et al. (1992) proposed an osmotic consolidometer based on the use of semi-permeable membranes and an aqueous solution of large sized organic molecules (PEG 20000). As the authors stated, the advantage of this apparatus is to provide a closer reproduction of the natural conditions of soils under suction compared to the classical one based on the axis-translation method. By means of this new consolidometer, they performed suction-controlled consolidation tests on a unsaturated silt. The experimental results showed that the curves of settlement and water exchange versus time in a semi-logarithmic plot are similar to a classical

consolidation curve.

Al-Mukhtar et al. (1999) investigated the compressibility of highly compacted unsaturated smectites subjected to oedometer tests considering different relative humidities, i.e.,  $RH = 100\%$ ,  $98\%$  and  $11\%$  ( $s = 0$  MPa,  $2.7$  MPa and  $298$  MPa). Their test results shown in Figure 1.26 indicate that (i) the void ratio decreases with increasing axial stress; (ii) at a constant axial stress, the void ratio decreases as the relative humidity decreases (or the suction increases); (iii) the void ratio of the saturated specimen is considerably greater than those of the unsaturated specimens for all the values of axial stress.

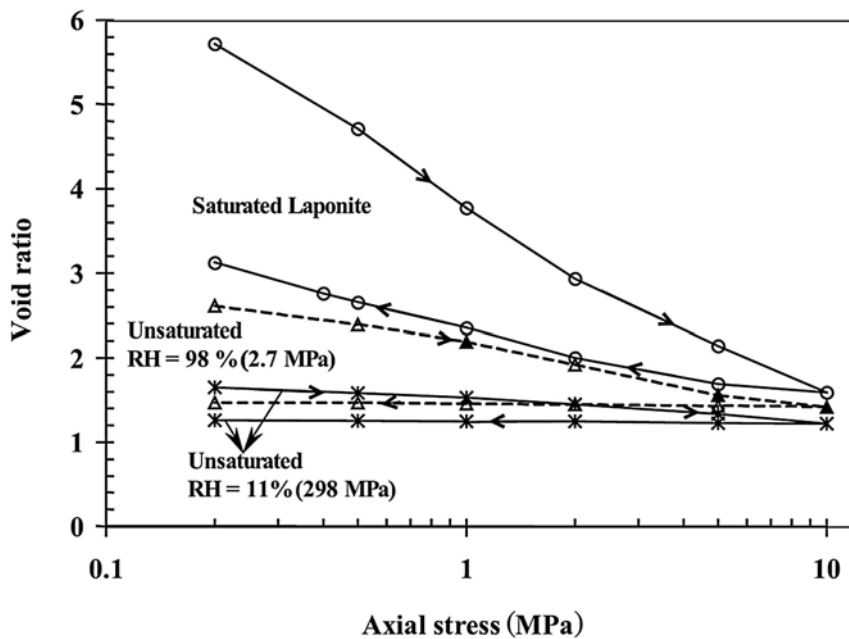


Figure 1.26 Oedometer results of compacted smectites (Al-Mukhtar et al., 1999)

Vesga (2008) performed three-dimensional compression tests on an unsaturated kaolinite clay during controlled drying process. The author noted a close relationship between the evolution of void ratio (represented by solid curve) and that of equivalent effective stress (EES, represented by dashed curve) due to capillary forces (Figure 1.27). He found that when the clay has a high water content (i.e., in the saturated funicular state), its volume significantly decreases as the water content is reduced and the equivalent effective stress is increased. If the clay has a water content in an intermediate interval (i.e., in the complete pendular state), the volume is almost constant because the change in equivalent effective stress is small.

Mun and McCartney (2015) investigated the compression behaviour of unsaturated clay using undrained and drained isotropic consolidation tests with controlled matric suction. Their

results indicate that the specimens tested under undrained conditions are much stiffer than those tested under drained conditions (see Figure 1.28). The authors also noted that in both drained and undrained compression tests, the range of applied stresses is sufficient to cause collapse or dissolution of the air voids (pressurized saturation) and convergence of the virgin compression lines for unsaturated specimens with that measured for saturated specimens.

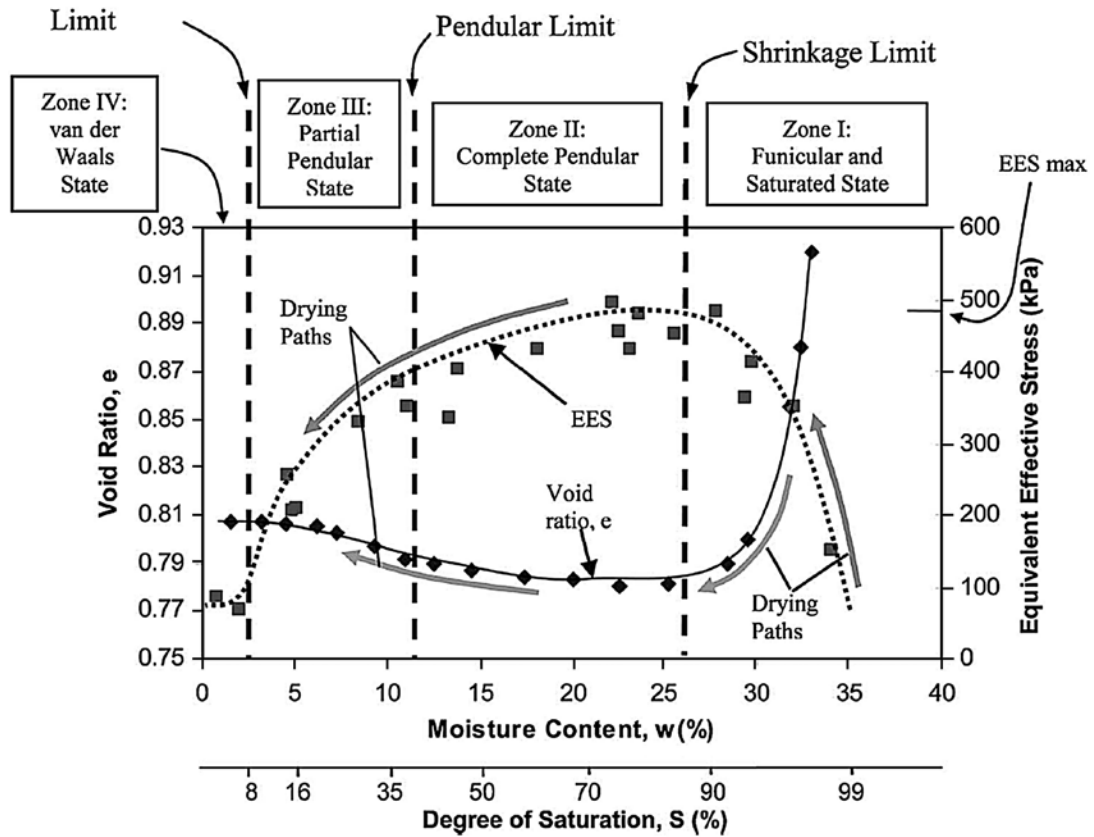


Figure 1.27 Void ratio and equivalent effective stress of clay during drying (Vesga, 2008)

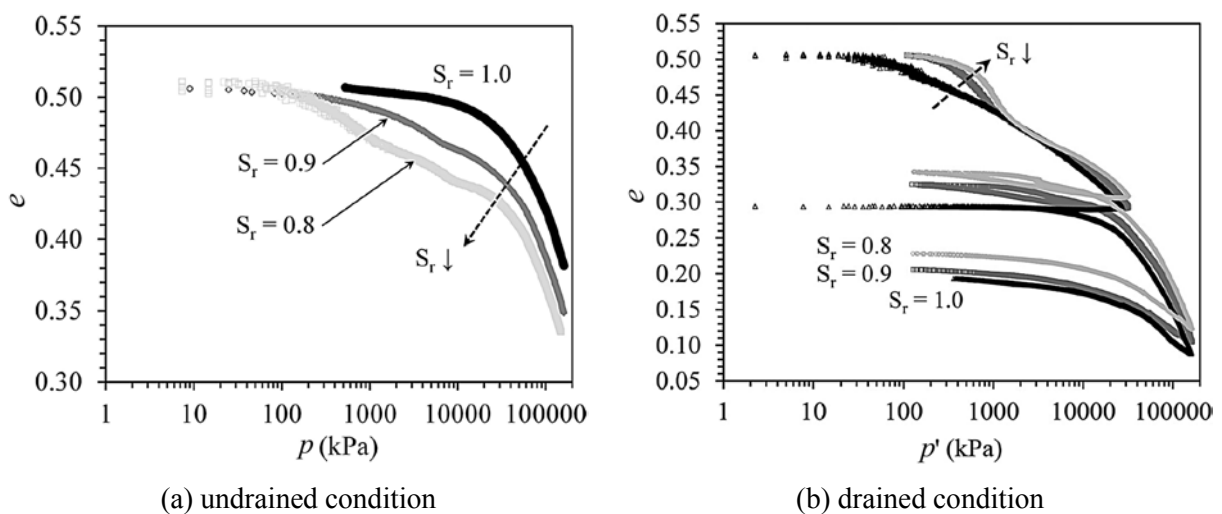


Figure 1.28 Compression behaviour of clay specimens (Mun and McCartney, 2015)

### 3.2.2 Shear strength of unsaturated clay under triaxial loading

Incorporating the techniques of suction control and measurement into a conventional triaxial testing system, many researchers and engineers have developed a series of unsaturated triaxial testing apparatus. Based on these setups, the hydromechanical behaviour of unsaturated remoulded clays under various triaxial loading conditions has been investigated (Wheeler and Sivakumar, 1995; Blatz et al., 2002; Sun et al., 2004b; Oh et al., 2008; Jotisankasa et al., 2009; Gao et al., 2015; Mun and McCartney, 2016).

Delage and Cui have developed triaxial testing apparatuses for unsaturated soil and carried out a series of unsaturated triaxial tests on various soils (Delage et al., 1987; Cui and Delage, 1996; Delage and Cui, 2008). For example, Cui and Delage (1996) conducted unsaturated triaxial tests on a silt using an osmotic-technique-based triaxial testing apparatus. Their results indicated that the initial moduli and maximum deviatoric stresses increase with increasing suction (Figure 1.29a). At a cell pressure of 50 kPa, an increasingly pronounced peak of deviatoric stress is observed at a reducing level of axial strain, showing an increasing brittleness of the specimen when suctions are larger than 400 kPa. At a higher cell pressure of 100 kPa (Figure 1.29b), the peaks are less pronounced and appear only at  $s = 800$  kPa and 1500 kPa, showing a lower brittleness.

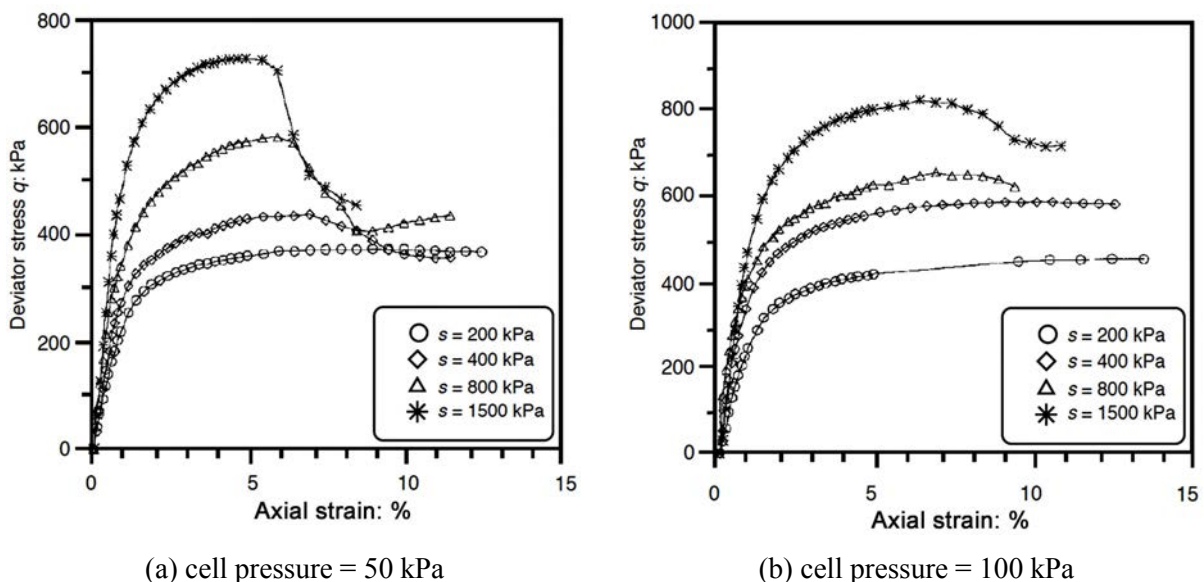


Figure 1.29 Stress-strain relationships of unsaturated silt (Cui and Delage, 1996)

Blatz et al. (2002) examined the influence of suctions on the strength and stiffness of a compacted sand-bentonite mixture. Quick undrained (i.e., unconsolidated undrained, UU)

triaxial tests were performed on suction-imposed specimens using a conventional triaxial testing setup. The application of suctions was achieved by placing the specimens in the headspace of sealed desiccators that contain salt solutions with known concentrations. Figure 1.30 shows the stress-strain relationships of soil specimens at various initial total suctions and confining pressures. The results show that: (i) at a low cell pressure, the specimens subjected to shear loading become stronger but also more brittle with increasing suction; (ii) at a high cell pressure, the specimens are generally ductile and are barrel-shaped after shearing. The unsaturated triaxial tests performed by Wiebe et al. (1998) on similar material (i.e., sand-bentonite mixture) and by Ma et al. (2009) on Yunnan red clay revealed similar results.

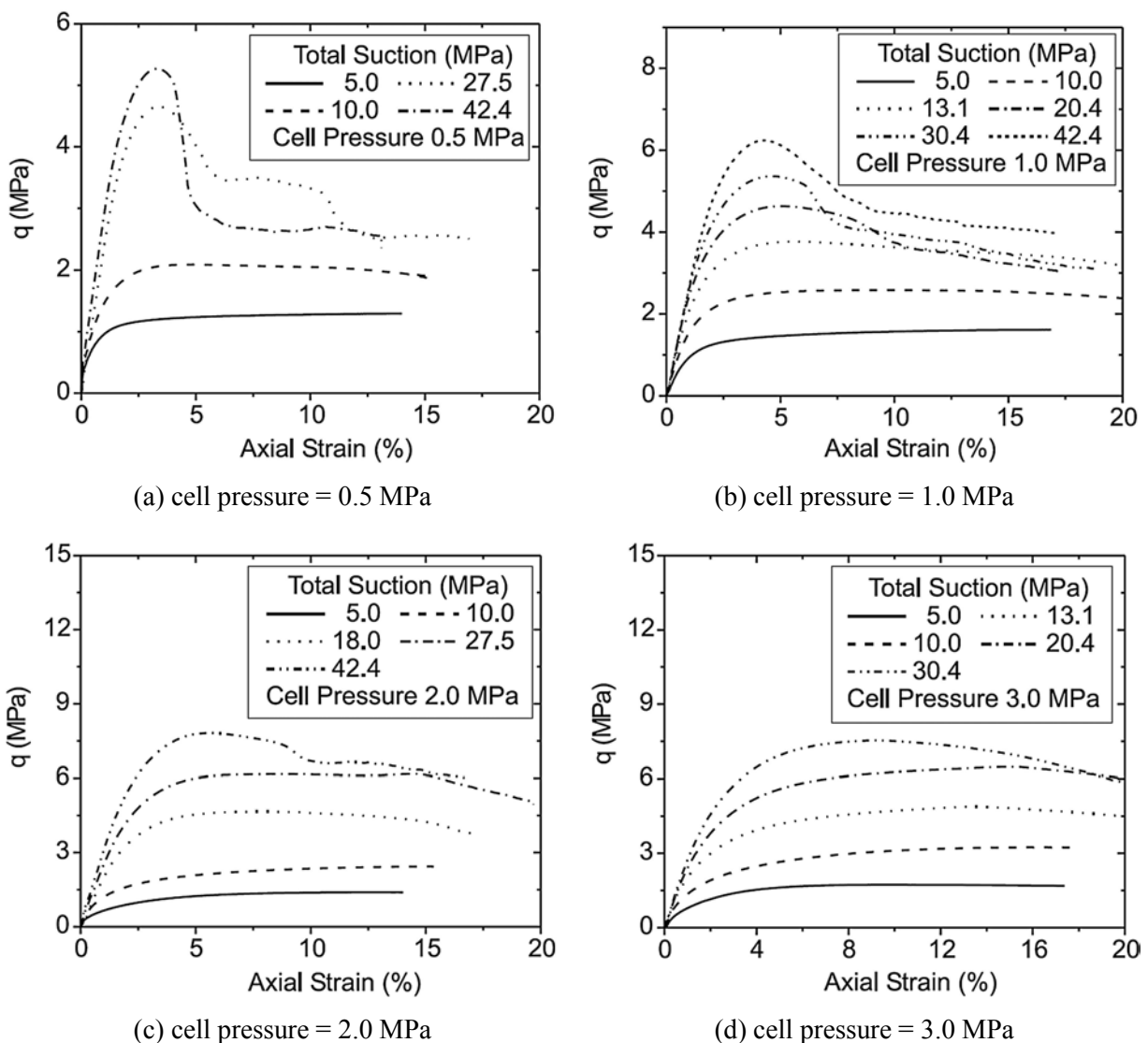
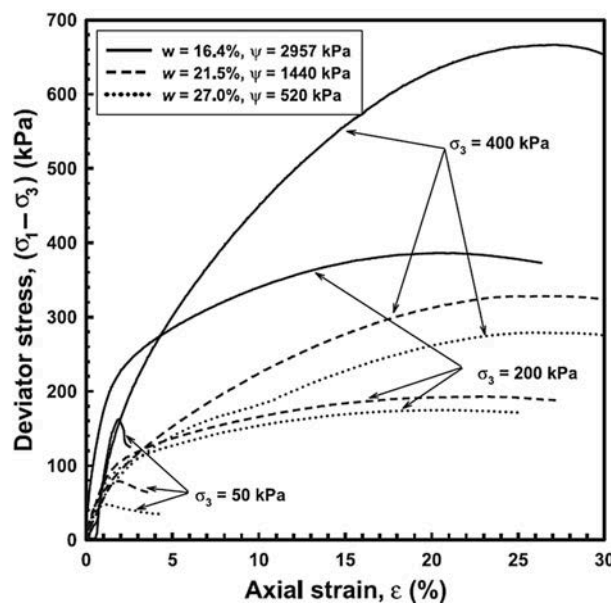


Figure 1.30 Triaxial test results of unsaturated sand-bentonite mixtures (Blatz et al., 2002)

Oh et al. (2008) performed three groups of triaxial tests on statically compacted unsaturated kaolin specimens using a conventional triaxial testing system. In the first group of tests (IU

test), the specimens were sheared immediately at a fast strain rate after the application of confining pressure under undrained conditions. In the second group of tests (I<sub>e</sub>U-f test), the specimens were first allowed to come to the equilibrium with respect to volume change and suction value under the applied confining pressure and then sheared at a fast strain rate. The third group of tests (I<sub>e</sub>U-s test) were similar to the second series but the specimens were sheared at a slow strain rate. Their results indicated that the test procedure affects the mechanical results, and only the specimens sheared under low confining pressures show brittle failures (Figure 1.31). Therefore, they concluded that the brittle failure occurs when the confining pressure is significantly low compared to the initial suction value. They also stated that the applied confining pressure has more significant influences on the shear strength behaviour of an unsaturated clay specimen than the initial suction.

The effect of suction levels on the shear strengths of unsaturated kaolin clay obtained by Oh et al. (2008) is presented in Figure 1.32. Figure 1.32a shows a nonlinear failure envelope on the plane of shear strength versus suction in the case of I<sub>e</sub>U-f tests with different confining pressures of 50 kPa, 200 kPa and 400 kPa. The notation  $\phi_u^b$  in Figure 1.32b is the internal friction angle associated with the matric suction in terms of total stress; it represents the contribution of suctions to the shear strength of the unsaturated clay. From Figure 1.32b, the authors concluded that  $\phi_u^b$  decreases with the increase in suction and increases with the increase in confining pressure.



(a) IU test results

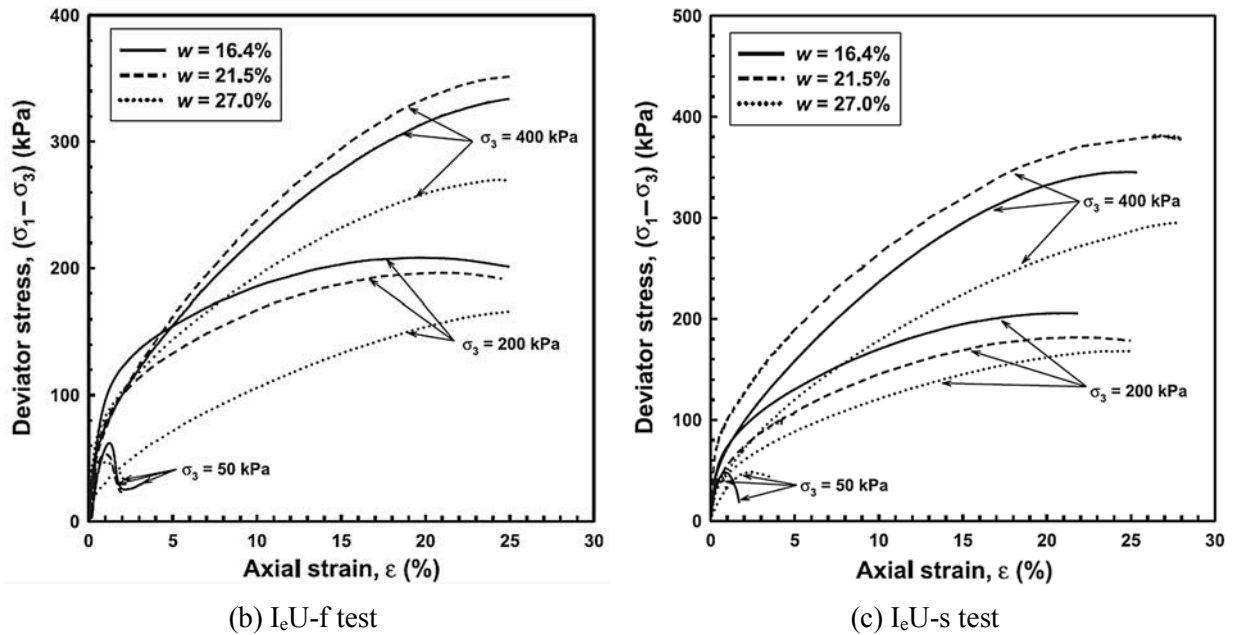


Figure 1.31 Triaxial tests on compacted unsaturated kaolin clay (Oh et al., 2008)

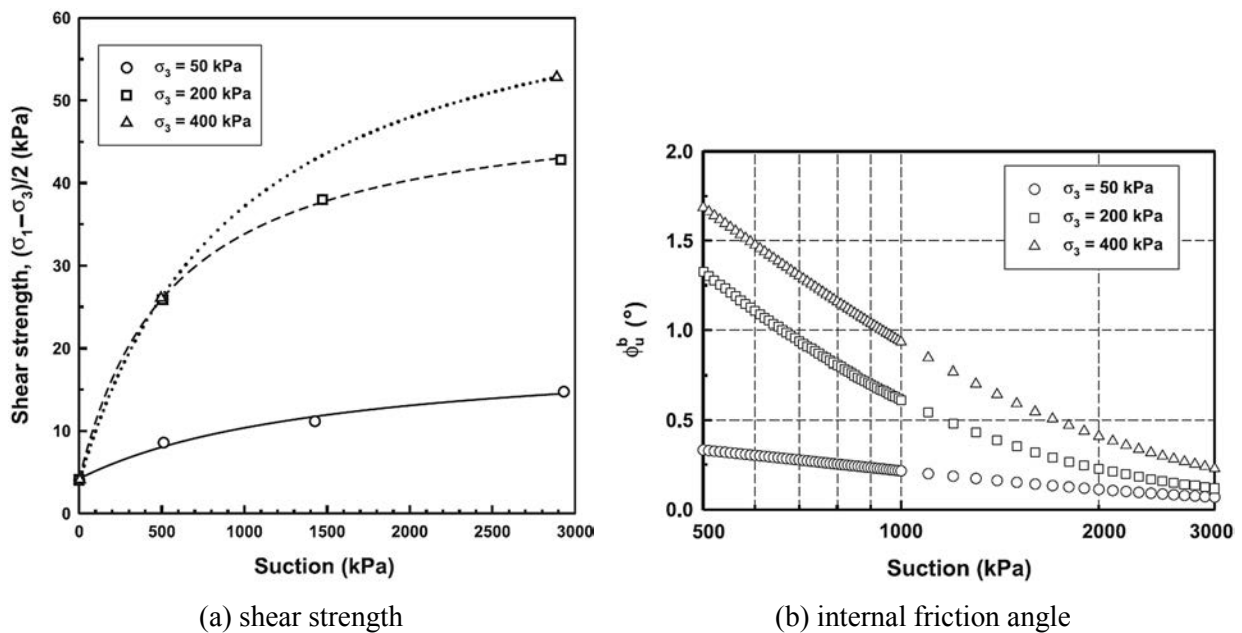


Figure 1.32 Effect of suctions on shear strength of clay (IeU-f test) (Oh et al., 2008)

Wheeler and Sivakumar (1995) performed a series of controlled suction triaxial tests on a compacted unsaturated kaolinite clay to investigate the critical state framework. Nuth and Laloui (2008) calculated the Bishop's generalized effective stresses based on the data of Wheeler and Sivakumar (1995). The critical state lines (CSL) plotted in the planes of deviatoric stress ( $q$ ) versus mean net stress ( $p_{net}$ ) and mean effective stress ( $p'$ ) are presented in Figure 1.33. It is noted that in the deviatoric stress versus mean net stress plane, the cohesion increases and the internal friction angle remains almost constant with increasing suction

(Figure 1.33a). By contrast, in the deviatoric stress versus mean effective stress plane, the critical state lines under different suction values coincide with that under saturated conditions (Figure 1.33b).

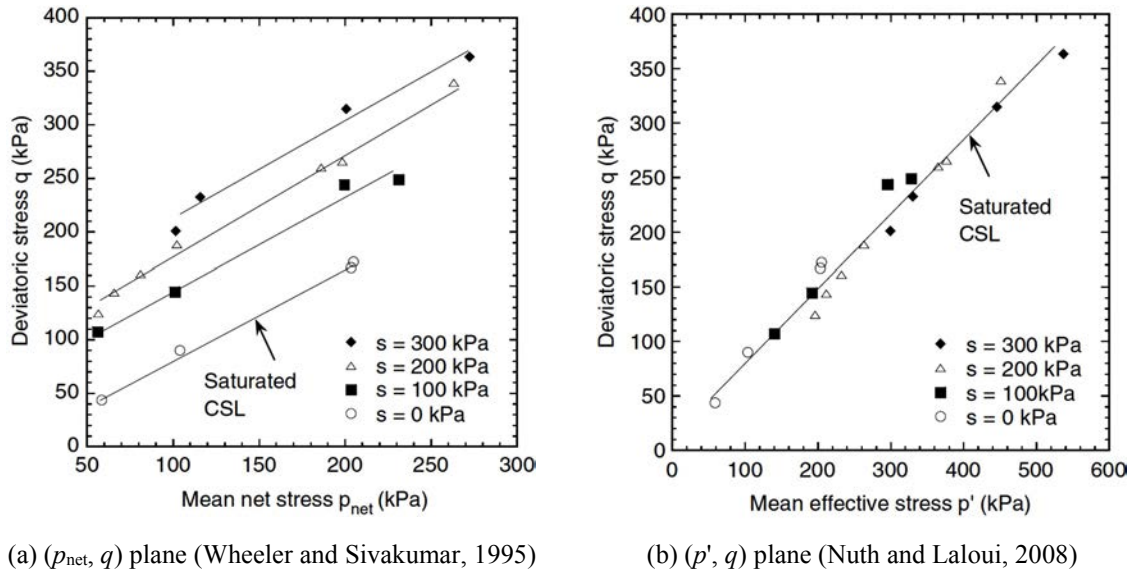
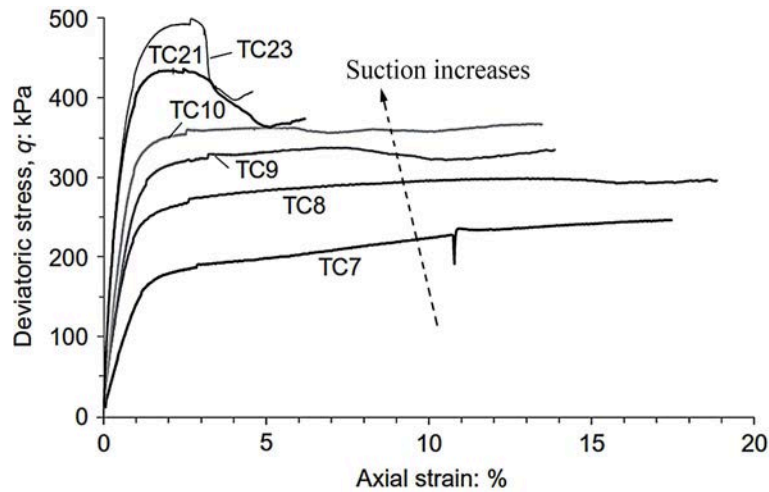


Figure 1.33 Critical state lines of unsaturated kaolinite clay

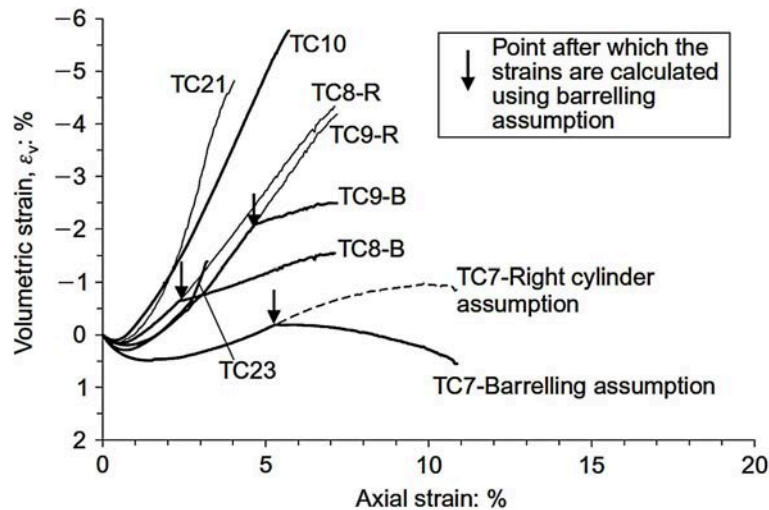
### 3.2.3 Volume change of unsaturated clay under triaxial loading

Sun et al. (2004b) investigated the influences of stress state, water content, void ratio and matric suction on the collapse behaviour of unsaturated clays using a suction-controlled triaxial testing setup. Their results show that the volume change induced by the collapse mainly depends on the initial void ratio and mean net stress under which the collapse occurs, irrespective of the imposed matric suction. When the imposed suction is decreased, a large collapse deformation takes place in the samples that compacted under the dry-of-optimum condition, while little collapse deformation takes place in the samples that compacted under the wet-of-optimum condition.

Jotisankasa et al. (2009) performed constant water content (CW) triaxial tests on an unsaturated compacted silty clay. Their results showed that the specimens become stiffer with increasing initial suction, as shown in Figure 1.34a. They also noted that the volumes of all the specimens regardless of their suction values exhibit an initial decrease followed by a continuous increase and show dilative behaviour in the end. In general, the higher the suction level, the more significant the dilation (Figure 1.34b).



(a) stress-strain relation



(b) volumetric strain

Figure 1.34 CW triaxial test results on unsaturated silty clay (Jotisankasa et al., 2009)

The volumetric deformations of silt specimens obtained by Cui and Delage (1996) through unsaturated triaxial tests are presented in Figure 1.35. It shows that at a cell pressure of 50 kPa, a tendency of contraction followed by dilation occurs when suction is larger than 200 kPa (Figure 1.35a). However, a positive volumetric strain is observed only at the end of the test when suction reaches 1500 kPa. It means that the higher the suction, the more pronounced the dilatancy. This result is consistent with those reported by many researchers such as Jotisankasa et al. (2009). In addition, the dilatancy phenomenon of the unsaturated silt specimen is restrained as the cell pressure increases (Figure 1.35b).

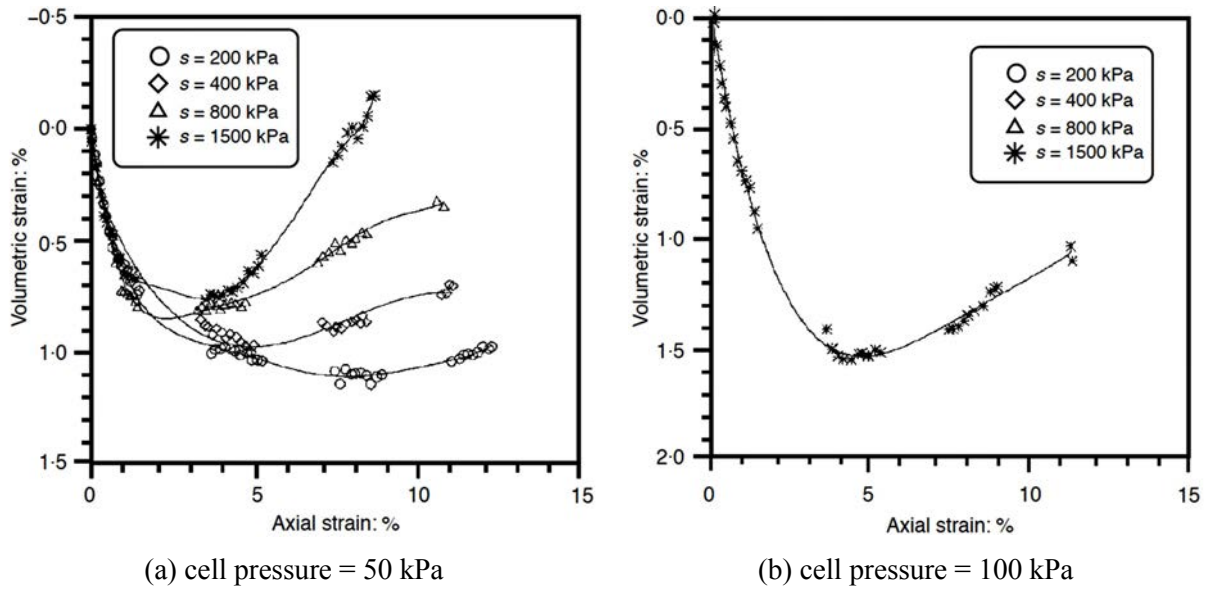


Figure 1.35 Volumetric deformations of unsaturated silt (Cui and Delage, 1996)

Gao et al. (2015) examined the effect of different specimen preparation methods (compaction/reconstitution) on the hydromechanical behaviour of an unsaturated, slightly expansive clay. They observed that under a confining net stress of 200 kPa, the shear strengths of both the compacted specimens (C2-C4) and reconstituted specimens (R2-R4) increase with the increase in suction values ( $s$ ) (see Figure 1.36). Moreover, the shear strengths of the reconstituted specimens are generally higher than those of the compacted specimens of identical density under the same suctions and net confining pressures. However, when the suction is relatively high, the reconstituted specimen tends to fail with a brittle feature and show dilative behaviour, while the compacted specimen is still ductile and contractive at the end of test.

To sum up, although many attempts have been made by many researchers to evaluate the hydromechanical behaviour of unsaturated soil, more experimental investigations on unsaturated remoulded clay under various suctions especially high suction levels are necessary, and the need to better understand the mechanical behaviour such as the shear strength and volume change still persists.

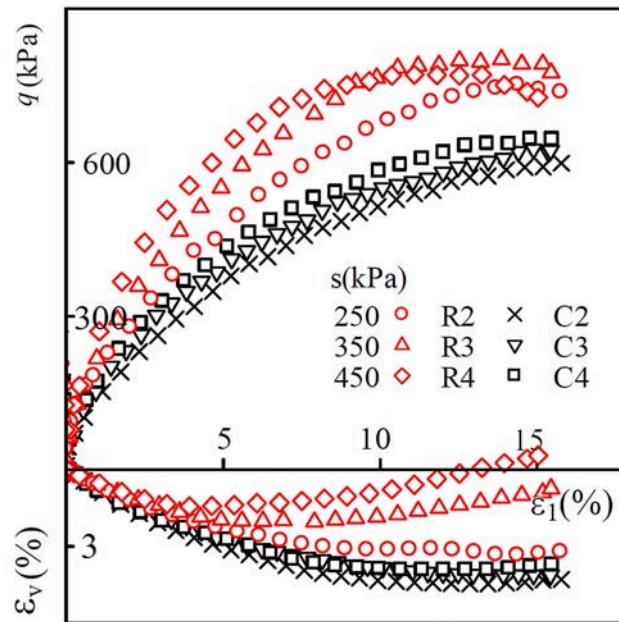


Figure 1.36 Triaxial test results of clay affected by preparation methods (Gao et al., 2015)

#### 4. Summary

This chapter presents a general review of the previous works involving the multiscale investigations of saturated and unsaturated remoulded clay. The state of the art has been presented from macromechanical behaviour to microstructural characteristics. The main findings from the literature review are stated below.

Regarding the saturated remoulded clay, plenty of experimental works in the literature has been devoted to studying its macroscopic behaviour such as the dilatancy phenomenon through a variety of mechanical tests. The microstructural changes of remoulded clay (especially in the normally consolidated state) under different loading conditions have also been investigated for several decades. To date, more and more researchers have recognized the importance of an in-depth understanding of microscopic characteristics for the interpretation of the macroscopic behaviour (e.g., shear strength, deformation and permeability) of remoulded clay. Nevertheless, there is still a long way to go to precisely quantify the macro-micro relationships.

Particularly, how the stress paths affect the mechanical behaviour of remoulded clay and how the dilatancy phenomenon in clay originates from the microscale (in other words, what the physical origin of dilatancy phenomenon is in clay) are interesting topics and need further investigations. In fact, a good knowledge of the mechanism of clay dilatancy is of great

significance for the development of constitutive models and the determination of shear strength parameters. Because of dilatancy, the friction angle increases as the confinement increases. However, after the peak shear strength of the soil is reached, the friction angle significantly decreases. Therefore, the foundations of buildings and structures, the slopes and the tunnels in such soils have to consider the potential decrease in shear strength.

Regarding the unsaturated remoulded clay, the review indicated that the experimental investigations are rather difficult and time-consuming compared to those on saturated remoulded clay. For example, specific devices and sensors used for suction control and measurement must be incorporated into the conventional testing apparatus. Because of the complexity of unsaturated clay and the difficulties of testing, the experimental research of unsaturated clay is far behind that of saturated clay. However, a better understanding of the hydromechanical behaviour especially the shear strength and volume change of unsaturated remoulded clay on various suction-stress paths is urgently needed to answer the questions of both geotechnical engineers and geoenvironmental engineers.

On the one hand, the safety of engineering structures mainly depends on the shear strength of the underlying soil, which is usually in the unsaturated state. Actually, the shear strength occupies an important position in unsaturated soil mechanics since the determination of shear strength is usually the fundamental step when dealing with various geotechnical problems such as those related to bearing capacity, slope stability, lateral earth pressure, pavement design and foundation design. On the other hand, many problems associated with the behaviour of unsaturated clay are related to the volume change due to the variation in water content (or suction). The soil shrinkage and the formation of desiccation cracks should be well controlled; otherwise, not only the compressibility, strength and permeability of unsaturated clay would be highly affected, but also the integrity of clay barriers such as in landfills and nuclear waste storages could be directly destroyed.

## Chapter 2

# Material properties and experimental methods

<b>1. Material properties and specimen preparations.....</b>	<b>47</b>
1.1 Mineralogy analyses.....	47
1.2 Grain size distribution.....	49
1.3 Physical properties and compressibility.....	50
1.4 Specimen preparations.....	51
<b>2. Experimental programme.....</b>	<b>52</b>
2.1 Experiments on saturated clay.....	52
2.2 Experiments on unsaturated clay.....	53
<b>3. Mechanical experimental procedures.....</b>	<b>55</b>
3.1 Triaxial tests on saturated clay.....	55
3.2 Triaxial tests on unsaturated clay.....	60
<b>4. Microscale experimental procedures.....</b>	<b>645</b>
4.1 Scanning electron microscopy (SEM) observations.....	66
4.1.1 Sample preparation and experimental procedures.....	66
4.1.2 Quantitative methods for the identification of particle orientation.....	68
4.1.3 Quantitative methods for the identification of pore properties.....	71
4.2 Mercury intrusion porosimetry (MIP) tests.....	78
4.2.1 Experimental principle.....	78
4.2.2 Experimental procedures.....	79
4.2.3 Quantification of 3D pore properties.....	80
4.3 X-ray microtomography (XR- $\mu$ CT) scans.....	81
4.3.1 Sample preparation and experimental procedures.....	81
4.3.2 Validation of the proposed sample preparation methods.....	83
4.3.3 Quantitative methods for the identification of local cracks.....	85
<b>5. Summary.....</b>	<b>86</b>



In this chapter, the basic properties of the studied materials and the employed multiscale experimental methods are presented. The experiments may be divided into two groups.

The first group includes macroscopic tests (i.e., triaxial tests) and microscopic tests (i.e., scanning electron microscopy (SEM) observations, mercury intrusion porosimetry (MIP) tests and X-ray microtomography (XR- $\mu$ CT) scans) on saturated remoulded Kaolin K13 clay. Notice that the triaxial tests in this first experimental group were performed by Dr. Lamine Ighil Ameer in the framework of his doctoral dissertation (Ighil Ameer, 2016) at the LEM3 laboratory of University of Lorraine.

The second group of experiments consists of macroscopic tests (i.e., soil-water characteristic tests and triaxial tests) and mesoscopic tests (i.e., XR- $\mu$ CT scans), on unsaturated remoulded Kaolin K13 clay and M35 clay considering different levels of initial suctions and mean stresses.

## **1. Material properties and specimen preparations**

Two clayey materials, i.e., Kaolin K13 and M35, were studied in this research. Kaolin K13 clay is a commercial synthetic clay supplied by the Sibelco Company (Paris, France). Its mineral composition, physical and mechanical properties are similar to those of Kaolin P300 clay, which has been extensively studied in the literature. M35 clay is a mixture composed of 65% Kaolin K13 and 35% Ca-montmorillonite. Ca-montmorillonite is a natural clayey material obtained from the Milos Island, Greece. The material properties were obtained at the LEM3 laboratory of University of Lorraine, and at the MSSMat laboratory of CentraleSupélec, University Paris-Saclay.

### **1.1 Mineralogy analyses**

The technical document provided by the manufacturer indicates that the chemical composition of Kaolin K13 clay is: SiO<sub>2</sub> (60%), Al<sub>2</sub>O<sub>3</sub> (28%), Fe<sub>2</sub>O<sub>3</sub> (1%), K<sub>2</sub>O (0.6%) and CaO (0.5%).

X-ray diffraction analysis performed on Kaolin K13 clay shows that this material contains a large proportion of kaolinite, some illite and quartz grains (Figure 2.1).

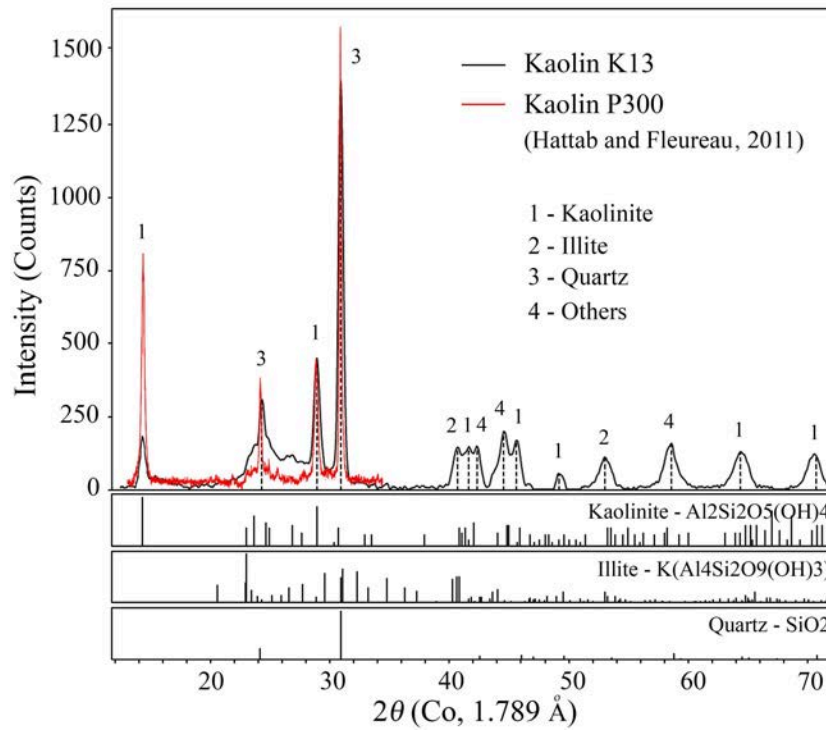


Figure 2.1 X-ray diffraction analysis of Kaolin K13 clay

Kaolinite is a common clay mineral with the chemical formula of  $Al_2Si_2O_5(OH)_4$ . It is a layered silicate mineral, with a tetrahedral sheet of silica ( $SiO_4$ ) linked through oxygen atoms to an octahedral sheet of alumina ( $AlO_6$ ) octahedra. Kaolinite usually has a low shrink-swell capacity and a low cation-exchange capacity.

The result of X-ray diffraction analysis also indicates that Ca-montmorillonite is a calcium "nearly pure" montmorillonite (see Figure 2.2). Montmorillonite has two tetrahedral sheets of silica sandwiching a central octahedral sheet of alumina. The individual crystals of montmorillonite are not tightly bound; hence water can intervene, causing the material easy to swell. The chemical formula of montmorillonite is  $(Na,Ca)_{0.33}(Al,Mg)_2(Si_4O_{10})(OH)_2 \cdot nH_2O$ .

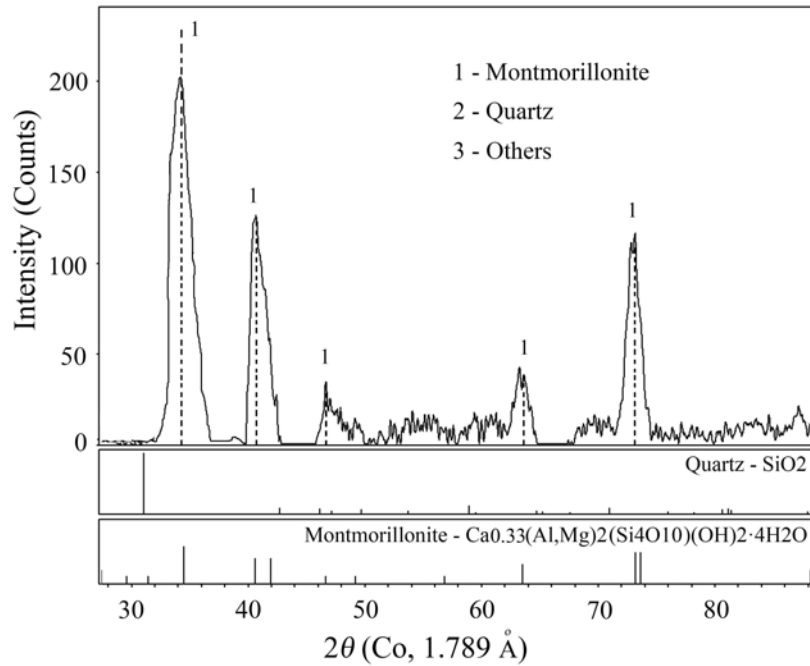


Figure 2.2 X-ray diffraction analysis of Ca-montmorillonite

## 1.2 Grain size distribution

The SEM observation on the raw Kaolin K13 clay powder without grinding reveals that kaolinite particles are mainly assembled in face-to-face form, and most of the clay aggregates have a size between 5  $\mu\text{m}$  and 10  $\mu\text{m}$  (Figure 2.3). Meanwhile, it is noted that kaolinite particle is plate-like, and the size of an individual kaolinite particle is generally less than 2  $\mu\text{m}$ .

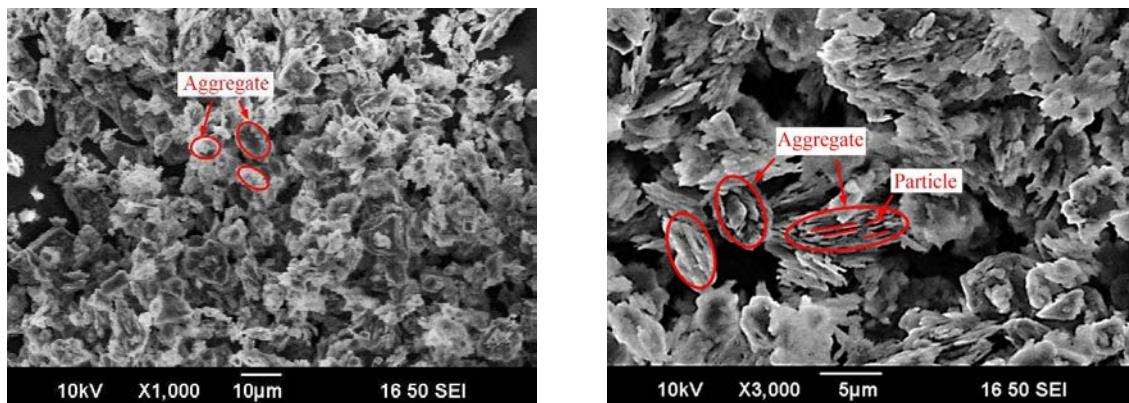
(a) 1000 $\times$  magnification(b) 3000 $\times$  magnification

Figure 2.3 SEM images of the raw Kaolin K13 clay powder

Figure 2.4 presents the "particle size distribution" of the raw material identified by the laser diffraction method. Note that the "particle size" given in Figure 2.4 for the raw Kaolin K13 clay might be in reality the "aggregate size". It shows that approximately 60% of the clay

aggregates are smaller than 9  $\mu\text{m}$ , and nearly 20% of the clay aggregates have sizes greater than 20  $\mu\text{m}$  with a maximum size of 80  $\mu\text{m}$ . These results are consistent with the information revealed by the SEM observation.

The particle size distribution of well dispersed powder of Ca-montmorillonite is also presented in Figure 2.4. It shows that about 80% of the Ca-montmorillonite particles are less than 2  $\mu\text{m}$ , and the maximum particle size is approximately 30  $\mu\text{m}$ .

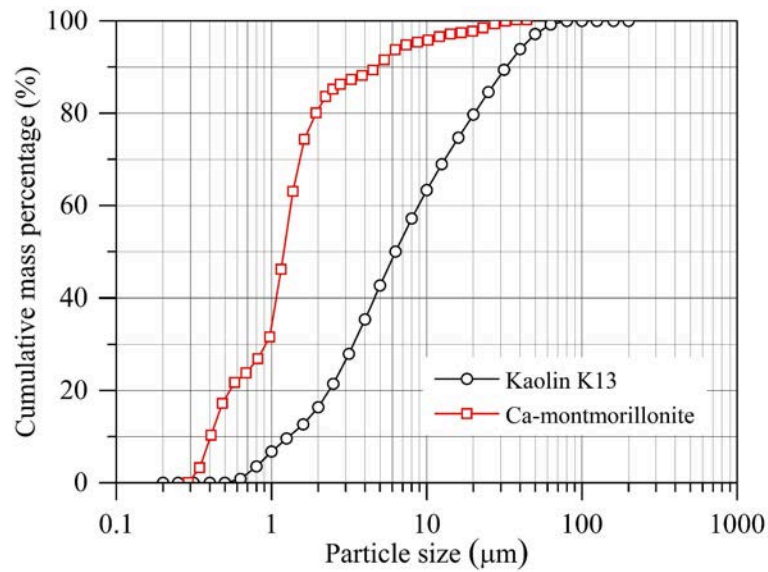


Figure 2.4 Particle size distributions of the studied materials

### 1.3 Physical properties and compressibility

The physical properties and compressibility parameters of the studied materials were determined through a series of laboratory experiments carried out by my colleagues (Hammad, 2010; Ighil Ameer, 2016; Zhao, 2017). The results are summarised in Tables 2.1-2.2. The properties of Kaolin P300 clay are also presented for comparison purposes.

Table 2.1 Physical properties of studied materials (Hammad, 2010; Zhao, 2017)

Material	Specific gravity $G_s$	Liquid limit $w_L$ (%)	Plastic limit $w_P$ (%)	Plastic index $I_P$ (%)	Specific surface area $S_s$ ( $\text{m}^2/\text{g}$ )
Kaolin P300	2.65	40	21	19	/
Kaolin K13	2.63	42	21	21	27
Ca-montmorillonite	2.73	170	60	110	/
M35	2.67	82	30	52	/

Table 2.2 Compressibility (Hammad, 2010; Ighil Ameer, 2016; Zhao, 2017)

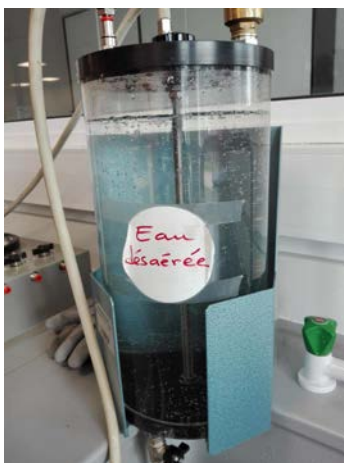
Material	Oedometer test		Isotropic loading	
	Compression index $C_c$	Swelling index $C_s$	Compression index $C_c$	Swelling index $C_s$
Kaolin P300	0.24	0.06	0.23	/
Kaolin K13	0.28	0.09	0.26	0.06
Ca-montmorillonite	1.81	0.19	1.80	/
M35	0.65	0.09	0.64	/

### 1.4 Specimen preparations

- *Slurry preparation*

The clay specimens used for mechanical testing were prepared from a slurry state, following the method employed for example by Ighil Ameer (2016) and Zhao (2017).

In the beginning, a certain amount of de-aired water (Figure 2.5a) was added to the clay powder to bring the initial water content to 1.5  $w_L$ . In order to obtain a homogeneous slurry, the material was then mechanically stirred at a rotation speed of 280 revolutions per minute for 15 minutes (Figure 2.5b). Afterwards, the slurry was sealed with plastic film and aluminium foil, and then rested for 24 hours at room temperature.



(a) de-aired water



(b) mixer



(c) consolidometer

Figure 2.5 Preparation of pre-consolidated clay material

- *One-dimensional pre-consolidation*

The cured slurry was filled, layer by layer, into a double-drained consolidometer, which is 95 mm in diameter and 1200 mm in height (Figure 2.5c). A total vertical effective stress of 120 kPa was then applied to the sediment clay in several steps. The one-dimensional consolidation of the slurry lasted for at least 3 weeks after the total vertical effective stress reached the desired value.

- *Triaxial test specimen*

After the one-dimensional pre-consolidation, the initial mechanical state of the material was generated. A section of the clay core was extracted from the consolidometer and then trimmed gently into a cylindrical specimen with a height of 75 mm and a diameter of 50 mm for triaxial testing, as shown in Figure 2.6. Meanwhile, the void ratio (i.e.,  $e_{00}$ ) of the pre-consolidated material was measured.



(a) preparation tools



(b) triaxial test specimen

Figure 2.6 Extraction of triaxial test specimens

## 2. Experimental programme

### 2.1 Experiments on saturated clay

- *Experimental objectives*

The purpose of the experiments on saturated remoulded clay is to examine the influence of stress paths on the mechanical behaviour and microstructure of the clay, and then to identify the dilatancy mechanism from the local (microscopic and mesoscopic) point of view.

- *Experimental plan*

The saturated remoulded Kaolin K13 clay was used for study. The experiments consisted of both mechanical tests (i.e., consolidated drained triaxial tests) and microscopic tests (i.e., SEM observations, MIP tests and XR- $\mu$ CT scans) (see Figure 2.7).

In order to evaluate the effect of stress paths, two different stress paths, i.e., the conventional constant  $\sigma'_3$  stress path (S) and the purely deviatoric stress path (P), were applied during triaxial loading. To investigate the dilatancy phenomenon, both normally consolidated (NC) and over-consolidated (OC) conditions were considered. In addition, two different stress levels (P2 and P3) on the same stress path (P) were also taken into account. The triaxial loading paths employed in the saturated triaxial tests are illustrated in Figure 2.8.

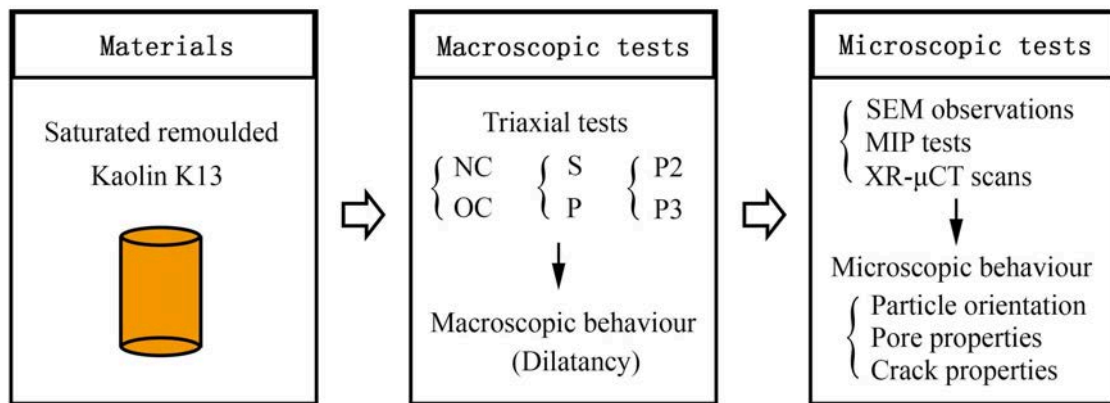


Figure 2.7 Experimental programme on saturated remoulded clay

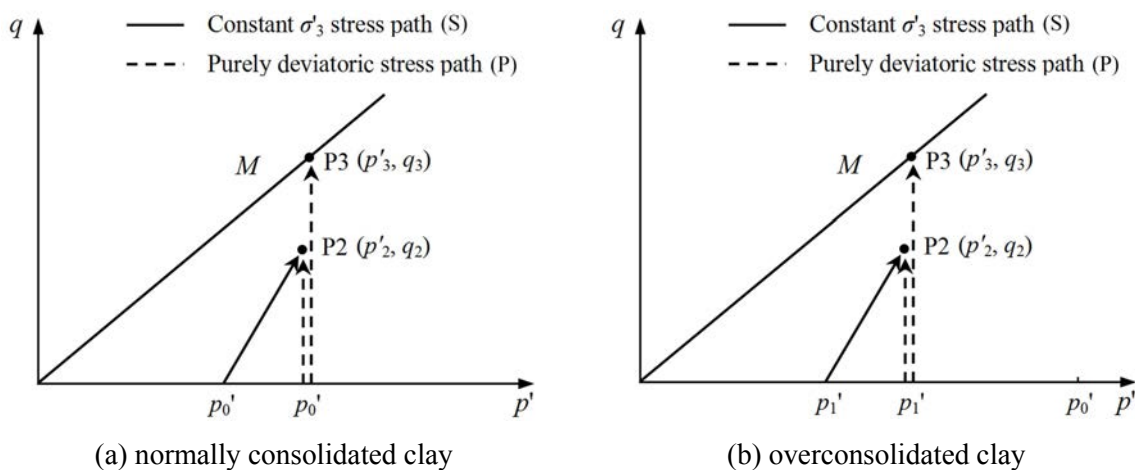


Figure 2.8 Loading paths used in saturated triaxial tests

## 2.2 Experiments on unsaturated clay

- *Experimental objectives*

The purpose of the experiments on unsaturated remoulded clay is mainly to investigate the shear strength and volume change of the clay on various high suction-stress paths.

- *Experimental plan*

The experiments also consisted of both macroscopic tests (i.e., soil-water characteristic tests and unconsolidated undrained triaxial tests) and mesoscopic tests (i.e., XR- $\mu$ CT scans) according to the test plan shown in Figure 2.9. The tests were performed on two unsaturated remoulded materials: Kaolin K13 clay and M35 clay.

Three levels of initial total suctions (i.e.,  $s_{01}$ ,  $s_{02}$  and  $s_{03}$ ) were imposed on small cubic samples and large cylindrical specimens using the vapour equilibrium method. Once the soil mass and gravimetric water content reached equilibrium, the liquid displacement technique and the oven drying method were employed to measure the soil-water characteristic parameters (Péron et al., 2007). Meanwhile, unsaturated triaxial tests were performed on these cylindrical normally consolidated (NC) specimens considering three levels of mean stress (i.e.,  $p_1$ ,  $p_2$  and  $p_3$ ) and the purely deviatoric stress path (P), as shown in Figure 2.10. Finally, XR- $\mu$ CT scans were performed on the sheared cylindrical specimens to identify the mesoscopic structural properties.

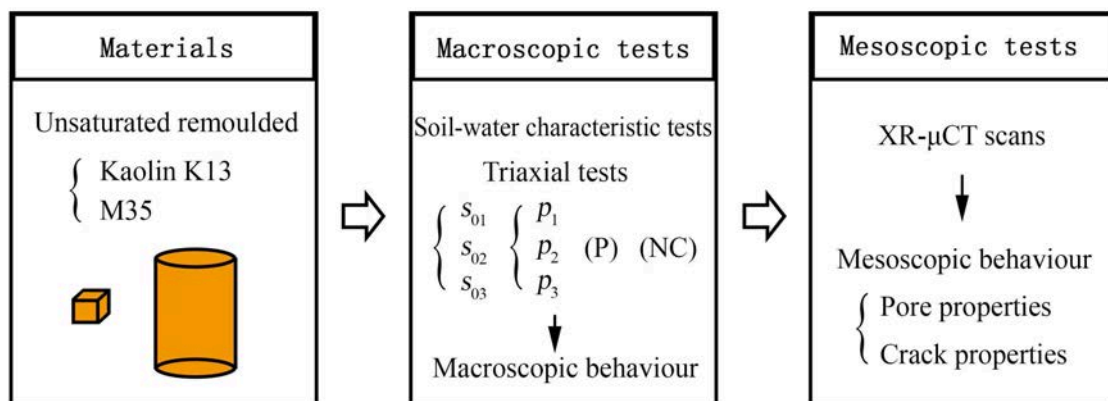


Figure 2.9 Experimental programme on unsaturated remoulded clay

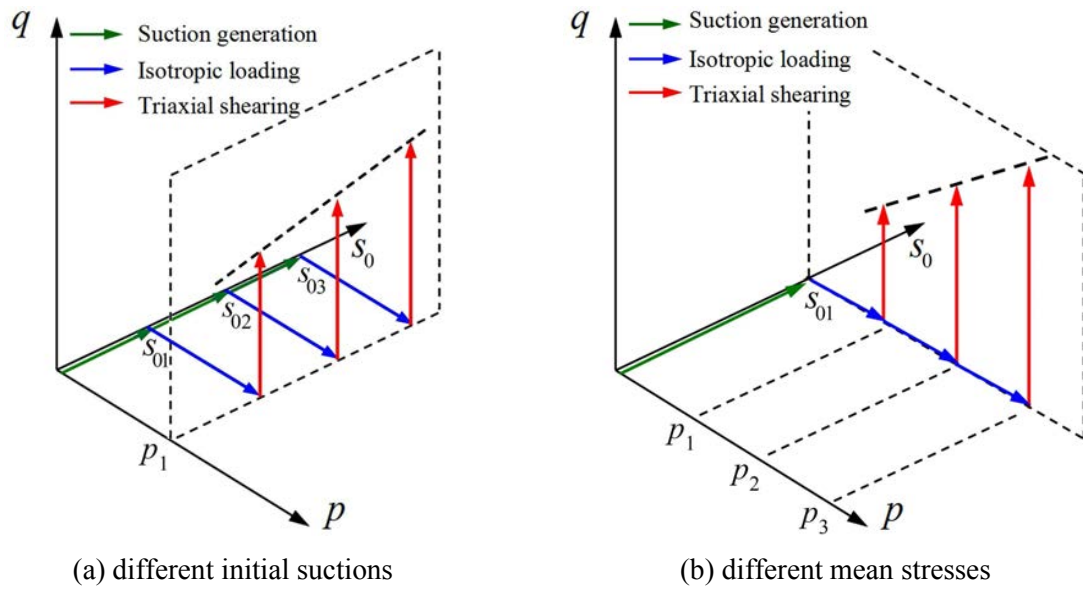


Figure 2.10 Loading paths used in unsaturated triaxial tests

### 3. Mechanical experimental procedures

#### 3.1 Triaxial tests on saturated clay

The consolidated drained (CD) triaxial compression tests were performed on saturated remoulded Kaolin K13 clay specimens.

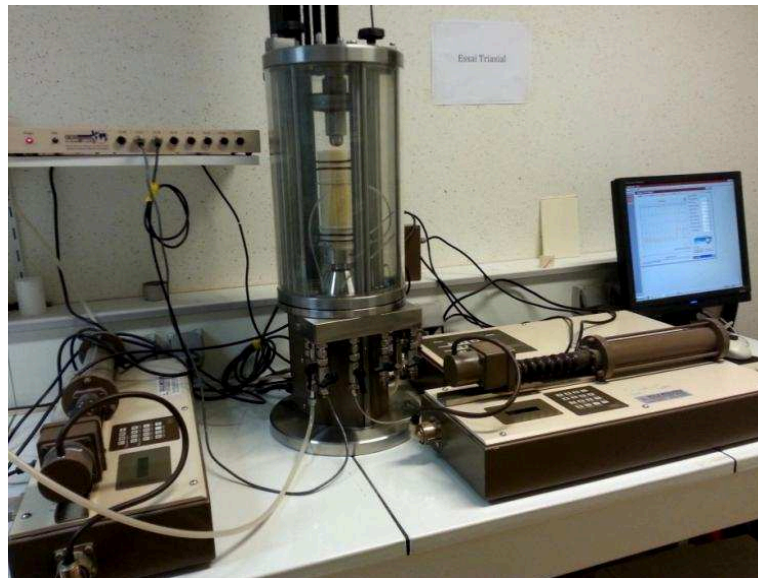


Figure 2.11 Photo of the GDS Triaxial Testing System

- *Experimental setup*

Triaxial tests were carried out using the GDS Triaxial Testing System (Figure 2.11). This system is based on the classic Bishop & Wesley type stress path triaxial cell, which controls stress directly on the specimens. It consists of a triaxial cell, a loading frame, two pressure / volume controllers, an axial loading controller, some transducers, a channel serial pad and a computer with data acquisition software (e.g., GDSLAB).

In a triaxial test, the inhomogeneity caused by the end restraint is a noticeable problem. In this study, a “sandwich” anti-frictional device proposed by Hattab and Hicher (2004) was applied to reduce the effect of end restraints. This "sandwich" device includes an aluminium plate, a thin layer of grease and a layer of rubber membrane fragments (Figure 2.12).



(a) "sandwich" device



(b) specimen between two "sandwiches"

Figure 2.12 Anti-frictional device for reducing end restraints

- ***Experimental procedures***

Prior to testing, the specimen drainage lines and the pore-water pressure measurement device were filled with de-aired water. The prepared cylindrical specimens together with filter papers, anti-frictional devices and porous discs at the ends were mounted into the triaxial chamber. They were then carefully sealed with a rubber membrane and O-rings. After the assembly of triaxial chamber and the filling of de-aired water, triaxial tests were carried out following three stages: the saturation stage, the isotropic consolidation stage and the shearing stage.

#### First stage: saturation

The objective of the saturation stage is to fill all voids in the specimen with water, thereby making the specimen fully saturated. In this study, the saturation of specimens was

accomplished using the back pressure method (Figure 2.13). The radial stress ( $\sigma_3$ ) and the back pressure ( $BP$ ) were simultaneously increased from initial small values (40 kPa and 10 kPa) to relatively large values (240 kPa and 210 kPa) with a constant difference ( $\Delta = \sigma_3 - BP = 30$  kPa). The duration of this stage was 48 hours. A good saturation of specimens was achieved when the Skempton's coefficient ( $B = \Delta u / \Delta \sigma_3$ ) approached 100%. Afterwards, the back pressure was kept constant over the following stages to ensure the specimen saturation.

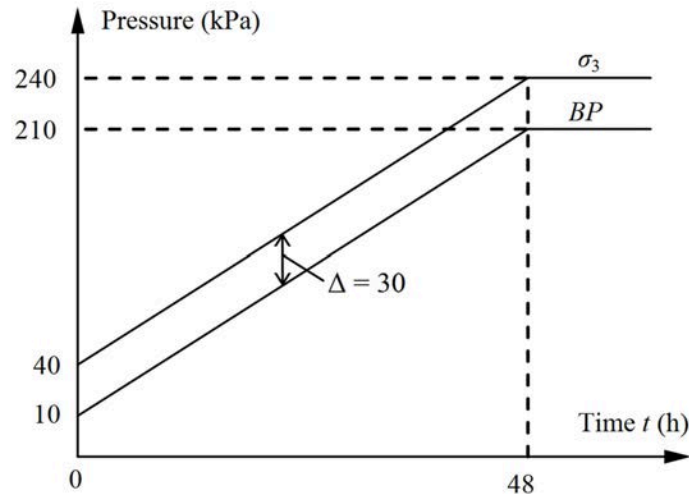


Figure 2.13 Specimen saturation stage

### Second stage: isotropic consolidation

After the saturation stage, isotropic consolidation was performed on the specimen by increasing the effective consolidation stress to the desired value  $p'_0$ . After this step, the normally consolidated condition was achieved. To meet the overconsolidated condition, the effective consolidation stress was firstly increased up to  $p'_0 = 1000$  kPa and then decreased down to the desired value  $p'_1$ . OCR can then be defined by  $OCR = p'_0 / p'_1$ . Figure 2.14a illustrates the loading path in the  $(p', q)$  plane at the isotropic consolidation stage.

Notice that the isotropic loading at this stage was applied in several steps. In order to ensure the completion of the primary consolidation of each step, a minimum consolidation duration ( $t_{100}$ ) was required. According to the French standard NF P 94-071,  $t_{100}$  is identified at the time corresponding to the turning point of the volume change  $(\Delta V) - \sqrt{t}$  curve (see Figure 2.14b).

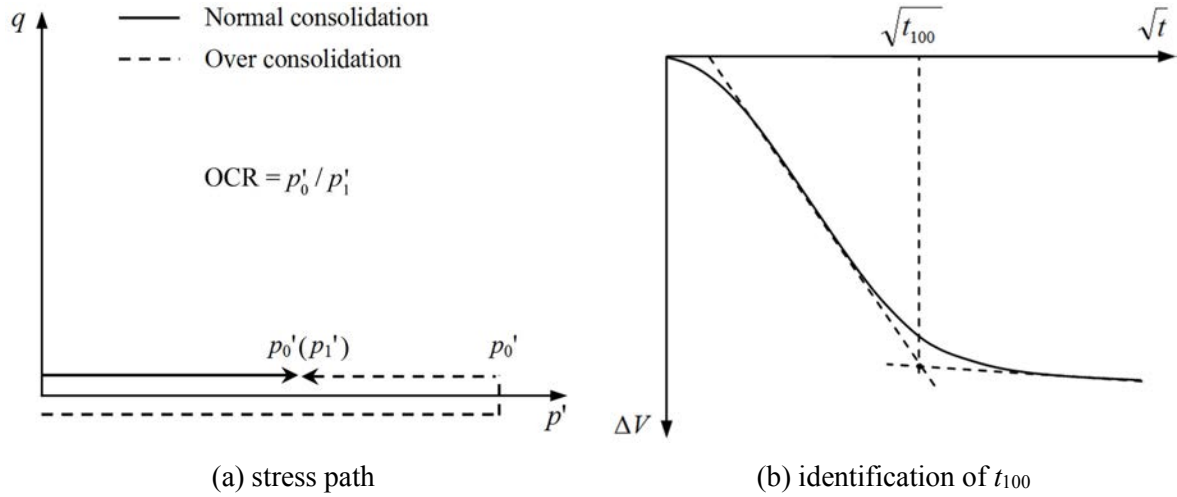


Figure 2.14 Isotropic consolidation stage

After isotropic loading, the void ratio ( $e_0$ ) was calculated using the following equation:

$$e_0 = e_{00} - (1 + e_{00}) \frac{\Delta V}{V_{00}} \quad (2.1)$$

where  $e_{00}$  is the initial void ratio;  $V_{00}$  is the initial volume of the specimen;  $\Delta V$  is the volume change of the specimen.

### Third stage: shearing

Triaxial shearing was performed using the strain-controlled method. The maximum loading velocity is calculated according to the French standard NF P 94-074:

$$v_{\max} = \frac{H_0 \cdot \varepsilon_f}{\bar{a} \cdot t_{100}} \quad (2.2)$$

where  $v_{\max}$  is the maximum loading velocity;  $H_0$  is the specimen height;  $\varepsilon_f$  is the estimated failure strain that depends on the soil type (6% for soft soil);  $\bar{a}$  is a parameter related to the drainage condition (8.5 for simple drainage).

In this section, a loading velocity of 0.0076 mm/min was employed for triaxial shearing on Kaolin K13 clay under drained conditions. In this stage, two different stress paths, i.e., the conventional constant  $\sigma'_3$  stress path (S) and the purely deviatoric stress path (P), were considered (Figure 2.15). Triaxial shearing continued up to the desired stress level in the  $(p', q)$  plane. One stress level (termed P2 with  $p'_2 = 300$  kPa and  $q_2 = 150$  kPa) is situated below the estimated critical state line and the other (termed P3 with  $p'_3 = 300$  kPa and  $q_3 = 257$  kPa) is

very close to the estimated critical state line. After triaxial shearing, the void ratio ( $e_f$ ) was systematically measured.

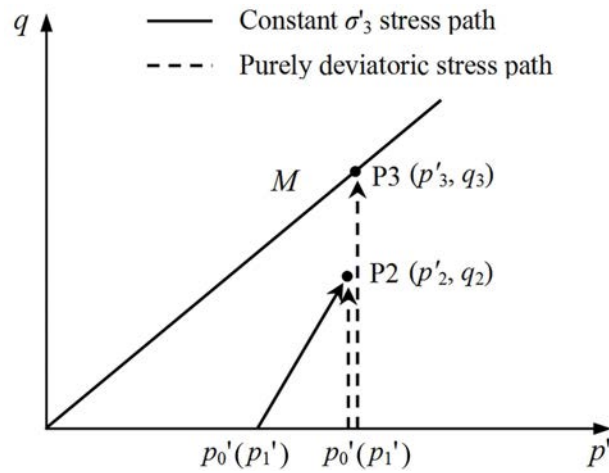


Figure 2.15 Triaxial shearing stage

Table 2.3 summarises the testing conditions used in the saturated triaxial tests on Kaolin K13 clay. Note that  $p'_0$  is the effective consolidation stress before triaxial shearing for NC clay;  $p'_1$  is the effective consolidation stress before triaxial shearing for OC clay;  $p'_f$  and  $q'_f$  are respectively the real mean effective stress and the real deviatoric stress approaching the P2 or P3 stress level;  $e_{00}$  is the void ratio after one-dimensional pre-consolidation;  $e_0$  is the void ratio after the consolidation stage and before triaxial shearing;  $e_f$  is the void ratio at the end of triaxial shearing. Two isotropic consolidation tests (without triaxial shearing), i.e., ISO\_300 and ISO\_1000, were also taken into account for comparison purposes.

Table 2.3 Specifications of mechanical tests on saturated Kaolin K13 clay

Test	Specimen	OCR	Stress path	Stress level	$p'_0$ (kPa)	$p'_1$ (kPa)	$p'_f$ (kPa)	$q'_f$ (kPa)	$e_{00}$	$e_0$	$e_f$
Isotropic consolidation	ISO_300	/	/	/	295.1	/	/	/	0.78	0.59	/
	ISO_1000	/	/	/	999.6	/	/	/	0.91	0.66	/
	NC_S250_P2	1.0	S	P2	251.1	/	298.9	149.7	0.92	0.79	0.77
	OCR4.0_S250_P2	4.0	S	P2	1000.0	251.5	314.5	192.1	0.81	0.61	0.60
Triaxial compression test	NC_P300_P2	1.0	P	P2	299.2	/	300.9	140.8	0.89	0.76	0.74
	OCR3.3_P300_P2	3.3	P	P2	1000.0	299.5	300.2	158.4	0.97	0.73	0.74
	NC_P300_P3	1.0	P	P3	299.4	/	303.4	265.0	0.93	0.78	0.74
	OCR3.3_P300_P3	3.3	P	P3	1000.0	301.0	308.4	268.1	0.97	0.72	0.75

### 3.2 Triaxial tests on unsaturated clay

- *Imposition of suction*

In order to bring cylindrical specimens to a given unsaturated state, suction was applied to specimens before triaxial testing. The axis translation technique, the osmotic technique and the vapour equilibrium method are three common methods used for suction control. In the current research, the vapour equilibrium method that developed based on the Kelvin's equation (Equation 1.2) was used. Since all of the mechanisms that act to reduce the potential of pore water (i.e., dissolved solutes, hydration effects and capillary effects) are accounted for, the suctions generated by this method are total suctions (Lu and Likos, 2004). Therefore, if no specific explanations, the suctions mentioned in this research hereafter are all referred to as total suctions.

Table 2.4 Saturated salt solutions used for controlling suctions

Salt	Temperature (°C)	Relative humidity (%)	Total suction (MPa)
Na <sub>2</sub> SO <sub>4</sub>	20	93	10.0
NaCl	20	76	37.8



(a) desiccator



(b) specimens

Figure 2.16 Imposition of suctions in clay specimens in desiccators

Apart from the zero suction (i.e., in the saturated state), two different levels of total suctions (i.e., 10.0 MPa and 38 MPa) were considered for unsaturated tests. The suctions were imposed in initially saturated clay specimens under the atmospheres of two relative humidities

(i.e., 93% and 76%) respectively generated by two saturated, pure salt solutions (i.e.,  $\text{Na}_2\text{SO}_4$  and  $\text{NaCl}$ ) (see Table 2.4) in desiccators (Figure 2.16). The temperature and relative humidity in the laboratory were controlled to be nearly constant (i.e., Temperature =  $20\text{ }^\circ\text{C} \pm 1\text{ }^\circ\text{C}$  and  $RH = 50\% \pm 2\%$ ).

- **Measurement of suction**

Once the vapour equilibrium was reached, the relative humidity of air around the clay specimens was measured using a chilled-mirror hygrometer, which is also referred to as "hygrobutton" (Wimesure, France). Subsequently, the corresponding total suction was calculated by Equation 1.2.

All hygrobuttons were calibrated using the saturated salt solutions in desiccators without clay specimens. Some calibration results are presented in Figure 2.17. It shows that the measured relative humidity slightly deviates from the expected value with respect to a given saturated salt solution. The deviation of relative humidity from the expected value leads to some noticeable errors in the calculation of total suction. Therefore, the read of relative humidity of each hygrobutton should be corrected according to the gap between the measured data and the expected value.

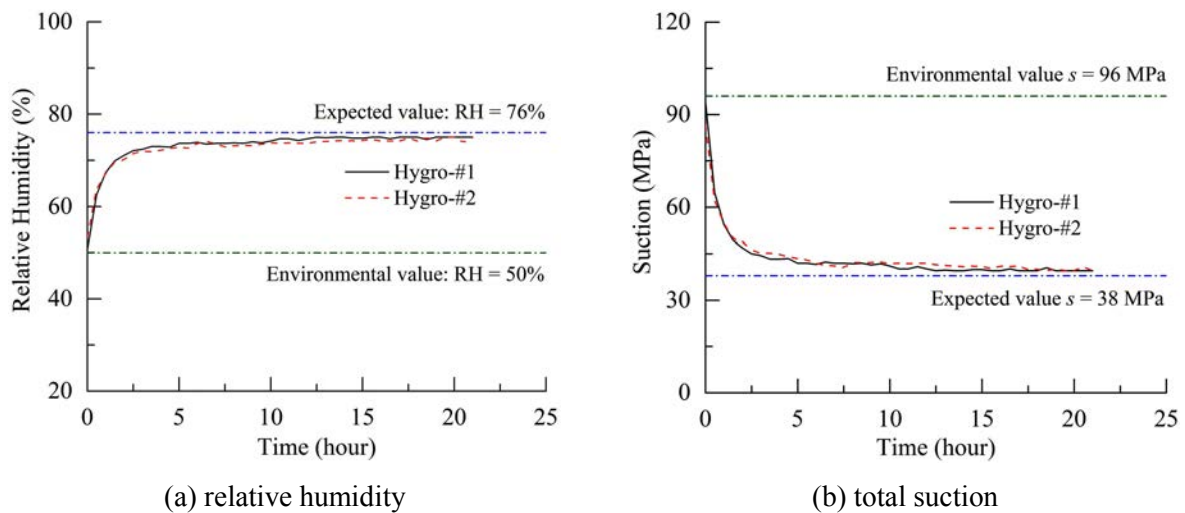


Figure 2.17 Calibration of hygrobutton using saturated NaCl solution

The calibrated hygrobuttons were then used to measure the total suction of the clay specimens before and during triaxial tests. Prior to triaxial testing, all the accessories inside the triaxial cell including the rubber membrane, the filter papers, the porous disks, the anti-friction devices, the PMMA disks as well as the hygrobuttons were placed in the same

desiccator that contained the specimen to be tested for one night. In this way, these accessories had the same initial total suctions as the specimen and would not affect the suction measurement during the test. To start an unsaturated triaxial test, two hygrobuttons were fixed in the pre-drilled holes of two PMMA disks, and then they were installed on the top and bottom ends of the specimen (Figure 2.18). Therefore, the variation of total suction around the specimen ends during triaxial loading could be indirectly measured.

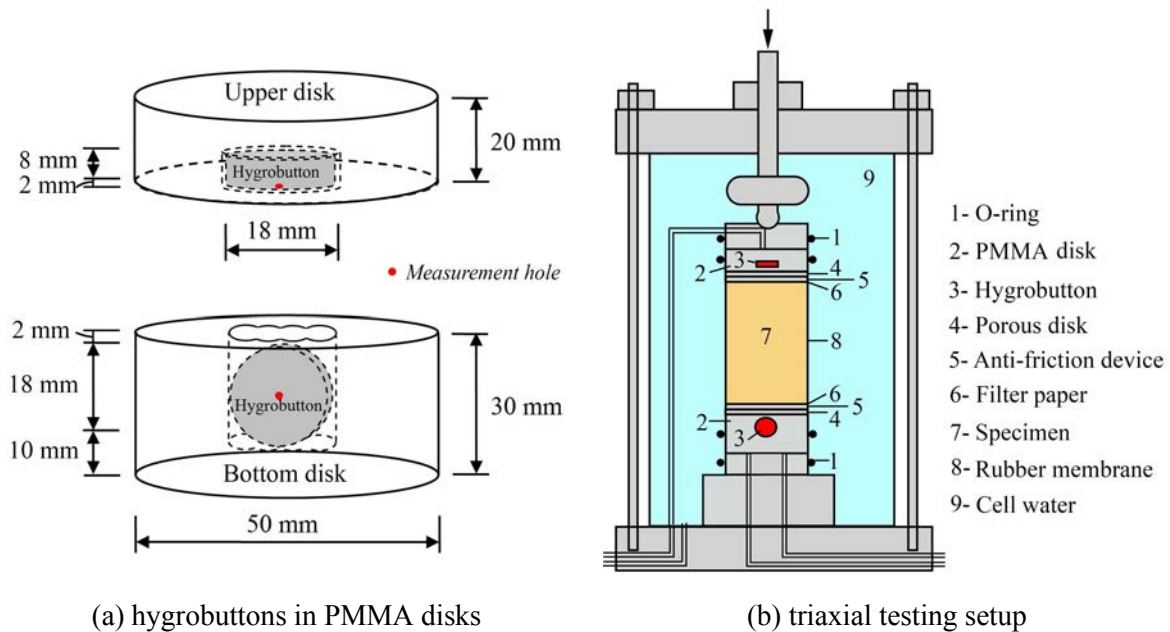


Figure 2.18 Triaxial testing setup with suction measurement

- **Unconsolidated undrained triaxial tests**

Unconsolidated undrained (UU) triaxial compression tests were carried out on the suction-imposed cylindrical specimens using the aforementioned GDS Triaxial Testing System (Figure 2.18b). After the installation of the specimen and the hygrobuttons, the triaxial chamber was assembled and then filled with de-aired water. Subsequently, the desired isotropic stress  $p$  was applied to the specimens in several steps under undrained (both water and air) conditions. Afterwards, triaxial shearing was performed following the purely deviatoric stress path until the failure of the specimen, as illustrated in Figure 2.19.

Notice that the loading velocity during triaxial shearing must be very slow, so that the vapour equilibrium can be satisfied in every small loading step. With respect to unconsolidated undrained triaxial tests on saturated specimens, the strain-controlled method is recommended, and a loading velocity between 0.5 %/min and 1.5 %/min is suggested in the

French Standard NF P 94-074. In terms of unconsolidated undrained triaxial tests on unsaturated clays with relative humidity measurement, no corresponding value of loading velocity was found in the literature. In this case, a very slow loading velocity calculated from Equation (2.2) was employed. Therefore, the relative humidity measured by hygrobutton could be considered reasonable.

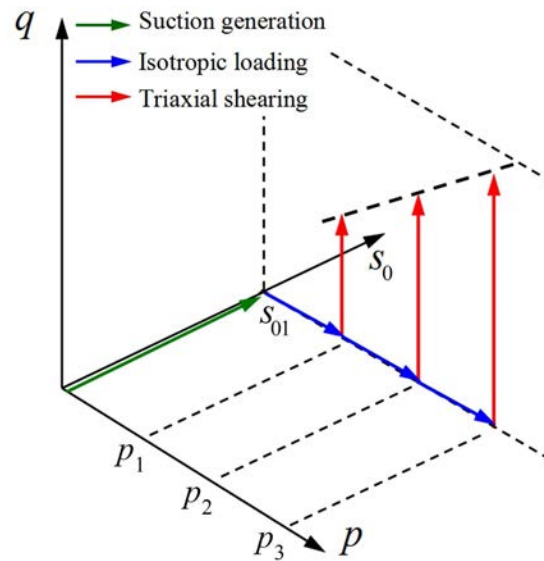


Figure 2.19 Stress path used for unsaturated triaxial testing

Table 2.5 Specifications of triaxial tests on Kaolin K13 clay

Material	Saturation condition	Number	Specimen	Salt solution	$s_0$ (MPa)	$p$ (kPa)	$p'$ (kPa)	
Kaolin K13	Saturated	1	K13_S0_P200	/	0.0	/	200	
		2	K13_S0_P600	/	0.0	/	600	
		3	K13_S0_P1000	/	0.0	/	1000	
	Unsaturated	Unsaturated	1	K13_S10_P200	Na <sub>2</sub> SO <sub>4</sub>	10.0	200	/
			2	K13_S10_P600	Na <sub>2</sub> SO <sub>4</sub>	10.0	600	/
			3	K13_S10_P1000	Na <sub>2</sub> SO <sub>4</sub>	10.0	1000	/
			4	K13_S38_P200	NaCl	38.0	200	/
			5	K13_S38_P600	NaCl	38.0	600	/
			6	K13_S38_P1000	NaCl	38.0	1000	/

For comparison purposes, drained triaxial compression tests were also conducted on saturated specimens on the same stress path. The experimental procedures were similar to those presented in Section 3.1. Tables 2.5-2.6 summarise the clay specimens and testing conditions used in the triaxial tests.

Table 2.6 Specifications of triaxial tests on M35 clay

Material	Saturation condition	Number	Specimen	Salt solution	$s_0$ (MPa)	$p$ (kPa)	$p'$ (kPa)
M35	Saturated	1	M35_S0_P1000	/	0	/	1000
		1	M35_S38_P200	NaCl	38.0	200	/
	Unsaturated	2	M35_S38_P600	NaCl	38.0	600	/
		3	M35_S38_P1000	NaCl	38.0	1000	/
		4	M35_S38_unconfined	NaCl	38.0	/	/

- **Measurement of volume change**

The volume change of a saturated specimen is directly related to water exchange. In general, there are three types of methods for the determination of volume change: (i) the first one is the measurement of fluid volume change in specimen; (ii) the second one is the measurement of volume change of triaxial cell water; and (iii) the third one is the direct measurement of specimen deformation by means of local axial and radial strain sensors, laser technique and digital photography (Rifai et al., 2002; Laloui et al., 2006).

With respect to an unsaturated specimen, the measurement of volume change is much more complex because the total volume change is not only dependent on water exchange but also affected by air exchange and air compression. In this study, the unconsolidated undrained triaxial tests were employed, and thus the drainage of both air and water was not allowed. In this case, the first method is not possible for the measurement of volume change. Furthermore, the volume change of triaxial cell water can not correctly reflect the volume change of specimen because the cell pressure decreases on the purely deviatoric stress path. Therefore, the third method is only feasible one to measure the volume change of unsaturated specimen.

In this study, the digital photography technique was employed. This method consisted in taking photographs of specimen through the transparent triaxial cell during the test with a

computer-controlled digital camera. The camera was fixed at a constant distance from the triaxial cell. Two lamps were fixed on both sides of the specimen to offer a homogeneous lighting. After triaxial testing, the image processing technique was used to analyse the radial deformation of specimen. Finally, the volumetric strain was calculated from the axial strain measured by triaxial testing system and the radial strain measured by digital photography. It should be noted that this method offered only an approximation of specimen volume change, and the accuracy was affected by the direction of measurement. For instance, when the specimen fails with a clear shear plane, the volumetric strains determined from two perpendicular directions may be different (Figure 2.20).

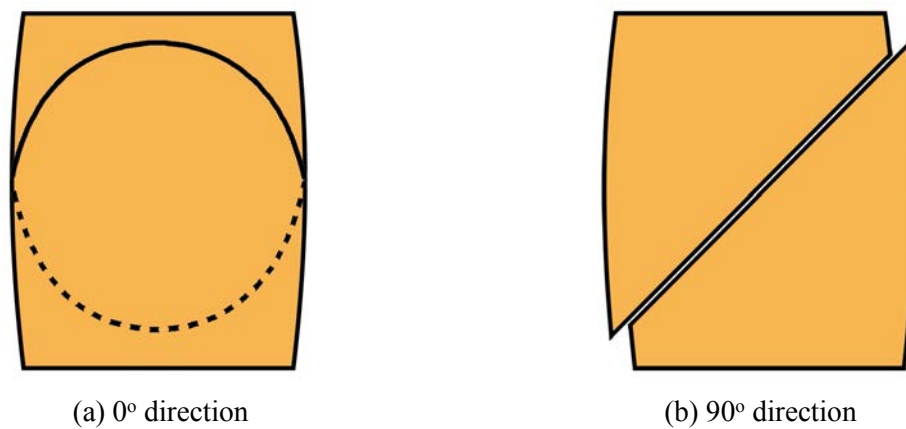


Figure 2.20 Limitations of digital photography for volume change measurement

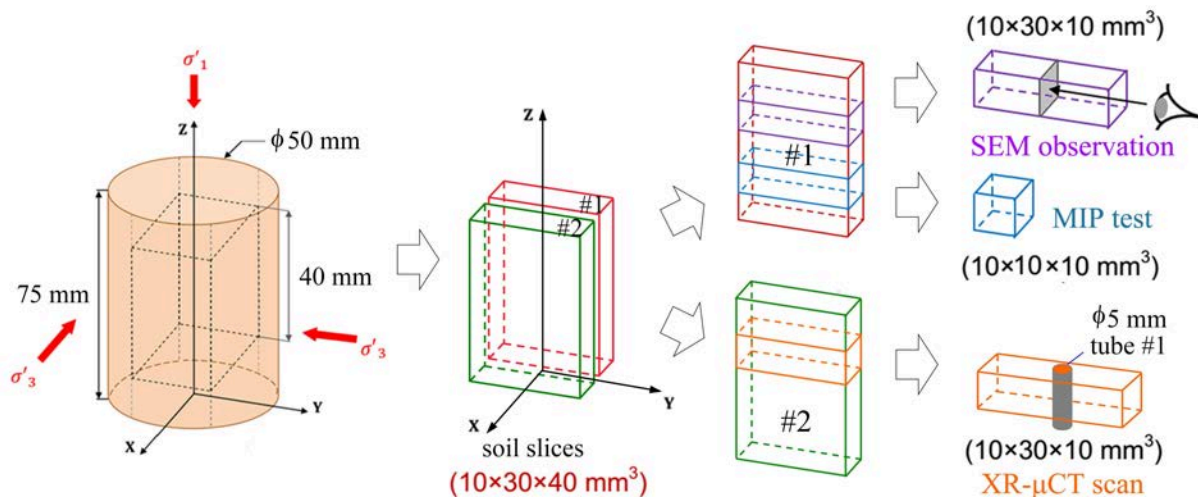


Figure 2.21 Sample preparation for microstructural observations

#### 4. Microscale experimental procedures

After triaxial testing, the clay specimens were recovered, by first removing the deviatoric stress and then the isotropic stress under undrained conditions. Subsequently, two soil slices (see #1 and #2 in Figure 2.21) with 40 mm in height, 10 mm in thickness and 30 mm in width were extracted from the core of every specimen, for microscopic observations.

## 4.1 Scanning electron microscopy (SEM) observations

---

### 4.1.1 Sample preparation and experimental procedures

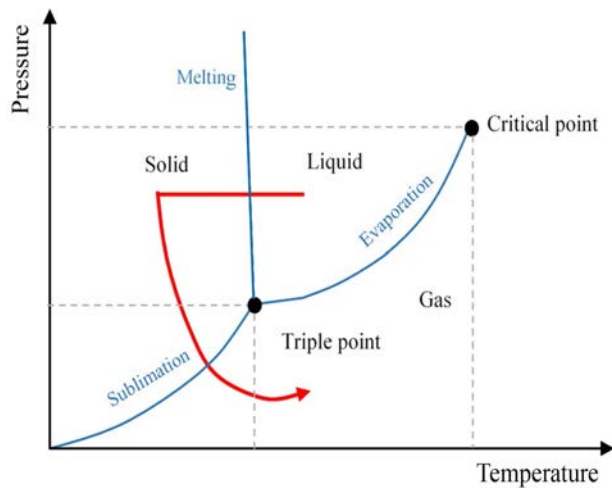
---

Rectangular subsamples (10 mm × 30 mm × 10 mm) used for SEM observation were cut from the soil slice #1 with a blade (see Figure 2.21). Because the SEM observation requires dried samples, we lyophilised the subsamples using the method advocated by Delage and Pellerin (1984). The whole lyophilisation (freeze-drying) process consists of three primary phases, i.e., freezing phase, primary drying phase (ice sublimation) and secondary drying phase (moisture desorption):

i. *Freezing phase.* Samples were placed in a freeze-drying container, which was filled with liquid nitrogen. In this phase, it is important to cool the clay below its triple point (Figure 2.22a), the lowest temperature at which the solid and liquid phases can coexist. This ensures that sublimation rather than melting will occur in the following phases.

ii. *Primary drying phase.* Samples were transferred into a vacuum desiccator, then the pressure was lowered (in the range of a few millibars), and enough heat was supplied to the clay for the ice to sublimate. In this drying phase, about 95% of the water in the clay can be removed. This phase may be slow, because, if too much heat is added, the clay microstructure could be altered.

iii. *Secondary drying phase.* This phase aims to remove unfrozen water molecules, since the ice was removed in the primary drying phase. In this phase, the temperature was raised higher than that in the primary drying phase, and it can even be above 0 °C. The pressure was also lowered in this phase to encourage desorption. At the end of the operation, the final residual water content in the sample was extremely low, which would not affect SEM observations.



(a) phase diagram of water



(b) Alpha 2-4 LSC

Figure 2.22 Lyophilisation (freeze-drying) technique

The sample lyophilisation was performed using the Alpha 2-4 LSC (Martin Christ) freeze-dryer (Figure 2.22b) at the MSSMat laboratory of CentraleSupélec, University Paris-Saclay. Notice that all the rectangular subsamples were cut in the middle section during freezing phase to generate flat and fresh observation surfaces, which were parallel to the axial stress  $\sigma_1$  during triaxial tests (Figure 2.21). The lyophilised subsamples were stored in a desiccator.

Before SEM observation, the observation surfaces of subsamples were vacuum coated with thin layers of gold, making them electrically conductive to prevent electrostatic charge build up on the samples. This metallisation process was carried out using the 108 auto sputter coater (Cressington) at 30 mA and 15 mbar for 20 s. Afterwards, SEM samples were mounted on a holder and positioned in the electron chamber of a JSM-6490 microscope (JEOL USA) for observations (Figure 2.23).

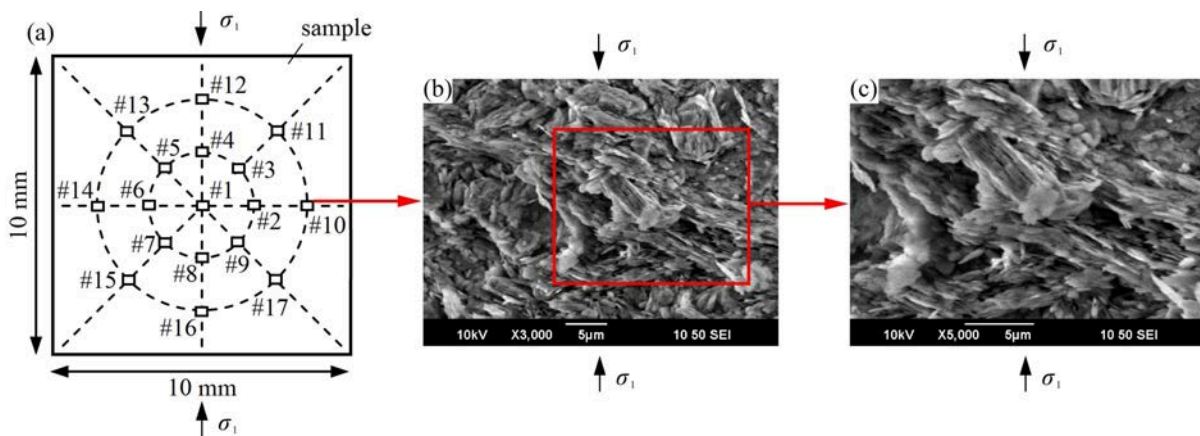
The SEM technique uses a focused electron beam to generate a variety of signals containing information about the sample surfaces and converts these signals into visual images. In this research, we saved SEM images of different magnifications (e.g., 3000 $\times$  and 5000 $\times$ ) from more than 17 typical positions on the vertical observation surface of each clay subsample (see Figure 2.24).



(a) samples on a holder

(b) JSM-6490 microscope

Figure 2.23 SEM setup and metallised samples



(a) observation surface; (b) 3000× image; (c) 5000× image

Figure 2.24 Acquisition of SEM images from the vertical observation surface

#### 4.1.2 Quantitative methods for the identification of particle orientation

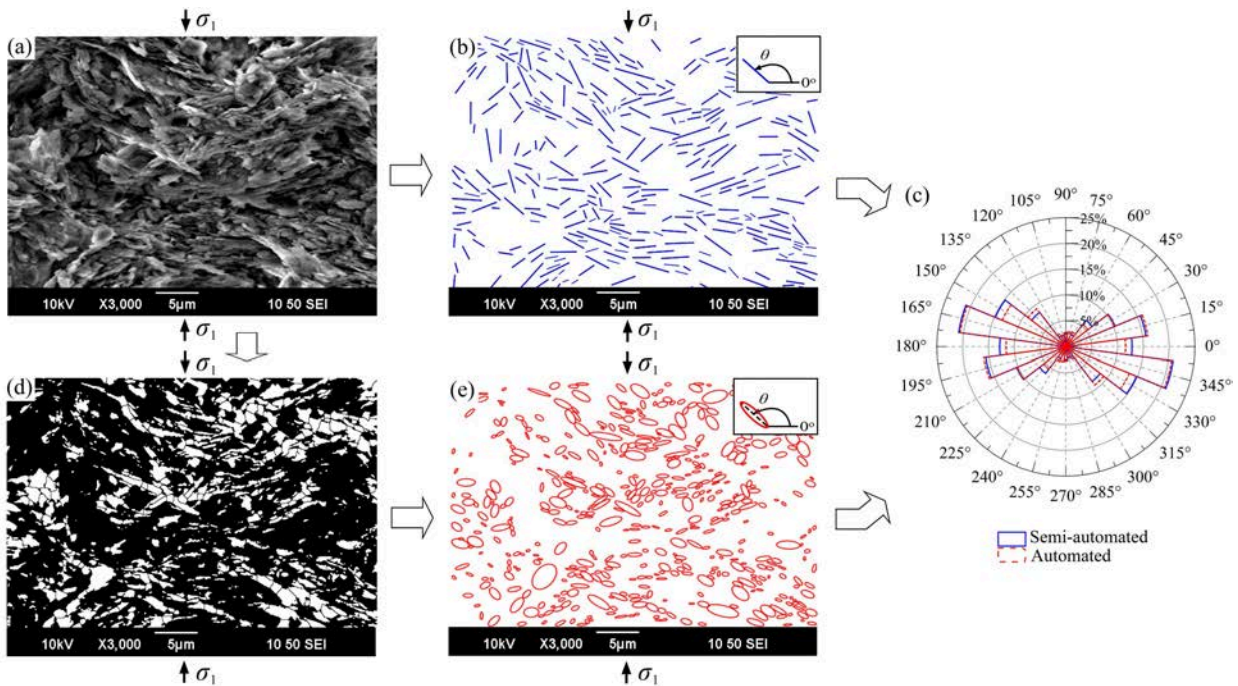
- **Image processing method**

Two methods were used to acquire the orientation (anticlockwise angles) of clay particles with respect to the horizontal plane. Note that an orientation angle of  $0^\circ$  corresponds to the horizontal direction (which is perpendicular to the direction of axial stress  $\sigma_1$  during triaxial tests) and an orientation angle of  $90^\circ$  corresponds to the vertical direction (which is parallel to  $\sigma_1$ ). An example of image processing by means of both the semi-automated method and the automated method is presented in Figure 2.25.

The first method consists in a semi-automated method relying on the joint application of the Photoshop software and ImageJ software, as used by Hattab et al. (2010). Firstly, via the Photoshop software, we drew straight lines representing the skeletons of clay particles (Figure

2.25a and b). Each straight line has a given orientation with respect to the horizontal plane (Figure 2.25b). Then the ImageJ software was used to measure the angles of all drawn straight lines and calculate the number of oriented clay particles in a given narrow range of orientation (Figure 2.25c).

The second method consists in an automated method based on the ImageJ programme (Schindelin et al., 2015; Rueden et al., 2017). In this method, the raw SEM image (Figure 2.25a) was converted into a binary image by setting a proper threshold; the binary image was then segmented using the adjustable watershed algorithm (Figure 2.25d); next, the particles (with an area larger than 50 square pixels and an aspect ratio greater than 1.5) in the image were fitted with ellipses (Figure 2.25e); and finally the particle orientation was obtained by measuring the tilt angle of the ellipses with respect to the horizontal plane (Figure 2.25c).



(a) raw image; (b) semi-automated method; (c) rose diagram; (d-e) automated method

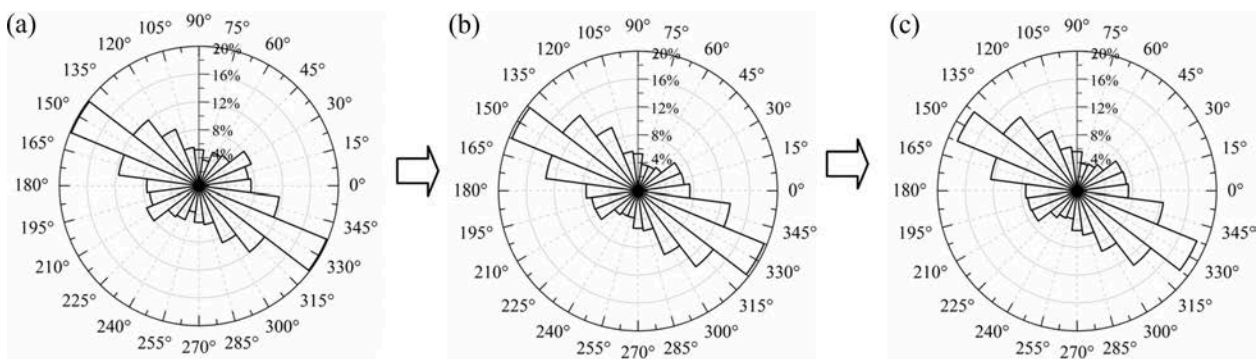
Figure 2.25 Analysis methods of particle orientation

Figure 2.25c shows that the two methods have a quasi-similar angular representation of the percentage of particles as a function of their orientation. Nevertheless, the kaolin particles appeared mainly by edges on the vertical plane (Figure 2.25a), indicating that it was quite reasonable to fit the particles by straight lines. In addition, by manually neglecting round or small particles as well as those appearing by faces, we can obtain more reliable results. For these reasons, we selected the semi-automated method to process SEM images in this study.

- **Representative analysis of SEM images**

According to the study by Zhang and Cui (2017), the SEM images with magnifications of 1000× up to 5000× are all suitable for the identification of clay microstructure. It is also suggested that 400 - 500 measurements would give a good representation of the pore distribution on a rose diagram, referring to Barton (1974). In this study, a 5000× magnified image with a zone of 25 μm × 19 μm often contained 150 - 200 distinct particles (Figure 2.24c), and a 3000× magnified image with a zone of 42 μm × 32 μm usually had more than 400 clear-cut particles (Figure 2.24b and Figure 2.25). To make it more representative, the results obtained from 3000× magnified images were selected to characterise the microstructure of each specimen.

Figure 2.26 presents the relationship between the global orientation (statistic data) of clay particles and the number of 3000× magnified images (particle numbers). It appears that the preferential orientation (e.g., from 127° to 172°) does not change when the counted particle number increased from 1940 in 4 images to 5984 in 12 images. The minor orientation direction varies a little, but not in a significant manner. Therefore, 10 representative 3000× magnified images (containing 5000 particles or more) of each SEM sample were carefully selected and processed, to identify the global orientation of clay particles. The particle number and image number were considered sufficient to give reasonable and accurate enough results.



(a) 1940 particles in 4 images; (b) 4096 particles in 8 images; (c) 5984 particles in 12 images

Figure 2.26 Relationship between global particle orientation and image numbers

- **Characterisation of clay particle orientation**

Clay particle orientation is usually described using rose diagrams, as shown in Figures 2.25c, 2.26 and 2.27a. In a rose diagram, the angle ( $\theta$ ) from 0° to 360° is divided into 24 equal intervals ( $\Delta\theta = 360^\circ / 24 = 15^\circ$ ). Therefore, the percentage of clay particles with orientation

towards a given angle range ( $\theta_i$ ) is calculated by:

$$P(\theta_i) = \frac{N_{\theta_i}}{N} \times 100\% \quad (i = 1, 2, 3, \dots, 24) \quad (2.3)$$

where  $\theta_i$  is the  $i$ th angle range from  $(15i - 22.5)^\circ$  to  $(15i - 7.5)^\circ$ , especially it is between  $352.5^\circ$  and  $360^\circ$  and between  $0^\circ$  and  $7.5^\circ$  when  $i = 1$ ;  $P(\theta_i)$  is the percentage of clay particles with orientation towards  $\theta_i$ ,  $P(\theta_j) = P(\theta_{j+12})$  ( $j = 1, 2, 3, \dots, 12$ ) due to centered-symmetry;  $N_{\theta_i}$  is the number of clay particles with orientation towards  $\theta_i$ ;  $N$  is the total number of clay particles.

In addition, clay particle orientation can be characterised by the orientation curve (see Figure 2.27b). In Figure 2.27b, the  $x$ -axis is the orientation angle ( $\theta$ ) from  $0^\circ$  to  $180^\circ$  with an interval of  $15^\circ$  and the  $y$ -axis is the percentage of clay particles with orientation towards a given angle range ( $\theta_i$ ). The depolarization (D) line represents a perfectly isotropic microstructure for a fictional clayey material (Hattab and Fleureau, 2010).

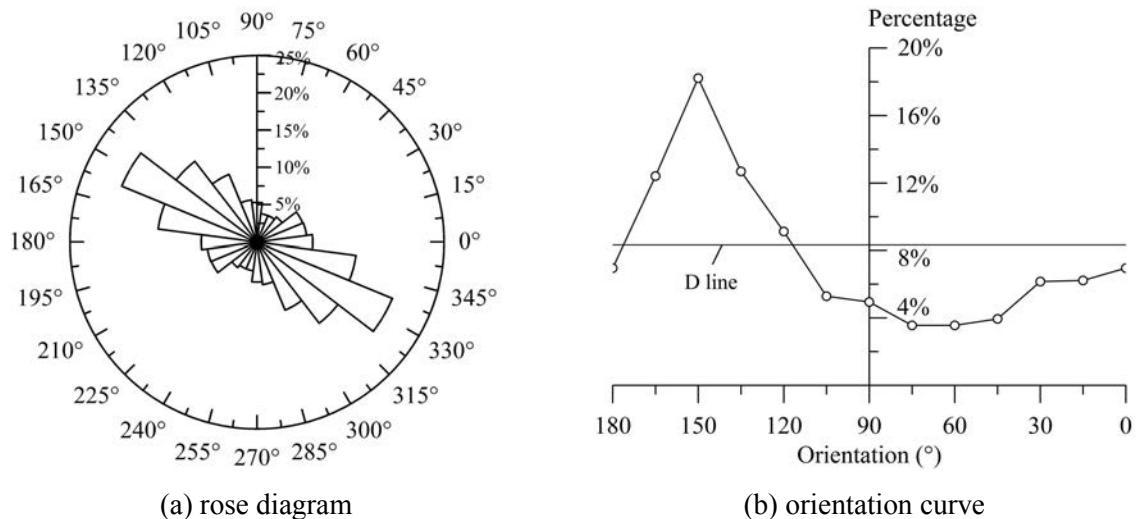


Figure 2.27 Quantitative characterisation of clay particle orientation

#### 4.1.3 Quantitative methods for the identification of pore properties

- **Image processing method**

Raw SEM images are represented by greyscale micrographs, in which the morphology of a sample surface is stored as shades of grey, varying from black to white. In general, the pore space in samples falls in a darker greyscale in comparison with the solid material. Therefore, the pore space and the solid material can be discriminated by greyscales (Figure 2.28).

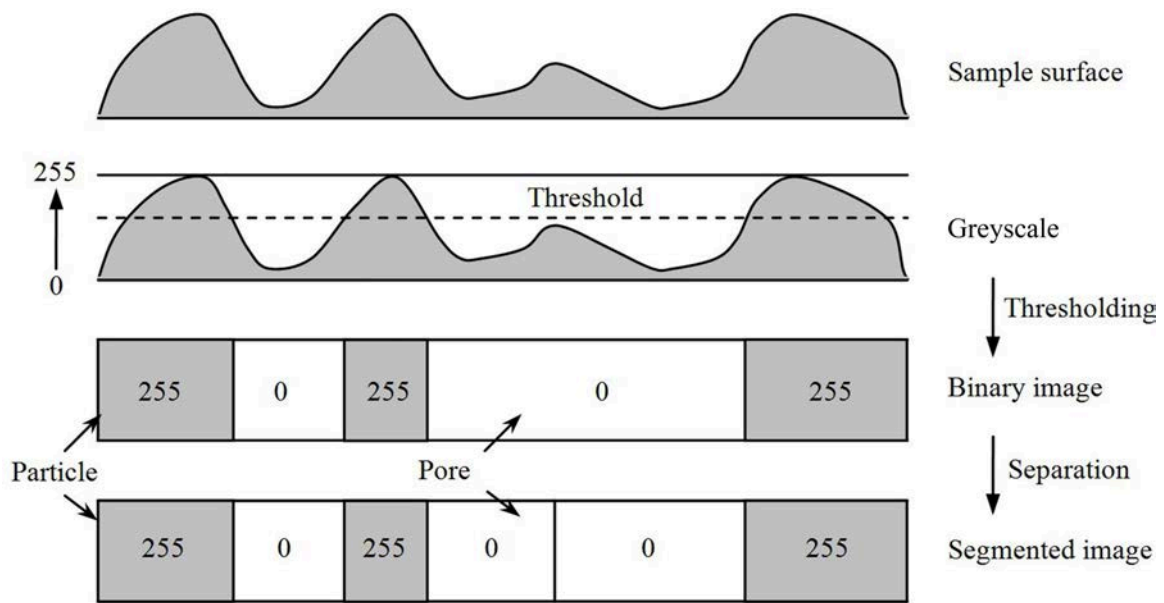
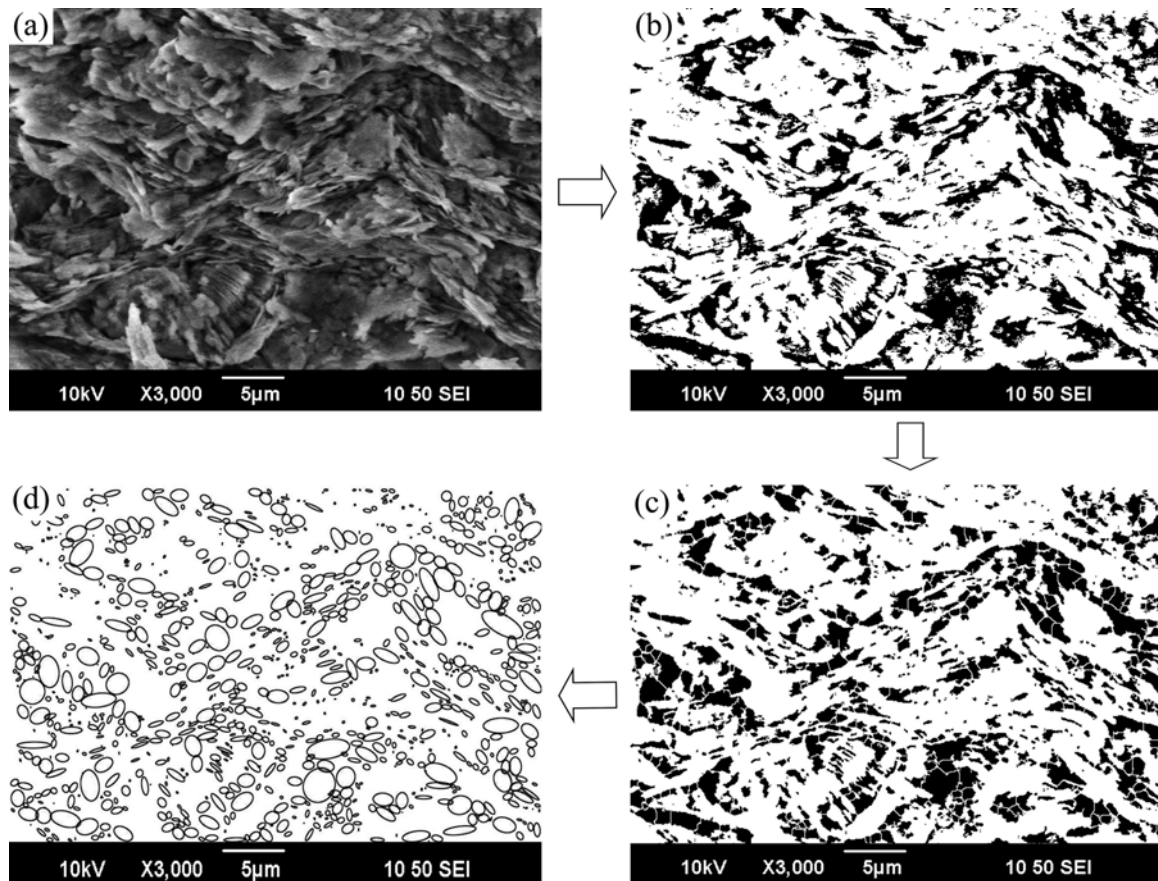


Figure 2.28 Principle of image segmentation

An image processing method based on the ImageJ programme was employed to identify the pore structure from SEM images, as shown in Figure 2.29. In the beginning, the greyscale images were pre-processed using the smooth, sharpen and filter functions to improve the image quality and reduce the image noise (Figure 2.29a). Secondly, the segmentation using thresholding procedures was carried out to transform the greyscale images to binary images (Figure 2.29b). Next, the adjustable watershed algorithm method was used to separate the connected pores (Figure 2.29c). Finally, the segmented pores were fitted with ellipses (Figure 2.29d), and then the pore geometric parameters (e.g., the pore area, the pore perimeter, the major axis length, the minor axis length and the tilt angle) were measured. It should be noted that too small pores are difficult to measure correctly due to the insufficient number of pixels. In our case, the pores represented by less than 50 pixels (corresponding to an area of approximately  $0.05 \mu\text{m}^2$ ) were neglected. It means that the minimum size of the detected pores is about  $0.23 \mu\text{m}$ .



(a) pre-processed image; (b) threshold; (c) separation; (d) ellipses fitting  
 Figure 2.29 Image processing procedures for pore structure identification

During the image processing, the thresholding procedure was critical since it controlled the analysis accuracy. Thus, the thresholding operation was repeated several times independently, and every time the threshold was determined according to the maximum similarity between the raw image and the segmented one. The average threshold was then used in our final analyses.

Pores separation was another important step to get reasonable results. A manual operation of pore merging was sometimes necessary due to the over-segmentation problem of the watershed algorithm method.

- *Characterisation of the morphology of 2D pores*

The complexity of pore structures can usually be characterised using a parameter referred to as fractal dimension. In this study, the perimeter-area fractal dimension based on the slit-island method (Mandelbrot et al., 1984) was employed. If a pore system can be described in fractal terms, then the relationship between the pore area and the pore perimeter is

characterised by (Liu et al., 2011; Zhang and Cui, 2017):

$$\log L = \frac{D_f}{2} \log A + C \quad (2.4)$$

where  $D_f$  is the fractal dimension, varying between one and two (a larger value indicates a more complicated pore structure);  $A$  is the pore area;  $L$  is the pore perimeter;  $C$  is a constant.

The shape of a pore is characterised by the roundness, which is defined by:

$$R_s = \frac{4A}{\pi a^2} = \frac{b}{a} \quad (2.5)$$

where  $R_s$  is the pore roundness: it varies from nearly zero for a very elongated pore to nearly one for an equiaxed pore (see Figure 2.30a);  $a$  is the major axis length of the fitting ellipse;  $b$  is the minor axis length of the fitting ellipse.

The definition of pore orientation is similar to that of clay particle orientation. The orientation of a pore is the direction of the major axis of the pore (ellipse) with respect to the horizontal direction (Figure 2.30b).

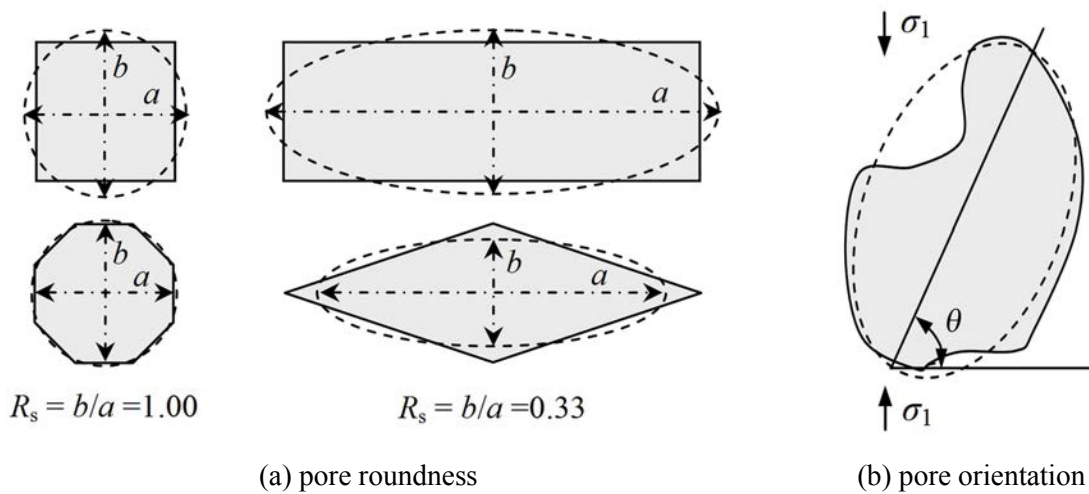


Figure 2.30 2D characterisation of micropore structure

The anisotropy of pore structure can be quantified by the orientation index  $I_{or}$  proposed by Hicher et al. (2000):

$$I_{or} = \frac{k + l + m}{h + i + j} \quad (2.6)$$

where  $I_{or}$  is the orientation index: it varies from one for an isotropic structure to zero for an extremely anisotropic structure;  $i$  is the maximum percentage of pore orientation (Figure 2.31a);  $h$  and  $j$  are the percentages of pore orientation of two zones beside the maximum percentage zone;  $k, l, m$  are the percentages of pore orientation of the zones perpendicular to the zones  $h, i$  and  $j$ , respectively.

Similar to the clay particle orientation, the pore orientation can also be characterised by rose diagrams and orientation curves (Figure 2.31). The  $D^{pore}$  line in Figure 2.31b means a depolarization line, which represents a perfectly isotropic pore structure for a fictional clayey material.

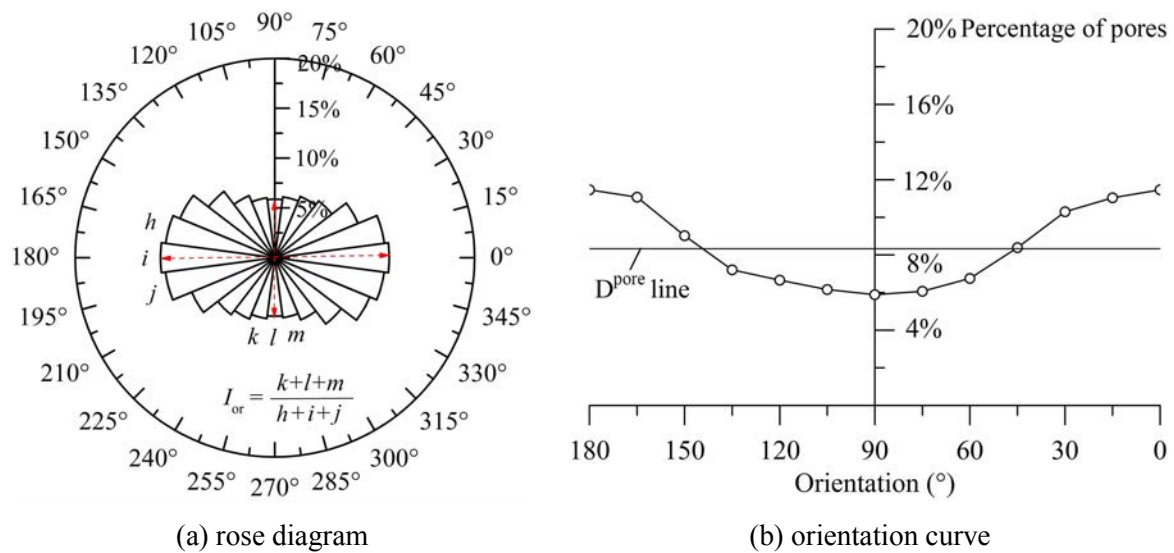


Figure 2.31 Quantitative characterisation of pore orientation

- **Characterisation of porosity and pore size distribution (PSD)**

With the aid of image processing methods, the equivalent size, microvoid ratio and pore size distribution of 2D pores were readily obtained from SEM images. The equivalent size of a 2D pore is defined as the diameter of a circle that has the same area as the pore:

$$d_e = \sqrt{\frac{4A}{\pi}} \quad (2.7)$$

where  $d_e$  is the equivalent size of a 2D pore.

The 2D microvoid ratio of specimens is calculated by the following equation:

$$e_{2D} = \frac{A_p}{A_T - A_p} \tag{2.8}$$

where  $e_{2D}$  is the 2D microvoid ratio;  $A_T$  is the total area of the imaging surface;  $A_p$  is the total area of the pores on the imaging surface.

However, it is necessary to note that a cutting plane does not generally cut the clay specimen through the centre of every 3D pore when generating the SEM observation surface. Hence, it may lead to some problems with 2D PSD to characterise a real 3D PSD. For example, as illustrated in Figure 2.32, when a plane cuts a specimen through the centres of all equal-sized spheres (3D pores), then equal-sized circles (2D pores) could be obtained by analysing the cross-section and the 2D pore sizes are exactly equal to the 3D pore sizes. Nevertheless, when the plane cuts the specimen in other directions, random-sized circles (2D pores) may be obtained, and the 2D pore sizes are no longer equal to the 3D pore sizes. This indicates that the 2D pore sizes, microvoid ratio and PSD measured from the cross-section of soil specimens are not sufficient to represent 3D pore structures. For this reason, the stereological technique was herein adopted to estimate the 3D pore sizes, microvoid ratio and PSD from the 2D pore parameters.

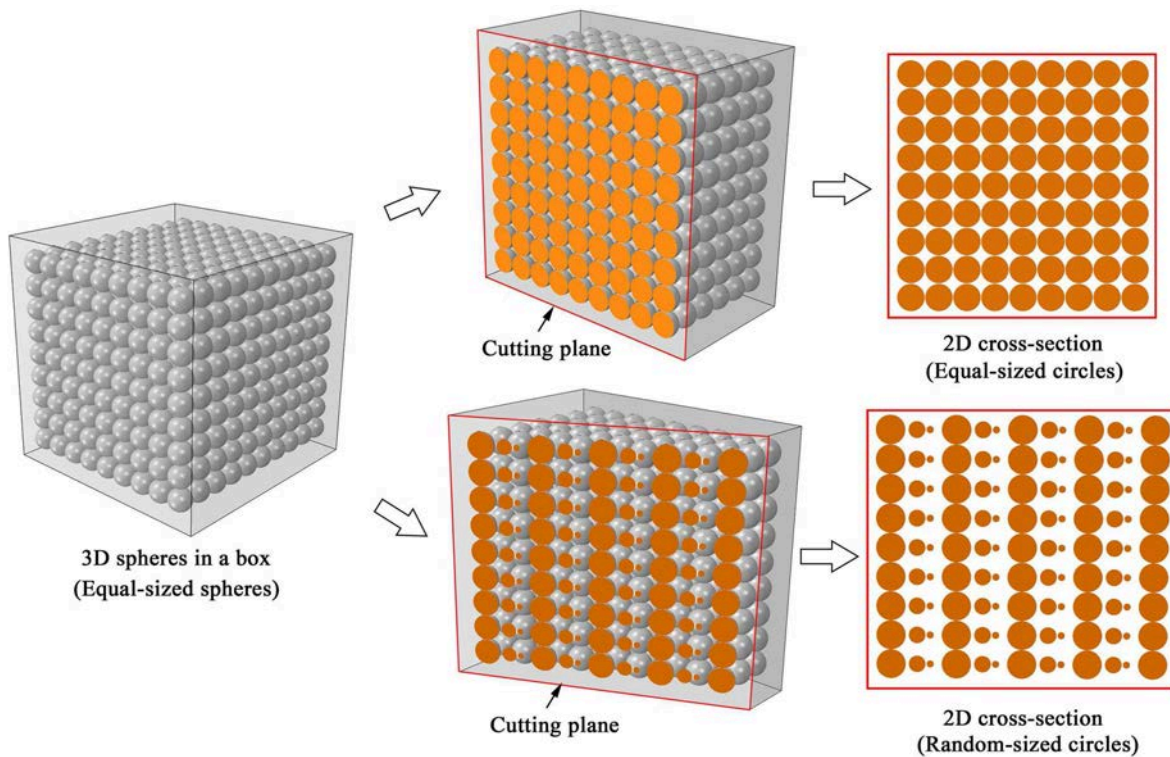


Figure 2.32 Problems with 2D pore size characterisation

Stereology is a widely used method for the investigation of 3D space when only 2D sections through objects of interest are available. According to Sahagian and Prousevitch (1998), the concept of stereology can be illustrated using a system of three spherical objects, as shown in Figure 2.33. The random cuts of each 3D sphere produce a series of 2D cross-sections. The maximum 2D cross-section has the same diameter as the 3D sphere. The generation of each 2D cross-section from a 3D sphere has a particular probability, which is plotted below the corresponding 2D cross-section. The 2D PSD is, in fact, an accumulation of the probabilities of all 2D cross-sections. As expected, the 2D PSD is different from the 3D PSD. However, if the probability that a given 2D cross-section came from a certain class of 3D spheres is determined, then the 3D PSD can be deduced from the 2D PSD.

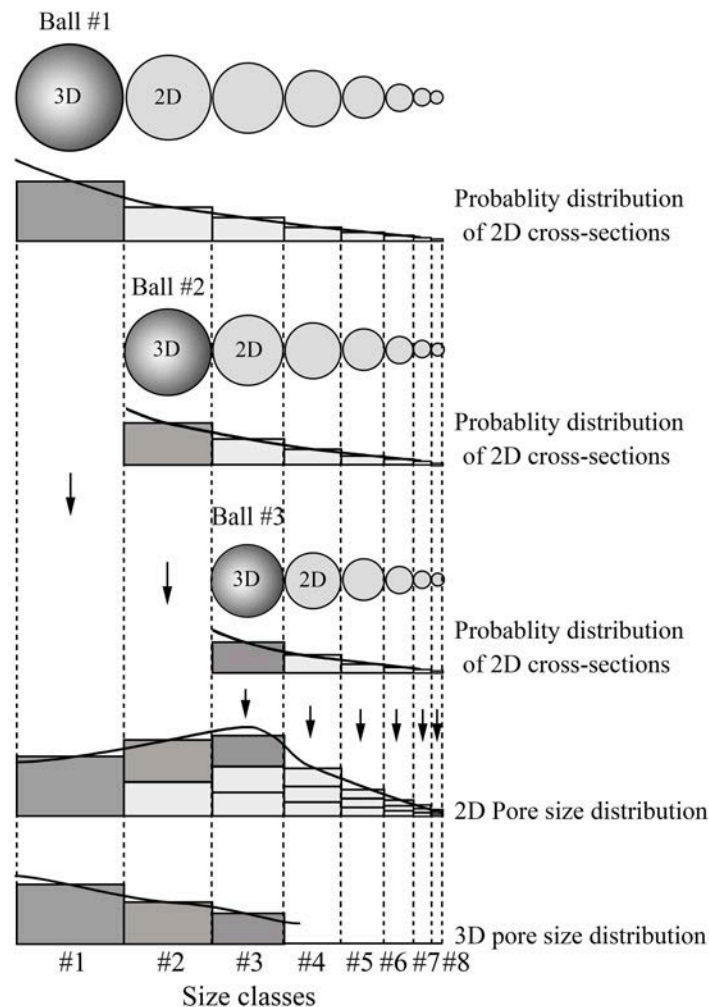


Figure 2.33 Principle of stereology (after Sahagian and Prousevitch, 1998)

In this study, a stereological approach referred to as the 25F association method developed by Xu and Pitot (2003) was used. The 3D pores in a clay specimen were assumed to be spheres of 25 size-classes ranging from  $10^{-1.4}$  (0.04)  $\mu\text{m}$  to  $10^{1.1}$  (10.0)  $\mu\text{m}$ . A logarithm size-

class interval ( $\log(\Delta D)$ ) of 0.1 was considered.

It is noteworthy that the stereology was developed based on the assumption that all the 3D objects (i.e., pores) have the same shape and are randomly oriented in space. However, the fact is that the real shapes of clay pores are neither identical nor spherical, and the pores are more or less preferentially oriented due to mechanical loading. This leads to estimation errors when using the stereology to evaluate the 3D pore structure of clay. Nevertheless, the results estimated from SEM images using the stereology make sense when serving as a supplement to the MIP results.

Figure 2.34 compares the SEM-based 2D PSD and the SEM-stereology-based 3D PSD of a specimen. One can note that the 2D pore sizes are between 0.2  $\mu\text{m}$  and 8.0  $\mu\text{m}$  with the mean pore size of 3.16  $\mu\text{m}$ . The 3D PSD curve has a similar shape as the 2D PSD curve, while the mean size of 3D pores is slightly smaller than that of 2D pores.

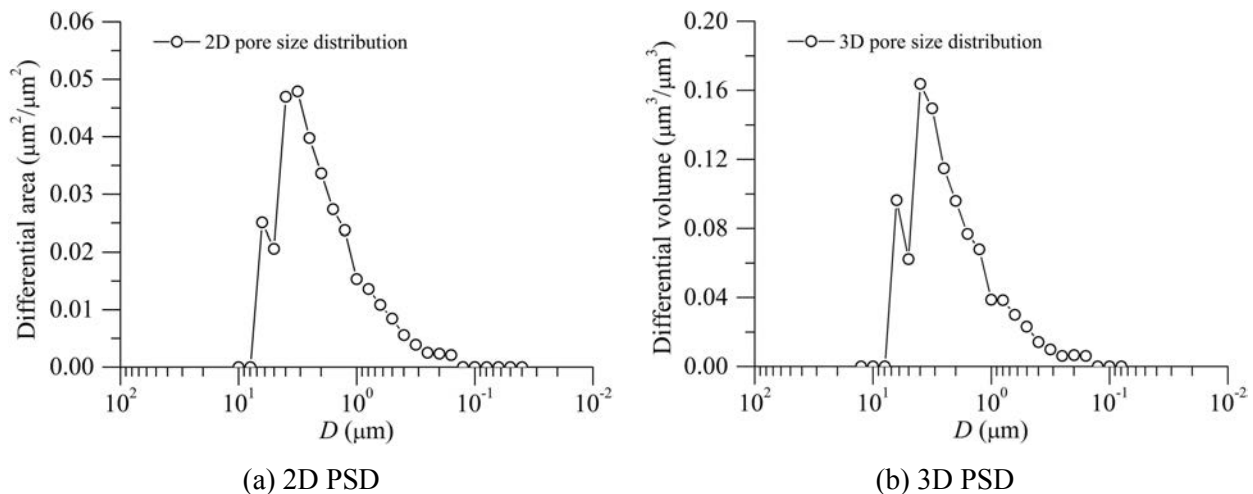


Figure 2.34 Examples of SEM-based 2D PSD and SEM-stereology-based 3D PSD

## 4.2 Mercury intrusion porosimetry (MIP) tests

### 4.2.1 Experimental principle

MIP is widely used for the evaluation of PSD, porosity and pore volume of soil. It is a technique based on the fact that a non-wetting liquid can be intruded into the pore space when the pressure is sufficiently high. The unique relationship between the intrusion pressure and pore throat diameter was proposed by Washburn (1921):

$$D = -\frac{4\gamma \cos \Theta}{P_m} \quad (2.9)$$

where  $D$  is the pore diameter;  $\gamma$  is the surface tension of mercury;  $\Theta$  is the contact angle;  $P_m$  is the applied intrusion pressure of mercury.

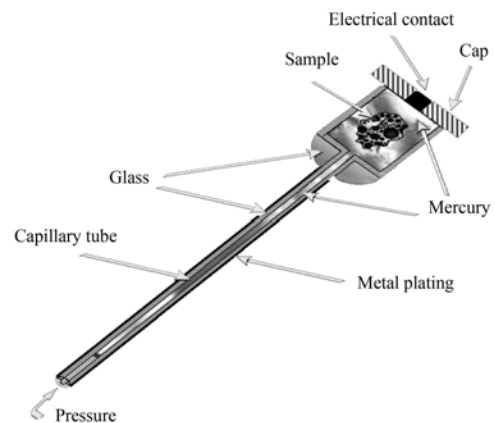
According to Equation (2.9), the pore diameter can be obtained as a function of the mercury intrusion volume by varying the applied pressure and measuring the mercury volume intruded into the clay. The accuracy of MIP is limited by three assumptions: (i) the pores are cylindrical; (ii) the wetting angle is constant throughout the microstructure; and (iii) the pore system remains undamaged during mercury intrusion.

#### 4.2.2 Experimental procedures

Small cubic subsample with the side length of 10 mm used for MIP testing was cut from the lower part of the soil slice #1 (see Figure 2.21). The freeze-drying method was also used to lyophilise the MIP subsamples without destroying the clay fabric. In this study, MIP tests were carried out using the AutoPore IV 9500 system (Micromeritics) at the MSSMat laboratory of CentraleSupélec, University Paris-Saclay (Figure 2.35).



(a) AutoPore IV 9500



(b) penetrometer

Figure 2.35 MIP test setup for pore structure quantification

To perform the tests, the lyophilised MIP samples were placed in the mercury penetrometers. The sealed penetrometers were inserted into the low-pressure ports of the system. In the first stage, the air in the penetrometers was evacuated and subsequently replaced by mercury up to a pressure of 265 kPa. In the second stage, the penetrometers filled

with mercury were removed from the low-pressure ports, weighed, and placed in the high-pressure ports. The mercury was then pressurised incrementally up to the maximum pressure of about 206 MPa. At such a pressure, a minimum pore-throat diameter of 6 nm can be measured considering the contact angle of  $\theta = 147^\circ$  and surface tension of  $\gamma = 0.484$  N/m at 25°C (ASTM D 4404, 2010). The samples were weighed before and after the experiments to estimate the amount of mercury that remained in the pore space.

---

#### 4.2.3 Quantification of 3D pore properties

---

- Pore size distribution

The results of MIP tests are usually represented by the curves of cumulative pore volume and differential pore volume. If the calculated pore diameters are successively numbered, the cumulative volume and differential volume of intruded mercury can be respectively calculated by:

$$V_{\text{Hg}} = \sum_i \Delta V_i \quad (2.10)$$

$$V_{\text{diff},i} = \frac{-\Delta V_i}{\Delta \log D_i} \quad (2.11)$$

where  $V_{\text{Hg}}$  is the cumulative volume of the intruded mercury;  $D_i$  is the median diameter of the  $i$ th pore class;  $V_i$  is the volume of the intruded mercury;  $V_{\text{diff},i}$  is the differential volume of the intruded mercury.

Figure 2.36 shows an example of the PSD deduced from an MIP test. It can be seen that the relationship between the cumulative volume and the pore diameter is characterised by an S-curve. The maximum cumulative volume of the pores in the tested specimen is approximately 0.25 ml/g. The differential volume curve has a unimodal form with the peak occurring at a pore size of 0.15  $\mu\text{m}$ . This indicates that the pores in the tested remoulded clay specimen are mainly inter-aggregate pores.

Notice that both values of  $V_{\text{Hg}}$  and  $V_{\text{diff},i}$  are usually expressed by ml/g (see Figure 2.36). To make them comparable to the results obtained by the SEM-stereology method, a normalised pore size distribution (pore diameter - frequency relationship) is introduced. The frequency of each pore size ( $D_i$ ) is calculated by  $V_{\text{diff},i} / V_{\text{Hg}}$ .

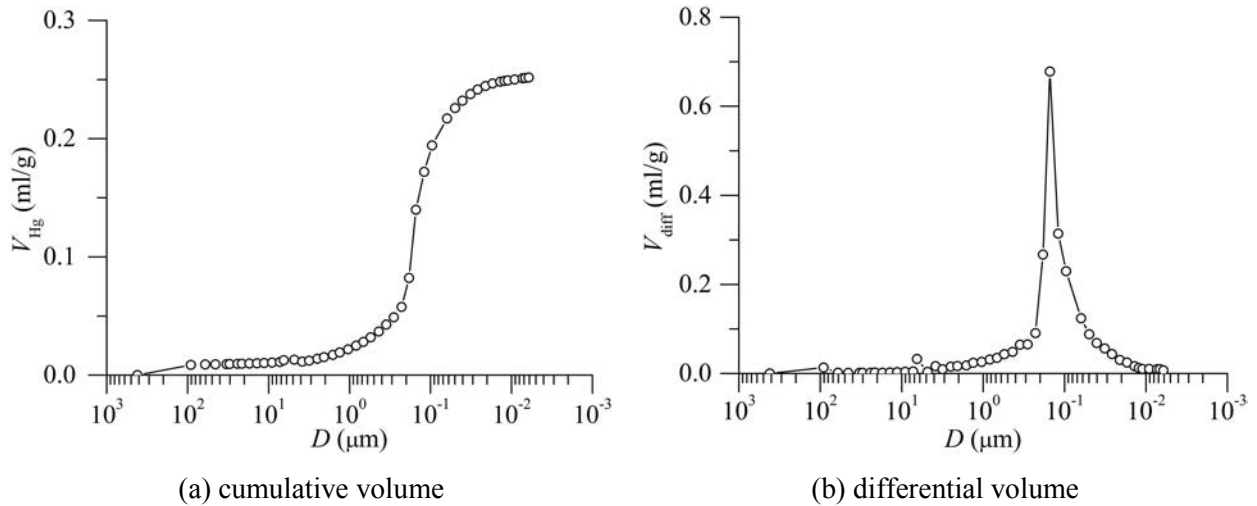


Figure 2.36 Example of PSD deduced from MIP test

- Microvoid ratio

Void ratio is defined as the ratio of void volume to solid volume. Dividing the void volume and the solid volume by the solid mass, we obtain the equation of void ratio as:

$$e = \frac{V_v}{V_s} = \frac{V_v / m_s}{V_s / m_s} \quad (2.12)$$

where  $e$  is the void ratio;  $V_v$  is the void volume;  $V_s$  is the solid volume;  $m_s$  is the soil solid mass.

Replacing  $V_v / m_s$  with  $V_{Hg}$  and  $V_s / m_s$  with  $1 / \rho_s$ , we derive the expression of the microvoid ratio from Equation (2.12):

$$e_{MIP} = V_{Hg} \cdot \rho_s \quad (2.13)$$

where  $e_{MIP}$  is the microvoid ratio calculated from the MIP data;  $\rho_s$  is the mass density of the clay solids.

### 4.3 X-ray microtomography (XR- $\mu$ CT) scans

#### 4.3.1 Sample preparation and experimental procedures

- *Small-sample preparation*

In order to example the development of local cracks within clay samples, the XR- $\mu$ CT

scans were carried out in this study.

To prepare the small samples for XR- $\mu$ CT scans, rectangular subsamples with the dimension of 10 mm  $\times$  30 mm  $\times$  10 mm were firstly extracted from the soil slice #2 (Figure 2.21). Afterwards, the sample preparation scheme shown in Figure 2.37 was used. Notice that  $\sigma_1$  in this figure is the axial stress applied during triaxial tests; it is represented here to indicate the direction of the analysed XR-  $\mu$ CT subsample.

In the first step, we inserted thin-walled plastic tubes (tube #1) into the rectangular subsamples from their upper surfaces (Figure 2.37a), and then gently pulled the tubes out from the lower surfaces. Through this step, small cylindrical samples with their axes parallel to the axial stress  $\sigma_1$  were obtained. These thin-walled tubes had an internal diameter of 5 mm and a height of 15 mm. In the second step, we nested the small cylindrical samples inside larger rigid tubes (tube #2) and sealed them with paraffin wax (Figure 2.37b). The purpose of this step is to protect the samples and preserve the soil fabric. Figure 2.37c presents the photograph of a referenced small sample used for XR- $\mu$ CT scan.

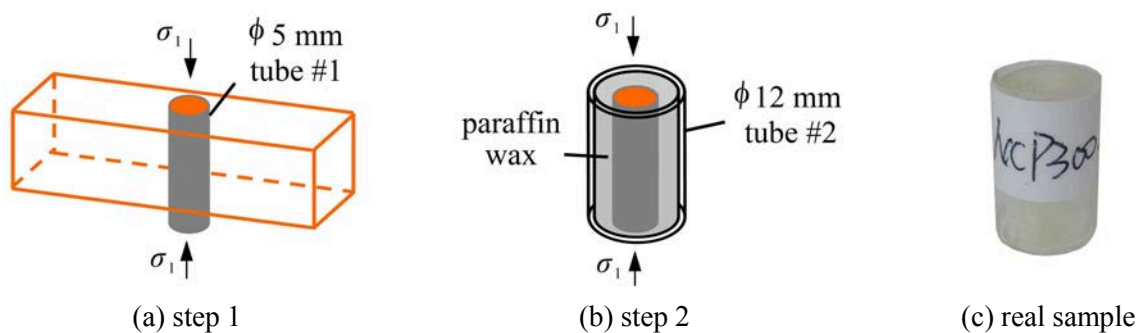


Figure 2.37 Sample preparation for XR- $\mu$ CT scans

- ***Experimental principle and procedures***

The XR- $\mu$ CT scans were performed in a High Resolution 3D Micro-computed Tomography (XR-Solutions Ltd). The testing system is primarily composed of an X-ray generator, a sample holder, a scintillator and a CCD detector (see Figure 2.38). The sample is placed on the holder, which is located between the X-ray generator and the scintillator. When X-rays propagate in the sample, they will be attenuated according to the geometry and material property of the scanned sample and the initial energy of X-rays. Hence, a detector could receive X-rays of different signal intensities to produce greyscale projections. In general, more than 1000 projections of the sample can be acquired over 360°. Afterwards, supporting

computer software can make use of these X-ray projections to produce cross-sectional slices, allowing the user to observe the internal structure of the sample without destroying it.

In our scans, the following imaging parameters were used: the tube voltage was 80-90 kV, the tube current was 70 - 80  $\mu\text{A}$ , and the exposure time was 3.0 s. The scanned domain of the sample was about 2.1 mm in height, 3.3 mm in length and width with the resolution of 1.70  $\mu\text{m}$ .

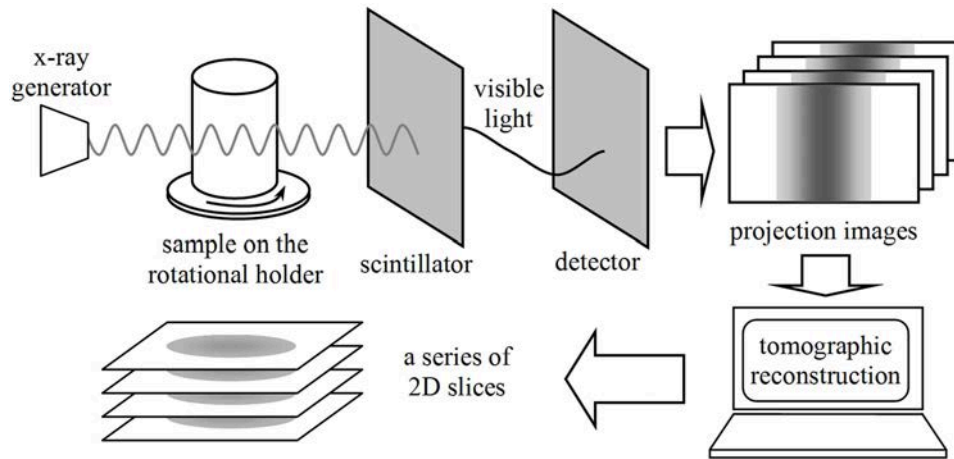


Figure 2.38 Schematic illustration of XR- $\mu$ CT scans (after Landis and Keane, 2010)

#### 4.3.2 Validation of the sample preparation methods

In order to examine if the heat of X-ray and the insertion of plastic tube (tube #1 in Figure 2.37) influence the soil fabric, XR- $\mu$ CT scans were carried out twice on the same clay sample. The first scan consists in identifying the microstructure of a sample without plastic tube, while the second scan consists in identifying the microstructural variation of the same sample with plastic tube insertion.

To perform the first scan, a cubic sample with the dimension of 15 mm  $\times$  15 mm  $\times$  15 mm was extracted from the one-dimensionally consolidated clay core. Afterwards, metal fibres (diameter = 0.2 mm) or organic fibres (diameter = 0.1 mm) were inserted into the sample. The purpose of using these fibres was to help identify the structural change of soil. Next, the sample was sealed with paraffin wax, and the weight ( $m_1$ ) of the sample was measured. Subsequently, the first XR- $\mu$ CT scan was performed on this sample, and then the weight ( $m_2$ ) of the sample was measured again after the test.

For the second scan, the paraffin wax was gently removed from the previously scanned

sample, and a thin-walled plastic tube (tube #1, wall thickness = 0.15 mm) was inserted into the cubic sample. In this way, the embedded fibres were enclosed in the plastic tube. After sealing with paraffin wax, the sample was scanned using the XR- $\mu$ CT technique.

The weight measurements show a variation of  $(m_1 - m_2)/m_1 = 0.4\%$  in soil mass after the first scan. This indicates that there is little water loss due to the heat of X-rays during the test. Meanwhile, it is noted that the paraffin wax whose melting point is around  $60^\circ\text{C}$  remains solid throughout the test. Therefore, it is reasonable to consider that the heat of X-rays does not greatly affect the soil fabric.

Figure 2.39a and b shows the projections of the sample with two metal fibres before and after the insertion of the plastic tube. Figure 2.39c is a sketch of the metal fibres in the sample. The influence of the insertion of the plastic tube on the soil fabric is characterised by the variation in the positions of fibres. The test results for a clay sample with two metal fibres are listed in Table 2.7. One can note that the change in the distance between two fibres is approximately 1.0%, while the variation in the angles varies from 0.4% to 4.8% depending on the absolute value of the angle: the larger the angle, the smaller the variation. The relatively large variations in the smallest angles are probably due to the measurement errors. Table 2.8 presents the test results of a clay sample with a soft organic fibre and large pores. It shows that both the distances and angles between the organic fibre and the pore centres change very little after the insertion of the plastic tube. The above results suggest that the influence of the plastic tube on soil fabric is negligible.

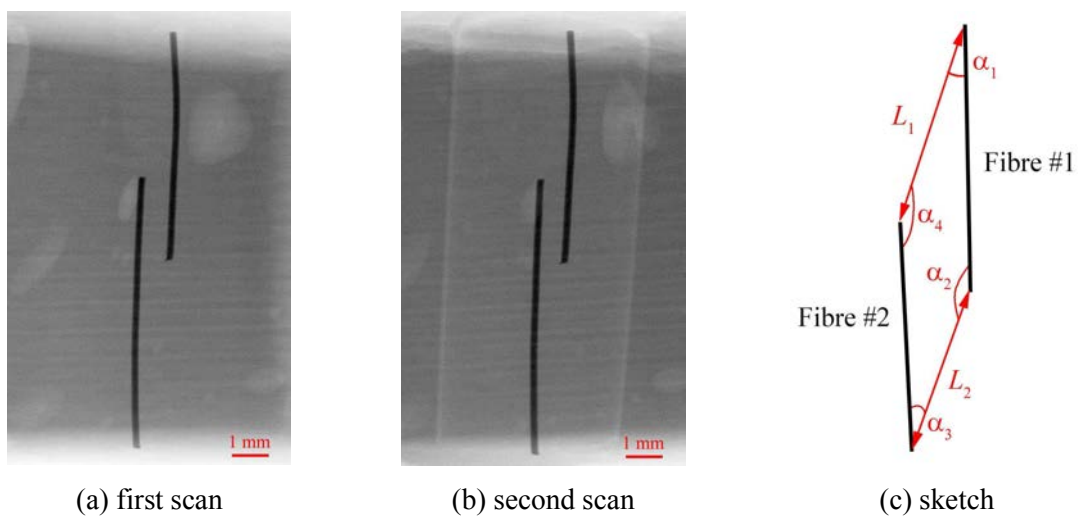


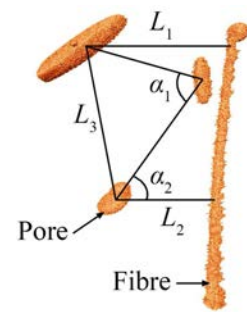
Figure 2.39 Calibration of sample preparation methods

Table 2.7 Test results of clay sample with two metal fibres

Test	Distance (mm)		Angle (°)			
	$L_1$	$L_2$	$\alpha_1$	$\alpha_2$	$\alpha_3$	$\alpha_4$
First scan	5.020	4.104	16.274	170.580	24.319	147.931
Second scan	5.071	4.159	15.490	169.862	23.547	149.004
Variation	1.0%	1.3%	-4.8%	0.4%	-3.2%	0.7%

Table 2.8 Test results of clay sample with an organic fibre

Test	Distance (mm)			Angle (°)	
	$L_1$	$L_2$	$L_3$	$\alpha_1$	$\alpha_2$
First scan	4.714	2.166	3.617	136.338	39.893
Second scan	4.699	2.142	3.640	135.222	40.357
Variation	-0.32%	-1.11%	0.64%	-0.82%	1.16%



#### 4.3.3 Quantitative methods for the identification of local cracks

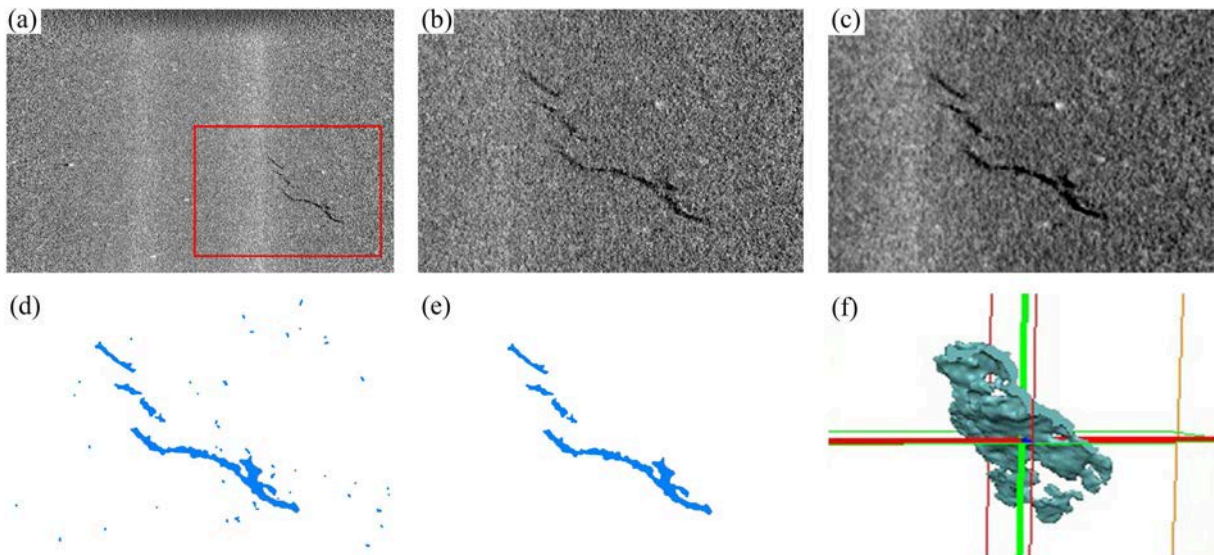
- **Microcracks and mesocracks**

The local cracks within small samples were divided into two groups, i.e., the microcracks and the mesocracks. The microcracks, identified at the microscopic level, were observed by the SEM technique. They were represented by the narrow gaps between two adjacent highly parallel face-to-face particle groups oriented in the same direction towards a certain plane. These microcracks could appear as open or closed. On the other hand, the local cracks at the mesoscopic level could be identified by the XR- $\mu$ CT technique.

- **Identification of mesocracks**

To identify mesocracks, nearly 2000 slices were derived from CT projections with the help of the bundled software X-Act. Slice data were then analysed with the commercial image visualisation package Avizo 8.0. Subimages (Figure 2.40b) containing the mesocracks were firstly extracted from the raw slices (Figure 2.40a). Gaussian and median filters were then applied to smooth the images while preserving the boundary contrast (Figure 2.40c). Next, the

slices were segmented using the "Interactive Thresholding" function available in the Avizo software to distinguish voids from the material phase (Figure 2.40d). Because there were many small voids in the images around the cracks that blurred them, slices were further modified by "Removing Island" to eliminate the isolated voids (Figure 2.40e). In the end, a 3D cracking surface was created (Figure 2.40f), and the geometric parameters (i.e., length, thickness and tilt angles) of cracks could then be measured.



(a) raw image; (b) extracted image; (c) filtered image; (d) segmented image; (e) islands-removed image; (f) 3D crack generation

Figure 2.40 Image processing method for identification of mesocracks

## 5. Summary

In this chapter, the mineralogical, chemical and physical properties of the two studied clay materials (i.e., Kaolin K13 and M35) were clarified, and then a detailed description of the methodology applied in this research was presented.

The experiments on the saturated remoulded clay (i.e., Kaolin K13) consist in performing consolidated drained triaxial compression tests followed by a series of microscopic tests such as SEM observations, MIP tests and XR- $\mu$ CT scans. A primary purpose was to examine what would happen in both the macromechanical behaviour and the microstructure when the remoulded clay is subjected to a given P2 stress level in the ( $p'$ ,  $q$ ) plane following different stress paths. The other important purpose was to try revealing the dilatancy mechanism of remoulded clay from the local (microscopic and mesoscopic) point of view.

The laboratory tests on the unsaturated remoulded clays (i.e., Kaolin K13 and M35) consist in imposing different levels of initial suctions on clay specimens and then performing soil-water characteristic tests and unconsolidated undrained triaxial compression tests on these specimens. Thereafter, mesoscopic tests especially the XR- $\mu$ CT scans were carried out on the recovered triaxial test specimens. With this group of experiments, the mechanical behaviour (i.e., shear strength and volume change) and mesoscopic characteristics (i.e., pore and crack properties) of remoulded clays on various suction-stress paths would be identified.



## Chapter 3

# Multiscale behaviour of saturated remoulded clay

<b>1. Experimental approach.....</b>	<b>91</b>
<b>2. Macromechanical results.....</b>	<b>93</b>
2.1 Determination of plastic volumetric strains.....	93
2.2 Mechanical behaviour under triaxial loading.....	94
2.3 Discussion on volumetric strain mechanisms.....	98
<b>3. Microstructural results.....</b>	<b>100</b>
3.1 Global orientation of clay particles and pores.....	100
3.1.1 On isotropic consolidation path.....	100
3.1.2 On triaxial loading path.....	103
3.2 Pore morphology and pore size distribution.....	108
3.2.1 Fractal dimension of pore structure.....	109
3.2.2 Characterisation of pore roundness.....	111
3.2.3 Pore size distribution and void ratio.....	115
3.3 Microscopic and mesoscopic cracks.....	118
3.3.1 Microscopic cracks identified by SEM.....	118
3.3.2 Mesoscopic cracks identified by XR- $\mu$ CT.....	119
<b>4. Mechanism of dilatancy phenomenon.....</b>	<b>121</b>
4.1 Conceptual modes of particle orientation.....	121
4.2 Discussion on dilatancy mechanisms.....	126
<b>5. Summary.....</b>	<b>129</b>



This chapter aimed to examine the multiscale behaviour of saturated remoulded clay under various triaxial loading conditions. Specific emphases were put on the influence of stress paths at a given stress level and the microscopic mechanism of dilatancy phenomenon.

## **1. Experimental approach**

The experimental approach consisted in performing several macroscopic tests followed by a series of microscopic tests. The whole experimental programme adopted in this chapter is summarised in Table 3.1. The details are presented in the Sections 4-5 of Chapter 2.

The macroscopic tests included triaxial compression tests and isotropic consolidation tests. The triaxial tests were performed on both normally consolidated and overconsolidated remoulded clay specimens on two different stress paths (i.e., the conventional constant  $\sigma'_3$  stress path and the purely deviatoric stress path) and at two different stress levels (one is below the critical state termed P2 and the other is close to the critical state termed P3). The microscopic tests consisted of scanning electron microscopy (SEM) observations, mercury intrusion porosimetry (MIP) tests and X-ray microtomography (XR- $\mu$ CT) scans, which were performed on small subsamples extracted from the recovered triaxial test specimens. The results of these microscopic tests were related to the mechanical behaviour of the remoulded clay and helped interpret the mechanisms of some macroscopic phenomena such as the volumetric dilatancy.

Table 3.1 Overview of the experimental programme

Macroscopic tests		Consolidated drained (CD) triaxial compression tests			
Type	Isotropic consolidation tests				
Sample	ISO_300 ISO_1000	NC_S250_P2 NC_P300_P2 NC_P300_P3	OCR4.0_S250_P2 OCR3.3_P300_P2 OCR3.3_P300_P3	OCR4.0_S250_P2 OCR3.3_P300_P2 OCR3.3_P300_P3	OCR4.0_S250_P2 OCR3.3_P300_P2 OCR3.3_P300_P3
SEM					
MIP	—				
XR- μCT	—				—

## 2. Macromechanical results

### 2.1 Determination of plastic volumetric strains

The evolution of volumetric strains is led by two components of the stress tensor. The isotropic part of the stress tensor always produces a positive volumetric strain showing contraction. On the other hand, the deviatoric part of the stress tensor produces a volumetric strain that can be positive (contractive) or negative (dilative) depending on the stress path and the overconsolidation ratio, as presented by Hattab and Hicher (2004).

The total volumetric strain can generally be expressed by:

$$d\varepsilon_v = d\varepsilon_v^{(p)} + d\varepsilon_v^{(q)} \quad (3.1)$$

where  $d\varepsilon_v$  is the total volumetric strain increment;  $d\varepsilon_v^{(p)}$  is the volumetric strain increment induced by the isotropic part of the stress tensor  $dp'$ ;  $d\varepsilon_v^{(q)}$  is the volumetric strain increment induced by the deviatoric part of the stress tensor  $dq$ .

It is assumed that the isotropic component  $d\varepsilon_v^{(p)}$  of the volumetric strain can be deduced from the swelling path in the  $(\log p', e)$  plane. Thus,  $d\varepsilon_v^{(p)}$  can be calculated by the following equation:

$$d\varepsilon_v^{(p)} = \frac{C_s}{2.3 (1 + e_0)} \frac{dp'}{p'} \quad (3.2)$$

where  $C_s$  is the swelling index;  $e_0$  is the void ratio at the end of isotropic loading.

Therefore, the expression of  $d\varepsilon_v^{(q)}$  can be written as:

$$d\varepsilon_v^{(q)} = d\varepsilon_v - \frac{C_s}{2.3 (1 + e_0)} \frac{dp'}{p'} \quad (3.3)$$

In the case of the purely deviatoric stress path ( $dp' = 0$ ), Equation (3.3) becomes:

$$d\varepsilon_v^{(q)} = d\varepsilon_v \quad (3.4)$$

If we assume that  $d\varepsilon_v^{(q)}$  is mainly composed of the plastic volumetric strain increment, the plastic volumetric strain increment ( $d\varepsilon_v^p$ ) can be expressed as follows:

$$d\varepsilon_v^p = d\varepsilon_v - \frac{C_s}{2.3(1+e_0)} \frac{dp'}{p'} \quad (3.5)$$

The deviatoric strain, considered as totally plastic, can be calculated by:

$$d\bar{\varepsilon}^p = d\bar{\varepsilon} = d\varepsilon_1 - \frac{d\varepsilon_v}{3} \quad (3.6)$$

where  $d\bar{\varepsilon}^p$  is the plastic deviatoric strain increment;  $d\bar{\varepsilon}$  is the deviatoric strain increment;  $d\varepsilon_1$  is the axial strain increment.

The total plastic strain increment is thus obtained after the calculation of its two components, i.e.,  $d\varepsilon_v^p$  and  $d\bar{\varepsilon}^p$ . The vector of the total plastic strain increment is plotted in the  $(d\varepsilon_v^p, d\bar{\varepsilon}^p)$  plane, and it basically represents the direction of plastic flow during triaxial loading.

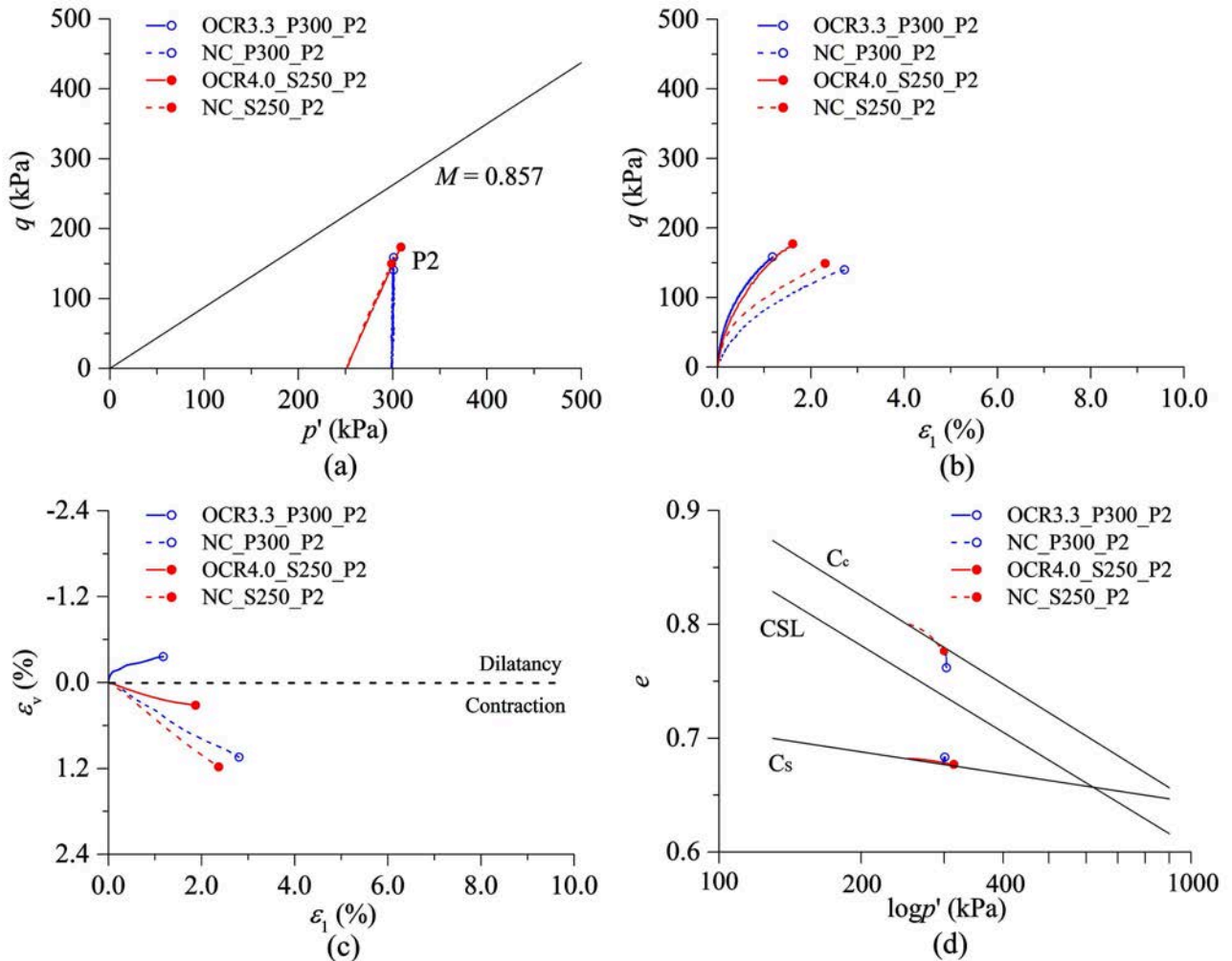
## 2.2 Mechanical behaviour under triaxial loading

- *Influence of OCRs at a given stress level*

Figure 3.1 shows the mechanical results of both normally consolidated and overconsolidated remoulded clay specimens at a given stress level (i.e., the P2 stress level) in the  $(p', q)$  plane.

Concerning the two specimens (i.e., NC\_S250\_P2 and OCR4.0\_S250\_P2) sheared to the P2 stress level following the conventional constant  $\sigma'_3$  stress path, it is observed that these two specimens of different overconsolidation ratios show different variations in the axial strain (Figure 3.1b) even though they are at the same stress level. The axial strain of the specimen NC\_S250\_P2 appears clearly larger than that of the specimen OCR4.0\_S250\_P2, indicating that the overconsolidated clay is less compressible than the normally consolidated clay. It is also seen that both the normally consolidated specimen (NC\_S250\_P2) and the overconsolidated specimen (OCR4.0\_S250\_P2) exhibit contractive behaviour (Figure 3.1c). However, it is clear that the overconsolidated specimen (OCR4.0\_S250\_P2) shows a smaller volumetric strain than the normally consolidated specimen (NC\_S250\_P2). As a consequence, one can note in the  $(\log p', e)$  plane (Figure 3.1d) that the void ratio of the specimen

OCR4.0\_S250\_P2 decreases gradually following the swelling line ( $C_s$ ) without the development of dilatancy until the test is stopped, whereas the void ratio of the specimen NC\_S250\_P2 decreases with a higher rate.



(a) ( $p'$ ,  $q$ ) plane; (b) ( $\epsilon_1$ ,  $q$ ) plane; (c) ( $\epsilon_1$ ,  $\epsilon_v$ ) plane; (d) ( $\log p'$ ,  $e$ ) plane

Figure 3.1 Triaxial test results at a given stress level reached along different stress paths

Regarding the two specimens (i.e., NC\_P300\_P2 and OCR3.3\_P300\_P2) sheared to the P2 stress level following the purely deviatoric stress path, one can note that these two specimens of different overconsolidation ratios also present different variations in the axial strain (Figure 3.1b). It suggests that the deformation of remoulded clay is significantly affected by the overconsolidation ratio. This result is consistent with that of the two specimens following the conventional constant  $\sigma'_3$  stress path. One can also note that the overconsolidated specimen (OCR3.3\_P300\_P2) shows clearly dilatative behaviour, while the normally consolidated specimen (NC\_P300\_P2) is always contractive during triaxial loading (Figure 3.1c). This feature of volumetric deformation is also noted in the ( $\log p'$ ,  $e$ ) plane: the void ratio of the

specimen OCR3.3\_P300\_P2 slightly increases while the void ratio of the specimen NC\_P300\_P2 decreases.

- *Influence of stress paths at a given stress level*

The influence of stress paths at a given stress level (i.e., the P2 stress level) on the mechanical behaviour of remoulded clay specimens can also be seen in Figure 3.1.

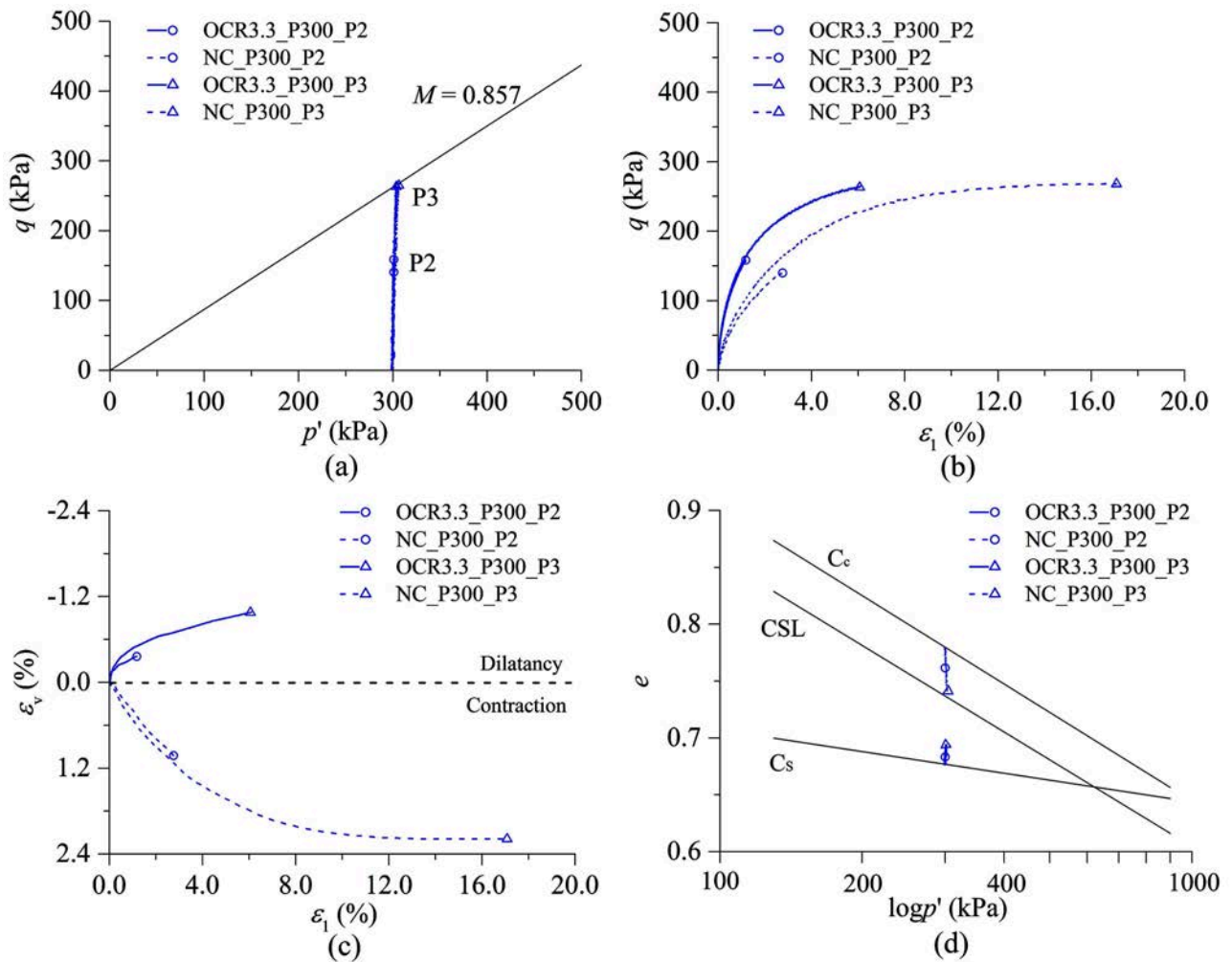
With respect to the two normally consolidated specimens (i.e., NC\_S250\_P2 and NC\_P300\_P2) sheared to the P2 stress level, it is noted that these two specimens on different stress paths show different axial strains (Figure 3.1b); however, the difference is not very large. From Figure 3.1c, one can see that the specimen NC\_S250\_P2 shows a relatively larger positive volumetric strain than the specimen NC\_P300\_P2. This is probably because when a specimen (e.g., NC\_S250\_P2) is sheared following the constant  $\sigma'_3$  stress path, both the isotropic component,  $p'$ , and the deviatoric component,  $q$ , of the stress tensor evolve, exerting a combined effect on the volumetric strain; however, when a specimen (e.g., NC\_P300\_P2) is sheared along the purely deviatoric stress path, only the variation in the deviatoric component,  $q$ , of the stress tensor leads to the evolution of volumetric strain. As a result, the decrease in the void ratio of specimen NC\_S250\_P2 appears more significant than that of the specimen NC\_P300\_P2 at the same P2 stress level (Figure 3.1d).

Regarding the two overconsolidated specimens (i.e., OCR4.0\_S250\_P2 and OCR3.3\_P300\_P2) sheared to the P2 stress level, they exhibit similar axial strains and completely different volumetric deformations (Figure 3.1b and c). As shown in Figure 3.1c, the specimen OCR3.3\_P300\_P2 on the purely deviatoric stress path experiences volumetric dilatancy. By contrast, the specimen OCR4.0\_S250\_P2 following the constant  $\sigma'_3$  stress path exhibits slight contraction at the P2 stress level. Obviously, one can expect that, along the constant  $\sigma'_3$  stress path, the dilatancy development would be activated when the specimen is further sheared to the characteristic state (Luong, 1978), and the dilatancy would persist up to the critical state as shown by many previous works in the literature. The dilatancy phenomenon of the specimen OCR3.3\_P300\_P2 is also characterised by the slight increase in the void ratio, as shown in Figure 3.1d.

- *Influence of stress levels on a given stress path*

Figure 3.2 presents the mechanical results of remoulded clay specimens sheared to two

different stress levels (i.e., P2 and P3) along a given stress path (i.e., the purely deviatoric stress path).



(a) ( $p'$ ,  $q$ ) plane; (b) ( $\varepsilon_1$ ,  $q$ ) plane; (c) ( $\varepsilon_1$ ,  $\varepsilon_v$ ) plane; (d) ( $\log p'$ ,  $e$ ) plane

Figure 3.2 Triaxial test results at different stress levels following a given stress path

Concerning the two normally consolidated specimens (i.e., NC\_P300\_P2 and NC\_P300\_P3) following the purely deviatoric stress path, it is observed that both the axial strain and the volumetric strain of the specimen NC\_P300\_P3 are larger than the corresponding values of the specimen NC\_P300\_P2, indicating that, as expected, a higher stress level results in greater axial and volumetric deformations (Figure 3.2b and c). As shown in Figure 3.2d, at a higher stress level, the specimen (i.e., NC\_P300\_P3) has a smaller void ratio due to more significant contraction compared to the specimen (i.e., NC\_P300\_P2) subjected to a lower stress level. One can also notice that, at P3 stress level, the specimen NC\_P300\_P3 reaches the critical state in both the ( $p'$ ,  $q$ ) and the ( $\log p'$ ,  $e$ ) planes.

With respect to the two overconsolidated specimens (i.e., OCR3.3\_P300\_P2 and OCR3.3\_P300\_P3) on the purely deviatoric stress path, it is noted that the specimen OCR3.3\_P300\_P3 at P3 stress level exhibits a larger axial strain than the specimen OCR3.3\_P300\_P2 at P2 stress level (Figure 3.2b). A larger absolute volumetric strain and a larger increase in void ratio occur in the specimen OCR3.3\_P300\_P3 at a higher stress level compared to the specimen OCR3.3\_P300\_P2 at a lower stress level (see Figure 3.2c and d). Therefore, concerning the strongly overconsolidated clay, a higher stress level enhances the dilative behaviour on the purely deviatoric stress path. It is also noted that, in this case, the critical state has not been reached yet at P3 stress level for the overconsolidated specimen (i.e., OCR3.3\_P300\_P3) in the  $(\log p', e)$  plane.

### 2.3 Discussion on volumetric strain mechanisms

Figure 3.3a shows the evolution of the plastic volumetric strain  $d\varepsilon_v^p$ , as defined in Section 2.1, versus the deviatoric stress  $q$  at the P2 stress level in the  $(p', q)$  plane (see Figure 3.1a). Figure 3.3b presents the directions of the plastic strain increment vectors in the  $(p', q)$  plane normalised by the effective consolidation stress  $p'_0$ .

The values of plastic strain component increments and the directions of plastic strain increment vectors at P2 stress level are summarised in Table 3.1. Notice that the values of plastic strain increments are taken considering a deviatoric stress increment of  $dq = 1.0$  kPa.  $\alpha$  is the direction of the plastic strain increment vector with respect to the  $d\bar{\varepsilon}^p$ -axis of the  $(d\varepsilon_v^p, d\bar{\varepsilon}^p)$  plane: a positive value represents contraction while a negative value represents dilation.

Three domains, i.e., the dilatancy domain, the “no volume change” domain (consistent with the pseudoelastic domain of Biarez and Hicher (1994)) and the contraction domain, on the purely deviatoric stress path proposed by Hattab and Hicher (2004) are reproduced in Figure 3.3b. Note that the volumetric strain developed in the pseudoelastic domain appears only due to the isotropic component of the stress tensor whatever the direction of the stress path. Outside this domain, the volumetric strain is the result of a coupling between the isotropic part and the deviatoric part of the stress tensor.

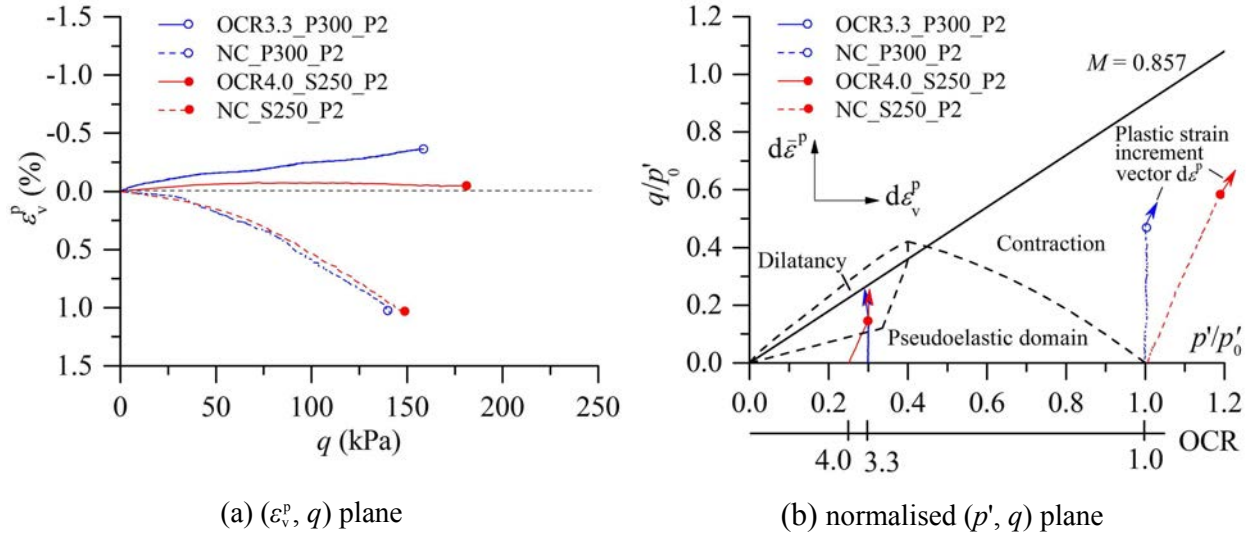


Figure 3.3 Volumetric strain mechanisms during triaxial loading

Table 3.2 Values and directions of plastic strain increment vectors

Specimen	OCR	Stress path	$d\bar{\varepsilon}^p$	$d\varepsilon_v^p$	$\alpha$ ( $^\circ$ )
NC_S250_P2	1.0	S	0.026%	0.010%	21.0
NC_P300_P2	1.0	P	0.045%	0.015%	18.7
OCR4.0_S250_P2	4.0	S	0.014%	0.0002%	0.9
OCR3.3_P300_P2	3.3	P	0.020%	-0.002%	-5.7

The results in Figure 3.3a clearly show that, in the normally consolidated state, the plastic volumetric strains are almost the same whatever the stress path, i.e., the constant  $\sigma'_3$  stress path or the purely deviatoric stress path. In the overconsolidated state, the results show that the purely deviatoric stress path leads to the development of a negative plastic volumetric strain, indicating a clear dilatancy phenomenon. On the other hand, the constant  $\sigma'_3$  stress path produces a negligible plastic volumetric strain, which is consistent with the concept of Hattab and Hicher (2004). As a consequence, one can observe very close directions of the plastic strain vectors with respect to the two normally consolidated specimens at the same P2 stress level reached by following different stress increment vectors (i.e., stress paths). In the dilatancy domain, the results indicate that the direction of the plastic strain vector depends on the direction of the stress increment vector. However, at the same P2 stress level, the influence of the stress incremental vector on the direction of plastic strain increment is not very significant. Similar results were previously shown by Hattab and Hicher (2004).

In the following sections, the microstructural characteristics of the same clay specimens are

examined and then linked to the mechanical behaviour, so as to better understand the macroscopic behaviour of remoulded clay such as the volumetric dilatancy.

### 3. Microstructural results

#### 3.1 Global orientation of clay particles and pores

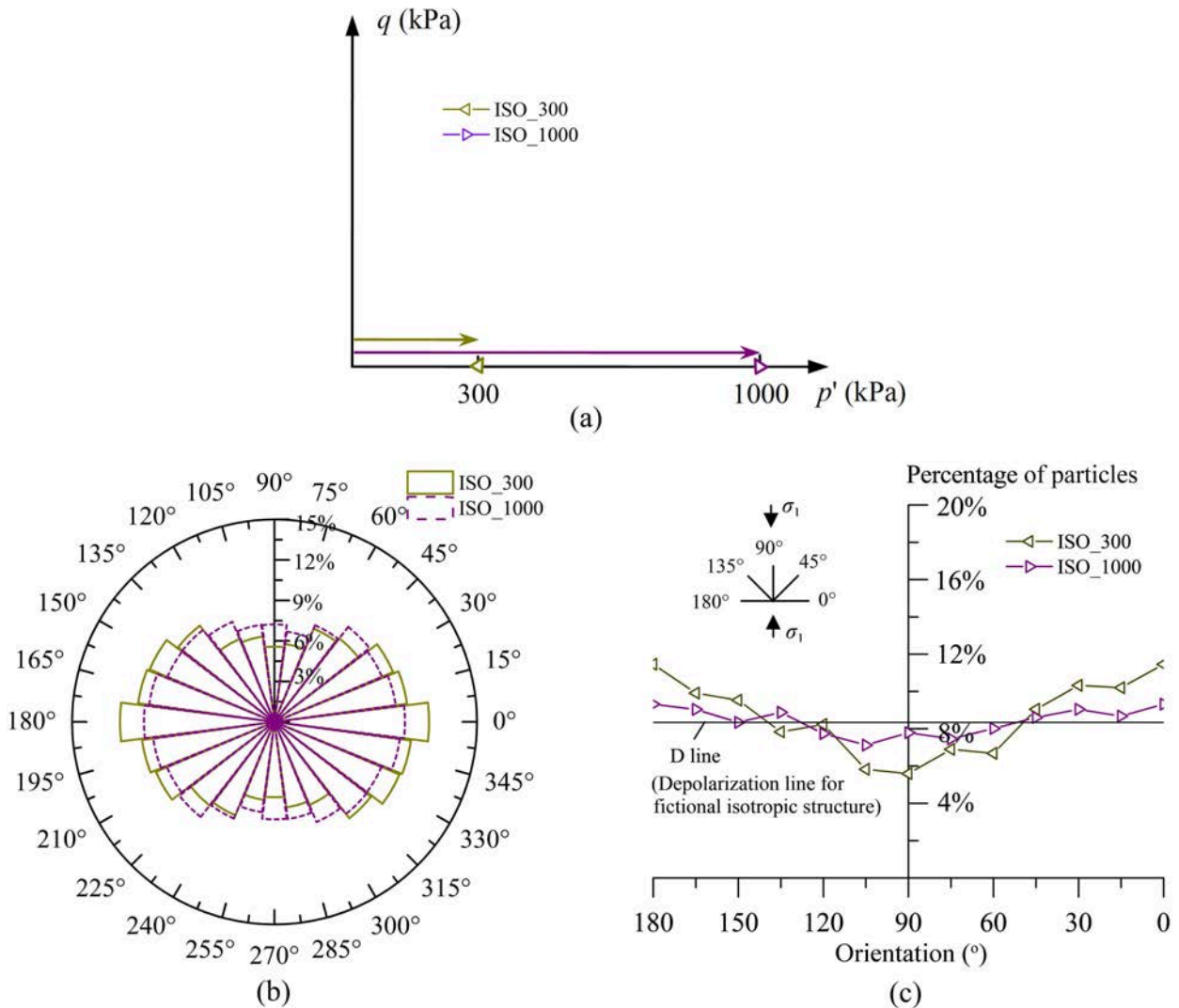
Following the experimental procedure described in the Section 4 of Chapter 2, the global clay particle orientation and the global pore orientation of remoulded clay specimens are obtained and analysed under various triaxial loading conditions.

---

##### 3.1.1 On isotropic consolidation path

---

Figure 3.4a illustrates the stress paths of two isotropic consolidation tests. One test is performed on a remoulded clay specimen (i.e., ISO\_300) under an isotropic consolidation stress of  $p'_0 = 300$  kPa, and the other is carried out on a remoulded clay specimen (i.e., ISO\_1000) under  $p'_0 = 1000$  kPa. The rose diagrams of clay particle orientation corresponding to these two specimens are shown in Figure 3.4b. It is observed that the clay particles almost evenly rotate towards each direction showing a feature of random orientation, and the clay fabric may be considered as isotropic. However, a slight tendency of preferential orientation towards the horizontal plane can be noted, particularly for the specimen (e.g., ISO\_300) under a lower isotropic stress. The results indicate that the initial preferential orientation of clay particles produced by the one-dimensional compression during specimen preparation is not completely erased. Note that this initial preferential orientation of clay particles formed before triaxial loading may be regarded as “initial anisotropy” of the material. On the other hand, the orientation of clay particles activated during triaxial loading can be considered to be “induced anisotropy”.



(a) stress path; (b) rose diagram; (c) orientation curve

Figure 3.4 Global particle orientation of clay specimens under isotropic loading

The global orientation of clay particles can also be represented by the orientation curves, as shown in Figure 3.4c, where the percentage of clay particles is drawn as a function of particle orientation. The depolarization line (D line) represents a perfectly isotropic microstructure of a fictional clayey material, as defined by Hattab and Fleureau (2010, 2011). Comparing the curves in Figure 3.4c, one can note that the curve of specimen ISO\_1000 under a higher isotropic stress is closer to the D line, exhibiting a well isotropic microstructure. The orientation curves are equivalent to the rose diagrams, but this kind of representation allows highlighting more phenomena regarding the microstructure. Therefore, in the following analyses, the orientation curves are used to illustrate the global orientation of both clay particles and pores.

The global pore orientation curves of the specimens (i.e., ISO\_300 and ISO\_1000) under isotropic loading are presented in Figure 3.5. The definition of  $D^{pore}$  line for pore orientation is similar to the D line with respect to clay particle orientation. It is noted that the pore orientation curves of both specimens approach the  $D^{pore}$  line with a very slight preferential orientation towards the horizontal plane. This result is consistent with the characteristics of clay particle orientation (see Figure 3.4c).

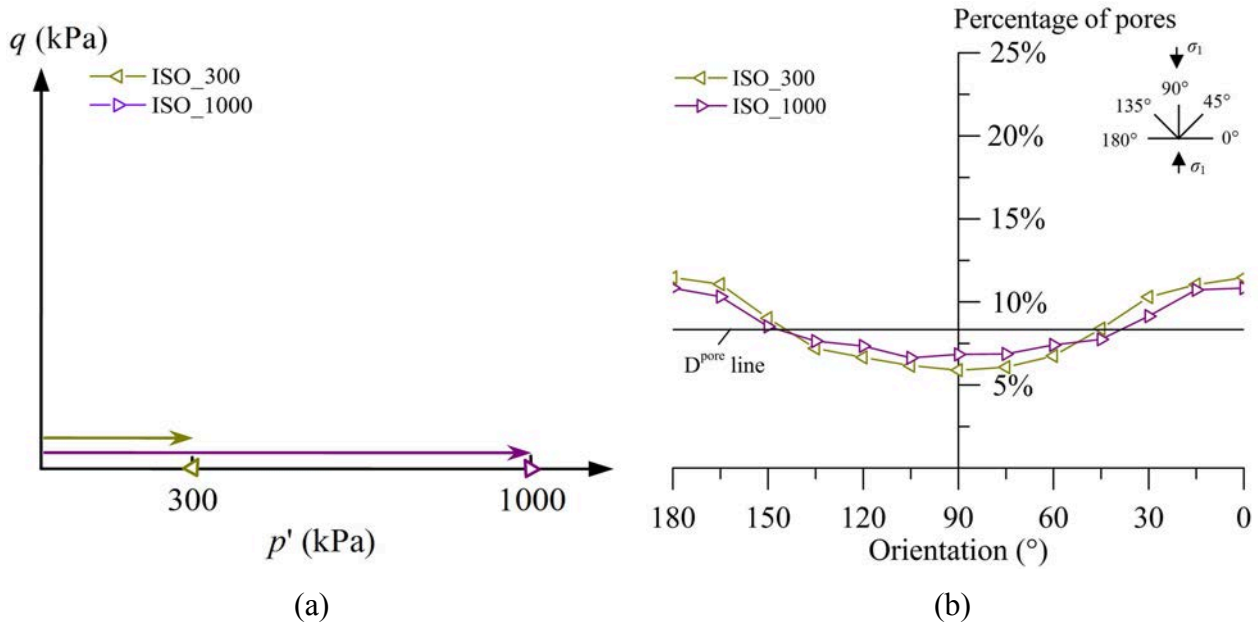


Figure 3.5 Global pore orientation of clay specimens under isotropic loading

Table 3.3 Pore orientation indexes of different clay specimens

Specimen	OCR	Stress path	Stress level	$\epsilon_v$ (%)	$\epsilon_1$ (%)	$I_{or}$
ISO_300	/	/	/	/	/	0.540
ISO_1000	/	/	/	/	/	0.638
NC_S250_P2	1.0	S	P2	1.18	2.37	0.307
OCR4.0_S250_P2	4.0	S	P2	0.32	1.87	0.196
NC_P300_P2	1.0	P	P2	1.04	2.81	0.180
OCR3.3_P300_P2	3.3	P	P2	-0.36	1.18	0.435
NC_P300_P3	1.0	P	P3	2.19	17.08	0.173
OCR3.3_P300_P3	3.3	P	P3	-0.98	6.10	0.449

The anisotropy due to the pore orientation is characterised by orientation indexes ( $I_{or}$ ), as

listed in Table 3.3. Generally, the larger the orientation index, the more isotropic the pore structure. One can note that the two specimens under isotropic loading have the highest orientation indexes among all the specimens. Moreover, it is clear that the higher the isotropic consolidation stress, the larger the orientation index. It indicates that a good isotropy of the pore structure is developed in clay specimens especially under a high isotropic consolidation stress.

---

### 3.1.2 On triaxial loading path

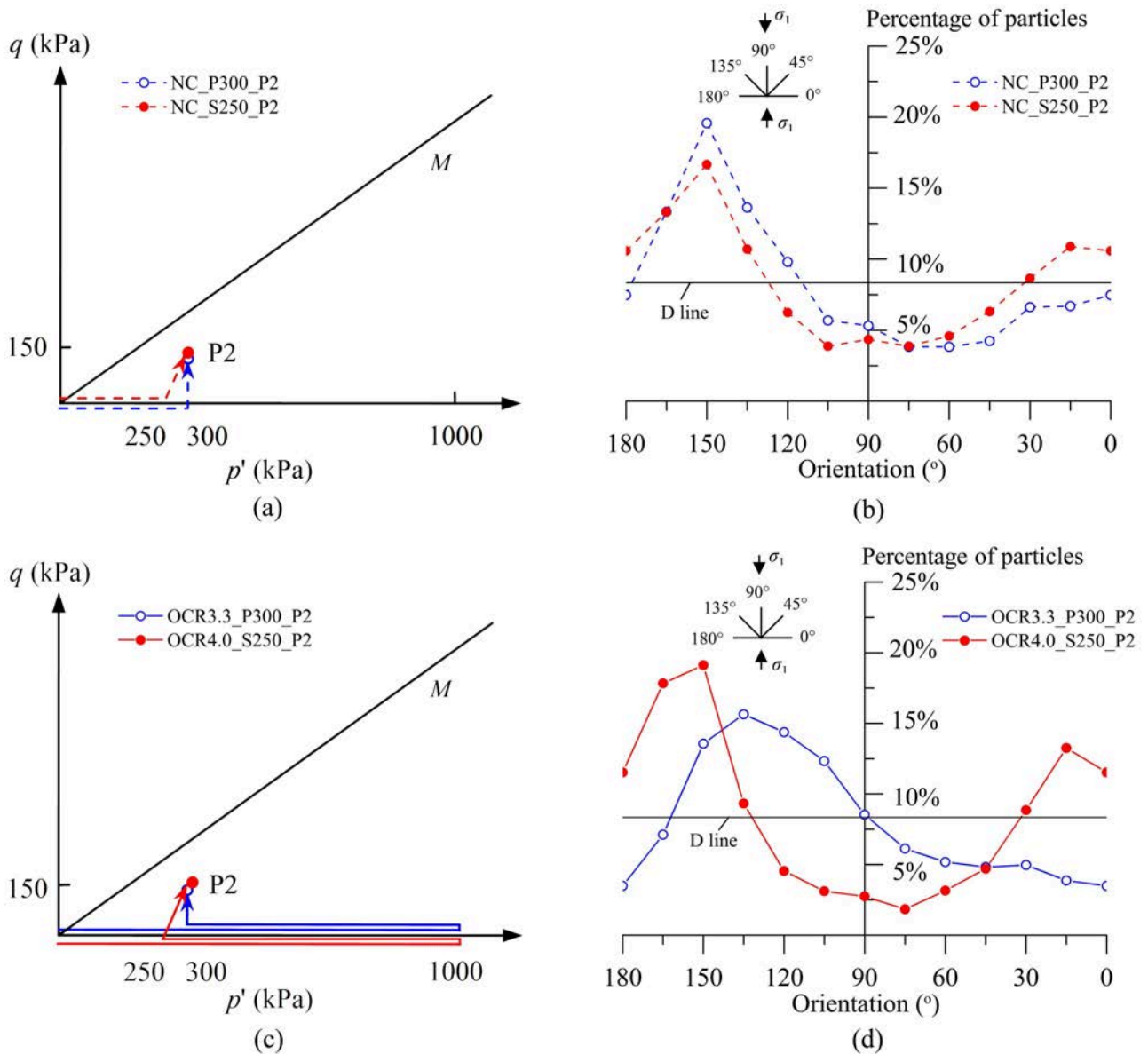
---

- *Influence of OCRs at a given stress level*

Figure 3.6 shows the global orientation curves of clay particles in both the normally consolidated and the overconsolidated specimens.

Regarding the two specimens (i.e., NC\_S250\_P2 and OCR4.0\_S250\_P2) sheared to the P2 stress level following the conventional constant  $\sigma'_3$  stress path, it is observed that the particle orientation curves of these two specimens are characterised by sharp peaks showing evident preferential orientation of  $150^\circ$  (which in fact corresponds to an angle of  $30^\circ$  versus the horizontal plane). This result indicates that the remoulded clay tends to develop an anisotropic microstructure during triaxial loading regardless of the overconsolidation ratio. However, compared to the normally consolidated specimen (i.e., NC\_S250\_P2), the overconsolidated specimen (i.e., OCR4.0\_S250\_P2) has a larger number of clay particles rotate towards  $165^\circ$ .

With respect to the two specimens (i.e., NC\_P300\_P2 and OCR3.3\_P300\_P2) sheared to the P2 stress level along the purely deviatoric stress path, different preferential orientations are noted. The preferential orientation of the clay particles in the normally consolidated specimen (i.e., NC\_P300\_P2) is  $150^\circ$  while the preferential orientation of the clay particles in the overconsolidated specimen (i.e. OCR3.3\_P300\_P2) approximates  $135^\circ$ . Moreover, one can see that the percentage of clay particles with the preferential orientation is significantly higher than those of clay particles in other directions concerning the normally consolidated specimen (i.e., NC\_P300\_P2); on the other hand, for the overconsolidated specimen (i.e., OCR3.3\_P300\_P2), the percentages of clay particles with orientations adjacent to the preferential orientation are also very large, and thus the peak of the orientation curve is relatively smooth. The latter feature of clay particle orientation seems related to the dilatancy phenomenon.



(a-b) normally consolidated specimens; (c-d) overconsolidated specimens

Figure 3.6 Global particle orientation of clay specimens on different triaxial stress paths

Figure 3.7 illustrates the global orientation curves of pores in both the normally consolidated and the overconsolidated specimens. A significant influence of OCRs or more precisely of the dilatancy on the pore orientation is observed. The percentage of pores with the preferential orientation is close to, or greater than, 17% for the normally consolidated specimens (i.e., NC\_S250\_P2 and NC\_P300\_P2). The overconsolidated specimen (i.e., OCR4.0\_S250\_P2) with contractive behaviour also experiences a similar pore orientation tendency. However, the dilative specimen (i.e., OCR3.3\_P300\_P2) has a smaller peak percentage, and the orientation curve is closer to the  $D^{pore}$  line. This trend corresponds to that of the particle orientation curves as shown in Figure 3.6d. It indicates that the orientation of

pores tends thus to follow the orientation of clay particles. In addition, the results of orientation indexes also show that the dilative specimen (i.e., OCR3.3\_P300\_P2) has a relatively larger orientation index than the corresponding contractive specimen (i.e., NC\_P300\_P2) (Table 3.3), characterising a less anisotropic microstructure.

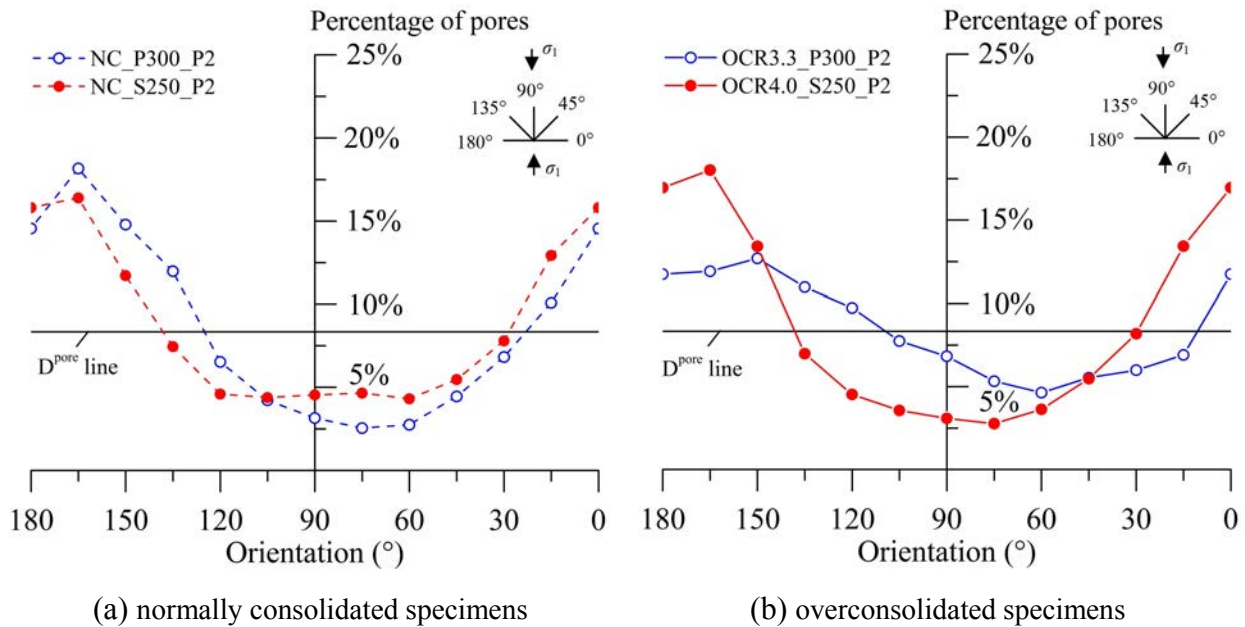


Figure 3.7 Global pore orientation of clay specimens on different triaxial stress paths

- *Influence of stress paths at a given stress level*

The influence of stress paths on the global particle orientation of specimens sheared to a given stress level (P2) is also illustrated by Figure 3.6.

Regarding the two normally consolidated specimens (i.e., NC\_S250\_P2 and NC\_P300\_P2), it is noted that both the particle orientation curves of these two specimens on different stress paths show high sharp peaks (Figure 3.6b) on the left side of the percentage-orientation plane. However, there is a slight difference with respect to the shapes of particle orientation curves on the right side of the percentage-orientation plane: some data points (in the range of 8°-22°) lie above the D line for the normally consolidated specimen (i.e., NC\_S250\_P2) on the constant  $\sigma'_3$  stress path while no data point lies above the D line for the normally consolidated specimen (i.e., NC\_P300\_P2) following the purely deviatoric stress path.

Concerning the two overconsolidated specimens (i.e., OCR4.0\_S250\_P2 and OCR3.3\_P300\_P2), one can note completely different shapes of clay particle orientation curves. On the one hand, a relatively sharp peak of the particle orientation curve on the left

side, more or less similar to that of the normally consolidated specimen (e.g., NC\_S250\_P2), is observed in the case of the specimen (i.e., OCR4.0\_S250\_P2) on the constant  $\sigma'_3$  stress path; by contrast, a smooth peak of the particle orientation curve is noted on the left side concerning the specimen (i.e., OCR3.3\_P300\_P2) along the purely deviatoric stress path. On the other hand, the orientation curves of these two overconsolidated specimens characterise two different shapes on the right side of the percentage-orientation plane. A low sharp peak is noted for the specimen OCR4.0\_S250\_P2 while no peak is observed for the specimen OCR3.3\_P300\_P2 on the right side. The feature of the particle orientation curve of specimen OCR4.0\_S250\_P2 seems associated with the slightly contractive behaviour and the great influence of the isotropic part of the stress tensor during the early stage of triaxial loading along the constant  $\sigma'_3$  stress path.

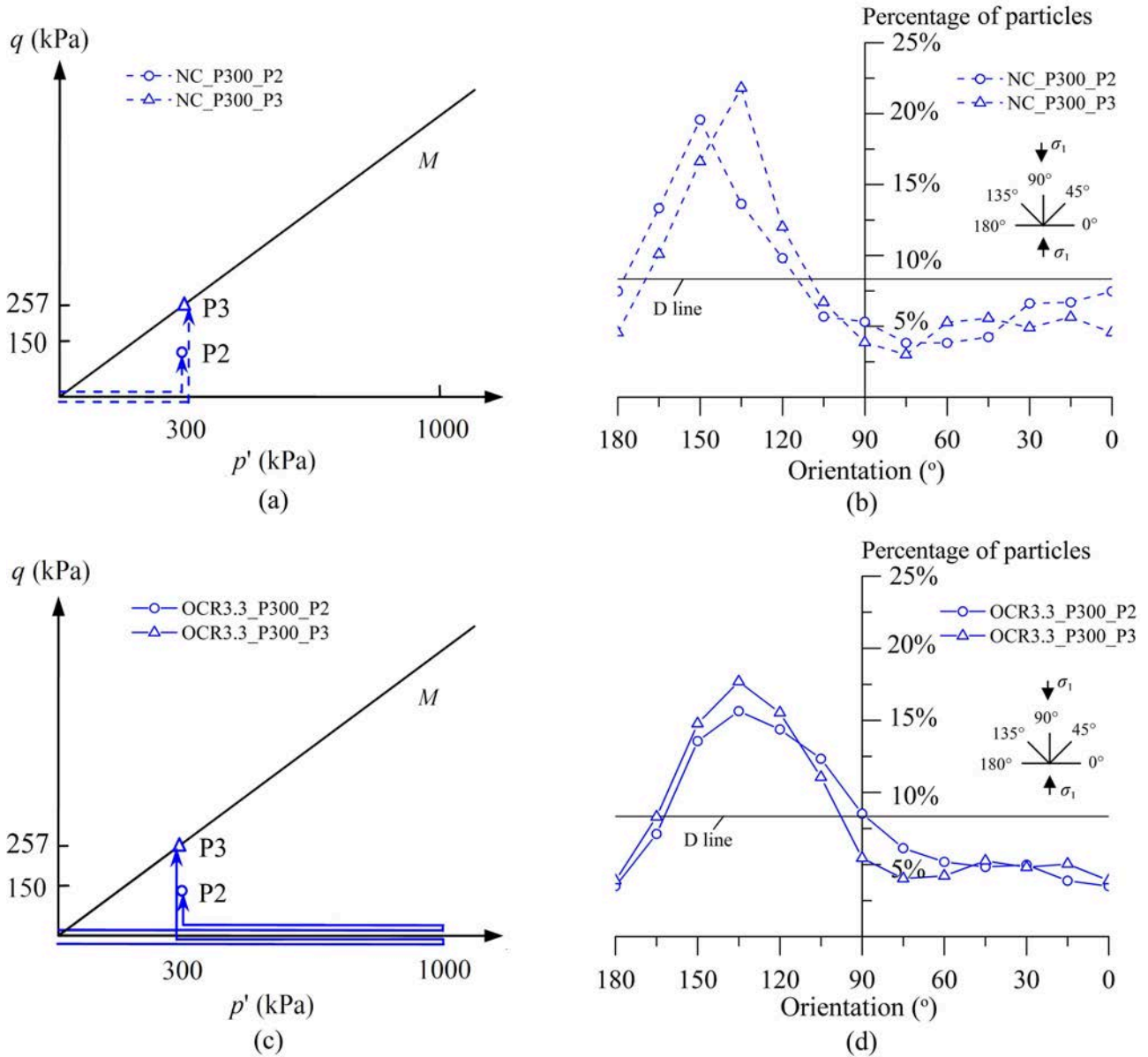
The global pore orientation of specimens sheared to a given stress level (P2) following different stress paths is presented in Figure 3.7. It shows that the global pore orientation curves of the two normally consolidated specimens (i.e., NC\_S250\_P2 and NC\_P300\_P2) are very close. Comparing the pore orientation with the clay particle orientation (Figure 3.6b), one can consider that the influence of stress paths on the pore orientation is relatively less than that on the clay particle orientation with respect to the normally consolidated specimens. However, concerning the two overconsolidated specimens (i.e., OCR4.0\_S250\_P2 and OCR3.3\_P300\_P2), a major difference between the pore orientation curves is noted. The specimen OCR4.0\_S250\_P2 on the constant  $\sigma'_3$  stress path shows an evident preferential pore orientation while the specimen OCR3.3\_P300\_P2 along the purely deviatoric stress path exhibits a relatively random orientation characterising, more or less, an isotropic pore structure.

- *Influence of stress levels along a given stress path*

Figure 3.8 presents the global particle orientation of clay specimens sheared to two different stress levels (named P2 and P3 in the  $(p', q)$  plane) along the same purely deviatoric stress path.

As for the two normally consolidated specimens (i.e., NC\_P300\_P2 and NC\_P300\_P3) following the purely deviatoric stress path, it is observed that both the orientation curves characterise a high sharp peak on the left side of the percentage-orientation plane and no data point on the right side (Figure 3.8b). However, a slight increase in the percentage of clay

particles with the preferential orientation and a slight evolution of the preferential orientation are noted as the stress level increases from the P2 level to the P3 level. The result indicates that a higher stress level enhances the preferential orientation of clay particles but not greatly changes the shape of the orientation curve.



(a-b) normally consolidated specimens; (c-d) overconsolidated specimens

Figure 3.8 Global particle orientation of clay specimens at different triaxial stress levels

Concerning the two overconsolidated specimens (i.e., OCR3.3\_P300\_P2 and OCR3.3\_P300\_P3) on the purely deviatoric stress path, one can note that the shape of the particle orientation curve at P3 stress level appears quite consistent with that at P2 stress level (Figure 3.8d). However, a gradual increase in the quantity of clay particles with preferential

orientation is also observed as the stress level increases from the P2 level to the P3 level. For instance, the peak percentage of particle orientation for the specimen OCR3.3\_P300\_P2 is about 15%, whereas it approximates 18% for the specimen OCR3.3\_P300\_P3 (Figure 3.8d).

Figure 3.9 illustrates the global pore orientation of clay specimens at different triaxial stress levels. It is observed that, for both the normally consolidated specimens (i.e., NC\_P300\_P2 and NC\_P300\_P3) and the overconsolidated specimens (i.e., OCR3.3\_P300\_P2 and OCR3.3\_P300\_P3), the pore orientation curves at P3 stress level are very close to those at P2 stress level with no significant increase in the percentage of pores of the preferential orientation. This result can also be obtained by analysing the pore orientation indexes (see Table 3.3). In Table 3.3, one can note that the pore orientation indexes of the two normally consolidated specimens are approximately equal (0.180 and 0.173, respectively), and the pore orientation indexes of the two overconsolidated specimens are also very close in value (0.435 and 0.449, respectively).

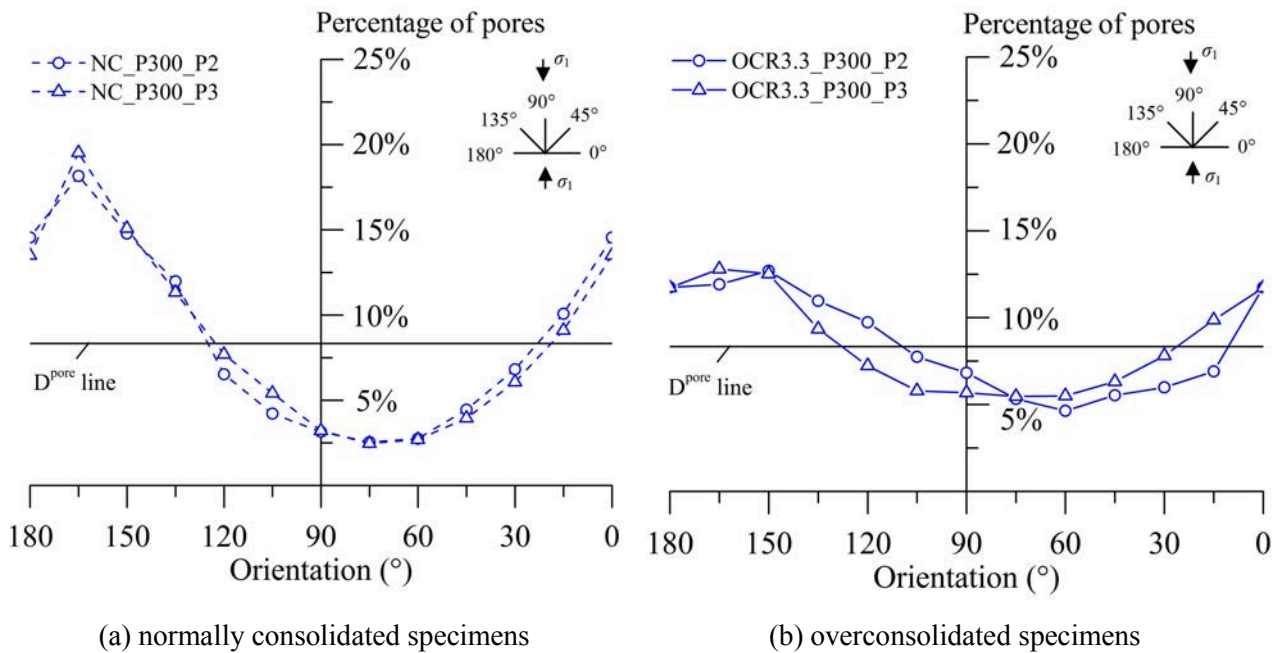


Figure 3.9 Global pore orientation of clay specimens at different triaxial stress levels

### 3.2 Pore morphology and pore size distribution

The characterisation of pore structures is a necessary complement to the analyses of particle orientation and pore orientation. Their combination permits to precisely quantify the clay microstructure and its relation to the macroscopic behaviour under triaxial loading.

---

### 3.2.1 Fractal dimension of pore structure

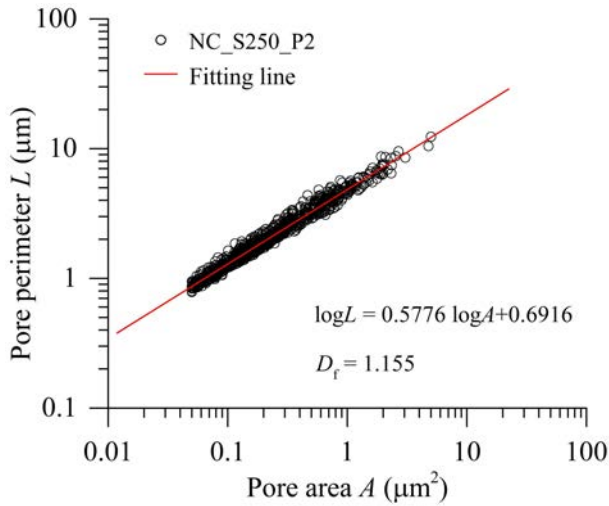
---

The fractal dimension ( $D_f$ ) characterises the complexity of pore structures. It varies between one for a simple pore structure and two for a very complicated pore structure.

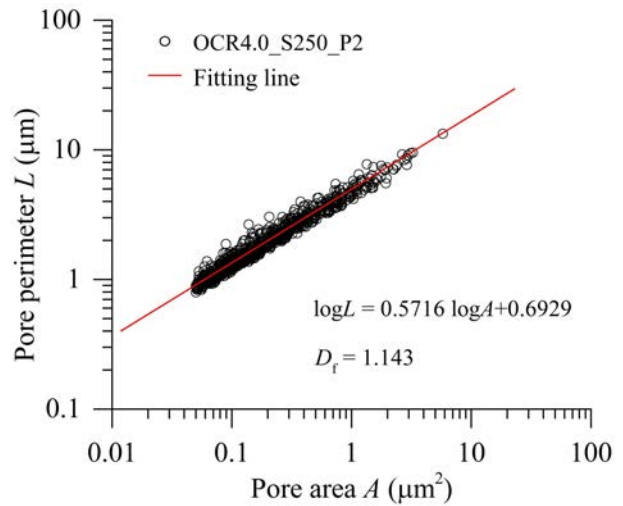
The fractal dimensions of clay specimens under different triaxial loading conditions are presented in Figure 3.10. The fitted results show clear linear relationship between the pore perimeter ( $L$ ) and the pore areas ( $A$ ) in a log-log scale coordinate system, which indicates that the pore structure of the studied material has obvious fractal characteristics. Therefore, according to the definition presented in Chapter 2, the fractal dimension of pore structures can be obtained by multiplying the absolute slope of the fitting line by two.

One can note that the fractal dimension of a normally consolidated specimen (e.g., NC\_S250\_P2, NC\_P300\_P2 and NC\_P300\_P3) is slightly larger than that of the corresponding overconsolidated specimen (i.e., OCR4.0\_250\_P2, OCR3.3\_P300\_P2 and OCR3.3\_P300\_P3) under the same loading condition of stress level and stress path. This means that the pore structure of a normally consolidated specimen seems to be more complicated than that of an overconsolidated specimen. Furthermore, at a given stress level (e.g., the P2 stress level), the fractal dimensions of the specimens (i.e., NC\_S250\_P2 and OCR4.0\_S250\_P2) on the constant  $\sigma'_3$  stress path have larger values compared to those of the specimens (i.e., NC\_P300\_P2 and OCR3.3\_P300\_P2) following the purely deviatoric stress path. In addition, it is noted that the fractal dimension increases, indicating a more complicated pore structure with increasing stress level regarding both normally consolidated and overconsolidated specimens. For example, the fractal dimension of the overconsolidated specimen (OCR3.3\_P300\_P2) at P2 stress level is 1.137 while that of the specimen (OCR3.3\_P300\_P3) at P3 stress level is 1.146.

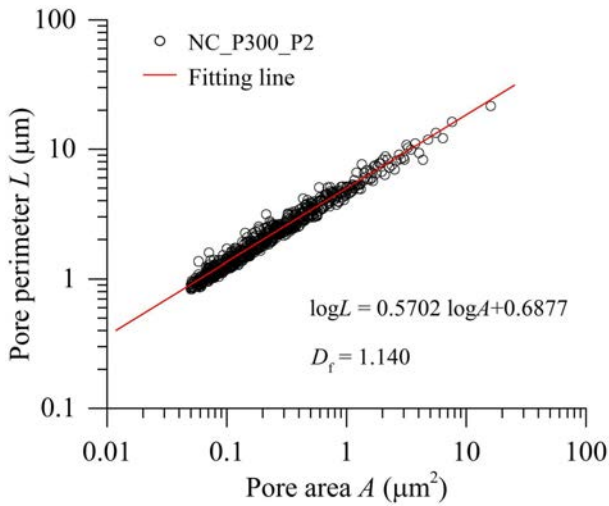
The fractal dimensions of the 2D pore structures of clay specimens vary between 1.137 and 1.155, which is generally smaller than those reported by Zhang and Cui (2017) for silty clay before and after freezing-thawing and cyclic triaxial loading, as well as those reported by Liu et al. (2011) for Hangzhou Clay before and after shear tests. It suggests that the fractal dimension of pore structure is not only dependent on loading conditions but also closely related to the material type.



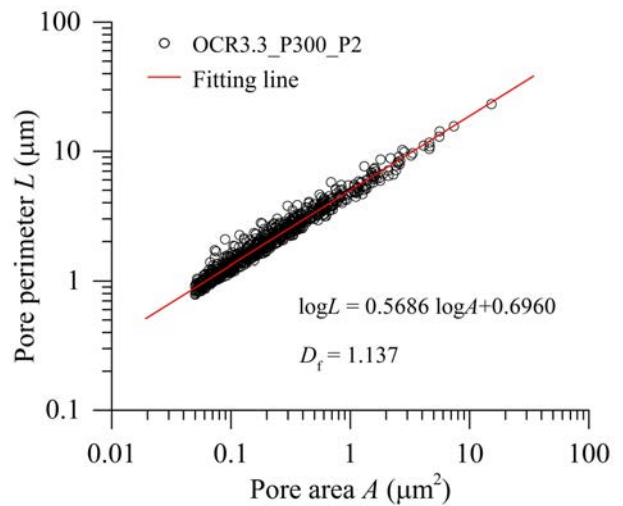
(a) NC\_S250\_P2



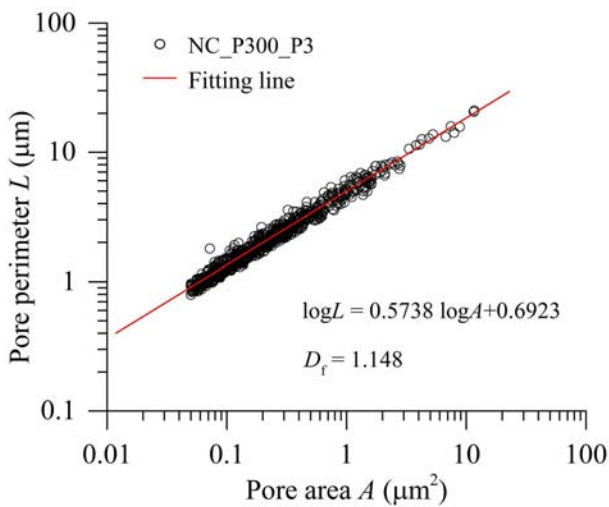
(b) OCR4.0\_S250\_P2



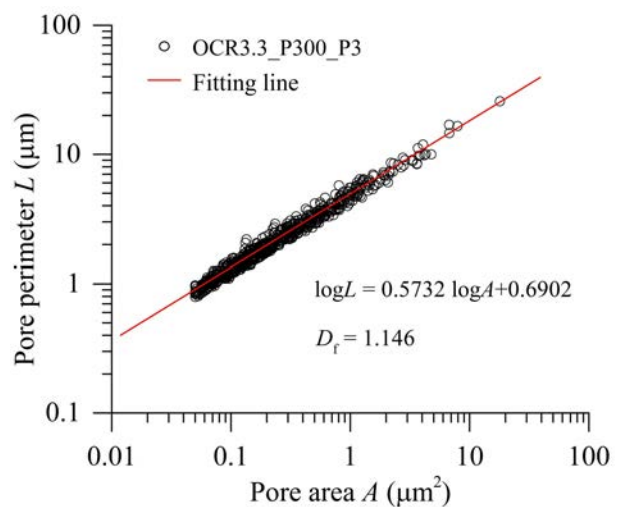
(c) NC\_P300\_P2



(d) OCR3.3\_P300\_P2



(e) NC\_P300\_P3



(f) OCR3.3\_P300\_P3

Figure 3.10 Fractal dimensions of different clay specimens under triaxial loading

## 3.2.2 Characterisation of pore roundness

The pore roundness ( $R_s$ ) characterises the geometric shape of pores. The method for the determination of pore roundness is presented in Chapter 2. Notice that  $R_s = 1$  represents an equiaxial shape of the pore.

- *Pore roundness under isotropic loading*

Figure 3.11 presents the pore roundness-percentage curves of the specimens under isotropic loading. It is observed that most of the pores within both the specimen ISO\_300 and the specimen ISO\_1000 have roundness values between 0.3 and 0.8. However, there is an evident difference between them regarding the shape of pore roundness curves. The dominant pore roundness of the specimen ISO\_300 is 0.5, while that of the specimen ISO\_1000 is 0.6. It can be inferred from the results that the specimen ISO\_1000 under a higher isotropic consolidation stress has more relatively round pores than the specimen ISO\_300 under a lower isotropic consolidation stress.

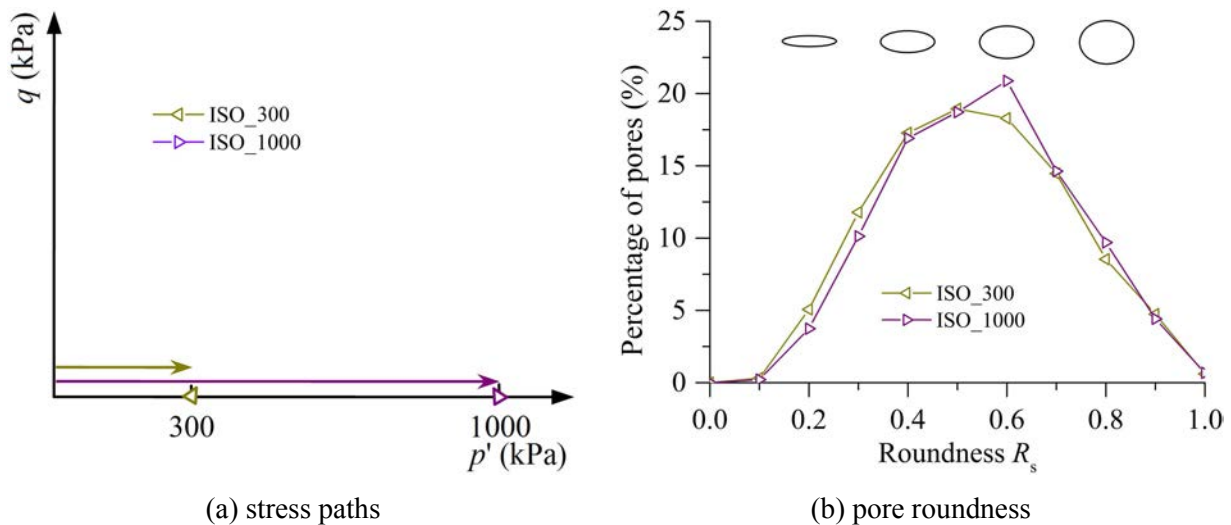
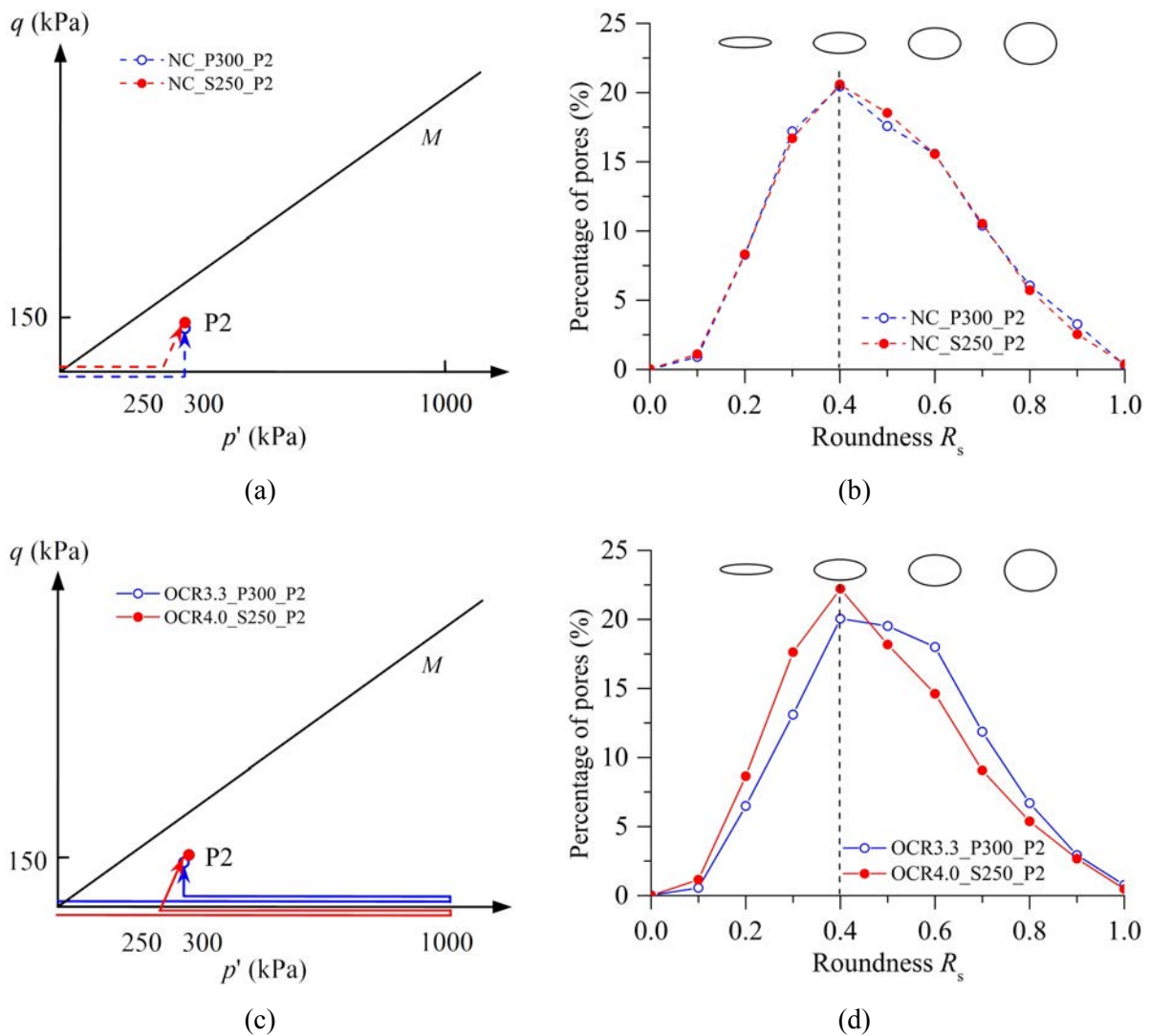


Figure 3.11 Pore roundness of clay specimens under isotropic loading

- *Pore roundness under triaxial shearing*

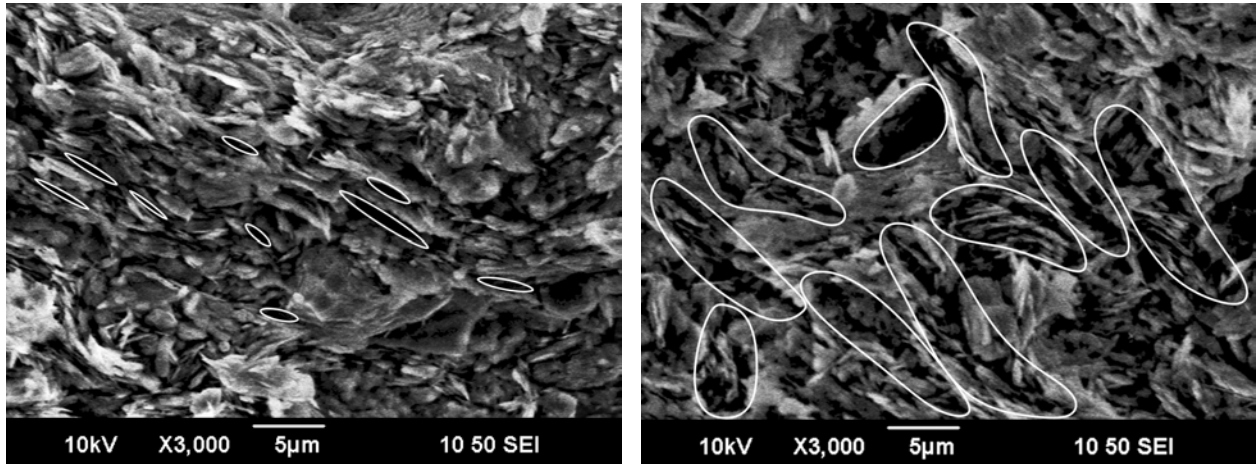
Figure 3.12 shows statistical results of the distribution of pore roundness. In this figure, the P2 stress level (see Figure 3.1a) is considered for both normally consolidated and overconsolidated specimens. All the curves show unimodal distributions with a marked peak of dominant roundness relatively distant from  $R_s = 1$ , which means that most of the pores in clay specimens under triaxial loading are more or less elliptical in shape. One can notice that,

for the normally consolidated specimens, the roundness distribution curves are very similar, and quite close to the curve of the overconsolidated specimen on the constant  $\sigma'_3$  stress path. For these specimens showing contractive behaviour, the pore shapes appear rather narrow (see Figure 3.13a). On the other hand, in the case of the overconsolidated specimen that exhibits dilatancy phenomenon at the macroscale, the curve shifts to the right, and the peak appears smoother. This result demonstrates that the pores in a dilative specimen are more open in shape than those in a contractive specimen (as illustrated in Figure 3.13). Therefore, one may consider that the open pores may form local weak points inside the material, leading to the initiation and propagation of microcracks during triaxial loading. On the other hand, one can note that, for the normally consolidated specimens, the stress path has no significant effect on pore shape, as shown in Figure 3.12b.



(a-b) normally consolidated specimens; (c-d) overconsolidated specimens

Figure 3.12 Pore roundness of specimens at a given stress level on different stress paths

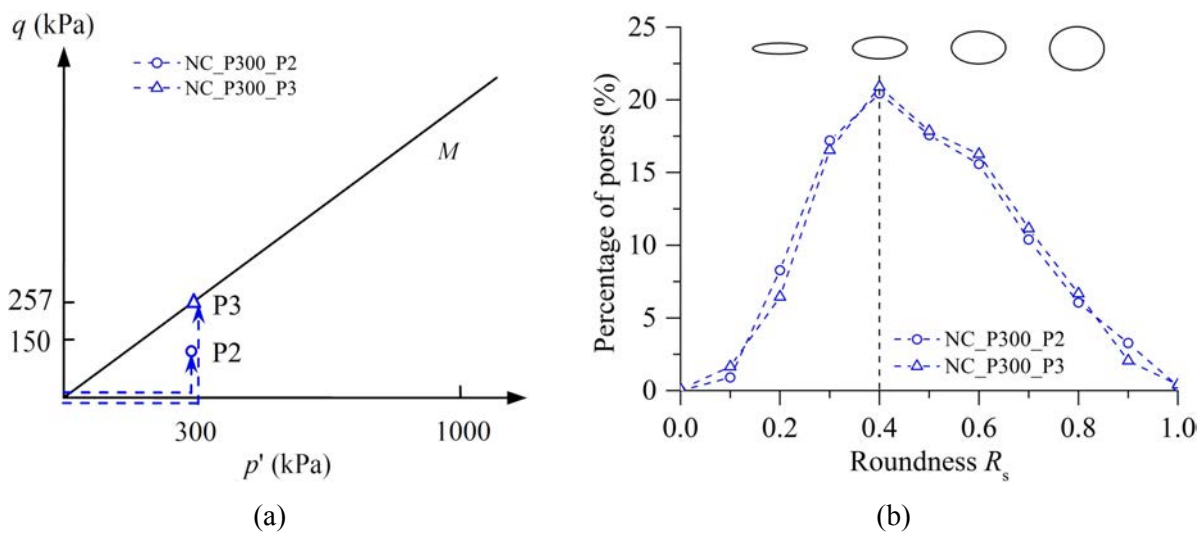


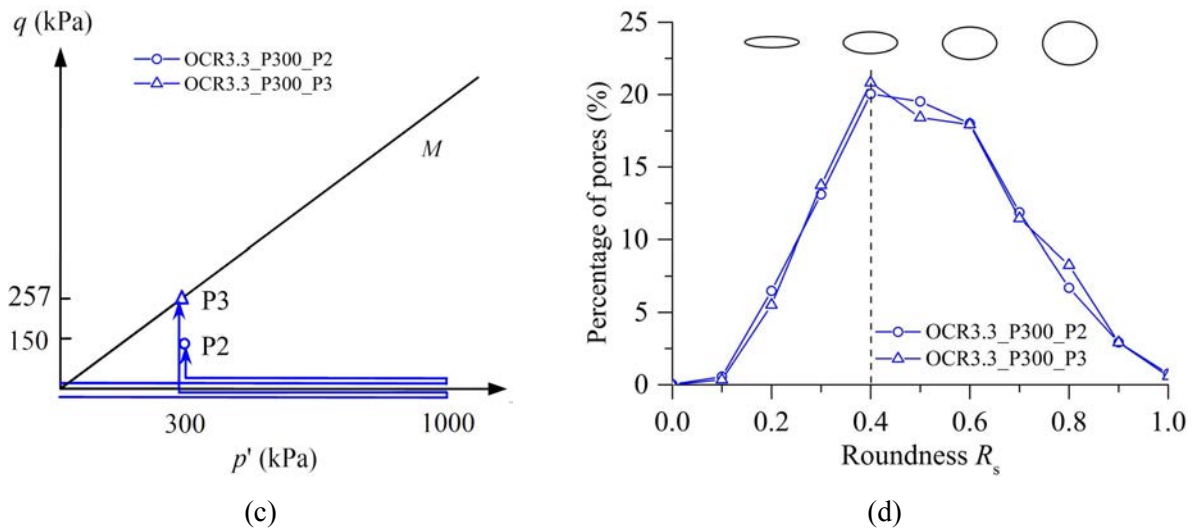
(a) narrow pores in NC\_P300\_P2

(b) open pores in OCR3.3\_P300\_P2

Figure 3.13 Micropore system (black areas) identified in different specimens

The influence of triaxial stress levels on the pore roundness of clay specimens following the purely deviatoric stress path is illustrated in Figure 3.14. It is observed that the specimens at a higher stress level (i.e., the P3 stress level) have nearly the same pore roundness distribution as those at a lower stress level (i.e., the P2 stress level), which indicates that the influence of stress levels on the pore shape is relatively limited. At the P3 stress level, the pore roundness-percentage curve of the contractive specimen (i.e., NC\_P300\_P3) exhibits a sharp unimodal shape while that of the dilative specimen (i.e., OCR3.3\_P300\_P3) shows a trend shifting to the right side of the dominant roundness value ( $R_s = 0.4$ ). This result is in good agreement with the findings obtained by analysing Figure 3.12.





(a-b) normally consolidated specimens; (c-d) overconsolidated specimens

Figure 3.14 Pore roundness of specimens at different stress levels on a given stress path

- *Relationship between pore roundness and pore diameter*

Figure 3.15 presents the relationship between mean pore roundness and pore diameter. One can note that all the specimens have similar pore shape distributions as a function of pore diameter. In general, the roundness of pores increases with decreasing pore diameter, which is especially true for the pores with a size smaller than  $1.0 \mu\text{m}$ . The result indicates that under triaxial loading the large pores are more vulnerable (i.e., less open) than the small ones to compression. This finding is similar to the results of natural soils subjected to wetting and drying cycles obtained by Pires et al. (2008): most of the small pores are round, while the roundness decreases with increasing pore size. An oblique line expressed by  $R_s = -\log D/6 + 0.5$  passing through two extreme points, i.e., ( $D = 1000 \mu\text{m}$ ,  $R_s = 0$ ) and ( $D = 0.001 \mu\text{m}$ ,  $R_s = 1$ ), can be proposed as a function to fit the measured data (Figure 3.15) of both normally consolidated and overconsolidated specimens.

From Figure 3.15, one can also note a slight difference regarding the curves between dilative specimens and contractive specimens. It seems that the roundness of the large pores ( $D \geq 2.0 \mu\text{m}$ ) in dilative specimens (see Figure 3.15b except for OCR4.0\_S250\_P2) is slightly larger than that of the large pores in contractive specimens (Figure 3.15a). This suggests that the relatively large pore roundness of a dilative clay (Figure 3.12b) is probably due to the increase in the roundness of large pores (i.e., pores become more open).

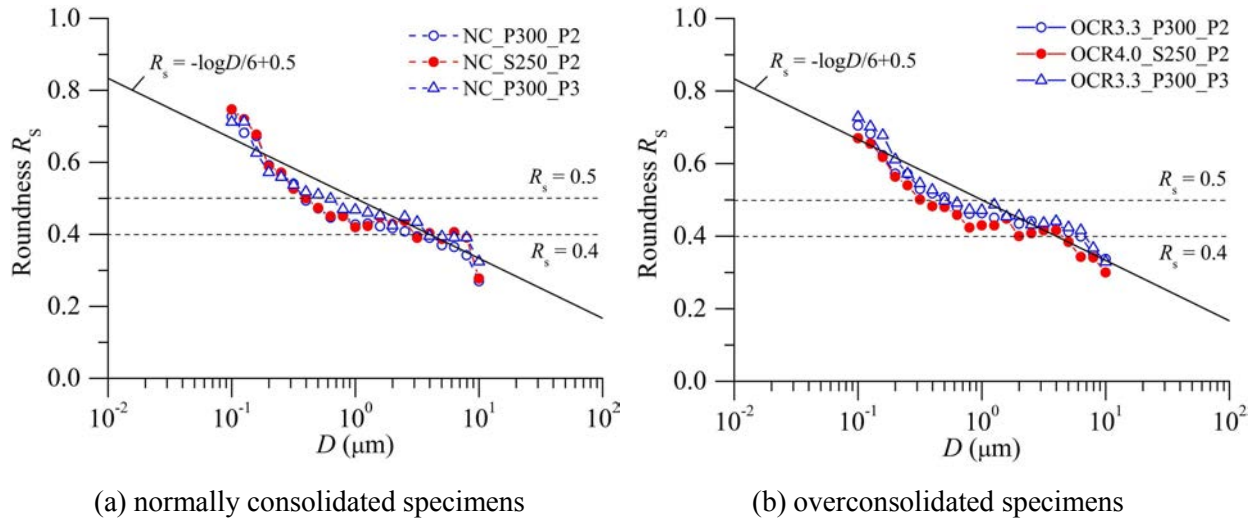


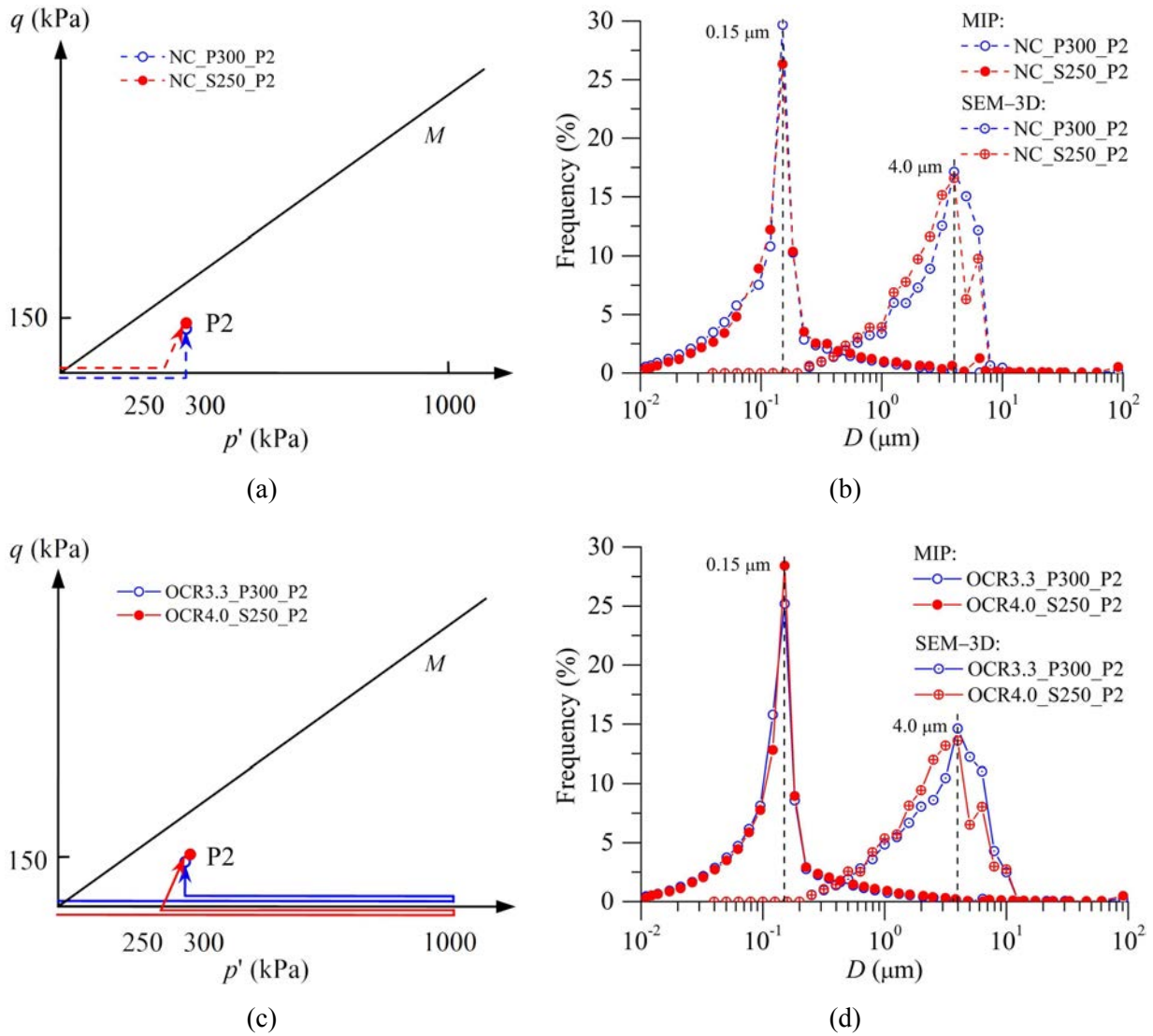
Figure 3.15 Relationship between pore roundness and pore diameter

### 3.2.3 Pore size distribution and void ratio

- *Pore size distribution*

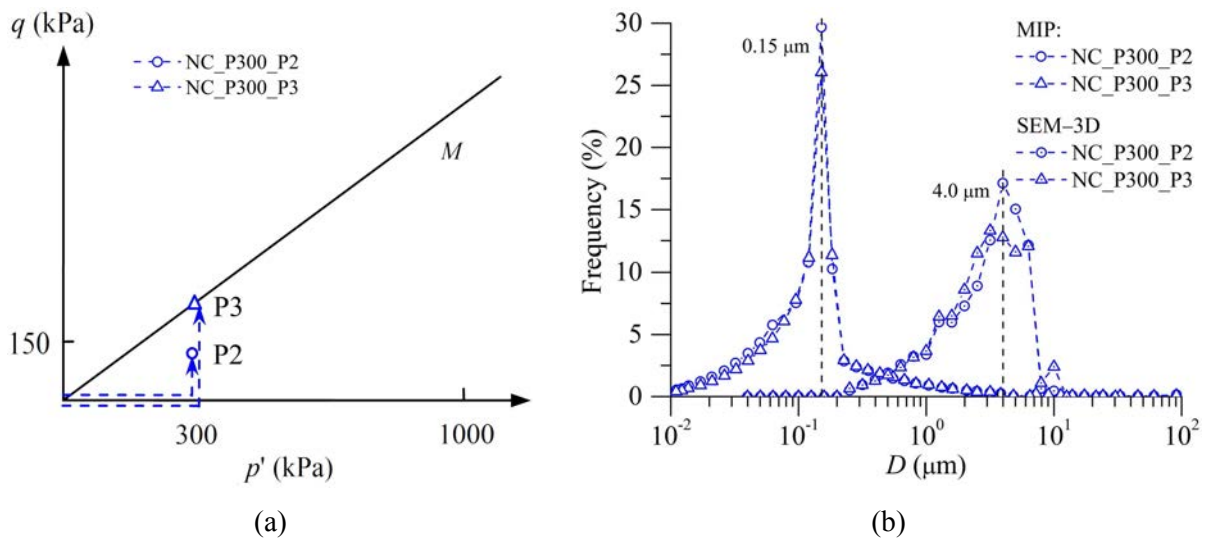
The curves of frequency versus pore diameter (i.e., pore size distribution, PSD) measured by MIP tests combined with those estimated via the SEM-stereology method are presented in Figures 3.16-3.17. It is observed that the pore diameters estimated via the SEM-stereology method fall into the range between 0.25  $\mu\text{m}$  and 10  $\mu\text{m}$  with the mean value of about 4.0  $\mu\text{m}$ . By contrast, the pore diameters measured by the MIP technique show a relatively wide range from 0.01  $\mu\text{m}$  up to 100  $\mu\text{m}$  with the mean value of 0.15  $\mu\text{m}$ . The appearance of differences between the results of the SEM-stereology method and MIP is understandable because these two techniques were developed based on distinct principles and have different characterisation scales of pore structures, as mentioned in Chapter 2.

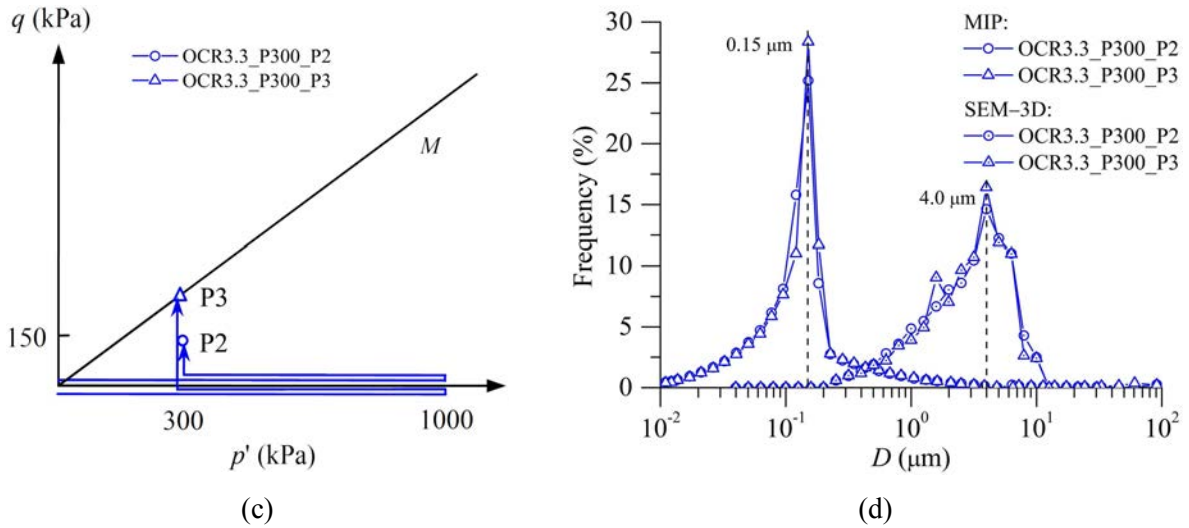
One can also note that the PSD curves measured by MIP have almost the same shape for all the specimens, suggesting that the stress paths, stress levels and OCRs employed in this study have no significant influence on the PSD of remoulded kaolin clay. However, when focussing on a specific range of pore size, the shape of the PSD seems to be different between dilative specimens and contractive specimens. For example, as shown in Figure 3.17, the PSD estimated via SEM-stereology shows that the number of large pores (e.g.,  $D \geq 4 \mu\text{m}$ ) in a dilative specimen (e.g., OCR3.3\_P300\_P2 or OCR3.3\_P300\_P3) appears slightly larger than that of the corresponding contractive specimen (e.g., NC\_P300\_P2 or NC\_P300\_P3). This is likely because of the induced-opening of large pores when a specimen exhibits dilatancy phenomenon at the macroscale.



(a-b) normally consolidated specimens; (c-d) overconsolidated specimens

Figure 3.16 PSD of clay specimens at a given stress level on different stress paths

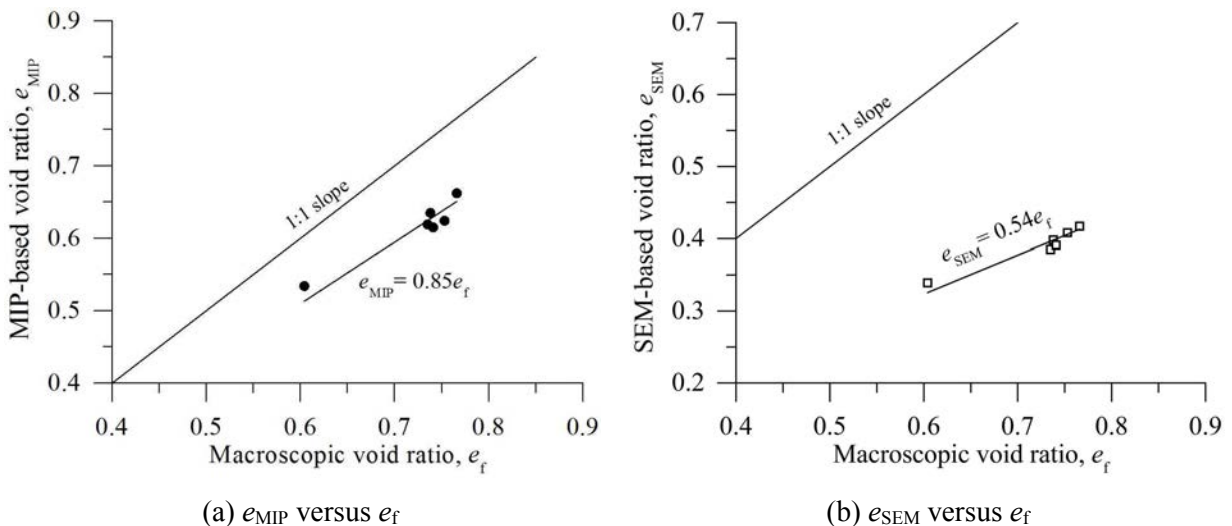




(a-b) normally consolidated specimens; (c-d) overconsolidated specimens  
 Figure 3.17 PSD of clay specimens at different stress levels on a given stress path

- *Void ratio*

This section aims to reveal the possible relationship between the microvoid ratios (i.e.,  $e_{MIP}$  and  $e_{SEM}$ ) and the macrovoid ratios ( $e_f$ ). Figure 3.18 shows  $e_{MIP}$  measured by MIP tests and  $e_{SEM}$  that is the 3D microvoid ratio estimated via the SEM-stereology method. Linear relationships between the microvoid ratios and the macrovoid ratios are observed. One can note that the values of  $e_{MIP}$  are approximately 85 percent of  $e_f$ , while the values of  $e_{SEM}$  are less than 60 percent of  $e_f$ .



(a)  $e_{MIP}$  versus  $e_f$  (b)  $e_{SEM}$  versus  $e_f$   
 Figure 3.18 Relationship between microvoid ratios and macrovoid ratios

The values of  $e_{MIP}$  are slightly less than  $e_f$ , which can be explained by the fact that the MIP technique cannot take into account the closed, isolated pores. On the other hand, the values of

$e_{SEM}$  are smaller than  $e_{MIP}$ , which is consistent with the results obtained by You et al. (2017) for silty clay. This finding is reasonable, since very small pores are discarded due to the limited resolution of images and the macropores are also neglected because of the limited imaging areas when using the SEM-image analysis method.

### 3.3 Microscopic and mesoscopic cracks

The aim of this section is to examine the development of local cracks in the remoulded clay specimens during triaxial loading. The SEM-based technique and the XR- $\mu$ CT technique are respectively employed to identify two different scales of cracks: microcracks and mesocracks. The detailed methods of investigations have been presented in Chapter 2.

---

#### 3.3.1 Microscopic cracks identified by SEM

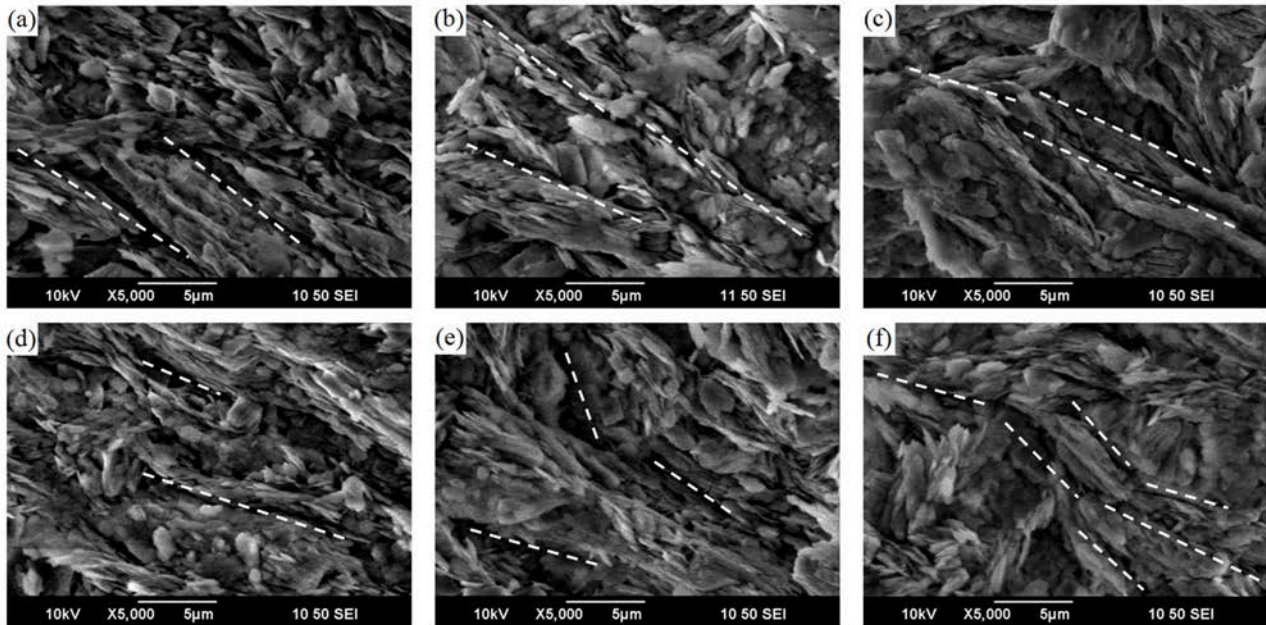
---

Figure 3.19 presents the SEM images of remoulded clay specimens under different triaxial loading conditions. The results highlight the appearance of microcracks within both normally consolidated and overconsolidated specimens whatever the consolidation state, the stress path and the stress level. These microcracks have different lengths varying from 5  $\mu\text{m}$  or less to 15  $\mu\text{m}$  and small thicknesses between 0.5  $\mu\text{m}$  and 1.0  $\mu\text{m}$ . The microcracks generally appear between the adjacent strongly parallel-oriented particle groups, which are formed from the assembly of several particles with face-to-face contacts.

Comparing Figure 3.19a with Figure 3.19d, one can note that the microcracks within the overconsolidated specimen (i.e., OCR4.0\_S250\_P2) sheared to the P2 stress level following the constant  $\sigma'_3$  stress path exhibit similar distributions as those within the normally consolidated specimen (i.e., NC\_S250\_P2) under the same condition of stress path and stress level. In the case of the purely deviatoric stress path, it appears that the microcracks within the overconsolidated specimen (i.e., OCR3.3\_P300\_P2, see Figure 3.19e) exhibiting dilatancy behaviour at the P2 stress level are more often nonparallel compared to those within the normally consolidated specimen (i.e., NC\_P300\_P2, see Figure 3.19b) showing contractive behaviour. Similar results are also obtained by analysing the SEM images of the specimens (i.e., OCR3.3\_P300\_P3 and NC\_P300\_P3) at the P3 stress level following the purely deviatoric stress path (Figure 3.19c and f).

It should be noted that the microcracks are observed only in some areas of the observed

planes, other regions of clay samples remain quite continuous.



(a) NC\_S250\_P2; (b) NC\_P300\_P2; (c) NC\_P300\_P3; (d) OCR4.0\_S250\_P2;  
(e) OCR3.3\_P300\_P2; (f) OCR3.3\_P300\_P3

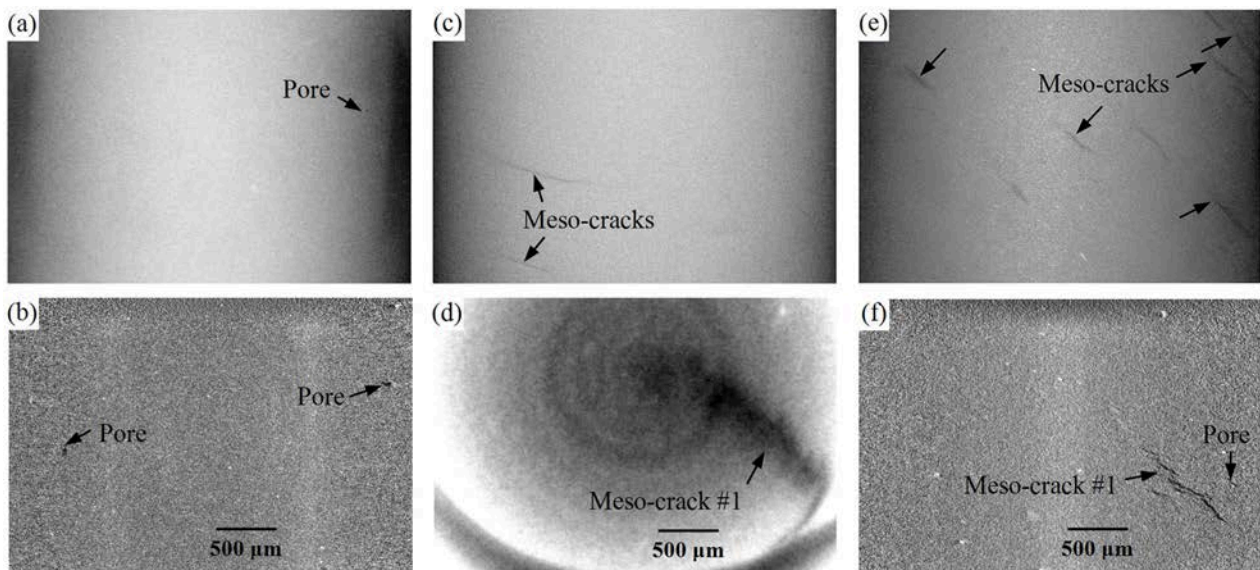
Figure 3.19 Microcracks within clay specimens observed by SEM

### 3.3.2 Mesoscopic cracks identified by XR- $\mu$ CT

Two normally consolidated specimens (i.e. NC\_P300\_P2 and NC\_S250\_P2) and two overconsolidated specimens (i.e. OCR3.3\_P300\_P2 and OCR4.0\_S250\_P2) sheared to the same P2 stress level following different stress paths were scanned with the XR- $\mu$ CT technique. The XR- $\mu$ CT images presented in Figure 3.20 show a major difference between the mesoscopic structures of the normally consolidated specimens and those of the overconsolidated specimens. Many open mesocracks are identified in the overconsolidated specimens (i.e., OCR4.0\_S250\_P2 in Figure 3.20c-d and OCR3.3\_P300\_P2 in Figure 3.20e-f), particularly the specimen OCR3.3\_P300\_P2 on the purely deviatoric stress path. By contrast, only some mesoscale pores are observed within all the normally consolidated specimens (e.g., NC\_P300\_P2 in Figure 3.20a-b). It should be mentioned that this result does not mean no development of mesocracks at all within the normally consolidated specimens, closed mesocracks might exist, but they are difficult to detect using the XR- $\mu$ CT technique.

The influence of stress paths on the formation of mesocracks can be noted. In the case of the overconsolidated specimen (i.e., OCR3.3\_P300\_P2) that exhibits dilative behaviour along

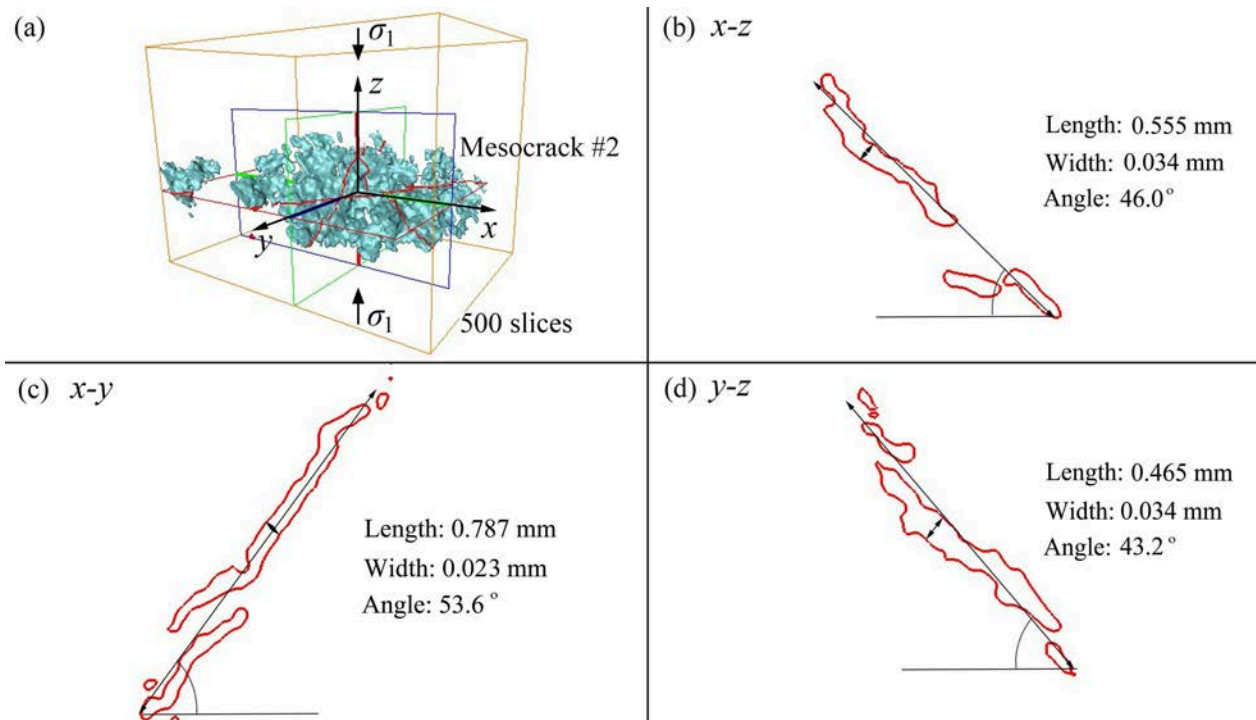
the purely deviatoric stress path, numerous open mesocracks, more or less parallel-distributed towards a certain direction, are clearly observed (see Figure 3.20e-f). One can note that these results combined with the SEM observations (Figure 3.19e) confirm the reasonable assumption that some of the microcracks are able to propagate up to the mesoscale. However, in the case of the overconsolidated specimen (i.e., OCR4.0\_S250\_P2) showing contractive behaviour along the constant  $\sigma'_3$  stress path, less in quantity but more regular in shape mesocracks are observed (see Figure 3.20c-d).



(a-b) NC\_P300\_P2; (c-d) OCR4.0\_S250\_P2; (e-f) OCR3.3\_P300\_P2

Figure 3.20 XR- $\mu$ CT projections and slices of remoulded clay specimens

Figure 3.21 illustrates the 3D surface and three cross-sections of a typical mesocrack in the dilative specimen OCR3.3\_P300\_P2. One can note that the surface of the 3D mesocrack is rather tortuous and fragmented. The thickness and length of the cross-sections of the mesocrack are 20 - 35  $\mu$ m and 0.4 - 0.8 mm, respectively. The tilt angles of two vertical cross-sections of the mesocrack respectively approximate 46° and 43°, resulting in a spatial tilt angle of around 50° with respect to the horizontal plane. This value is acceptably consistent with the global preferential particle orientation (about 135° or 45°) of the same specimen (see Figure 3.6d).



(a) 3D surface; (b) (x, z) plane; (c) (x, y) plane; (d) (y, z) plane

Figure 3.21 A typical mesocrack within the specimen OCR3.3\_P300\_P2

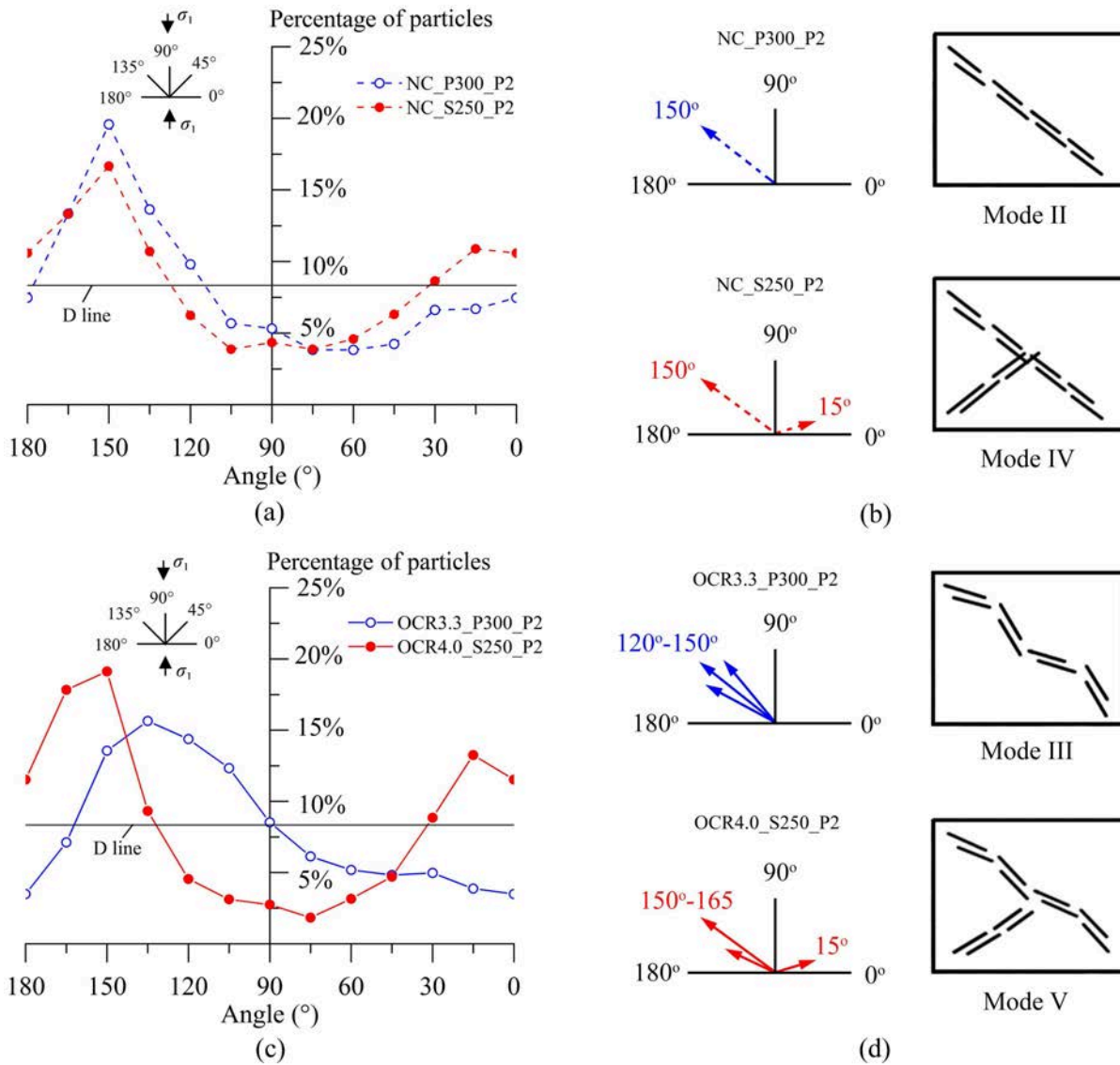
## 4. Mechanism of dilatancy phenomenon

### 4.1 Conceptual modes of particle orientation

In the previous section, the global particle orientation of clay specimens under different triaxial loading conditions is analysed (Figures 3.4, 3.6 and 3.8). Taking the four specimens (see Figure 3.6) sheared to the P2 stress level for example, one can note four different particle orientation modes:

- i. The orientation curve of the normally consolidated specimen (i.e., NC\_P300\_P2) on the purely deviatoric stress path shows a single sharp peak. This result indicates that a majority of clay particles rotate towards the same direction, and the particle arrangement may be characterised by the first sketch (mode II) in Figure 3.22b.
- ii. The orientation curve of the normally consolidated specimen (i.e., NC\_S250\_P2) on the constant  $\sigma_3$  stress path exhibits an evident sharp peak on the left and a low peak on the right. It means that not only a large number of clay particles rotate towards one direction, but also many clay particles rotate towards a second direction. The clay particle

arrangement may be characterised by the second sketch (mode IV) in Figure 3.22b.



(a-b) normally consolidated specimens; (c-d) overconsolidated specimens

Figure 3.22 Different features of clay particle orientation affected by stress paths

- iii. The orientation curve of the overconsolidated specimen (i.e., OCR3.3\_P300\_P2) on the purely deviatoric stress path exhibits a single smooth peak. One can infer from this result that a large number of clay particles rotate towards a narrow range of direction, and the clay particle arrangement may be characterised by the first sketch (mode III) in Figure 3.22d.
- iv. The orientation curve of the overconsolidated specimen (i.e., OCR4.0\_S250\_P2) on the constant  $\sigma_3$  stress path exhibits an evident peak (with a shape not so sharp as that of the normally consolidated specimen) on the left and a low peak on the right. The result

indicates that a large number of clay particles rotate towards a narrow range of direction as well as many clay particles rotate towards a second direction. The clay particle arrangement may be characterised by the second sketch (mode V) in Figure 3.22d.

Similarly, from the results of clay particle orientation shown in Figures 3.4 and 3.8, one can also identify different modes. Table 3.4 summarises all the identified modes of clay particle orientation. These conceptual orientation modes are interpreted as follows:

- i. *Depolarization mode (Mode I as defined by Hattab and Fleureau (2010 and 2011))*: This mode is characterised by clay particles with a highly random orientation. In this case, the material shows a perfectly isotropic microstructure. Mode I usually develops during isotropic consolidation of clay, and the orientation curve approaches the D line without exhibiting evident peaks. The particle orientation curves (Figure 3.4c) as well as the SEM images (Figure 3.23a) of the specimens (i.e., ISO\_300 and ISO\_1000) under isotropic loading clearly highlight this orientation mode.
- ii. *Oblique lines mode (Mode II)*: In this case, the clay particles are associated in face-to-face form and highly reorient by groups towards a certain plane. With this orientation mode, the particle orientation curve is characterised by a single sharp peak. This mode is identified in the normally consolidated clay especially that on the purely deviatoric stress path (i.e., NC\_P300\_P2 and NC\_P300\_P3, see Figure 3.8b for particle orientation curves and Figure 3.23c for SEM image illustration).
- iii. *Tortuous-oblique lines mode (Mode III)*: It is characterised by clay particle groups oriented along tortuous lines towards a certain global direction. This mode appears when the clay is highly overconsolidated, and the tortuous feature seems to be related to the dilatancy phenomenon. With this type of orientation mode, the orientation curve displays one evident smooth peak (cases of OCR3.3\_P300\_P2 and OCR3.3\_P300\_P3, see Figure 3.8d for particle orientation curves and Figure 3.23e for SEM image illustration).
- iv. *Crossed-oblique lines mode (Mode IV)*: This orientation mode corresponds to the "oblique lines" mode, but it consists of two "oblique planes" in a T-shaped form. When the clay particles rotate following this mode, one evident sharp peak combined with some points slightly above the D line on the other side of the percentage-orientation plane can be observed (case of NC\_S250\_P2, see Figure 3.6b for particle orientation curve and Figure 3.23b for SEM image illustration).

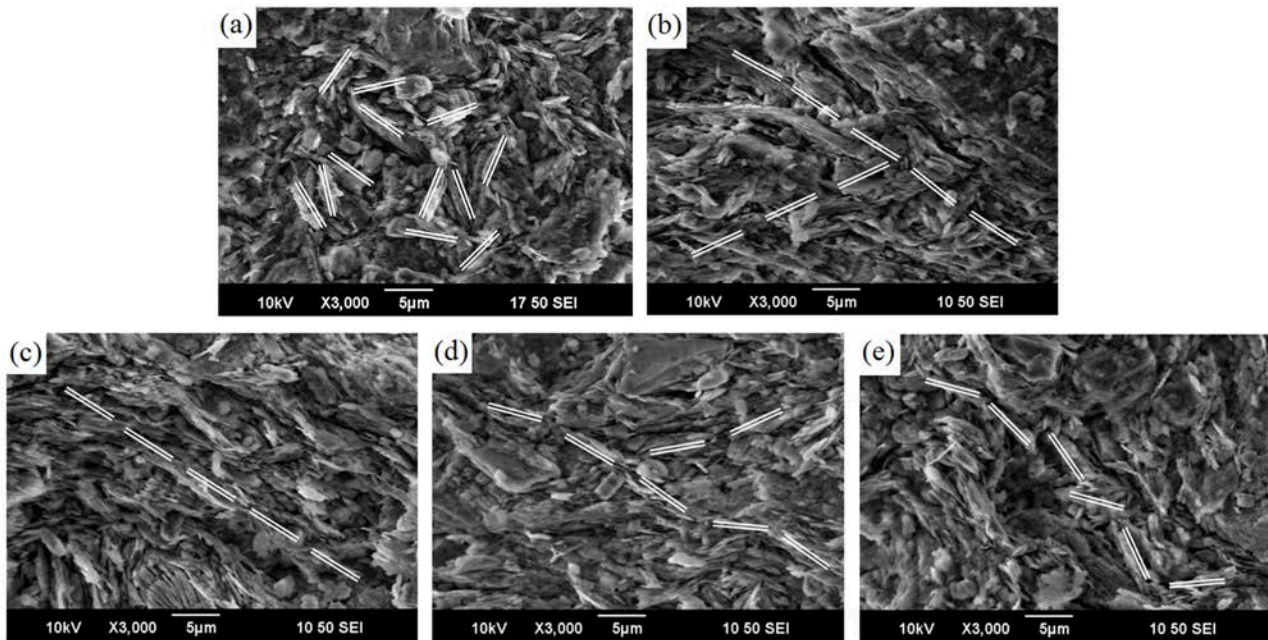
- v. *Crossed-tortuous-oblique lines mode (Mode V)*: This orientation mode corresponds to the “tortuous-oblique lines” mode, but it consists of two “tortuous-oblique planes” in a T-shaped form. The development of this mode is assumed to be possible in highly overconsolidated clay, and it is also related to the dilatancy phenomenon. In this case, an evident smooth peak as well as a low peak present on both sides of the percentage-orientation plane.

The specimen OCR4.0\_S250\_P2 with macroscopic contractive behaviour exhibits a complex microstructure that seems more similar to Mode V (although the particles are not so tortuous) than to Mode IV (Figure 3.23d). The occurrence of this microstructure is probably related to the stress state is in the dilatancy activation domain, as shown in Figure 3.3b.

Table 3.4 Identified modes of clay particle orientation

Test	Specimen	OCR	Stress path	Stress level	Dilation/Contraction	Orientation mode	Graphical representation
Isotropic consolidation test	ISO_300	/	/	/	/	Mode I	
	ISO_1000	/	/	/	/	Mode I	
	NC_S250_P2	1.0	S	P2	Contraction	Mode IV	
	OCR4.0_S250_P2	4.0	S	P2	Slight Contraction	Mode V*	
Triaxial compression test	NC_P300_P2	1.0	P	P2	Contraction	Mode II	
	OCR3.3_P300_P2	3.3	P	P2	Dilation	Mode III	
	NC_P300_P3	1.0	P	P3	Contraction	Mode II	
	OCR3.3_P300_P3	3.3	P	P3	Dilation	Mode III	

Note: \* specimen OCR4.0\_S250\_P2 characterises a slight Mode V, which means its particles are not as tortuous as those in specimens OCR3.3\_P300\_P2 and OCR3.3\_P300\_P3. In this case, the dilatancy mechanism is not fully activated.

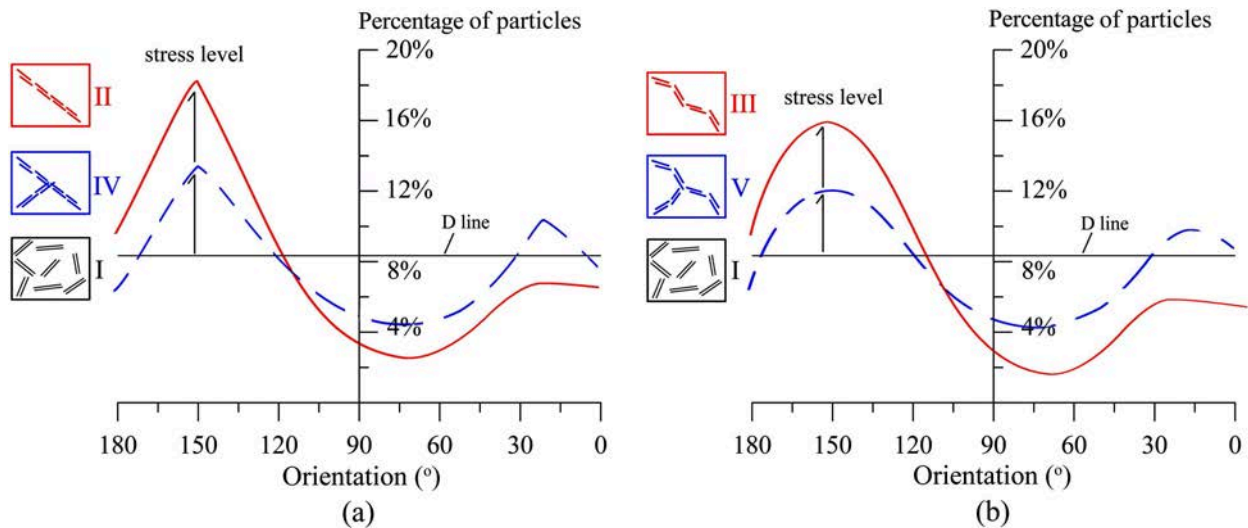


(a) ISO\_300; (b) NC\_S250\_P2; (c) NC\_P300\_P2; (d) OCR4.0\_S250\_P2; (e) OCR3.3\_P300\_P2

Figure 3.23 Representative SEM images observed in the vertical plane of specimens

The identified conceptual orientation modes appear quite consistent with the results obtained by Hattab and Fleureau (2010 and 2011). Through a multiscale investigation, they demonstrated that, for the normally consolidated and slightly overconsolidated kaolinite specimens, the isotropic loading leads to a microstructure similar to Mode I, and the conventional triaxial stress path (i.e., the constant  $\sigma'_3$  stress path) leads to a microstructure of Mode IV or Mode II (which appears particularly clear when the stress level approaches the critical state line). However, in the contraction domain and close to the pseudoelastic domain of the  $(p', q)$  plane, the authors observed a persistence of Mode I. As they explained, this typical microstructure state is probably related to the important role played by the isotropic part of the stress tensor during triaxial loading.

Based on the above analyses, the evolution of particle orientation modes at different stress levels can be illustrated in Figure 3.24. The particle orientation appears mainly dependent on the loading history and stress level, especially the domain of the  $(p', q)$  plane (Figure 3.3b) where the stress state is located. When the stress state is in the pseudoelastic domain, the depolarization mode (Mode I) is observed. On the other hand, if the stress state is in the contraction domain, Mode II/IV is probably to develop; if the stress state is in the dilatancy domain, Mode III/V may be activated.



(a) contractive phenomenon; (b) dilative phenomenon

Figure 3.24 Evolution of particle orientation of remoulded clay under triaxial loading

#### 4.2 Discussion on dilatancy mechanisms

Compared with the normally consolidated or slightly overconsolidated remoulded clay ( $OCR \leq 2.5$ ), the strongly overconsolidated remoulded clay ( $OCR > 2.5$ ) usually has a smaller void ratio and a higher shear strength, and exhibits more complicated macroscopic behaviour such as shear dilatancy. The above characteristics, especially the dilatancy phenomenon, of strongly overconsolidated remoulded clay may be interpreted using the conceptual orientation modes identified in this research, as shown in Figure 3.25.

One can note that the particle arrangements (Figure 3.25a and e) within both the normally consolidated and the overconsolidated specimens are consistent with the depolarization mode (mode I) under isotropic loading. However, the clay fabric of a strongly overconsolidated specimen is much denser due to the preconsolidation under an isotropic effective stress of 1000 kPa.

When the deviatoric stress is applied on the strongly overconsolidated specimen during triaxial loading, the dense microstructure restricts the free movement of clay particles, leading to the tortuous particle arrangement (i.e., the "crossed-tortuous-oblique lines" mode (Mode V), see Figure 3.25f). In this case, if the shear stress overcomes the effect of inter-particle friction, some particle groups move over each other. This local movement may result in the formation of new microcracks as well as the opening of existing pores and the opening and propagation of existing microcracks, which is supported by the previous analyses of pore roundness and

local cracks (see Figures 3.14 and 3.19). At the macroscopic level, it is characterised by the activation of dilatancy phenomenon. A simple model for explaining the dilatancy mechanism within the strongly overconsolidated remoulded clay is illustrated in Figure 3.26. This model is similar to the sawtooth concept model, which is usually employed to interpret the dilatancy phenomenon in granular materials (Rowe, 1962; De Josselin de Jong, 1976; Bolton, 1986).

It should be noted that the point at which dilatancy occurs depends on triaxial loading conditions. For example, if the specimen is sheared on the constant  $\sigma'_3$  stress path, the volumetric contraction may be induced before the activation of dilatancy due to the mechanism of the isotropic part of the stress tensor, as discussed in Section 2.3.

As the deviatoric stress level increases, the tortuous orientation of clay particles extends within the strongly overconsolidated specimen. At the same time, the global "tortuous-oblique lines" mode (mode III) with the preferential orientation aligned in the direction of the maximum shear stress plane is activated (Figure 3.25g). In this stage, more new microcracks appear and open mesocracks are formed due to the propagation and connection of existing microcracks. During this process, the shear strength of the strongly overconsolidated clay degrades with increasing number of open mesocracks. By contrast, the decrease in the shear strength of the normally consolidated or slightly overconsolidated specimen seems due to the considerable decrease in the internal friction angle as a result of the extending face-face organisation of clay particles (Figure 3.25c).

At the critical state, the shear stress becomes equal to the maximum strength, thus leading to the failure of clay specimens. The difference in the particle orientation modes might result in two different failure mechanisms in the normally consolidated or slightly overconsolidated specimens and the strongly overconsolidated specimens. The normally consolidated or slightly overconsolidated specimens fail along a potential sliding surface (Figure 3.25d), which is consistent with the slip mechanism revealed by Hattab (2011) and Hattab et al. (2015). By contrast, the strongly overconsolidated specimens are likely to be damaged due to the appearance of open macrocracks that were formed by the propagation and connection of open mesocracks (Figure 3.25h). Therefore, the failure surface is usually tortuous and rough with respect to the strongly overconsolidated clay specimens.

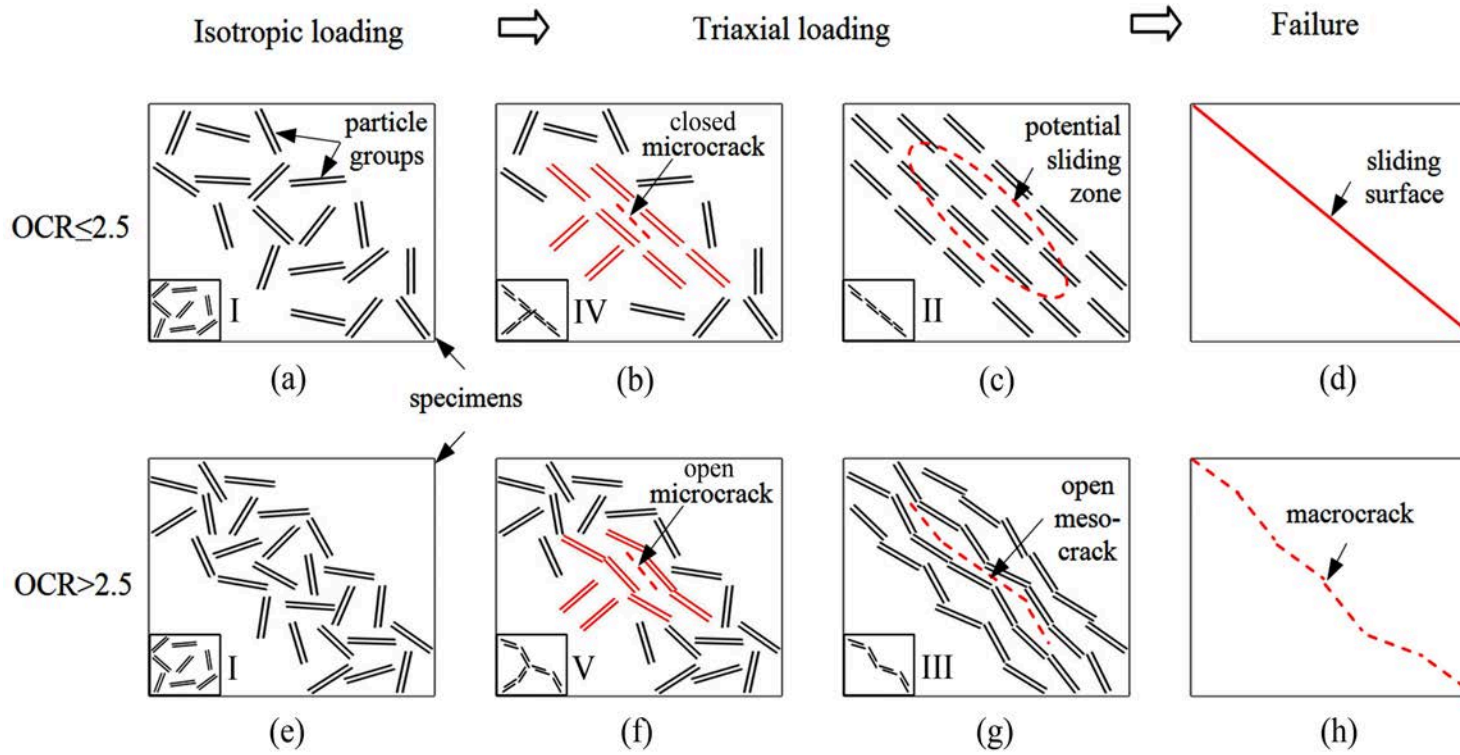


Figure 3.25 Microstructural evolution of remoulded clay under triaxial loading

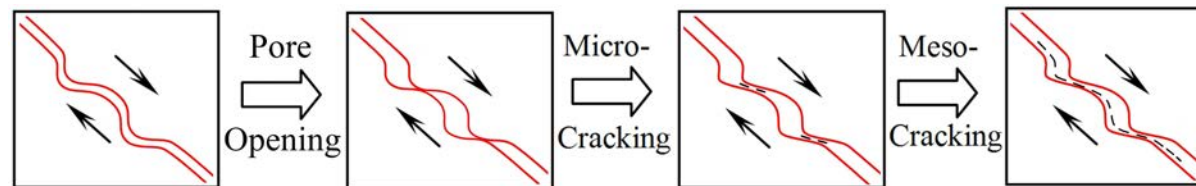


Figure 3.26 Dilatancy model for strongly overconsolidated remoulded clay

Notice that the dilatancy mechanism discussed in this section is more or less a speculation based on the limited results of this study, and that further experimental verifications are necessary.

## 5. Summary

This chapter presents a multiscale investigation of saturated remoulded clays subjected to various triaxial loading. The macromechanical behaviour as well as the microstructural characteristics of remoulded clays were systematically analysed. Particularly, the microscale mechanism of the dilatancy phenomenon is discussed. The following conclusions can be drawn from this chapter:

- (1) Macromechanical results demonstrate that, at a given stress level in the  $(p', q)$  plane, all the normally consolidated specimens show contractive behaviour. However, the overconsolidated specimens may exhibit different volumetric behaviour depending on the stress path. In the examined cases, dilatancy is activated in the overconsolidated specimens on the purely deviatoric stress path, whereas a negligible plastic volumetric strain is observed in the specimen along the constant  $\sigma'_3$  stress path.
- (2) Under isotropic loading, the clay particles present a global random orientation, even if the initial preferential orientation produced by the one-dimensional consolidation during the specimen preparation is not completely erased. The non-erased preferential orientation of clay particles may be defined as “initial anisotropy”; by contrast, the further preferential orientation of clay particles created by the subsequent external loads such as triaxial shearing could be defined as “induced anisotropy”.
- (3) Five orientation modes of clay particles are proposed as conceptual local features, i.e., the depolarization mode, the "oblique lines" mode, the "tortuous-oblique lines" mode, the "crossed-oblique lines" mode and the "crossed-tortuous-oblique lines" mode. The activation of the above orientation modes highly depends on the stress history (e.g., OCR, stress path and stress level) of the remoulded clay. These proposed conceptual modes allow interpreting the macroscopic volumetric mechanisms of remoulded clay from a microscopic point of view.
- (4) Different shape and orientation characteristics of pores are identified in contractive and dilative specimens under triaxial loading. The elliptical pores observed in a dilative

specimen are relatively more open than those in a contractive specimen. The open pores in a dilative specimen reorient themselves following the orientation of clay particles, forming weak zones in the clay material, which makes it possible for microcracks to initiate and propagate during a continuous loading.

- (5) Two scales of pore size distributions with mean sizes of  $0.15\ \mu\text{m}$  and  $4.0\ \mu\text{m}$  are revealed by the MIP technique and the SEM-stereology method, respectively. The results of SEM-stereology analyses also show that a dilative specimen has more large pores than a contractive specimen. This is probably due to the induced-opening of large pores in overconsolidated specimens exhibiting dilatancy phenomenon. In addition, clear linear relationships between the macrovoid ratios and the microvoid ratios are obtained.
- (6) Microcracks are observed between strongly parallel-oriented particle groups in both normally consolidated and overconsolidated specimens. However, the microcracks in a dilative specimen appear more open and able to propagate, forming a series of more or less parallel-distributed open mesocracks as observed by the XR- $\mu$ CT technique. They constitute the basic local mechanisms responsible for the macroscopic dilatancy phenomenon. In the case of normally consolidated specimens, potential closed mesocracks could not be observed by the XR- $\mu$ CT technique.

## Chapter 4

# Hydromechanical behaviour of unsaturated remoulded clay

<b>1. Experimental approach.....</b>	<b>133</b>
<b>2. Soil-water characteristics of unsaturated clay.....</b>	<b>135</b>
2.1 Unsaturated remoulded Kaolin K13 clay.....	135
2.1.1 Evolution of water contents on drying path.....	135
2.1.2 Soil-water characteristic curves.....	137
2.2 Unsaturated remoulded M35 clay.....	141
2.2.1 Evolution of water content on drying path.....	141
2.2.2 Soil-water characteristic curves.....	143
<b>3. Mechanical behaviour of remoulded Kaolin K13 clay.....</b>	<b>145</b>
3.1 Saturated test results affected by mean effective stress.....	145
3.2 Unsaturated test results affected by mean stress.....	147
3.2.1 Under initial total suction of 38 MPa.....	147
3.2.2 Under initial total suction of 10 MPa.....	155
3.3 Unsaturated test results affected by suction.....	161
3.3.1 Under the mean stress of 200 kPa.....	161
3.3.2 Under the mean stress of 600 kPa.....	162
3.3.3 Under the mean stress of 1000 kPa.....	164
<b>4. Mechanical behaviour of remoulded M35 clay.....</b>	<b>166</b>
4.1 Saturated test results affected by mean effective stress.....	166
4.2 Unsaturated test results affected by mean stress.....	169
<b>5. Theoretical calculation of apparent cohesions.....</b>	<b>174</b>
5.1 Theoretical equations.....	174
5.1.1 Suction stress concept.....	174
5.1.2 Capillary stress concept.....	174
5.2 Comparison between calculated and measured cohesions.....	175

**6. Summary.....176**

The hydromechanical behaviour of unsaturated clay is highly dependent on the degree of saturation (or suction) and has been a subject of great interest for both geotechnical and environmental engineers. This chapter aims to investigate the hydromechanical behaviour particularly the shear strength parameters of two unsaturated remoulded clays, i.e., Kaolin K13 and M35, subjected to various suction-stress paths. The purpose is achieved by first imposing different levels of suction and then performing unconsolidated undrained triaxial compression tests on clay specimens under different mean stresses.

## 1. Experimental approach

The experimental approach consists in performing a series of macroscopic tests and mesoscopic tests on two different unsaturated remoulded clays, i.e., Kaolin K13 and M35. The whole experimental programme adopted in this chapter is summarised in Figure 4.1. The details are presented in the Sections 3-4 of Chapter 2.

The macroscopic tests consisted of soil-water characteristic tests and unconsolidated undrained triaxial tests on unsaturated specimens, and consolidated drained triaxial tests on saturated specimens for comparison purposes. Regarding unsaturated tests, cylindrical specimens of 50 mm in diameter and 75 mm high and small samples with volumes of 2-5 cm<sup>3</sup> were extracted from the pre-consolidated slurries with an initial water content of 1.5w<sub>L</sub>. Afterwards, all the specimens were placed into several desiccators containing saturated Na<sub>2</sub>SO<sub>4</sub> or NaCl solutions to impose different initial total suctions (i.e., 10 MPa and 38 MPa). When the vapour equilibrium was attained in the desiccators, the small samples were used to measure the water content, void ratio and degree of saturation via the oven drying and liquid displacement methods (Péron et al., 2007). In this way, the soil-water characteristic curves of unsaturated clays were obtained. At the same time, unsaturated triaxial tests were performed on cylindrical specimens under different mean stresses (i.e., 200 kPa, 600 kPa and 1000 kPa) on the purely deviatoric stress path.

The mesoscopic tests were basically XR- $\mu$ CT scans performed on the cylindrical clay specimens after triaxial testing. The main purpose was try to identify the mesoscopic structural properties of unsaturated remoulded clays subjected to different suction-stress levels.

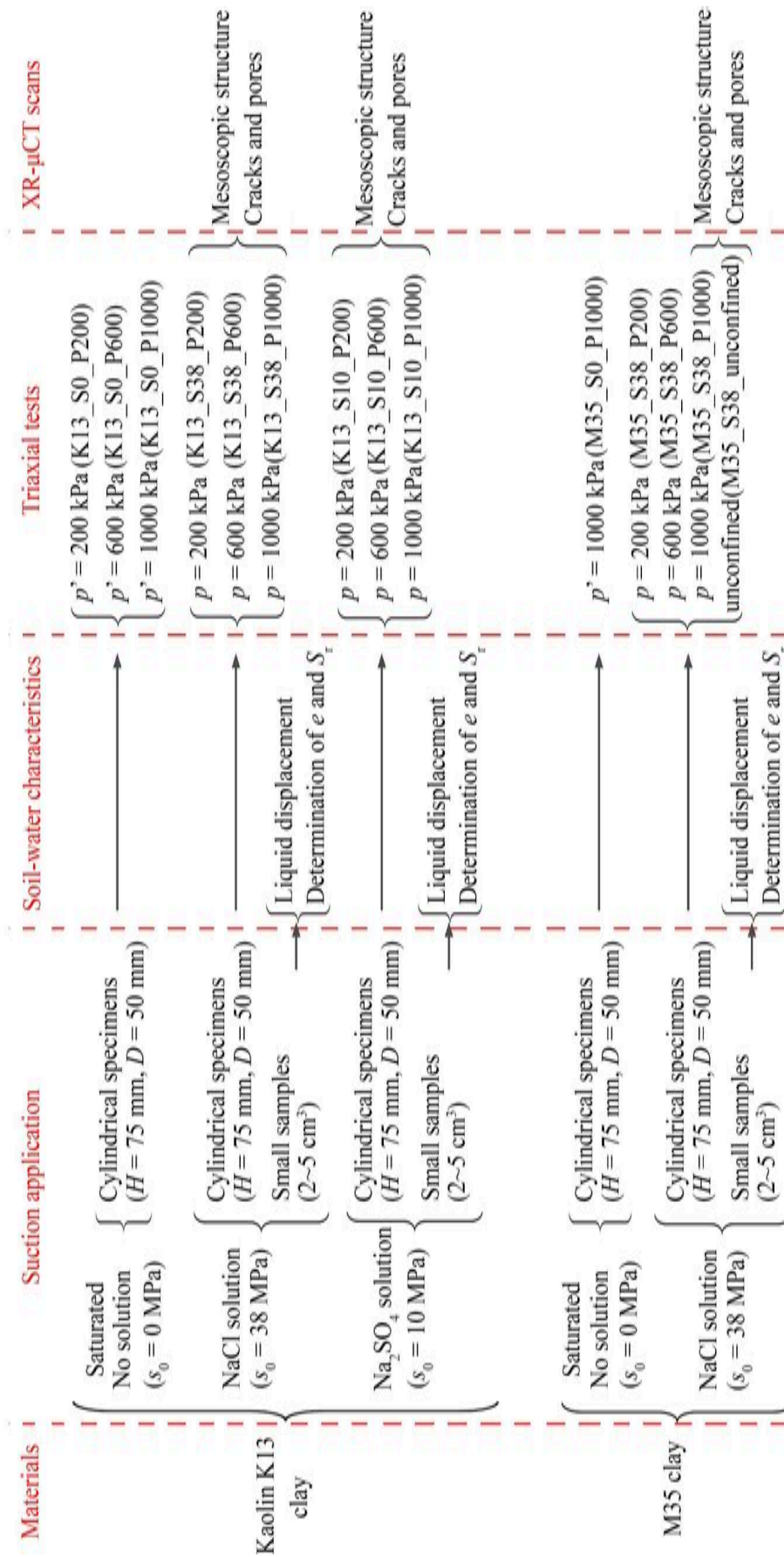


Figure 4.1 Experimental programme for unsaturated clays

## 2. Soil-water characteristics of unsaturated clay

Soil-water characteristic curves (SWCCs) contain the fundamental information needed to describe the mechanical behaviour (e.g., shear strength) of unsaturated soil. In this section, different levels of total suction were imposed on the cylindrical specimens and small samples using the vapour equilibrium method. Once the soil mass and gravimetric water content reached equilibrium under a given total suction in desiccator, the liquid displacement method combined with the oven drying were employed to determine the soil-water characteristic parameters (i.e., water content, void ratio and degree of saturation).

### 2.1 Unsaturated remoulded Kaolin K13 clay

#### 2.1.1 Evolution of water contents on drying path

Figure 4.2 presents the evolution of gravimetric water contents of Kaolin K13 clay specimens inside the desiccators containing two different saturated salt solutions (i.e.,  $\text{Na}_2\text{SO}_4$  solution and  $\text{NaCl}$  solution with the corresponding total suctions of 10 MPa and 38 MPa). Note that in Figure 4.2 “Specimen” represents large cylindrical specimens used for triaxial testing, and “Sample” represents small cubic samples used for soil-water characteristics testing.

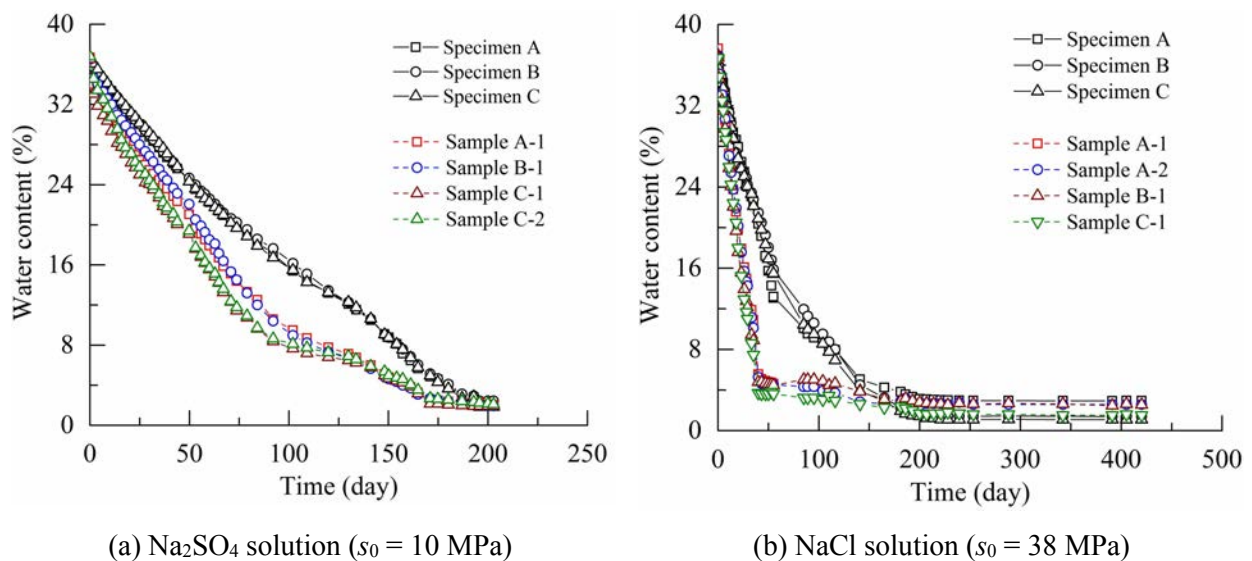


Figure 4.2 Water content evolution of remoulded Kaolin K13 clay

The results show the same tendency for all the specimens: the evolution of water content exhibits first a linear decrease followed by a nonlinear decrease and finally a plateau over the whole drying period. Meanwhile, it is found that the elapsed time to reach equilibrium of water content is generally more than 150 days (i.e., 5 months). Note that the equilibrium phase of the specimens under an initial total suction of 10 MPa is not very long before triaxial tests due to time constraints (Figure 4.2a). However, one can consider that these specimens have reached an acceptably good equilibrium of water contents by comparison with the results of the specimens under an initial total suction 38 MPa (Figure 4.2b) and with those of the M35 clay specimens that will be presented in the following section (Figure 4.6).

Moreover, it is observed in Figure 4.2 that the higher the imposed total suction, the faster the drying especially in the linear evolution phase, and thus the shorter the elapsed time to reach equilibrium of water content. For instance, the elapsed time for all the specimens (including both small and cylindrical ones) to reach equilibrium under the total suction of 10 MPa is about 180 days, while it is approximately 150 days for all the specimens under the higher total suction of 38 MPa. Nevertheless, the influence of total suction on the elapsed time to reach equilibrium is not so significant. This is probably because both levels of total suction are very high. In this case, the influence of the gap between 10 MPa and 38 MPa is not very important.

It should be noted that under the higher total suction of 38 MPa, an open crack is gradually initiated on the top surface of a cylindrical specimen in the linear evolution phase (see Figure 4.3). This is probably due to the uneven shrinkage of the large cylindrical specimen when the drying speed is very high. In fact, as shown in Figure 4.2b, the drying speed of the first phase under the total suction of 38 MPa (i.e., NaCl solution) is markedly larger than that under the total suction of 10 MPa (i.e., Na<sub>2</sub>SO<sub>4</sub> solution). This phenomenon in Figure 4.3 indicates that local cracks may be induced inside the cylindrical specimens of Kaolin K13 clay at a high level of total suction. Because of the apparent crack, the result of this specimen (Figure 4.3) is not included in Figure 4.2b, and this specimen is not used for triaxial testing. However, the remaining specimens may also contain local cracks that are internal and cannot be observed from the outside.

In addition, Figure 4.2 shows that the rate of decrease in water content for small samples is significantly larger than that of large cylindrical specimens. It is particularly true in the case of initial total suction of 38 MPa. This is reasonable since small samples have larger ratios of

surface area to volume and thus are more efficient in exchanging water with air than large cylindrical specimens. Nevertheless, it appears that the water contents at equilibrium are all very close regardless of specimen sizes. It should be noted that the initial water contents presented in Figure 4.2 are not the exact values of clay specimens but determined from small soil offcuts during specimen preparations.

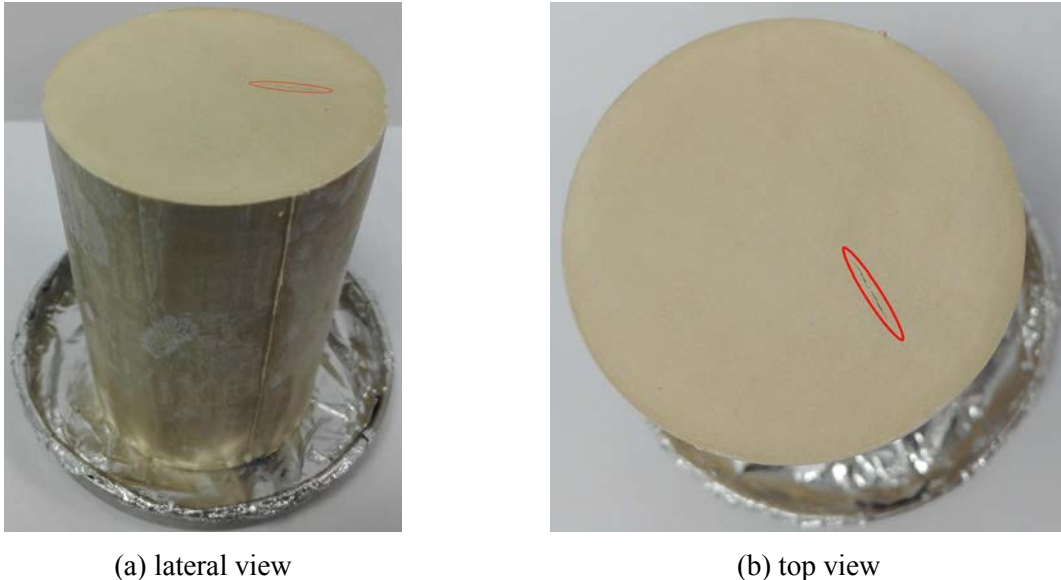


Figure 4.3 Open crack on a cylindrical specimen ( $s_0 = 38$  MPa, NaCl solution)

To sum it up, it is safe to consider that all the clay specimens have achieved good equilibrium of gravimetric water content, and thus, the desired initial total suctions (i.e., 10 MPa or 38 MPa) have been successfully imposed on them.

---

### 2.1.2 Soil-water characteristic curves

---

- *Theoretical and empirical equations*

For any soil, there is a given relationship between the gravimetric water content, the void ratio and the degree of saturation that may be expressed by:

$$S_r = \frac{G_s \cdot w}{e} \quad (4.1)$$

where  $S_r$  is the degree of saturation;  $G_s$  is the specific gravity of the solids;  $w$  is the gravimetric water content;  $e$  is the void ratio.

On a drying path (i.e., a monotonic decrease in  $S_r$  and  $w$ ), the relationship between  $e$  and  $w$  is described by the shrinkage curve (see Figure 4.4). In the saturated state,  $e$  decreases with decreasing  $w$  following the straight saturation line with the slope of  $G_s$ . Then, as  $w$  further decreases, the soil becomes unsaturated. In this case, the rate of decrease in  $e$  slows down and  $e$  gradually tends towards a constant value. The relation between  $e$  and  $w$  is no longer linear in the unsaturated state. The shrinkage limit ( $w_{SL}$ ) is defined as the intersection of the saturation line with the asymptote of the curve of  $w = 0$ . Many researchers have developed different empirical formulas to characterise the whole shrinkage curve. Among those formulas, the three-parameter function proposed by Fredlund et al. (2002) is widely used and has the following form:

$$e = a_0 \left[ \left( \frac{w}{b_0} \right)^{c_0} + 1 \right]^{1/c_0} \tag{4.2a}$$

$$b_0 = \frac{S_{r0} \cdot a_0}{G_s} \tag{4.2b}$$

where  $a_0 = e_{\min}$  is the minimum void ratio;  $b_0$  is a parameter determining the slope of the tangency line (Figure 4.4);  $c_0$  is the curvature of the shrinkage curve;  $S_{r0}$  is the initial degree of saturation.

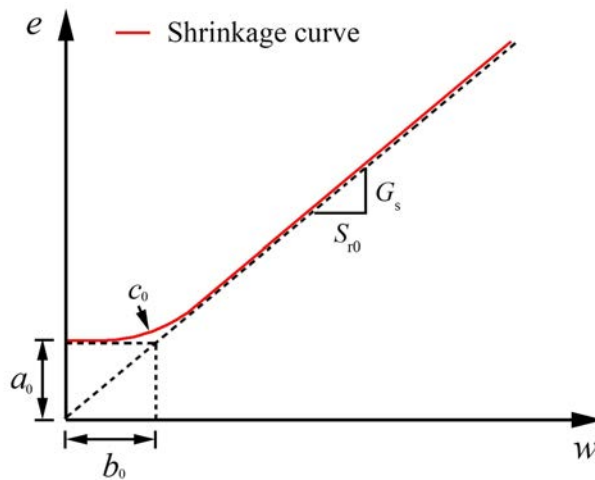


Figure 4.4 Sketch of a typical shrinkage curve

The soil-water characteristic curve is the relationship between the water content and the soil suction, and it is also referred to as the water retention curve. The soil-water characteristic

curve in terms of gravimetric water content can be expressed by the equation proposed by van Genuchten (1980):

$$w = \frac{w_s}{\left\{1 + (s / \alpha^*)^{n^*}\right\}^{1-1/n^*}} \quad (4.3)$$

where  $w_s$  is the saturated gravimetric water content;  $\alpha^*$  and  $n^*$  are model constants.

The van Genuchten model has another form, which expresses the effective degree of saturation as a function of soil suction:

$$S_r^e = \frac{S_r - S_{re}}{1 - S_{re}} = \left\{ \frac{1}{1 + (s / \alpha^*)^{n^*}} \right\}^{1-1/n^*} \quad (4.4)$$

where  $S_r^e$  is the effective degree of saturation;  $S_{re}$  is the residual degree of saturation.

- *Experimental and estimated results*

The soil-water characteristic results (i.e.,  $e-w$  curve,  $w-s$  curve,  $e-s$  curve and  $S_r-s$  curve) of Kaolin K13 clay specimens on drying path are presented in Figure 4.5. Note that we cannot obtain the entire soil-water characteristic curves of the material because only three levels of total suction (i.e., 10 MPa, 38 MPa and 0 MPa in the initial state) are considered in this study. For this reason, the results of Indarto (1991) and Wei (2013) derived from the laboratory tests on Kaolin P300 clay are plotted for comparison purposes. Kaolin P300 is a clay material similar to Kaolin K13 clay regarding mineralogical, physical and mechanical properties, as presented in Chapter 2. The clay specimens of Indarto (1991) were preconsolidated (from slurry with an initial water content of  $1.5 w_L$ ) under a vertical stress of 100 kPa, while those of Wei (2013) were clay pastes with an initial water content of  $w_L$ .

Figure 4.5a shows the shrinkage results of kaolinite clay specimens on the drying path. The dashed curve is estimated from the experimental data of this study based on Equation (4.2). It is observed that the estimated shrinkage curve shows a similar tendency as the results of Indarto (1991). However, the minimum void ratio ( $e_{min}$ ) and the shrinkage limit ( $w_{SL}$ ) of Kaolin K13 clay obtained in this study are respectively 0.68 and 26%, which are larger than those of Kaolin P300 clay reported by Indarto (1991). Furthermore, it is noted that the

estimated shrinkage curve of this study is close to the experimental data of Wei (2013) when  $w$  is larger than 10% while it is quite different from that of Wei (2013) when  $w$  is less than 10%. This is probably due to the void collapses in the paste specimens of Wei (2013) under a very low water content (or a very high suction value), as may be seen from Figure 4.5c.

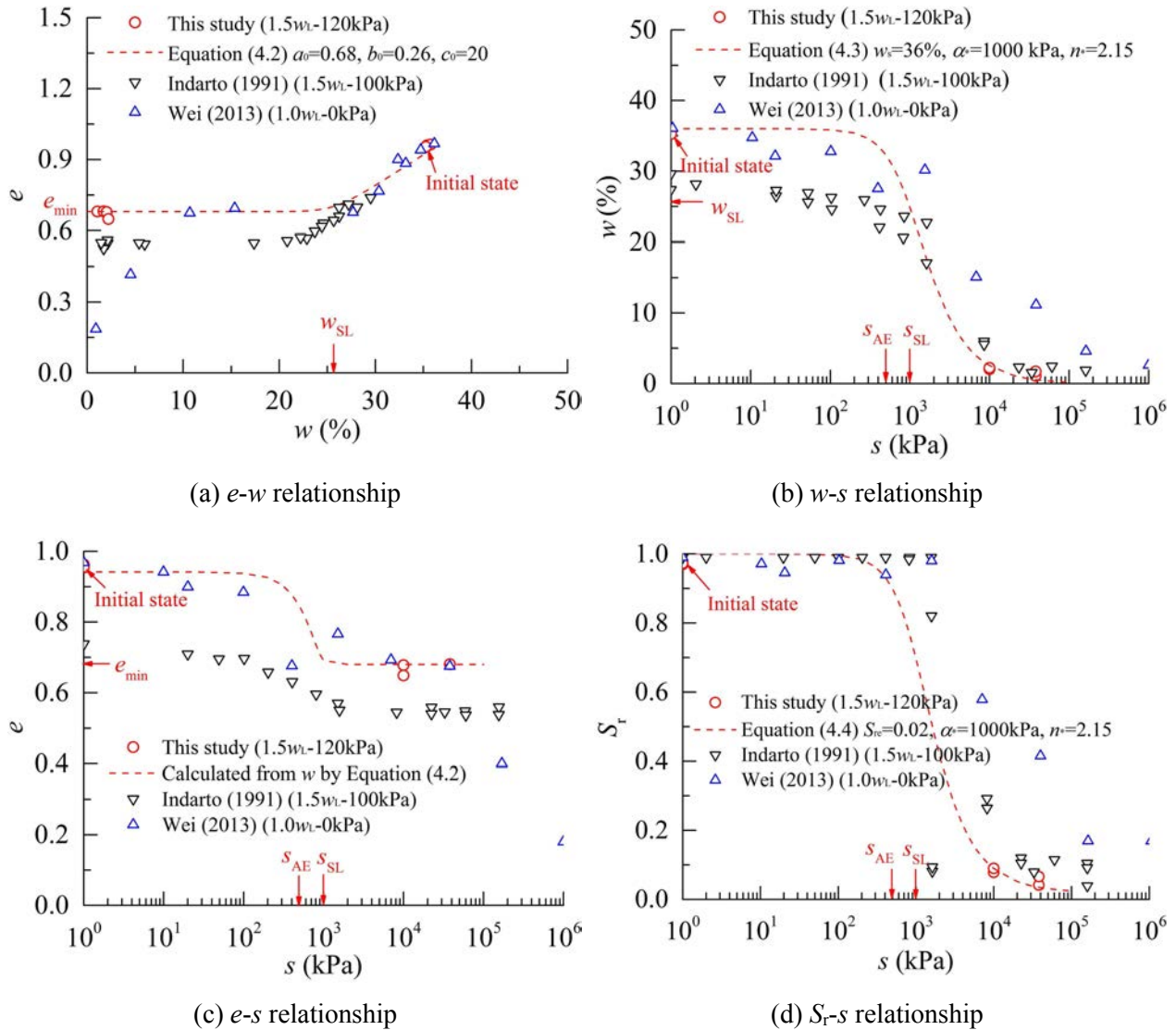


Figure 4.5 Soil-water characteristic curves of remoulded kaolinite clays

Figure 4.5b presents the relationship between water content and total suction. The dashed curve is estimated from the experimental data of this study based on Equation (4.3). The estimated curve shows that on the drying path (with an increase in total suction), the water content first remains almost constant in the quasi-saturated state, then rapidly drops when the total suction exceeds the air-entry suction ( $s_{AE}$ ) of about 500 kPa, and finally tends to a small residual value. However, the experimental results of Indarto (1991) and Wei (2013) indicate that in the quasi-saturated state the water contents are not constant but decrease at a small rate.

In addition, it is observed that the total suction ( $s_{SL}$ ) corresponding to the shrinkage limit of Kaolin K13 clay is about 1000 kPa. At the total suctions of 10 MPa and 38 MPa, the average gravimetric water contents of Kaolin K13 clay specimens are 2.1% and 1.4%, respectively.

Figure 4.5c describes the volume change (i.e., change in void ratio) of the clays during drying. The void ratios calculated from the water contents by Equation (4.2) are also plotted in this figure. One can note that the estimated curve has a similar shape as the normally consolidated compression curve under isotropic loading except for the data at suction levels larger than the shrinkage limit suction ( $s_{SL}$ ), where the void ratio does not go on decreasing. This result is consistent with the results of Indarto (1991). Concerning the data reported by Wei (2013), the void ratio showing a dramatic drop under high suctions, as previously presented, appears related to the void collapses of the paste specimens. One can note that at the total suctions of 10 MPa and 38 MPa, the average void ratios of Kaolin K13 clay specimens are all close to the minimum value, namely 0.68.

Figure 4.5d shows the soil-water characteristic results in terms of degree of saturation. The dashed curve is estimated from the experimental data of this study based on Equation (4.4). The estimated soil-water characteristic curve shows that on drying path the clay remains quasi-saturated until the total suction reaches the air-entry value (i.e.,  $s_{AE} = 500$  kPa), then the degree of saturation rapidly decreases, and finally it tends towards a residual value of about 0.02. It is observed that, under the total suctions of 10 MPa and 38 MPa, the degrees of saturation of this study are slightly smaller than those of Indarto (1991). This is reasonable because the water contents of this study are slightly less than those of Indarto (1991) while the void ratios of this study are larger than those of Indarto (1991). On the other hand, the degrees of saturation of the consolidated clay specimens obtained in this study are significantly less than those of paste specimens reported by Wei (2013). It is noted that at the applied total suctions of 10 MPa and 38 MPa, the average degrees of saturation of Kaolin K13 clay specimens approximate 0.085 and 0.054, respectively.

## **2.2 Unsaturated remoulded M35 clay**

---

### **2.2.1 Evolution of water content on drying path**

---

Figure 4.6 shows the evolution of the gravimetric water contents of M35 clay specimens inside the desiccator containing saturated NaCl solution with the corresponding total suction

of 38 MPa. Similar to Figure 4.2, “Specimen” in this figure represents large cylindrical specimens used for triaxial testing, and “Sample” represents small cubic samples used for soil water characteristic testing.

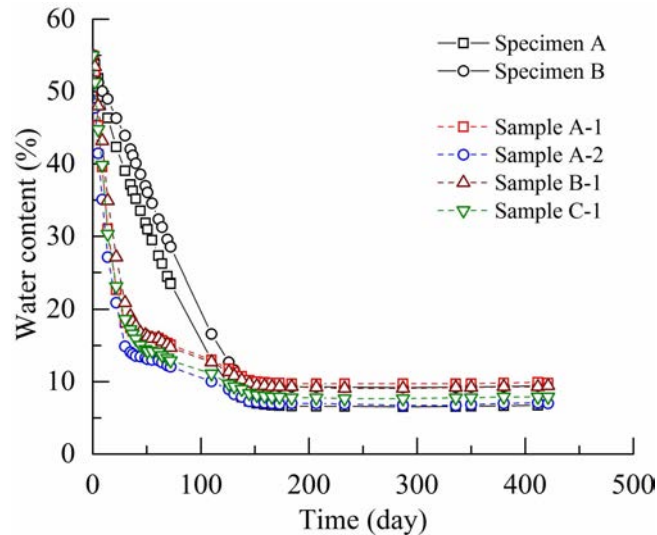


Figure 4.6 Water content evolution of remoulded M35 clay ( $s_0 = 38$  MPa, NaCl solution)

It is observed from Figure 4.6 that the evolution of water contents of M35 clay also shows, as that of Kaolin K13 clay, first a linear rapid decrease followed by a nonlinear slow decrease and finally a plateau over the whole drying period. It is found that the elapsed time for M35 clay to reach the equilibrium of water content is also very long and it is approximately the same as that for Kaolin K13 clay in the case of the same salt solution (i.e., NaCl) (Figure 4.2b). This means that at such a high total suction level (i.e., 38 MPa), the drying speed is not significantly related to the material type. However, compared to the possible development of apparent cracks in cylindrical Kaolin K13 clay specimens, there is no apparent crack observed on the surfaces of cylindrical M35 clay specimens.

Furthermore, one can note that the rate of decrease of the water content of the small samples is considerably larger than that of the large cylindrical specimens. This result of M35 clay is consistent with that of Kaolin K13 clay, as shown in Figure 4.2b. However, it is clearly seen that the elapsed time for the small samples to reach equilibrium of water content is affected by the evolution of water contents of large specimens. This influence is particularly evident in the nonlinear evolution phase. Therefore, the actual elapsed time is almost the same for both small samples and large specimens. In fact, this feature can also be found in Figure 4.2a and b with respect to remoulded Kaolin K13 clay under total suctions of 10 MPa and 38 MPa.

In addition, the results in Figure 4.6 show that the water contents at equilibrium have similar values regardless of specimen sizes. These findings are also in good agreement with the previous results of Kaolin K13 clay. From Figure 4.6, it is reasonable to consider that both small samples and large cylindrical specimens of M35 clay have attained good equilibrium of water contents. Therefore, the imposition of initial total suctions (i.e., 38 MPa) has been stopped, considering that these specimens are ready for soil-water characteristic testing and triaxial testing.

---

### 2.2.2 Soil-water characteristic curves

---

Figure 4.7 presents the soil-water characteristic results (i.e.,  $e-w$  curve,  $w-s$  curve,  $e-s$  curve and  $S_r-s$  curve) of M35 clay specimens on drying path. Since only two levels of total suction (i.e., 38 MPa and 0 MPa in the initial state) are considered in this section, it is not possible to obtain the entire soil-water characteristic curves of the material. For this reason, the experimental data obtained by Wei (2013) and Wei et al. (2016) on M35 clay are also plotted for comparison. Notice that the specimens employed by Wei (2013) and Wei et al. (2016) were clay pastes with initial water contents of  $w_L$ .

The shrinkage results of M35 clay are presented in Figure 4.7a. The dashed curve is estimated from the experimental data of this study based on Equation (4.2). The estimated shrinkage curve coincides with the results of Wei (2013) and Wei et al. (2016) although different specimen preparation methods are employed. It is noted that the void ratio decreases with decreasing water content down to the shrinkage limit ( $w_{SL}$ ) of about 20%, after which the void ratio remains at the minimum value ( $e_{min}$ ) of about 0.55. Compared with Kaolin K13 clay (Figure 4.5a), it appears that M35 clay has smaller shrinkage limits as well as smaller minimum void ratios.

Figure 4.7b illustrates the evolution of water content with increasing total suction. The estimated curve of this study using Equation (4.3) shows that the water content first remains almost constant until the total suction reaches the air-entry value ( $s_{AE} = 1000$  kPa), then significantly decreases, and finally exhibits a tendency towards a small residual value. However, the results of Wei (2013) and Wei et al. (2016) exhibit no evident constant phase of water contents at the beginning of drying for both paste specimens of Kaolin P300 clay (Figure 4.5b) and M35 clay (Figure 4.7b). This phenomenon seems to be related to the specimen type. It is observed that at the total suction of 38 MPa, the average gravimetric

water content of M35 clay specimens is about 6.5%, which is significantly larger than that of Kaolin K13 clay (i.e., 1.4%) under the same conditions.

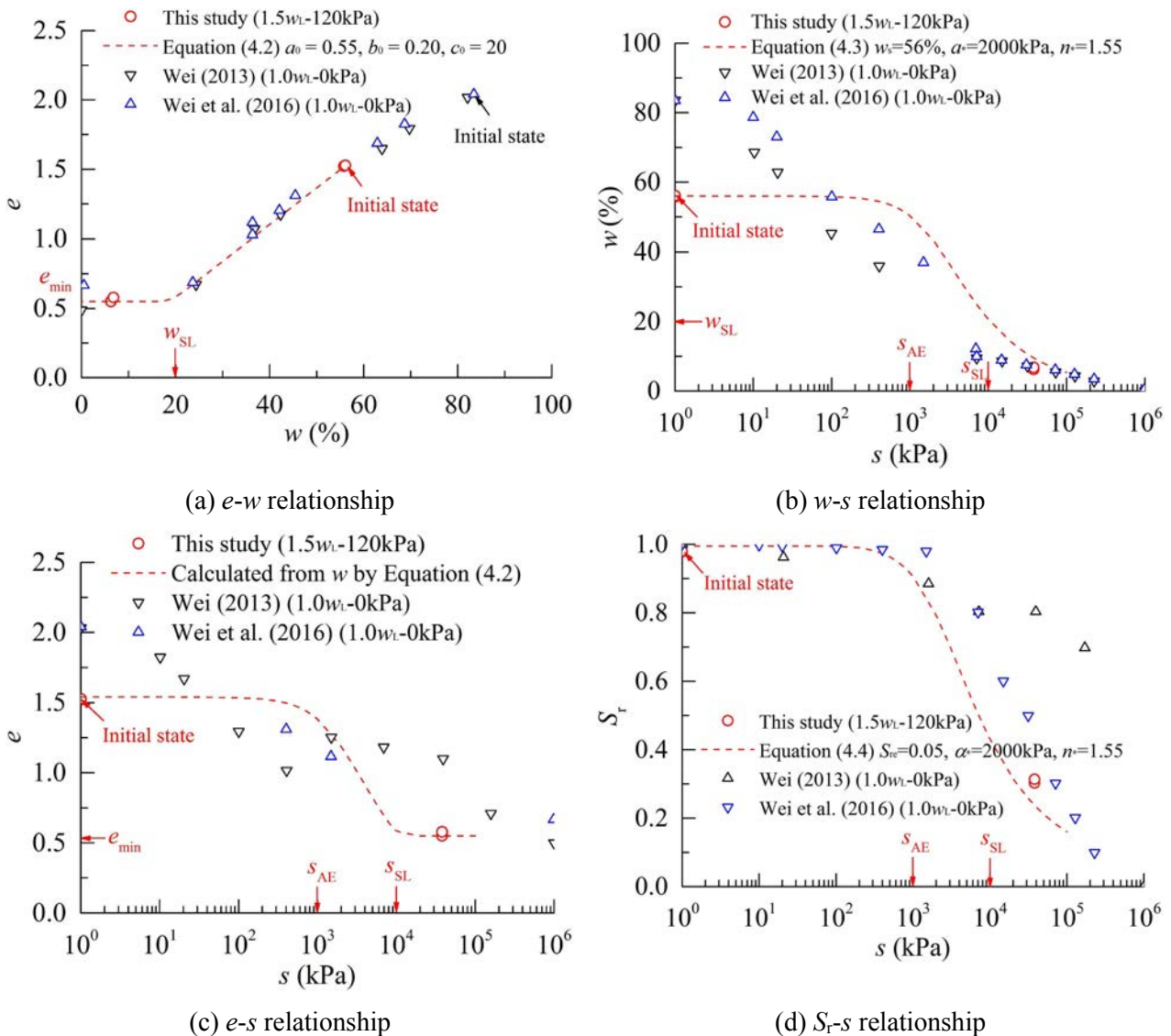


Figure 4.7 Soil-water characteristic curves of remoulded M35 clays

The compressibility behaviour of M35 clay on drying path is depicted in Figure 4.7c. It is noted from estimated curve that the evolution of void ratio begins with a slight decrease followed by a rapid decrease and finally a plateau as the total suction increases. Nevertheless, the estimated curve of this study is greatly different from the results of Wei (2013) and Wei et al. (2016). This is probably because the specimens employed in this study are preconsolidated materials while those of Wei (2013) and Wei et al. (2016) are clay pastes.

Figure 4.7d presents the change in the degree of saturation with increasing total suction. The dashed curve is estimated from the experimental data of this study based on Equation

(4.4). The estimated curve shows a similar tendency as the results of Wei et al. (2016). The degree of saturation first remains almost constant and then dramatically decreases as the total suction becomes larger than the air-entry value ( $s_{AE} = 1000$  kPa). However, one can note that the measured data of this study are located below the results of Wei et al. (2016) and particularly those of Wei (2013). It is observed that at the total suction of 38 MPa, the measured degree of saturation of M35 clay is approximately 0.308, which is considerably larger than the corresponding value of Kaolin K13 clay (Figure 4.5d).

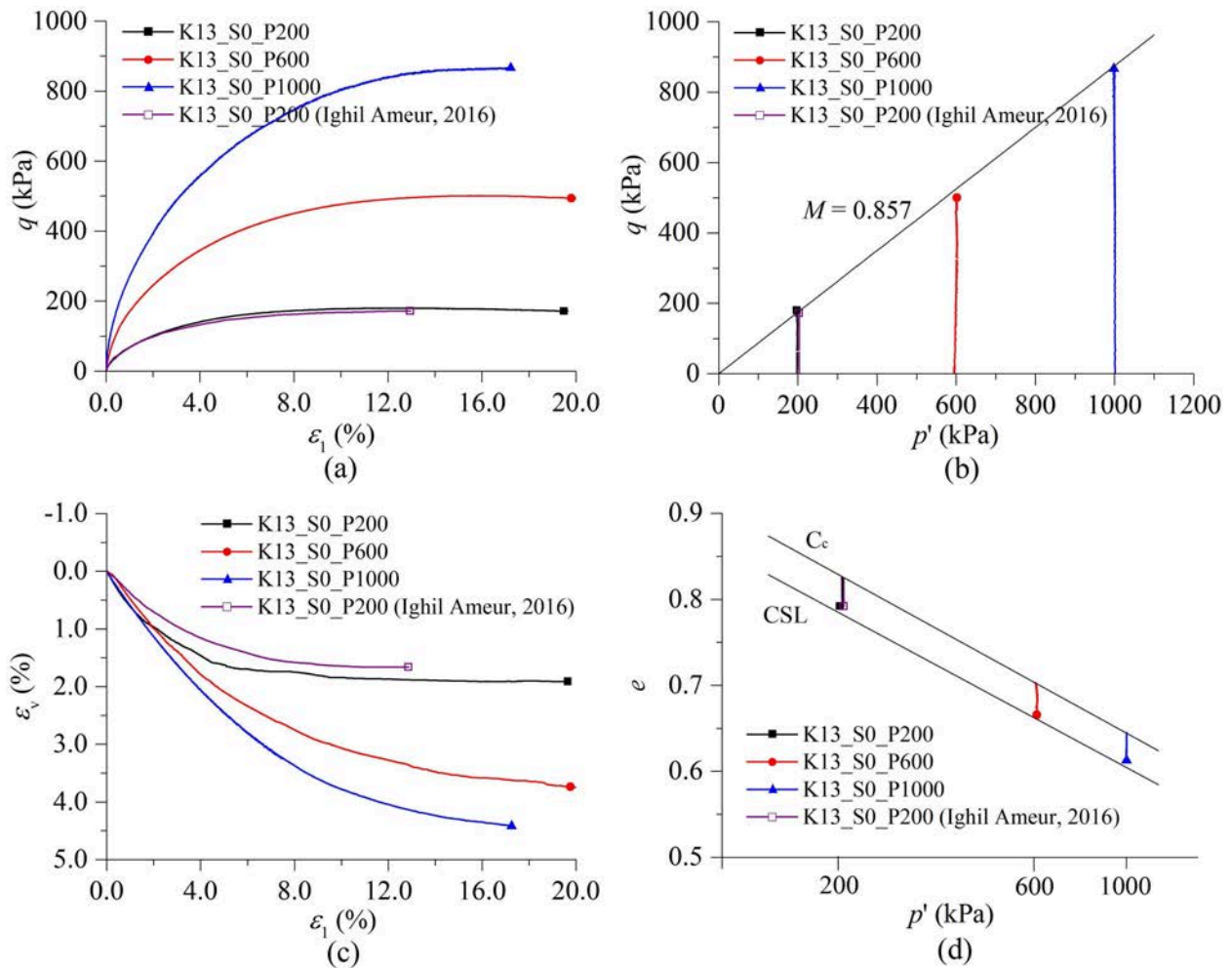
### 3. Mechanical behaviour of remoulded Kaolin K13 clay

#### 3.1 Saturated test results affected by mean effective stress

- *Mechanical results*

Figure 4.8 presents the mechanical results of saturated consolidated drained triaxial tests on remoulded Kaolin K13 clay under different mean effective stresses (i.e., 200 kPa, 600 kPa and 1000 kPa) on the purely deviatoric stress path. The clay specimens are all fully saturated and in the normally consolidated states. For comparison purposes, the results of a consolidated drained triaxial test performed by Ighil Ameer (2016) on the same clay material under the constant mean effective stress of 200 kPa were also plotted in this figure.

One can note from Figure 4.8a that the stress-strain relationship (i.e., specimen K13\_S0\_P200) of this study is consistent with that obtained by Ighil Ameer (2016) under the same triaxial loading condition. It is also observed that the deviatoric stresses of all specimens increase with the increase in axial strains, exhibiting evident non-linearity and strain-hardening behaviour. Furthermore, both the soil stiffness and shear strength significantly increase with the increase in the mean effective stress. For example, at the mean effective stress of 200 kPa, the maximum slope of the stress-strain curve is relatively small, and the peak deviatoric stress is about 180 kPa; by contrast, at the mean effective stress of 1000 kPa, the maximum slope of the stress-strain curve is clearly large, and the peak deviatoric stress reaches a value as high as around 860 kPa.



(a)  $(\epsilon_1, q)$  plane; (b)  $(p', q)$  plane; (c)  $(\epsilon_1, \epsilon_v)$  plane; (d)  $(\log p', e)$  plane

Figure 4.8 Behaviour of saturated Kaolin K13 clay under various mean effective stresses

Figure 4.8b shows the stress paths in the  $(p', q)$  plane during triaxial loading. It is found that all the tests follow exactly the desired purely deviatoric stress paths, namely the mean effective stress remains constant while the deviatoric stress increases. The slope of the critical state line is  $M = 0.857$ , and the corresponding effective angle of internal friction is  $22.0^\circ$ , which are in agreement with the results presented in Chapter 3. The curves of volumetric strain versus axial strain presented in Figure 4.8c demonstrate that the results of this study are in agreement with those of Ighil Ameer (2016). It is noted that all the clay specimens are contractive throughout the tests, and the maximum volumetric deformation increases with increasing mean effective stress. Figure 4.8d illustrates the evolution of void ratios of clay specimens during triaxial loading. It shows that the void ratios of all the specimens decrease from the compression line (with slope of  $C_c$ ) downwards to approach the critical state line (CSL) in the  $(\log p', e)$  plane.

- *Failure modes of specimens*

Figure 4.9 presents the photographs of the initial shapes of specimens and the failure modes of two specimens (i.e., K13\_S0\_P200 and K13\_S0\_P600) under the mean effective stresses of 200 kPa and 600 kPa, respectively.

It is observed that both clay specimens fail with single inclined shear planes across the top and bottom surfaces. The clay specimens are highly compressed in the axial direction while expanded in the lateral direction after triaxial loading. Moreover, these specimens are more or less in barrel-shapes, although this is not so significant because of the use of anti-friction devices at the specimen ends during triaxial shearing. The failure modes of saturated remoulded Kaolin K13 clay specimens are consistent with those reported by Ighil Ameer (2016) under similar loading conditions.

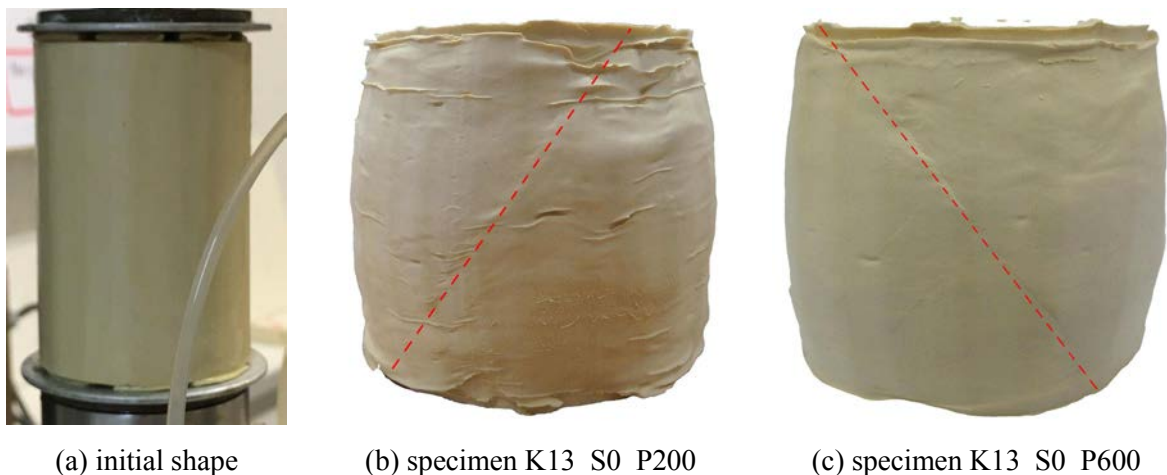


Figure 4.9 Failure modes of saturated remoulded Kaolin K13 clay

### 3.2 Unsaturated test results affected by mean stress

#### 3.2.1 Under initial total suction of 38 MPa

- *Initial total suction*

As presented in Chapter 2, prior to triaxial tests, all the accessories and devices (e.g., filter papers, porous disks, rubber membrane and anti-friction devices) in triaxial cell are placed in the desiccator to reach the same initial total suction as the specimen. Furthermore, in order to examine if the target value (i.e., 38 MPa) of initial total suction is successfully imposed on the cylindrical clay specimen, the hygrobuttons are started to measure the relative humidity in the

desiccator. After a new equilibrium of relative humidity in the desiccator, the specimen and hygrobuttons are installed in the triaxial cell for mechanical tests.

Figure 4.10 presents the evolution of measured relative humidities and calculated total suctions of a Kaolin K13 clay specimen before mechanical loading. It is observed that the initial relative humidity and total suction approximate their target values (i.e., 76% and 38 MPa) in the desiccator. During the process of specimen installation, the relative humidity shows a significant drop, and the total suction shows a great increase affected by laboratory environment (the relative humidity is 50%). However, the variations in both relative humidity and total suction recover in a few hours after the sealing of specimen in the triaxial cell. Furthermore, one can note that the measured relative humidity around the top end of the clay specimen is slightly larger than that around the bottom end, and this leads to the difference of about 1 MPa in calculated total suctions. However, this difference is negligible compared to the target value of total suction (i.e., 38 MPa). Therefore, it is considered that the target total suction is successfully imposed on this specimen.

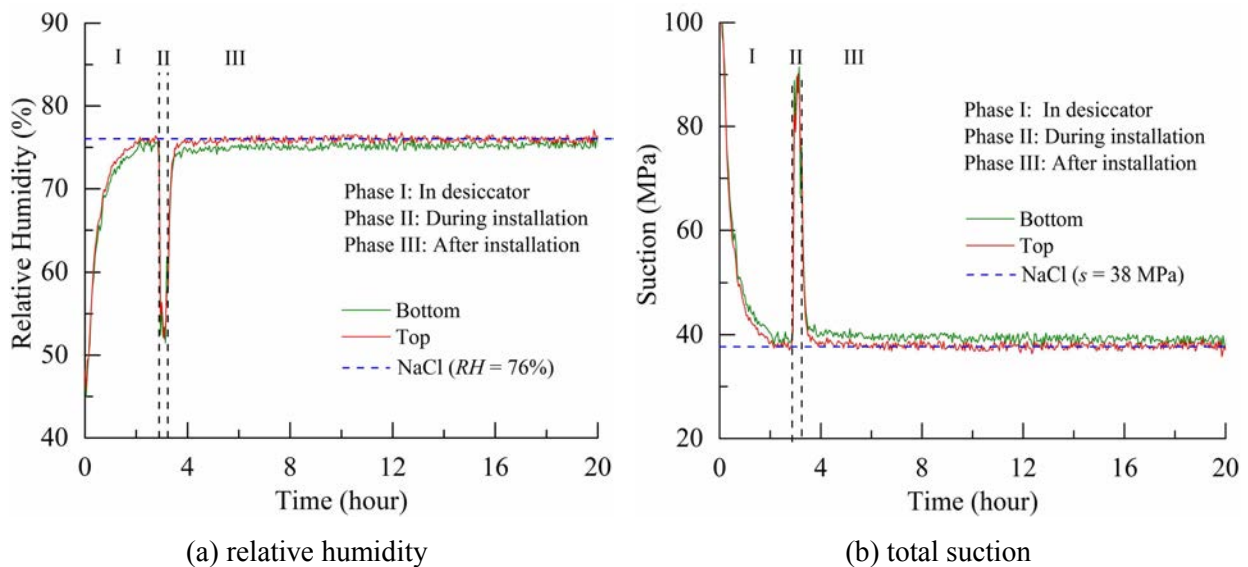
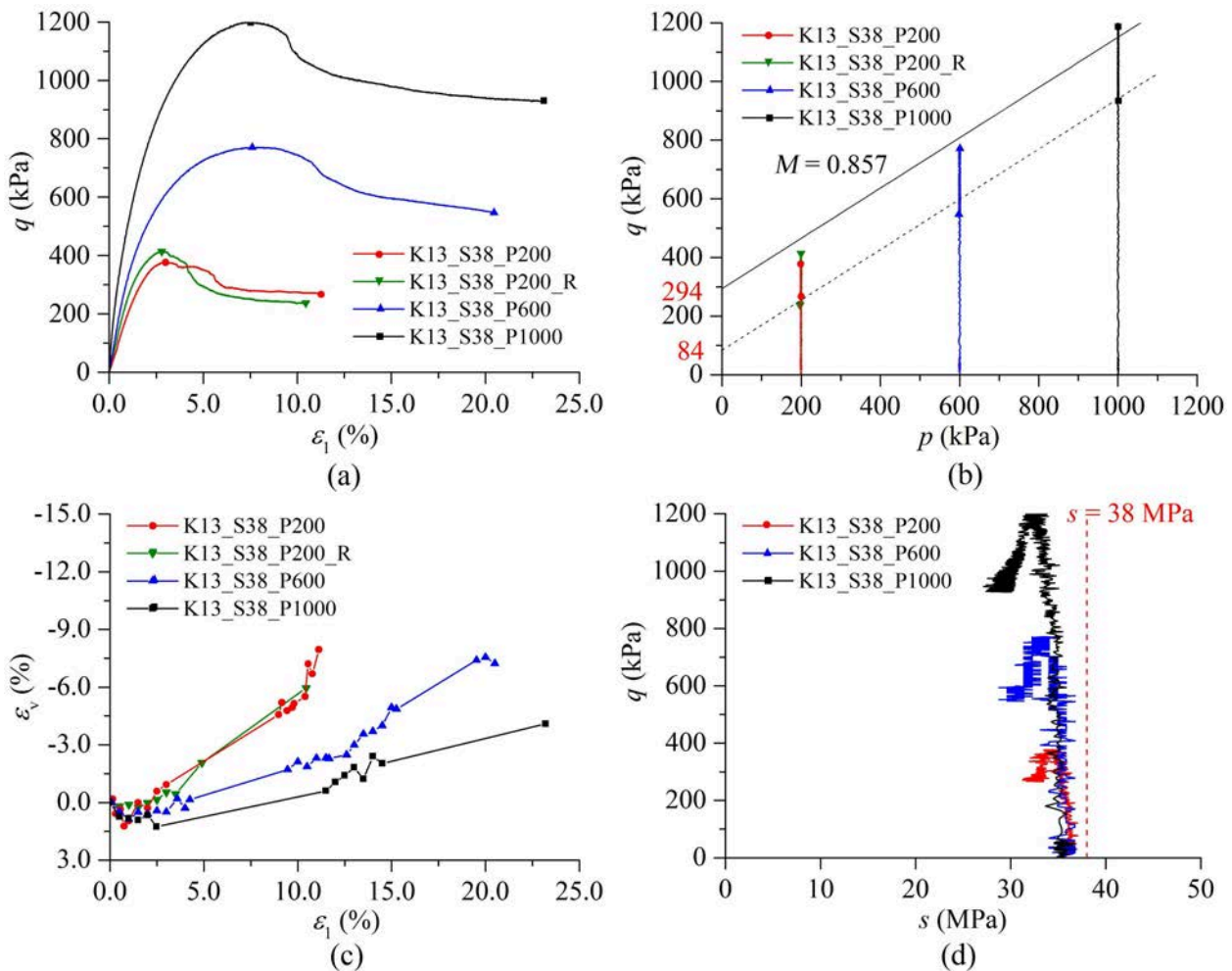


Figure 4.10 Relative humidity and total suction (Kaolin K13, NaCl) before triaxial tests

- *Mechanical results*

Figure 4.11 presents the results of unconsolidated undrained triaxial compression tests on unsaturated remoulded Kaolin K13 clay with an initial total suction of 38 MPa under different mean stresses (i.e., 200 kPa, 600 kPa and 1000 kPa). The data of a repeated test (i.e., K13\_S38\_P200\_R) under the mean stress of 200 kPa is also included to verify the obtained mechanical results. It shows that the mechanical behaviour of two specimens (i.e.,

K13\_S38\_P200 and K13\_S38\_P200\_R) is in good agreement, indicating the rationality and reproducibility of the test results.



(a) ( $\epsilon_1, q$ ) plane; (b) ( $p, q$ ) plane; (c) ( $\epsilon_1, \epsilon_v$ ) plane; (d) ( $s, q$ ) plane

Figure 4.11 Mechanical behaviour of unsaturated Kaolin K13 clay under  $s_0 = 38$  MPa

It is observed in Figure 4.11a that in all cases, the deviatoric stress first monotonically rises up to a peak and then decreases down to a certain residual value with the increase in axial strain. This means that the stress-strain relationship exhibits strain-softening behaviour. Meanwhile, the results indicate that brittle failure occurs when the mean stress of a specimen is significantly low compared to the initial total suction value. Furthermore, one can note that the soil stiffness, the maximum shear strength and the residual shear strength considerably increase with the increase in mean stress. For example, regarding the specimen K13\_S38\_P200 under a mean stress of 200 kPa, the maximum shear strength and residual shear strength are about 413.5 kPa and 237.0 kPa, respectively; however, for the specimen K13\_S38\_P1000 under a mean stress of 1000 kPa, the maximum shear strength rises up to

1200.2 kPa, and the residual shear strength approximates 928.5 kPa. Therefore, it is deduced that the shear strength behaviour of an unsaturated clay specimen is greatly dominated by the applied mean stress.

Figure 4.11b illustrates the actual stress paths in the  $(p, q)$  plane of clay specimens during triaxial loading. The equation of the shear strength envelope of unsaturated remoulded clay can be expressed by:

$$q = c^* + p \cdot M \quad (4.5)$$

$$M = \tan \varphi^* = \frac{6 \sin \varphi}{3 - \sin \varphi} \quad (4.6a)$$

$$c^* = \frac{6 \cos \varphi}{3 - \sin \varphi} \cdot c \quad (4.6b)$$

where  $c^*$  and  $\varphi^*$  are respectively the apparent cohesion and angle of internal friction defined in the  $(p, q)$  plane (Figure 4.11b);  $M$  is the slope of the critical state line;  $c$  and  $\varphi$  are respectively the classical cohesion and angle of internal friction defined in the  $(\sigma, \tau)$  plane.

Since the variation in the angle of internal friction with suction is relatively minor (Alonso et al., 1990; Wheeler and Sivakumar, 1995), it is assumed in this research that the critical state line has a constant slope under different total suction values. In addition, the apparent angle of internal friction is considered equal to the effective angle of internal friction of saturated clay (e.g.,  $\varphi^* = 40.6^\circ$  or  $\varphi = 22.0^\circ$  see Figure 4.8b). Therefore, the apparent cohesion is the only variable in Equation (4.5). The obtained shear strength parameters are given in Figure 4.11b. One can note that the apparent cohesions ( $c^*$ ) are 294 kPa and 84 kPa corresponding to the maximum shear strength and the residual shear strength, respectively. This indicates that the application of total suction greatly increases the shear strength of remoulded clay mainly by increasing the cohesion.

Figure 4.11c illustrates the evolution of volumetric strains of unsaturated clay specimens. Generally, no volume change would be observed during unconsolidated undrained triaxial tests on saturated clays because of no drainage of water. However, in the case of unsaturated clays with high total suctions, the volumetric deformation happens due to the compression of air and the appearance of cracks and shear bands although no water and air drainages are

allowed. It is observed from Figure 4.11c that all the specimens first show slight contractive behaviour and then evident dilative behaviour (dilation is plotted here as negative in volumetric strain). It seems that the first contraction is related to the compression of pore air and the subsequent dilation is related to the development of cracks and shear band.

Figure 4.11d presents the evolution of total suction during triaxial loading. Notice that the total suctions given here are the average values of the measured data around the top surfaces and the bottom surfaces of clay specimens. The total suctions at the beginning of triaxial shearing are generally less than the initial target values because of the applied isotropic loading. One can note that the measured total suctions of all specimens go on decreasing as the deviatoric stress increases.

- *Failure modes of specimens*

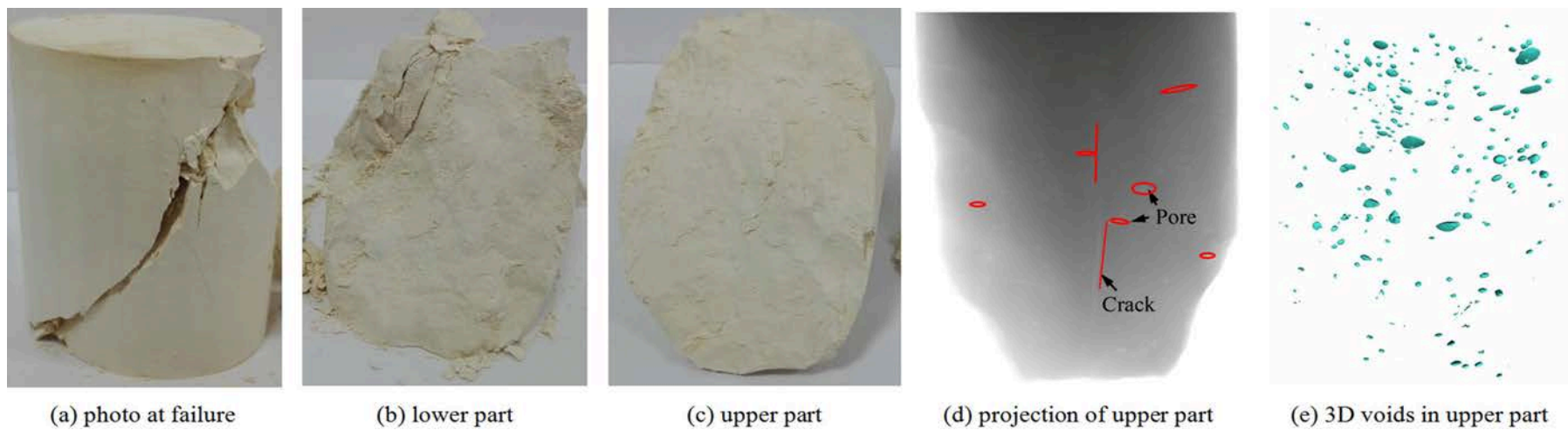
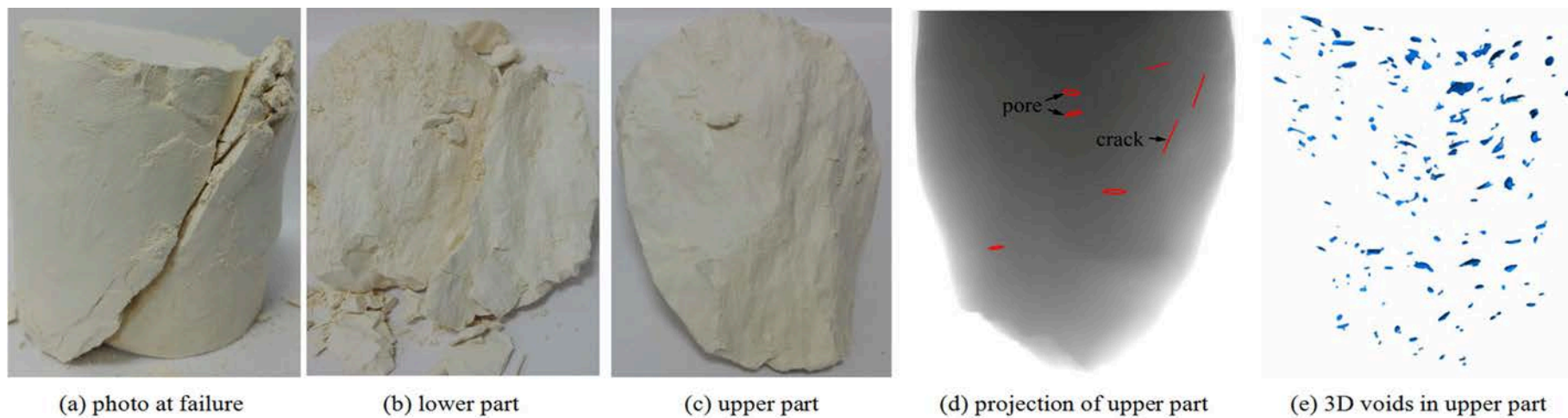
Figures 4.12-4.14 present the photographs of unsaturated remoulded Kaolin K13 clay specimens after triaxial loading under an initial total suction of 38 MPa and different mean stresses, as well as the XR- $\mu$ CT images (e.g., projections and 3D void space) of the upper parts of clay specimens separated by shear bands.

It is observed that all clay specimens are completely split into two parts by single shear planes and exhibit no evident barrel-shaped deformations. The shear plane of the clay specimen (e.g., K13\_S38\_P200 see Figure 4.12a) under a low mean stress is a little bit tortuous while it is relatively flat for the specimen (e.g., K13\_S38\_P1000 see Figure 4.14a) under a high mean stress. The clear slippage marks (Figures 4.12b and c, 4.13b and c, 4.14b and c) on the surfaces of all shear planes indicate the relative movement of two specimen parts after the failure of specimens. For this reason, a more evident dilative behaviour is observed in the clay specimen K13\_S38\_P200 under triaxial shearing due to the stronger interlocking, as shown in Figure 4.11c. This phenomenon is similar to that observed in overconsolidated saturated clay, meaning that the smaller the mean stress, the more pronounced the dilation.

Furthermore, from the CT projections, one can note a few cracks in all clay specimens after triaxial loading and the distribution of cracks seems related to the level of mean stresses. Two evident open vertical cracks with the length of about 15 mm and several small vertical and tilted cracks appear in the upper part of specimen K13\_S38\_P200; a few tilted cracks take place in the upper part of specimen K13\_S38\_P600; and an evident open horizontal crack

with the length of about 10 mm and several small horizontal and tilted cracks are exhibited in the upper part of specimen K13\_S38\_P1000.

In addition, many mesoscale pores (whose sizes are larger than 0.06 mm) are observed in all clay specimens (see Figures 4.12e, 4.13e and 4.14e). The 3D image analyses show that the total volumes of mesoscale pores are 48.5 mm<sup>3</sup>, 42.5 mm<sup>3</sup> and 6.4 mm<sup>3</sup> under mean stresses of 200 kPa, 600 kPa and 1000 kPa, respectively. This indicates that the void volume and void size in unsaturated remoulded clay decreases with the increase in mean stress. Furthermore, the average ratios of surface area to volume of the mesoscale pores in specimens K13\_S38\_P200, K13\_S38\_P600 and K13\_S38\_P1000 are respectively 26.6 mm<sup>-1</sup>, 29.6 mm<sup>-1</sup> and 47.7 mm<sup>-1</sup>. It is also observed that most of the pores particularly those with large sizes away from the shear plane rotate towards the horizontal plane, which is perpendicular to the major principal stress direction. These horizontal-oriented pores seem to be developed in the pre-consolidation stage (before the application of suctions). It indicates that the suction has little influence on the orientation of mesoscale pores.

Figure 4.12 Photographs and XR- $\mu$ CT images of specimen K13\_S38\_P200Figure 4.13 Photographs and XR- $\mu$ CT images of specimen K13\_S38\_P600

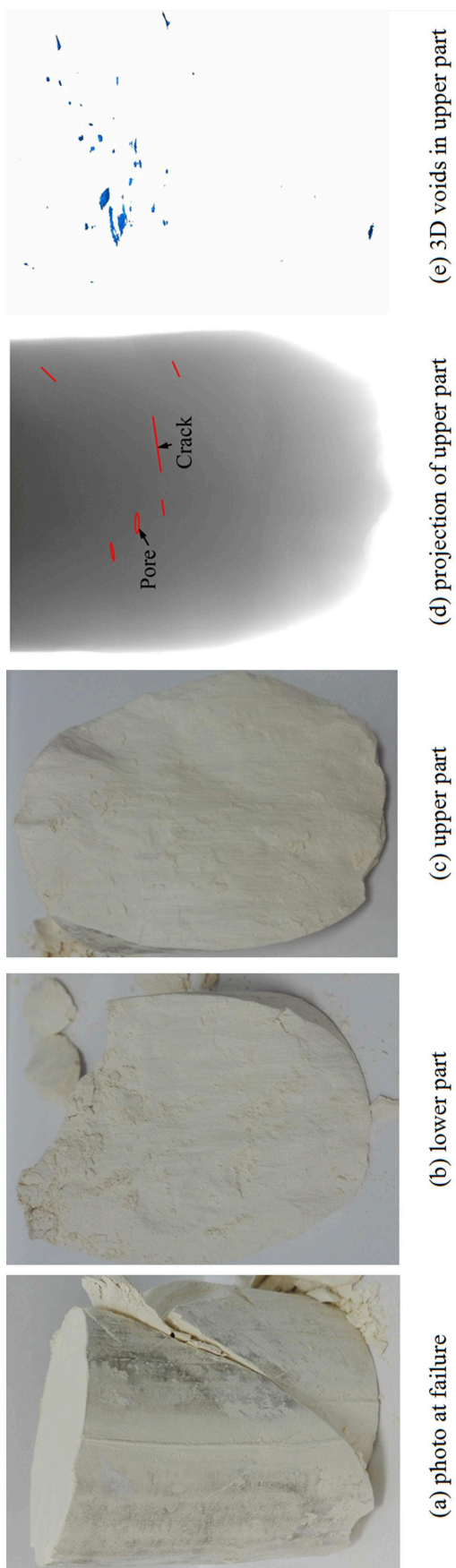


Figure 4.14 Photographs and XR- $\mu$ CT images of specimen K13\_S38\_P1000

## 3.2.2 Under initial total suction of 10 MPa

- *Initial total suction*

Figure 4.15 presents the evolution of measured relative humidities and calculated total suctions of a Kaolin K13 clay specimen in the atmosphere of saturated  $\text{Na}_2\text{SO}_4$  solution during the period from being in the desiccator to the beginning of mechanical loading.

One can note that both the relative humidity and total suction approximate the target values (93% and 10 MPa) corresponding to saturated  $\text{Na}_2\text{SO}_4$  solution in the desiccator. Similar to the case of saturated  $\text{NaCl}$  solution (Figure 4.10), the relative humidity significantly drops to about 50% (which is the controlled value of the laboratory), and the total suction considerably increases during the process of specimen installation. After the installation of specimen and hygrobuttons, both relative humidity and total suction show a tendency to reach the initial values. Notice that the full recovery of relative humidity and total suction is very hard and takes very long time; however, two hours are generally enough for the relative humidity and total suction to approximately achieve the initial values with differences of less than 5%. Therefore, it is reasonable to consider that this clay specimen is properly imposed with target total suction and thus is ready for triaxial testing.

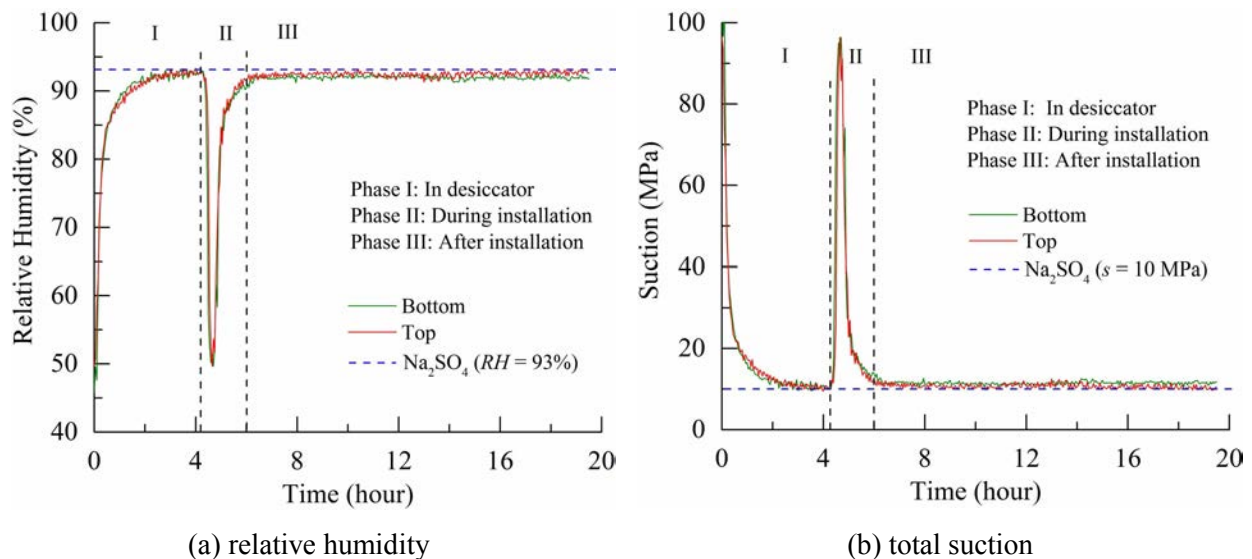


Figure 4.15 Relative humidity and total suction (Kaolin K13,  $\text{Na}_2\text{SO}_4$ ) before triaxial loading

- *Mechanical results*

Figure 4.16 shows the mechanical results of unsaturated remoulded Kaolin K13 clay under

an initial total suction of 10 MPa and different mean stresses (i.e., 200 kPa, 600 kPa and 1000 kPa). One can notice from Figure 4.16a that the deviatoric stress of all the clay specimens shows first a significant increase followed by a slight decrease and finally a plateau with increasing axial strain. Moreover, it is noted that the larger the mean stress, the larger the soil stiffness, the maximum shear strength and the residual shear strength. For instance, the maximum shear strength and the residual shear strength are respectively about 592.2 kPa and 369.0 kPa for the specimen K13\_S10\_P200 under a mean stress of 200 kPa, whereas they are about 1261.4 kPa and 946.1 kPa, respectively, for the specimen K13\_S10\_P1000 under a mean stress of 1000 kPa. This result indicates that the shear strength behaviour of an unsaturated clay specimen is highly dependent on the applied mean stress. The above findings on unsaturated remoulded Kaolin K13 clay under an initial total suction of 10 MPa are consistent with the triaxial tests results of the same material under a higher initial total suction of 38 MPa (see Figure 4.11).

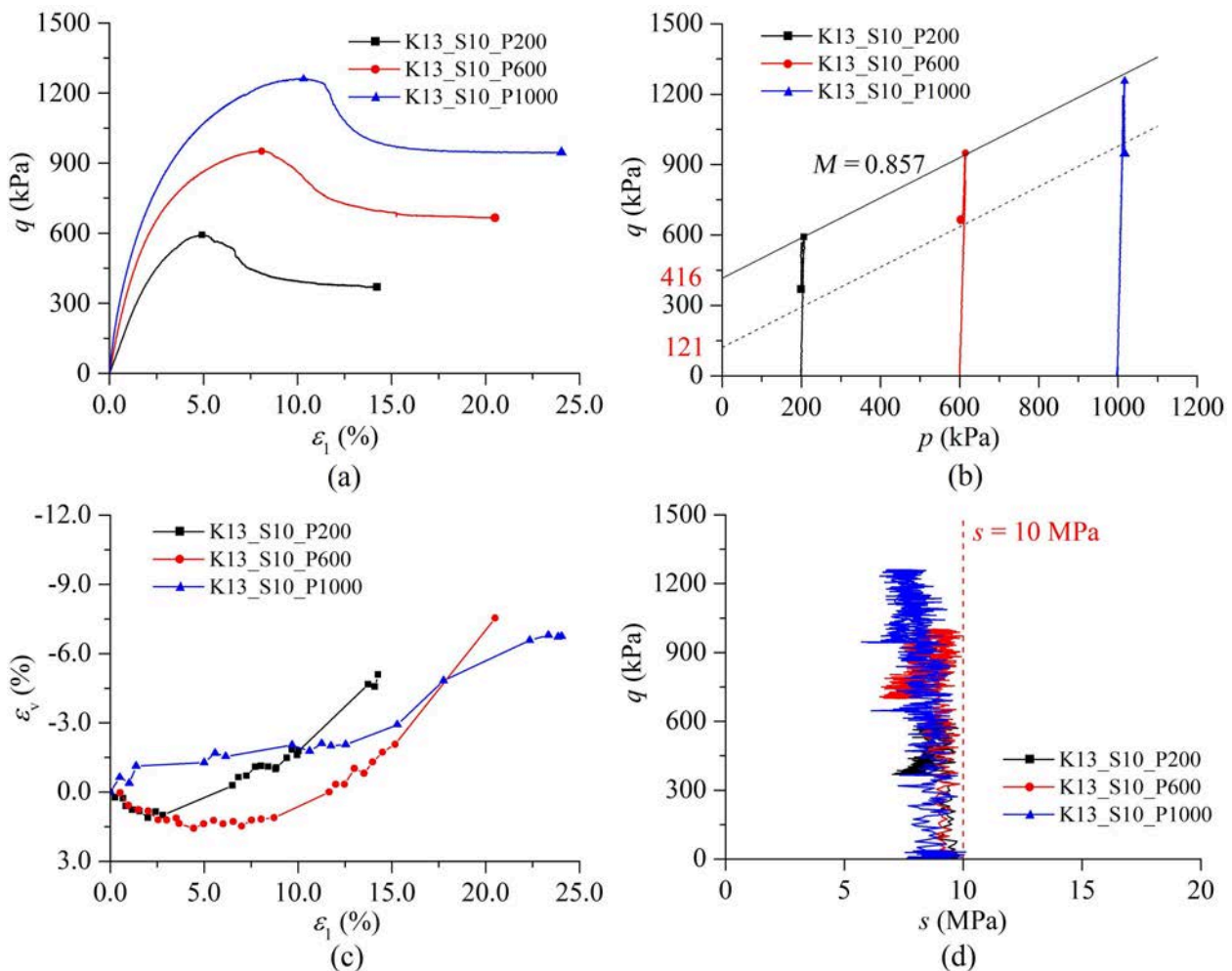


Figure 4.16 Mechanical behaviour of unsaturated Kaolin K13 clay under  $s_0 = 10$  MPa

Figure 4.16b illustrates the stress paths of the unsaturated remoulded Kaolin K13 clay with an initial total suction of 10 MPa. One can note that these specimens are sheared exactly following the desired purely deviatoric stress paths. It is also assumed in this section that the critical state line has a constant slope identical to that of saturated clay and the apparent angle of internal friction is equal to the effective angle of internal friction of saturated clay (i.e.,  $\phi^* = 40.6^\circ$  or  $\phi = 22.0^\circ$ ). With this in mind, one may obtain the apparent cohesions by fitting the experimental data with Equation (4.5). The shear strength parameters are presented in Figure 4.16b. It can be seen that the apparent cohesions ( $c^*$ ) corresponding to the maximum shear strength and the residual shear strength are 416 kPa and 121 kPa, respectively.

Figure 4.16c depicts the evolution of volumetric strains of unsaturated clay specimens with the increase in axial strains. One can note that after triaxial loading, all the clay specimens under the initial total suction of 10 MPa show clear dilative behaviour (i.e., negative volumetric strains) regardless of mean stresses. However, a short period of contraction is observed before the appearance of dilation for the clay specimens except for specimen K13\_S10\_P1000, which exhibits a dilative behaviour nearly from the beginning of shearing. In addition, unlike the finding of the specimens with an initial total suction of 38 MPa (Figure 4.11c) showing the specimen under a higher mean stress is less dilative, the specimen K13\_S10\_P1000 shows a more evident dilation than the specimen K13\_S10\_P600. This is probably due to the limitation and error of the 2D photographic technique for volumetric strain measurement.

Figure 4.16d illustrates the evolution of average total suctions around the clay specimen ends during triaxial shearing. It can be seen from Figure 4.16d that the total suction decreases slightly as the axial strain increases, and this tendency persists until the end of tests in all experimental cases. However, compared to the initial total suction (i.e., 10 MPa), the drop in total suction is relatively small.

- *Failure modes of specimens*

Figures 4.17-4.19 present the XR- $\mu$ CT projections of unsaturated Kaolin K13 clay specimens with an initial total suction of 10 MPa before and after triaxial tests and the photographs of the clay specimens at failure.

It is observed that, before triaxial testing, there are many initial mesoscale pores inside all the cylindrical specimens under a total suction of 10 MPa (Figures 4.17a, 4.18a and 4.19a)

without big differences among these three specimens. After triaxial loading, all the specimens are split into two parts by clear shear planes, showing brittle failures (see Figures 4.17b-d, 4.18b-d and 4.19b-d). However, one can note a difference between the specimens at a lower mean stress whose shear plane is rough and tortuous (e.g., specimen K13\_S10\_P200), and those at a higher mean stress whose shear plane is relatively planar (e.g., specimen K13\_S10\_P1000). This result is in good agreement with the findings obtained from the experiments on the clay specimens under a higher initial total suction of 38 MPa (Figures 4.12-4.14).

The CT projections of clay specimens after triaxial tests indicate that, under a mean stress of 200 kPa, the specimen K13\_S10\_P200 shows many mesoscale pores and several mesoscale cracks. Some of the mesocracks could be clearly observed by the eyes from the surface of the specimen. Under a mean stress of 600 kPa, the specimen K13\_S10\_P600 also exhibits many mesoscale pores as well as vertical and horizontal mesoscale cracks. Under a mean stress of 1000 kPa, the specimen K13\_S10\_P1000 shows mesoscale pores and horizontal mesoscale cracks. It is observed that the mesoscale pores tend to be more compressed as the mean stress increases. As a result, less mesoscale pores are observed in the specimen under a higher mean stress. Overall, although the number and size of mesoscale pores decrease after triaxial loading, macroscopic and mesoscopic cracks gradually appear, which leads to the increase in volume (i.e., dilation) of unsaturated clay.

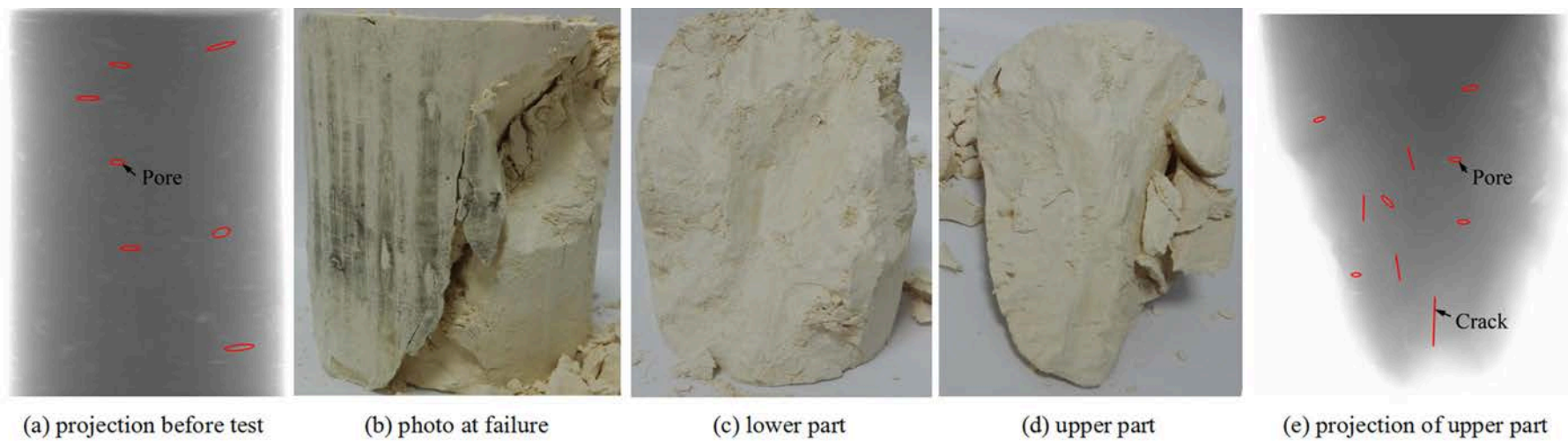


Figure 4.17 Photographs and XR- $\mu$ CT images of specimen K13\_S10\_P200

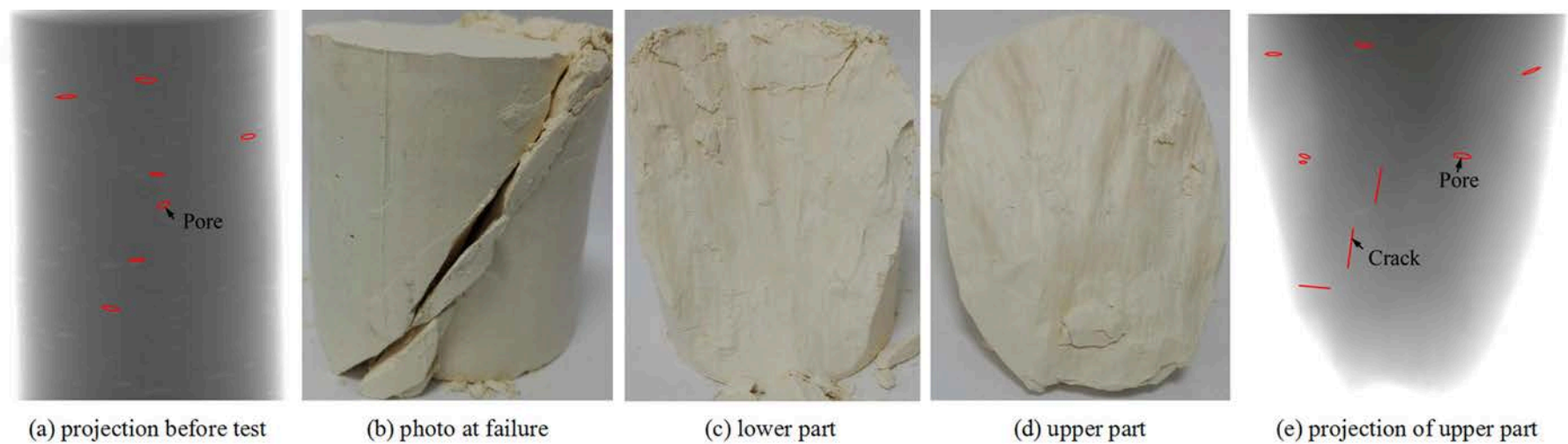


Figure 4.18 Photographs and XR- $\mu$ CT images of specimen K13\_S10\_P600

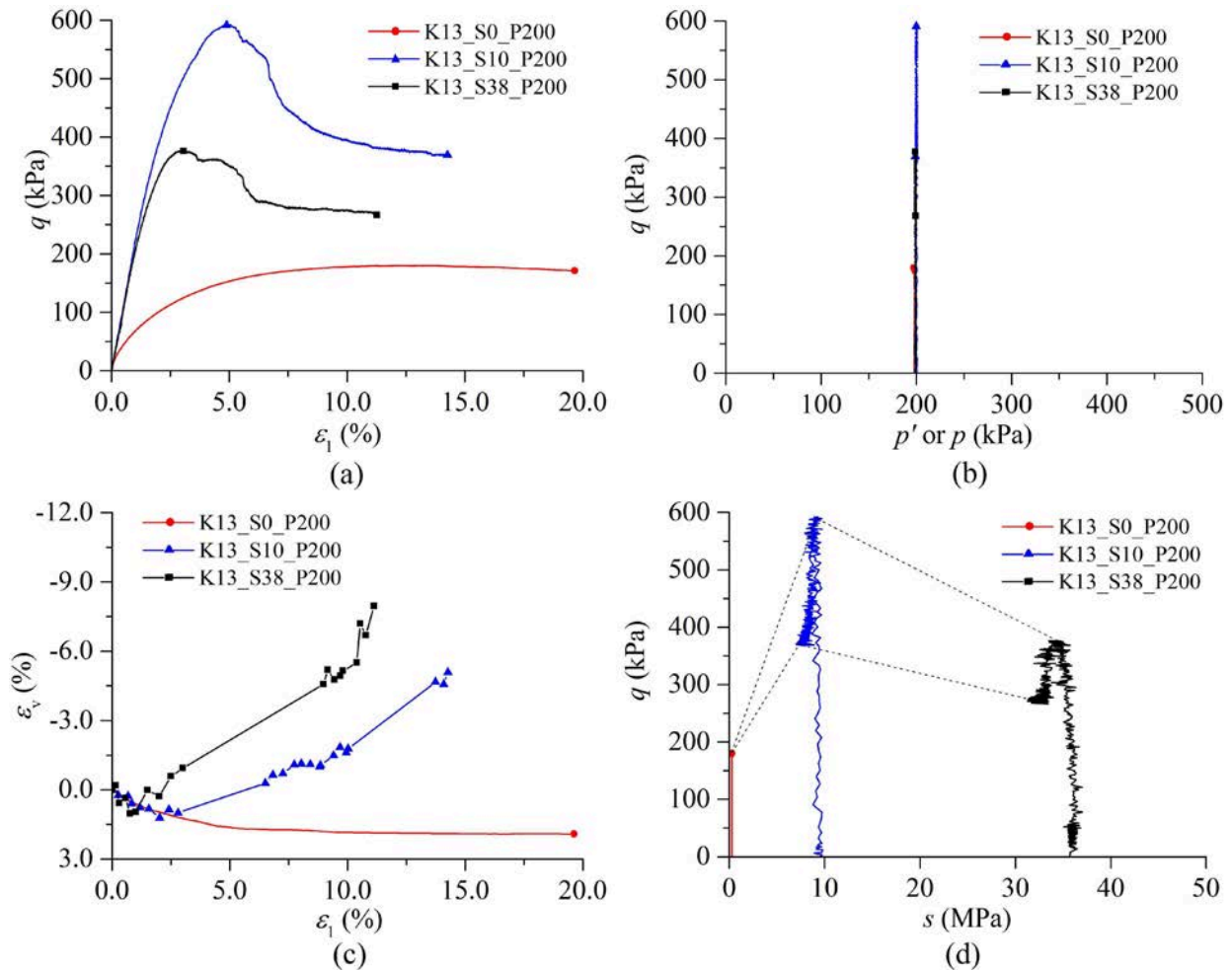


Figure 4.19 Photographs and XR- $\mu$ CT images of specimen K13\_S10\_P1000

### 3.3 Unsaturated test results affected by suction

#### 3.3.1 Under the mean stress of 200 kPa

Figure 4.20 presents the results of the triaxial tests on the saturated Kaolin K13 clay subjected to a mean effective stress of  $p' = 200$  kPa as well as the unsaturated Kaolin K13 clay under a mean stress of  $p = 200$  kPa and two initial total suctions of  $s_0 = 10$  MPa and 38 MPa.



(a)  $(\epsilon_1, q)$  plane; (b)  $(p, q)$  plane; (c)  $(\epsilon_1, \epsilon_v)$  plane; (d)  $(s, q)$  plane

Figure 4.20 Behaviour of Kaolin K13 clay under  $p = 200$  kPa affected by total suctions

It is noted from Figure 4.20a that in the saturated state (i.e.,  $s_0 = 0$  MPa), the deviatoric stress continuously increases with the increase in axial strain up to a plateau showing a ductile failure; however, in the unsaturated state (i.e.,  $s_0 = 10$  MPa or 38 MPa), the deviatoric stress first rapidly increases until meeting the peak and then decreases to the residual value with increasing axial strain, showing a brittle failure. One can also note that the shear strength of unsaturated clay is significantly larger than that of the corresponding saturated clay (see

Figure 4.20a and d). However, it is noted that both the maximum shear strength and residual shear strength of the specimen (i.e., K13\_S38\_P200) under a total suction of 38 MPa are smaller than those of the specimen (i.e., K13\_S10\_P200) under a lower total suction of 10 MPa. The decrease in shear strength is probably due to the existence of initial local cracks inside the clay specimen induced by the high suction in desiccator, as illustrated in Figure 4.3. Table 4.1 summarises the shear strength parameters of Kaolin K13 clay. From this table, one can notice a considerable decrease in apparent cohesions when the total suction increases from 10 MPa to 38 MPa.

Table 4.1 Shear strength parameters of remoulded Kaolin K13 clay

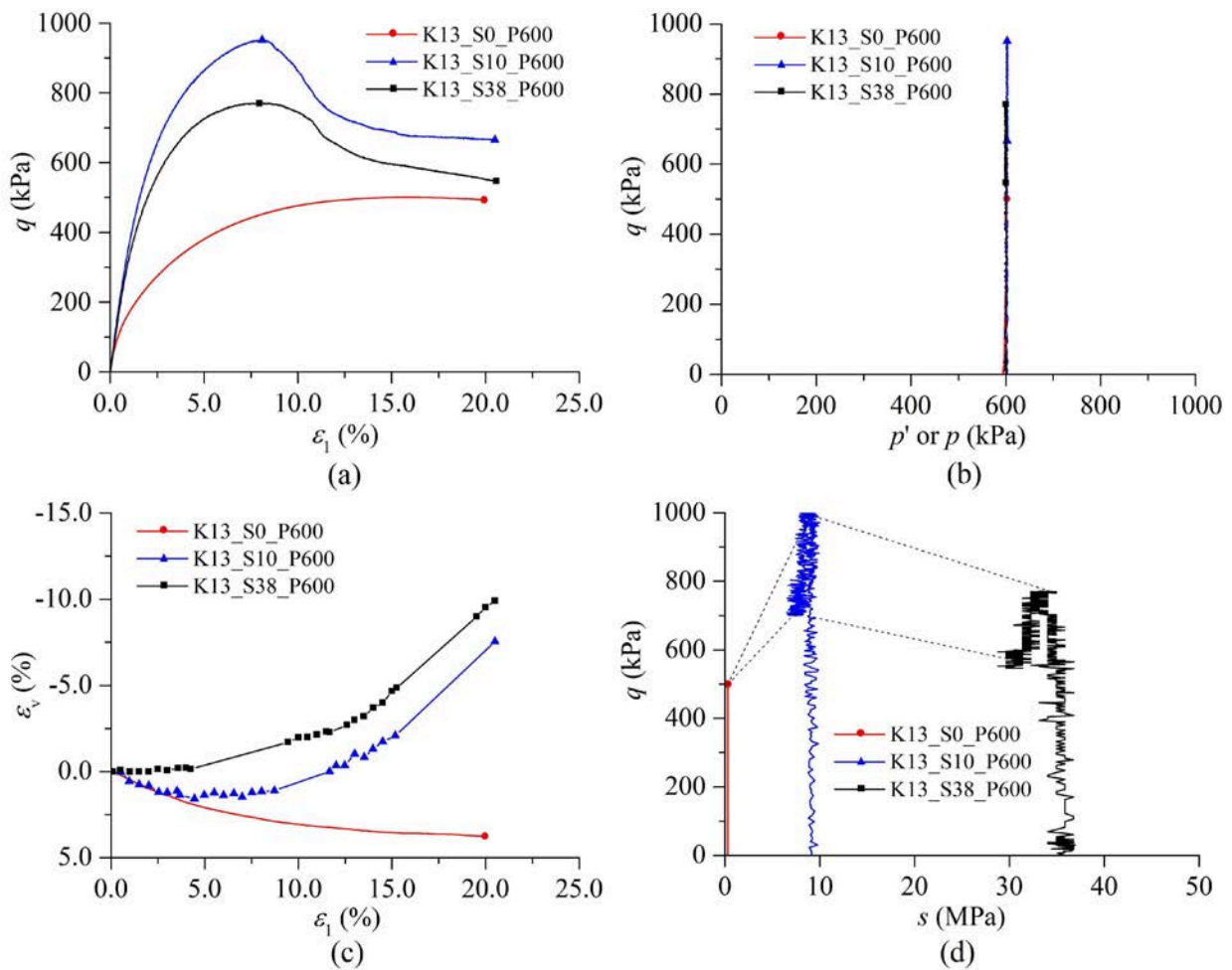
Material	Strength envelope	Slope $M$	Internal friction angle		Apparent cohesion	
			$\phi^*$ (°)	$\phi$ (°)	$c^*$ (kPa)	$c$ (kPa)
Unsaturated clay ( $s_0 = 38$ MPa)	Maximum shear strength	0.857	40.6	22.0	294	623
	Residual shear strength	0.857	40.6	22.0	84	178
Unsaturated clay ( $s_0 = 10$ MPa)	Maximum shear strength	0.857	40.6	22.0	416	881
	Residual shear strength	0.857	40.6	22.0	121	256
Saturated clay ( $s_0 = 0$ MPa)	Shear strength	0.857	40.6	22.0	0	0

The variations in volumetric strains of remoulded clay specimens during triaxial shearing are presented in Figure 4.20c. It is observed that the volumetric strain of the saturated clay specimen is always positive showing contractive behaviour. However, for the unsaturated specimens regardless of the imposed total suctions, the volumetric strains are first positive showing contractive behaviour and then negative showing dilative behaviour as the axial strains increase. Furthermore, the specimen (i.e., K13\_S38\_P200) with a higher initial total suction tends to compress less at the beginning and dilates more at the end. The result indicates that the total suction has a great influence on the volumetric behaviour of remoulded clay during triaxial loading.

### 3.3.2 Under the mean stress of 600 kPa

The triaxial tests results on saturated and unsaturated remoulded Kaolin K13 clay under a mean effective stress of  $p' = 600$  kPa (or a mean stress of  $p = 600$  kPa) and three different

initial total suctions of  $s_0 = 0$  MPa, 10 MPa and 38 MPa are illustrated in Figure 4.21.



(a)  $(\epsilon_1, q)$  plane; (b)  $(p, q)$  plane; (c)  $(\epsilon_1, \epsilon_v)$  plane; (d)  $(s, q)$  plane

Figure 4.21 Behaviour of Kaolin K13 clay under  $p = 600$  kPa affected by total suctions

One can note from Figure 4.21a that the deviatoric stress of the saturated clay specimen (i.e., K13\_S0\_P600) increases with increasing axial strain up to a plateau showing ductile failure behaviour. By contrast, with the increase in axial strain, the deviatoric stresses of the unsaturated clay specimens (i.e., K13\_S10\_P600 and K13\_S38\_P600) experience first a rapid increase until meeting the peaks and then a gradual decrease to approach the residual values. Moreover, the shear strengths of unsaturated clay specimens are considerably greater than that of saturated clay specimen (Figure 4.21a and d), which is consistent with the findings from the tests under a mean stress of 200 kPa (Figure 4.20a and d). However, as previously presented, the shear strengths of unsaturated clay specimens do not always increase with increasing total suctions since a very high total suction may induce initial local cracks within specimens.

Figure 4.21c shows the evolution of volumetric strain versus axial strain of the clay specimens during triaxial shearing. It is noted that the saturated clay specimen exhibits contractive behaviour while the unsaturated clay specimens show evident dilative behaviour after triaxial shearing. With respect to the unsaturated specimen (i.e., K13\_S10\_P600) under an initial total suction of 10 MPa, the volumetric strain is first positive and then negative as the axial strain increases. Nevertheless, the specimen (i.e., K13\_S38\_P600) with a much higher initial total suction of 38 MPa seems to directly show dilative behaviour without evident compression in the beginning. This is also in agreement with the previous finding that the smaller the initial total suction, the more significant the initial compression of the specimen.

---

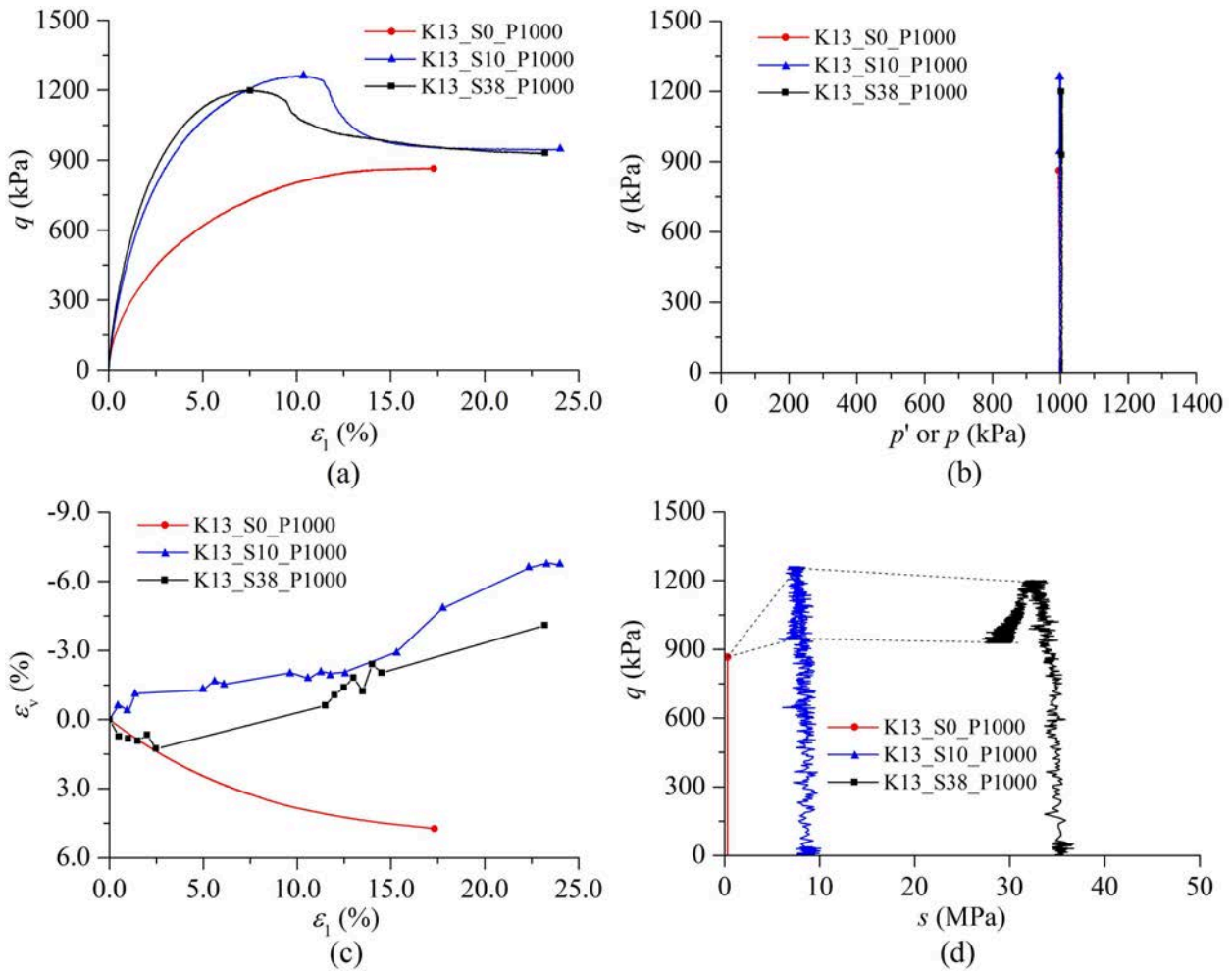
### 3.3.3 Under the mean stress of 1000 kPa

---

Figure 4.22 depicts the results of triaxial tests on saturated and unsaturated remoulded Kaolin K13 clay under a mean effective stress of  $p' = 1000$  kPa (or a mean stress of  $p = 1000$  kPa) and three different initial total suctions of  $s_0 = 0$  MPa, 10 MPa and 38 MPa.

It can be seen from Figure 4.22a that, similar to the previous findings, the deviatoric stress of the saturated clay continuously increases with increasing axial strain until a plateau; however, the deviatoric stress of the unsaturated clay first increases to meet the peak and then decreases to the residual value as the axial strain increases, showing strain-softening behaviour. Furthermore, the shear strength of unsaturated clay is larger than that of saturated clay.

Compared with the results shown in Figures 4.20a and 4.21a, one can note that the difference between the residual shear strengths of unsaturated clay and the shear strength of saturated clay decreases with increasing mean stress. For example, at the mean stress of 200 kPa, the shear strength of the saturated specimen K13\_S0\_P200 is about 171 kPa, and the residual shear strengths of the unsaturated specimens K13\_S10\_P200 and K13\_S38\_P200 are respectively 369 kPa and 267 kPa; by contrast, at a higher mean stress of 1000 kPa, the shear strength of the saturated specimen K13\_S0\_P1000 is approximately 866 kPa, and the residual shear strengths of the unsaturated specimens K13\_S10\_P1000 and K13\_S38\_P1000 are respectively about 946 kPa and 931 kPa.



(a) ( $\varepsilon_1, q$ ) plane; (b) ( $p, q$ ) plane; (c) ( $\varepsilon_1, \varepsilon_v$ ) plane; (d) ( $s, q$ ) plane

Figure 4.22 Behaviour of Kaolin K13 clay under  $p = 1000$  kPa affected by total suctions

Meanwhile, it can be seen that the gap between the maximum shear strengths of unsaturated clay under different initial total suctions shows a tendency to decrease with increasing mean stress. For instance, the difference between the maximum shear strengths of unsaturated specimens K13\_S10\_P200 and K13\_S38\_P200 is 57.7% at the mean stress of 200 kPa (Figure 4.20), while the difference of unsaturated specimens K13\_S10\_P1000 and K13\_S38\_P1000 is only 5.0% at the mean stress of 1000 kPa (Figure 4.22). The above results suggest that the influence of total suction on the shear strength of unsaturated clay reduces as the mean stress rises.

In addition, the ratio of shear strength drop after the peak (i.e., ratio of the gap between the maximum shear strength and residual shear strength to the maximum shear strength) of unsaturated clay decreases with increasing mean stress. For instance, with the consideration of an initial total suction of 10 MPa, the ratio of shear strength drop at the mean stress of 200

kPa is as high as 37.8% while that at the mean stress of 1000 kPa decreases to 24.9%. This means that as the mean stress increases, the unsaturated remoulded clay gradually shows a ductile characteristic.

The variation in volumetric strain of remoulded clay specimens under triaxial loading are shown in Figure 4.22c. It is also observed that the saturated clay specimen contracts during the whole period of test while the two unsaturated clay specimens dilate at the end of triaxial tests. However, a difference is noted regarding the unsaturated clay that the dilation of the specimen K13\_S10\_P1000 under an initial total suction of 10 MPa takes place from the beginning of test while a slight contraction is exhibited before the development of dilative behaviour with respect to the specimen K13\_S38\_P1000 under an initial total suction of 38 MPa. As presented in the Section 3.2.2 of this chapter, the strange volumetric strain of the specimen K13\_S10\_P1000 appears due to the problem with the 2D photography technique.

## 4. Mechanical behaviour of remoulded M35 clay

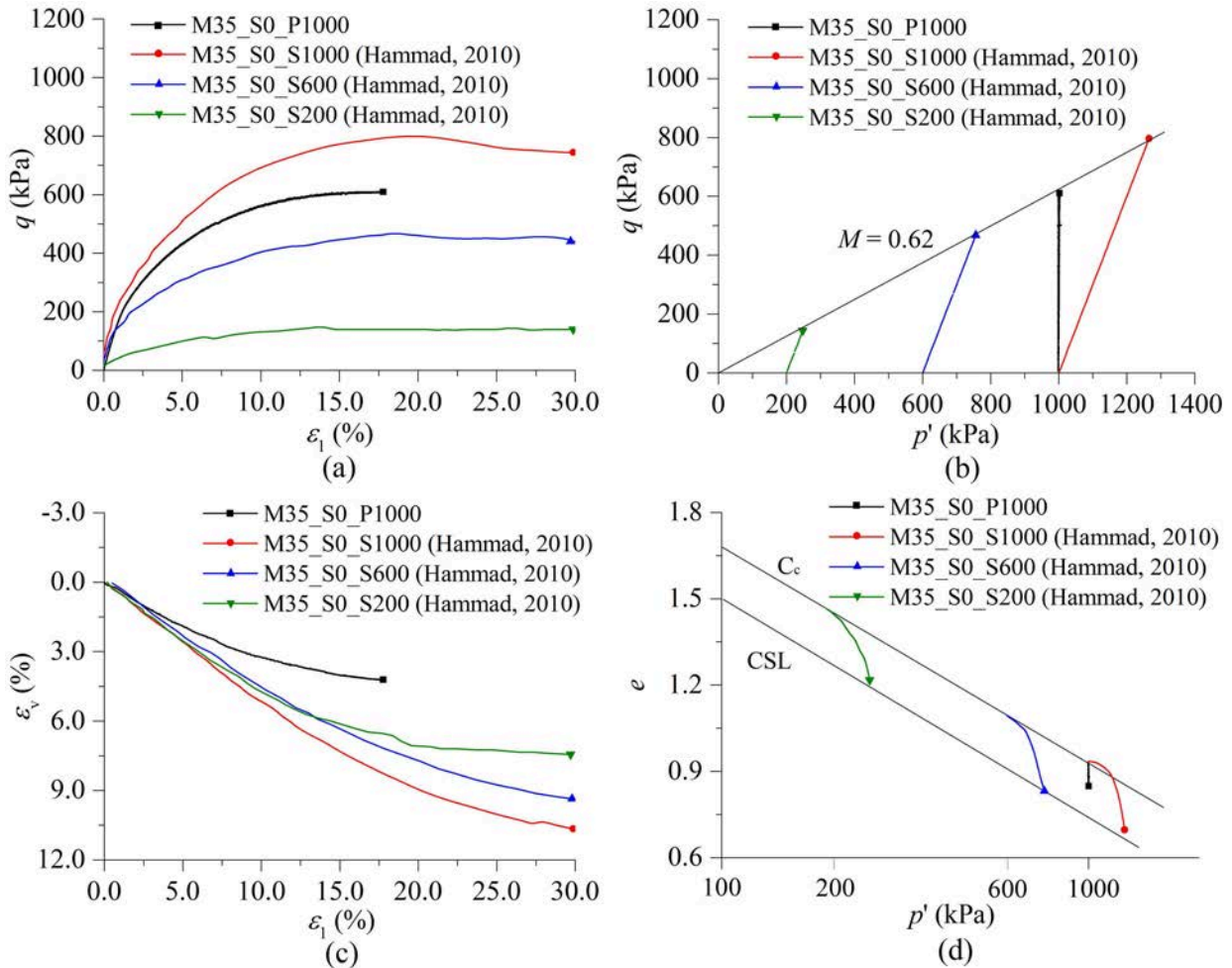
### 4.1 Saturated test results affected by mean effective stress

- *Mechanical results*

Figure 4.23 presents the mechanical results of a consolidated drained triaxial test on the saturated remoulded M35 clay specimen (i.e., M35\_S0\_P1000) under the mean effective stress of 1000 kPa along the purely deviatoric stress path. Notice that the drained triaxial shearing for M35 clay requires a very slow velocity, which is far less than that for Kaolin K13 clay. Due to time constraints, only one triaxial test considering one level of mean effective stress was carried out and presented in this section. In addition, the consolidated drained triaxial tests results of saturated M35 clay reported by Hammad (2010) are presented for comparison purposes. The tests of Hammad (2010) were performed under different confining effective pressures on the conventional constant  $\sigma'_3$  stress path.

One can note that, similar to the results of Kaolin K13 clay, the M35 clay also exhibits evident non-linearity and strain-hardening behaviour (Figure 4.23a). Meanwhile, the soil stiffness and the shear strength significantly increase with the increase in the confining effective stress. It is also observed that the shear strength of the specimen M35\_S0\_P1000 on the purely deviatoric stress path is smaller than that of the specimen M35\_S0\_S1000 on the

constant  $\sigma'_3$  stress path. This difference is mainly due to the increase in mean effective stress when the specimen is sheared following the constant  $\sigma'_3$  stress path. These results of M35 clay are consistent with many previous findings such as those of Kaolin K13 clay reported by Ighil Ameer (2016).



(a) ( $\epsilon_1, q$ ) plane; (b) ( $p', q$ ) plane; (c) ( $\epsilon_1, \epsilon_v$ ) plane; (d) ( $\log p', e$ ) plane

Figure 4.23 Behaviour of saturated M35 clay under various mean effective stresses

The stress paths in Figure 4.23b show that the failure of the specimen M35\_S0\_P1000 examined in this study shares the same critical state line in the ( $p', q$ ) plane as the specimens tested by Hammad (2010). The slope of the critical state line of M35 clay is  $M = 0.62$ , which is significantly smaller than that ( $M = 0.857$ ) of Kaolin K13 clay. This result indicates that M35 clay has a smaller effective angle of internal friction and thus a smaller shear strength than Kaolin K13 clay under the same loading conditions. The reduction in the effective angle of internal friction of M35 clay appears related to the existence of montmorillonite fraction.

Figure 4.23c illustrates the relationship between volumetric strain and axial strain. The

results demonstrate that the volumetric deformations in all the cases increase with increasing axial strains showing contractive behaviour. On the other hand, the volumetric strain exhibits a tendency of increase as the confining effective stress rises. For instance, at the axial strain of about 30%, the volumetric strain of specimen M35\_S0\_S200 is 7.4% while the volumetric strain of specimen M35\_S0\_S1000 reaches 10.7%. Furthermore, it is noted that the volumetric strain of the specimen (i.e., M35\_S0\_P1000) on the purely deviatoric stress path is considerably less than that of the specimen (i.e., M35\_S0\_S1000) on the constant  $\sigma'_3$  stress path at the same initial mean effective stress.

The evolution of void ratio, as illustrated in Figure 4.23d, demonstrates that the void ratios of all the specimens decrease from the compression line (with a slope of  $C_c$ ) to approach the critical state line (or the perfect plasticity line, CSL) in the  $(\log p', e)$  plane. However, a slight difference in the evolution paths between these M35 clay specimens is clearly noted. The void ratio of the specimen (e.g., M35\_S0\_P1000) on the purely deviatoric stress path evolves directly downwards to the critical state line but does not reach the critical state line. Nevertheless, the void ratio of the specimen (i.e., M35\_S0\_S1000) on the constant  $\sigma'_3$  stress path first exhibits a trend to follow the compression line and then decreases to reach the critical state line.

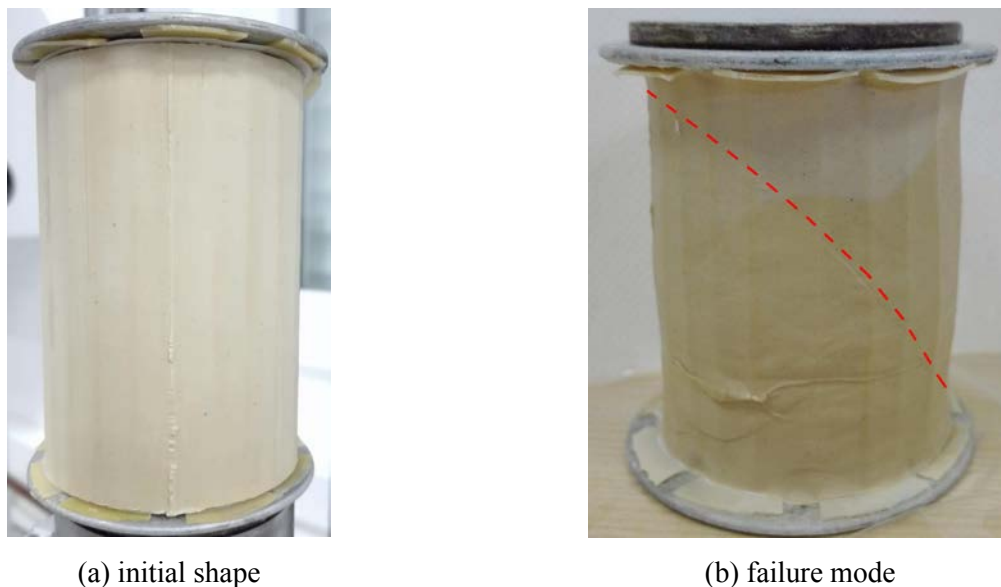


Figure 4.24 Failure mode of saturated remoulded M35 clay under  $p' = 1000$  kPa

- *Failure modes of specimens*

Figure 4.24 shows the photographs of the saturated remoulded M35 clay specimen (i.e.,

M35\_S0\_P1000) before and after the triaxial test under the mean effective stress of 1000 kPa. One can note that this specimen is characterised by a tilted shear plane without evident barrel-shape after triaxial shearing. The shear plane does not reach the top and bottom surfaces of the specimen. Compared to the failure mode of saturated Kaolin K13 clay (see Figure 4.9), it is observed that the tilt angle of the shear plane of M35 clay is less than that of Kaolin K13 clay. This is in agreement with the finding that M35 clay has a smaller effective angle of internal friction (or slope of critical state line,  $M$ ) than Kaolin K13 clay (Figures 4.11b and 4.23b).

#### 4.2 Unsaturated test results affected by mean stress

- *Initial total suction*

Figure 4.25 presents the evolution of measured relative humidities and calculated total suctions of a cylindrical specimen of M35 clay under the circumstance of saturated NaCl solution starting from being in the desiccator to the application of mechanical loading.

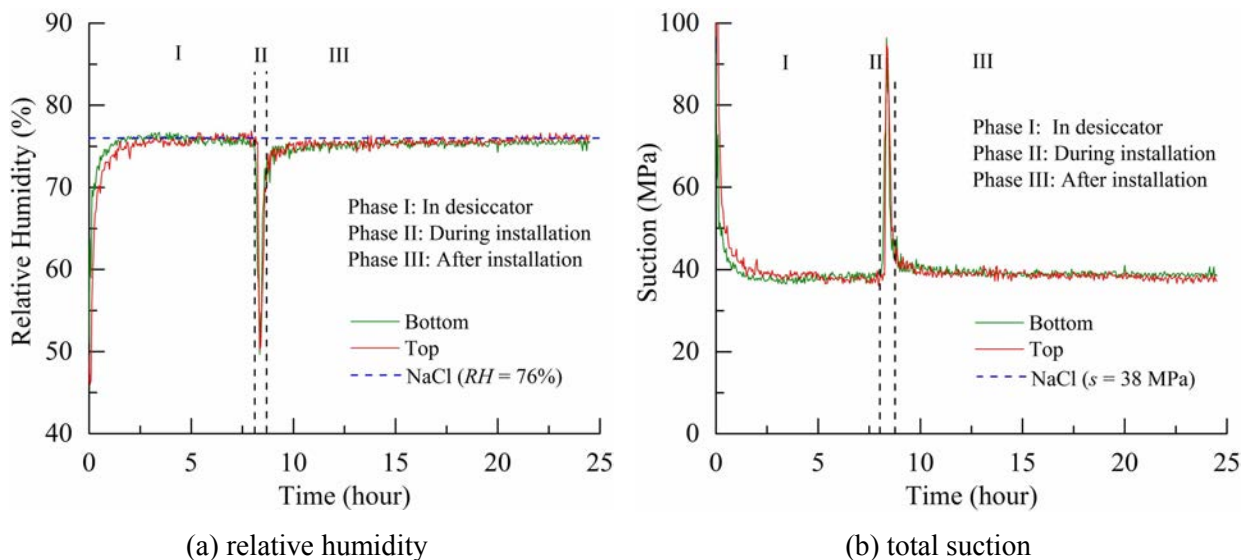


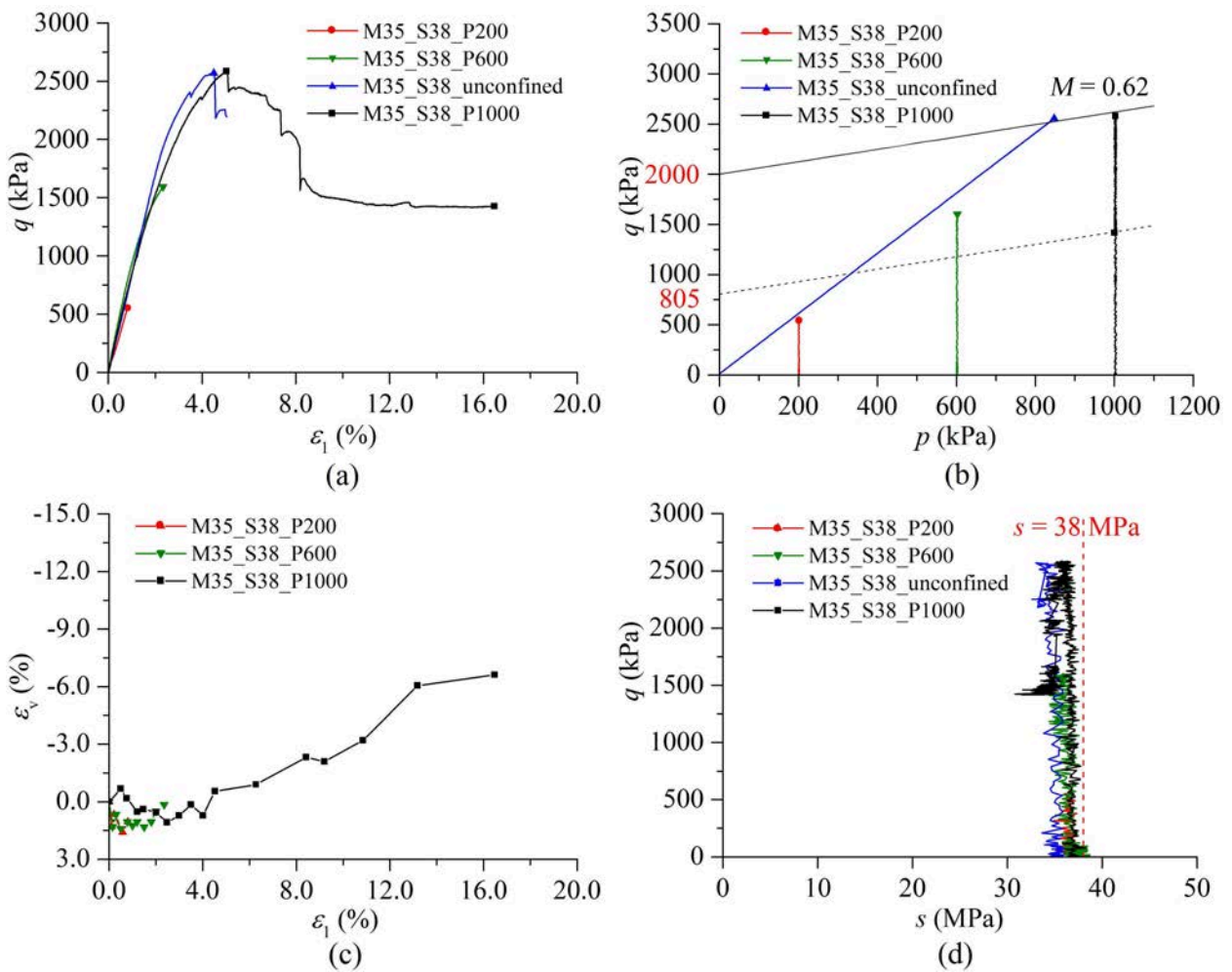
Figure 4.25 Relative humidity and total suction (M35, NaCl) before triaxial tests

It is noted that both the relative humidities and total suctions approximate the corresponding target values (i.e., 76% and 38 MPa) of the saturated NaCl solution. When the specimen is removed from the desiccator and installed in the triaxial cell, the measured relative humidities drop quickly to the environmental value (i.e., 50%). As expected, this causes the increase in total suctions of the specimen surfaces. After the specimen is mounted in the triaxial cell and sealed with rubber membrane and O-rings, a new equilibrium of relative humidities is gradually reached. In this phase, both relative humidity and total suction

show a tendency to recover to the initial values. Because the exposure time of the specimen in air is very short, the relative humidity and the total suction are able to almost fully recover in a few hours. Therefore, it is reasonable to consider that the target total suction of 38 MPa is properly imposed in the M35 clay specimen, and the specimen is ready for triaxial testing.

- *Mechanical results*

Figure 4.26 shows the mechanical results of unsaturated remoulded M35 clay under an initial total suction of 38 MPa and different mean stresses (i.e., 200 kPa and 1000 kPa) along the purely deviatoric stress path.



(a) ( $\epsilon_1, q$ ) plane; (b) ( $p, q$ ) plane; (c) ( $\epsilon_1, \epsilon_v$ ) plane; (d) ( $s, q$ ) plane

Figure 4.26 Mechanical behaviour of unsaturated M35 clay under  $s_0 = 38$  MPa

One can note that the deviatoric stress of the clay specimen (i.e., M35\_S38\_P1000) under the mean stress of 1000 kPa first increases up to around 2580 kPa and then decreases to a certain residual value, showing a brittle failure at an axial strain of about 5.0% (Figure 4.26a).

The volumetric strain in Figure 4.26c demonstrates that this specimen M35\_S38\_P1000 exhibits first slightly contractive behaviour and then clearly dilative behaviour during triaxial shearing.

Notice that when a clay specimen is sheared following the purely deviatoric stress path, the deviatoric stress increases while the confining stress decreases. Since the confining stress cannot be negative (i.e.,  $\sigma_3 = (3p - \sigma_1)/2 \geq 0$ ), the maximum deviatoric stress can be reached is threefold of the mean stress (i.e.,  $q = \sigma_1 - \sigma_3 \leq 3p$ ). During triaxial shearing, it was found that the clay specimen (i.e., M35\_S38\_P200) under a mean stress of 200 kPa did not fail even if the deviatoric stress was increased up to near 600 kPa, which is the maximum deviatoric stress that can be applied. It is observed from Figure 4.26a that the triaxial test on the specimen M35\_S38\_P200 was stopped at a very small axial strain of 0.8%, at which the deformation of the specimen was still elastic.

In order to obtain a complete shear strength envelope, the specimen was unloaded and then isotropically loaded to the mean stress of 600 kPa. Afterwards, a triaxial test was performed on the purely deviatoric stress path. However, the result shows that the specimen M35\_S38\_P600 (which is previously named M35\_S38\_P200) was still intact and the stress-strain relationship almost followed that of the initial test when the deviatoric stress increased up to nearly the maximum value (i.e.,  $3p = 1800$  kPa) (Figure 4.26a and b). Therefore, the specimen was unloaded again and an unconfined compression test was carried out on the same specimen with a new name of M35\_S0\_unconfined. In this case, the specimen failed in a brittle manner at an axial strain of about 4.5%.

Figure 4.26b presents the stress paths of the four mechanical tests. Notice that the unloading paths (i.e., reverses of loading paths) are not included in this figure. It is also assumed in this section that the critical state line has a constant slope identical to that of saturated clay. So, the apparent angle of internal friction is considered equal to the effective angle of internal friction of saturated clay (i.e.,  $\varphi^* = 31.8^\circ$  or  $\varphi = 16.3^\circ$ ). Therefore, the apparent cohesions are obtained by fitting the experimental data with Equation (4.5). It is noted that the apparent cohesions ( $c^*$ ) of unsaturated M35 clay under an initial total suction of 38 MPa are respectively about 2000 kPa and 805 kPa corresponding to the maximum shear strength and residual shear strength, which are considerably higher than those of unsaturated Kaolin K13 clay (i.e., 294 kPa and 84 kPa) under the same initial total suctions (see Figure 4.11b).

- *Failure modes of specimens*

Figures 4.27-4.28 show the photographs of two unsaturated remoulded M35 clay specimens (i.e., M35\_S38\_unconfined and M35\_S38\_P1000) after mechanical loading. In addition, the XR- $\mu$ CT projections of the upper parts of the specimens separated by shear bands are also presented here.

One can note that the specimen under unconfined compression test (i.e., M35\_S38\_unconfined) is divided into several parts by a shear plane and large vertical cracks (Figure 4.27a). By contrast, the specimen (i.e., M35\_S38\_P1000) under triaxial loading is split into two parts by a tilted shear plane without evident barrel-shaped deformation (Figure 4.28a). The specimen M35\_S38\_P1000 also shows several small vertical cracks, which are visible to naked eye. Furthermore, the XR- $\mu$ CT projections indicate that there are not many mesoscale pores in these two unsaturated M35 clay specimens compared to the unsaturated Kaolin K13 clay specimens. It is because the montmorillonite fraction has a high shrink-swell capacity and compressibility, the voids in M35 clay are considerably compressed at a high suction-stress level. This result is consistent with the finding of Wei (2013) that the dominant pore size of M35 clay is significantly less than that of Kaolin P300 clay under a suction of 1.5 MPa.

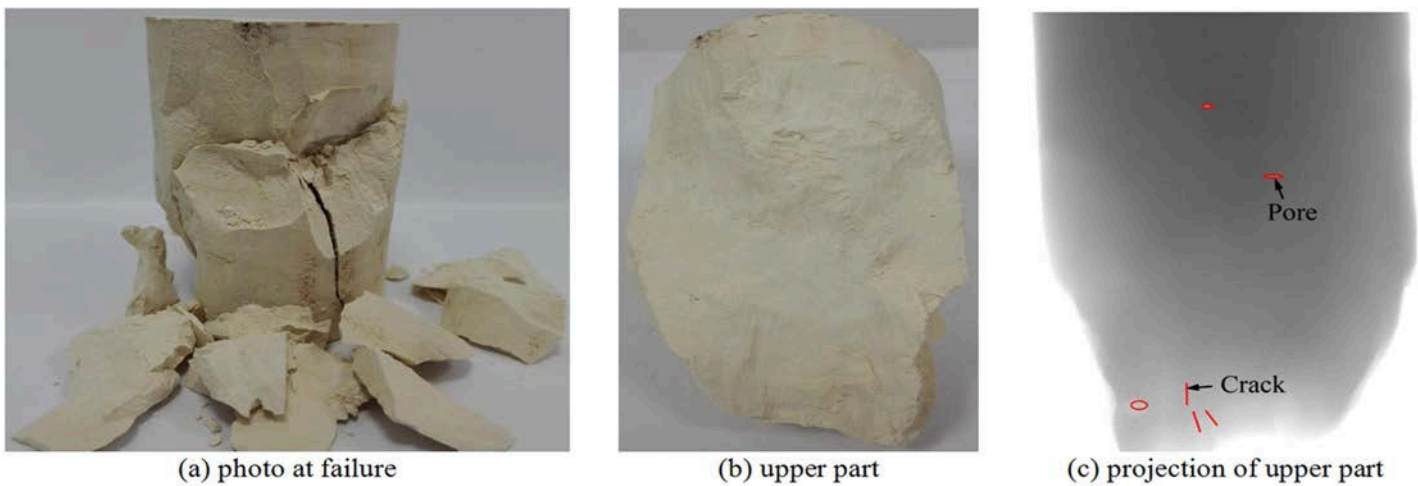


Figure 4.27 Photographs and XR- $\mu$ CT images of specimen M35\_S38\_unconfined

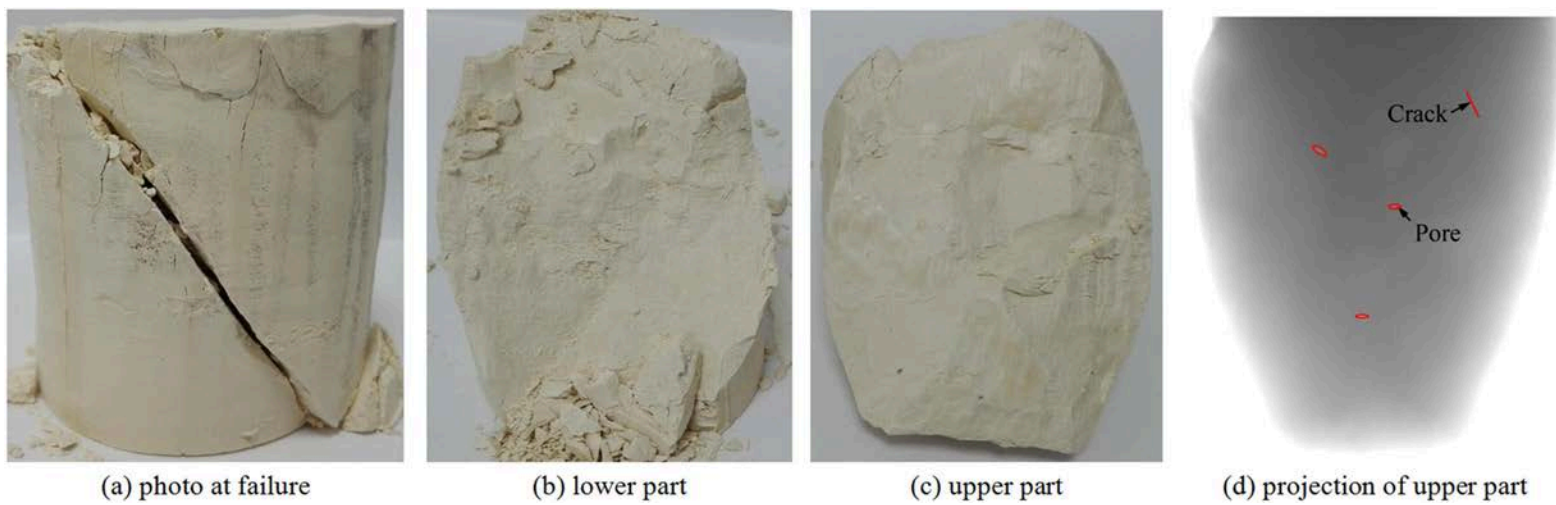


Figure 4.28 Photographs and XR- $\mu$ CT images of specimen M35\_S38\_P1000

## 5. Theoretical calculation of apparent cohesions

### 5.1 Theoretical equations

The apparent cohesion of unsaturated soil can be determined from the isotropic tensile strength by the following equation (Lu et al., 2009):

$$c = -\sigma_{t,iso} \tan \varphi \quad (4.7)$$

where  $c$  is the apparent cohesion;  $\varphi$  is the apparent angle of internal friction;  $\sigma_{t,iso}$  is the isotropic tensile strength.

---

#### 5.1.1 Suction stress concept

---

The isotropic tensile strength as a part of effective stress of unsaturated soil, is termed as suction stress by Lu and Likos (2004) and can be expressed in terms of the effective degree of saturation:

$$\sigma^s = -\alpha^* \cdot S_r^e \left[ (S_r^e)^{n^*/(1-n^*)} - 1 \right]^{1/n^*} \quad (4.8)$$

where  $\sigma^s$  is the suction stress;  $S_r^e$  is the effective degree of saturation;  $\alpha^*$  and  $n^*$  are two model constants, which are the same as those in the soil-water characteristic model proposed by van Genuchten (1980).

In this way, the isotropic tensile strength or the suction stress ( $\sigma^s$ ) is calculated by Equation (4.8) and thus the apparent cohesion ( $c$ ) can be determined by Equation (4.7).

---

#### 5.1.2 Capillary stress concept

---

In the framework of micromechanics, the soil is considered as an assembly of spheres with a constant radius of  $R$ . In this case, the capillary stress between spheres due to water can be derived from the following model (Taibi, 1994; Fleureau et al., 2003):

$$\sigma^c = \frac{\pi T_s}{2g(e)R^2} \left[ 4R + \frac{3(3T_s - \sqrt{9T_s^2 + 8T_s R s})}{s} \right] \quad (4.9)$$

where  $\sigma^c$  is the capillary stress;  $T_s$  is the surface tension of water;  $R$  is the representative radius of soil grains;  $s$  is the suction;  $g(e)$  is a function of void ratio, which can be expressed by:

$$g(e) = 0.32e^2 + 4.06e + 0.11 \quad (4.10)$$

Provided that the grain radius of clay ( $R$ ) is determined, the capillary stress ( $\sigma^c$ ) can readily be calculated from Equation (4.9). Therefore, the capillary cohesion can be calculated from Equation (4.7) by replacing  $\sigma_{t,iso}$  with  $\sigma^c$ .

## 5.2 Comparison between calculated and measured cohesions

The above two theoretical methods are used to calculate the apparent cohesions of Kaolin K13 clay and M35 clay under different total suctions. The calculation parameters are summarised in Table 4.2. The suctions ( $s$ ) are taken as the values imposed on clay specimens by the vapour equilibrium method.  $S_r^c$  is calculated from the measured degree of saturation.  $e$  is measured using the liquid displacement method (Figures 4.5 and 4.7).  $n^*$  and  $\alpha^*$  are determined from the soil-water characteristic curves (Figures 4.5 and 4.7).  $\phi$  is derived from triaxial tests (Table 4.1).  $R$  is empirically estimated from the grain size distribution curves and SEM images (Figures 2.3-2.4).

Table 4.3 compares the calculated apparent cohesions with the measured ones of unsaturated Kaolin K13 clay and M35 clay. It is noted that the cohesions calculated from suction stresses are one order of magnitude larger than those calculated from capillary stresses. On the other hand, all the calculated cohesions are significantly smaller than the measured apparent cohesions corresponding to the peak shear strengths. However, one can note that the cohesions calculated from suction stresses are very close to the measured values corresponding to the residual shear strengths. In addition, the cohesions calculated from suction stresses show a slight drop as the total suction increases from 10 MPa to 38 MPa, which is consistent with the tendency of the measured data. This is because the suction stress calculated from Equation (4.8) does not always increase with decreasing effective degree of saturation but sometimes first increases and then decreases depending on the exponential parameter  $n^*$  (Lu et al., 2010). By contrast, the cohesions calculated from capillary stresses cannot reflect this phenomenon.

Table 4.2 Summary of parameters for cohesion calculation

Material	Suction $s$ (MPa)	$S_r^c$	$n^*$	$\alpha^*$ (kPa)	$R$ ( $\mu\text{m}$ )	$e$	$\varphi$ ( $^\circ$ )
Kaolin K13	38	0.034	2.15	1000	2.0	0.68	22.0
	10	0.066	2.15	1000	2.0	0.68	22.0
M35	38	0.272	1.55	2000	1.0	0.55	16.3

Table 4.3 Comparison between calculated and measured apparent cohesions

Material	Suction $s$ (MPa)	Measured cohesion $c$ (kPa)		Calculated cohesion $c$ (kPa)	
		Peak strength	Residual strength	Suction cohesion	Capillary cohesion
Kaolin K13	38	623	178	261	29
	10	881	256	283	27
M35	38	4236	1705	1671	50

## 6. Summary

The hydromechanical behaviour of unsaturated remoulded Kaolin K13 clay and M35 clay are investigated by performing triaxial tests considering different levels of total suction and mean stress. The following conclusions can be drawn from this chapter:

(1) The water content of clay specimen exhibits first a linear decrease followed by a nonlinear decrease and finally a plateau during drying. The higher is the imposed total suction, the faster is the drying speed of the linear evolution phase. Under a high total suction of 38 MPa, open cracks may be induced in cylindrical specimen due to the uneven shrinkage at a fast drying speed. The shrinkage limit and minimum void ratio of Kaolin K13 clay are larger than those of M35 clay, while the water content and degree of saturation of Kaolin K13 clay are smaller than those of M35 clay at the same suction levels.

(2) During triaxial loading, the deviatoric stress of saturated Kaolin K13 clay and M35 clay continuously increases until a plateau, showing strain-hardening behaviour. By contrast, the deviatoric stress of unsaturated Kaolin K13 clay and M35 clay under a high total suction (i.e., 10 MPa and 38 MPa) first rises up to a peak and then slightly decreases to reach a small residual value, exhibiting evident strain-softening behaviour. Meanwhile, the measured total

suction of all unsaturated clay specimens goes on a decrease as the deviatoric stress increases throughout the tests.

(3) The shear strength of both saturated clay and unsaturated clay considerably increases with the increase in mean stress. The shear strength of unsaturated clay is greatly larger than that of saturated clay. Nevertheless, the difference between the residual shear strengths of unsaturated clay under different initial total suctions, and the shear strength of saturated clay decreases with increasing mean stress. In addition, as the mean stress increases, the influence of total suctions on shear strength reduces, and the unsaturated clay gradually shows a ductile characteristic.

(4) Total suction considerably improves the shear strength of remoulded clay by increasing the apparent cohesion. The angles of internal friction ( $\phi$ ) of Kaolin K13 clay and M35 clay are respectively 22.0° and 16.3°. The apparent cohesions ( $c$ ) corresponding to the maximum shear strength of Kaolin K13 clay under initial total suctions of 38 MPa and 10 MPa are 623 kPa and 881 kPa, respectively. The clay under a higher total suction showing a smaller cohesion is probably due to the existence of initial cracks induced by the high suction. The apparent cohesion ( $c$ ) of M35 clay under an initial total suction of 38 MPa is about 4236 kPa, which is considerably higher than that of unsaturated Kaolin K13 clay.

(5) The volumetric strain of saturated clay is always positive showing contractive behaviour during triaxial loading. However, for the unsaturated clays under high total suctions, the volumetric strains are first positive showing slightly contractive behaviour and then negative showing pronounced dilative behaviour. In general, the specimen under a higher initial total suction tends to compress less in the beginning and dilates more at the end of test. The appearance of dilatancy in unsaturated clay is probably due to the initiation of mesoscopic cracks and the interlocking generated by shear bands.

(6) After triaxial loading, all unsaturated clay specimens under high initial total suctions (i.e., 10 MPa and 38 MPa) are completely split into two parts by single shear planes and exhibit no evident barrel-shaped deformations. A few cracks appear in unsaturated clay specimens after triaxial loading, and the distribution of cracks seems related to the level of mean stresses. Many mesoscale pores are observed and the void volume decreases with the increase in mean stress. Most of the mesoscale pores particularly those with large sizes away from the shear plane rotate towards the horizontal plane, which is perpendicular to the major

principle stress direction.

## **Chapter 5**

# **Conclusions and perspectives**

<b>1. Conclusions.....</b>	<b>181</b>
1.1 Investigations of saturated remoulded clay.....	181
1.2 Investigations of unsaturated remoulded clay.....	183
<b>2. Future perspectives.....</b>	<b>185</b>



The overall goal of this research was to understand the link between macroscopic behaviour and microstructural evolution of remoulded clays on different triaxial stress paths and the shear strengths of unsaturated remoulded clays on various suction-stress paths. Based on the research objectives, a series of macroscopic and microscopic experiments was carried out, and the experimental results were presented in previous chapters. This chapter presents the main conclusions of this research and some future research suggestions.

## 1. Conclusions

### 1.1 Investigations of saturated remoulded clay

The first part of the experimental investigations revealed the following scientific findings about the mechanical behaviour and the macro-micro relationships of saturated remoulded clays:

#### (1) Macromechanical results:

- Under triaxial loading, at a given stress level below the critical state line in the  $(p', q)$  plane, all the normally consolidated specimens show contractive behaviour. However, the overconsolidated specimens may exhibit different volumetric behaviour depending on the stress path. For instance, the overconsolidated specimen along the purely deviatoric stress path dilates nearly from the beginning of shearing, while the overconsolidated specimen under the constant  $\sigma'_3$  stress path always shows contractive behaviour before the end of test.
- At a given stress level below the critical state line, the plastic volumetric strains of the normally consolidated specimens are almost the same regardless of stress paths. Concerning the overconsolidated state, the specimen on the purely deviatoric stress path shows a negative plastic volumetric strain; however, the specimen following the constant  $\sigma'_3$  stress path exhibits a negligible plastic volumetric strain. Nevertheless, the direction of plastic strain increment is insignificantly affected by stress paths regarding both normally consolidated and overconsolidated clays.
- Following a given stress path, i.e., the purely deviatoric stress path, the volumetric deformations of both normally consolidated and overconsolidated specimens are

enhanced as the stress level increases until the critical state. That is to say, with the increase in stress level, the contractive or dilative property of a clay specimen remains, and the absolute volumetric strain increases.

(2) Microstructural results:

- Five orientation modes of clay particles are proposed as conceptual local features, i.e., the depolarization mode, the "oblique lines" mode, the "tortuous-oblique lines" mode, the "crossed-oblique lines" mode and the "crossed-tortuous-oblique lines" mode. The activation of the above orientation modes highly depends on the stress history (e.g., OCR, stress path and stress level) of the remoulded clay. These proposed conceptual modes allow interpreting the macroscopic volumetric mechanisms of remoulded clay from a microscopic point of view.
- Different shape and orientation characteristics of pores are identified between contractive and dilative specimens under triaxial loading. The elliptical pores observed in a dilative specimen are relatively more open than those within a contractive specimen. The open pores within a dilative specimen reorient themselves, following the orientation of clay particles, forming weak zones in the clay material, which make it possible for microcracks to initiate and propagate during continuous loading.
- Two scales of pore size distributions with the mean size of 0.15  $\mu\text{m}$  and 4.0  $\mu\text{m}$  are respectively revealed by the MIP technique and the SEM-stereology method. The results of SEM-stereology analyses also show a slight increase in the number of large pores in dilative specimens. This is likely because of the induced-opening of large pores in overconsolidated specimens with dilatancy phenomenon. In addition, clear linear relationships between the macrovoid ratios and the microvoid ratios are obtained.
- Microcracks are observed between strongly parallel-oriented particle groups in both normally consolidated and overconsolidated specimens. However, the microcracks in a dilative specimen appear more open and enable to propagate, thus forming a series of more or less parallel-distributed open mesocracks as observed by the XR- $\mu\text{CT}$  technique. They constitute the basic local mechanisms responsible for the macroscopic dilatancy phenomenon. In the case of normally consolidated specimens, potential closed mesocracks could not be observed by the XR- $\mu\text{CT}$  technique.

### (3) Dilatancy mechanism:

- Based on the analyses of various microscopic results, the dilatancy mechanism in highly overconsolidated saturated remoulded clays was revealed. It seems that the appearance of dilatancy phenomenon is attributed to a complex microstructural evolution including the tortuous arrangement of clay particles, the expansion of large micropores, the extension of open microcracks as well as the formation and propagation of open mesocracks when remoulded clays are subjected to a certain strong triaxial loading.

## **1.2 Investigations of unsaturated remoulded clay**

The second part of the experimental investigations revealed the following scientific findings concerning the hydromechanical behaviour of unsaturated remoulded clays:

### (1) Soil-water characteristics:

- The water content of clay specimen exhibits first a linear decrease followed by a nonlinear decrease and finally a plateau during drying. The elapsed time to reach equilibrium of water content is generally long (more than 150 days) in all examined cases. In general, the higher the imposed suction, the faster the drying speed of the linear evolution phase. Under a high suction of 38 MPa, open cracks may be induced in cylindrical specimen due to the uneven shrinkage at a fast drying speed.
- The soil-water characteristic curves reveal that the shrinkage limit and the minimum void ratio of Kaolin K13 clay respectively approximate 27% and 0.68, which are larger than the corresponding values (i.e., 20% and 0.55) of M35 clay. As the total suction increases, both the water content and degree of saturation decrease. On the other hand, the water content and degree of saturation of Kaolin K13 clay are smaller than those of M35 clay under the same suction conditions.

### (2) Hydromechanical behaviour:

- At the saturated state, the deviatoric stress continuously increases with the increase in axial strain up to a plateau showing a ductile failure in the end; however, at the unsaturated state with high total suctions, the deviatoric stress of both Kaolin K13 clay and M35 clay under high total suctions first rises up to a peak and then slightly

decreases down to a certain residual value with increasing axial strain, exhibiting strain-softening behaviour.

- The soil stiffness and shear strength considerably increase with the increase in mean stress. The shear strength of unsaturated clay is significantly larger than that of the saturated clay. The total suction greatly increases the shear strength of remoulded clay mainly by increasing the cohesion. The angle of internal friction of Kaolin K13 clay is  $\varphi = 22.0^\circ$ . The apparent cohesions of unsaturated Kaolin K13 clay under  $s_0 = 38$  MPa are  $c = 623$  kPa and  $178$  kPa corresponding to the maximum shear strength and the residual shear strength. The apparent cohesions of unsaturated Kaolin K13 clay under  $s_0 = 10$  MPa are  $c = 881$  kPa and  $256$  kPa corresponding to the maximum shear strength and the residual shear strength. The angle of internal friction of M35 clay is about  $\varphi = 16.3^\circ$ , which is significantly smaller than that of Kaolin K13 clay. The apparent cohesions of unsaturated M35 clay under  $s_0 = 38$  MPa are  $c = 4236$  kPa and  $1705$  kPa corresponding to the maximum shear strength and the residual shear strength, which are considerably higher than those of unsaturated Kaolin K13 clay with the same initial total suction.
- The volumetric strain of the saturated clay specimen is always positive showing a contractive behaviour. However, for the unsaturated specimens under high total suctions, the volumetric strains are first positive showing a slight contractive behaviour and then negative showing a pronounced dilative behaviour as the axial strains increase. In general, the specimen with a higher initial suction tends to compress less in the beginning and dilates more in the end (the smaller is the initial total suction, the more significant is the initial compression of the specimen). The measured total suctions of all specimens go on decreasing as the deviatoric stress increases.
- Both the maximum shear strength and residual shear strength of the specimen under a total suction of  $38$  MPa are smaller than those of the specimen under a total suction of  $10$  MPa. The decrease in shear strength is probably because of the existence of initial local cracks inside the clay specimen induced by a high suction in desiccator. A considerable decrease in apparent cohesion when the total suction increases from  $10$  MPa to  $38$  MPa.

- The shear strength of unsaturated clay is larger than that of saturated clay. Nevertheless, the difference between the residual shear strengths of unsaturated clay with different initial total suctions and the shear strength of saturated clay decreases with increasing mean stress. Meanwhile, the gap between the maximum shear strengths of unsaturated clay with different initial total suctions shows a tendency to decrease with increasing mean stress.

(3) Failure mode:

- After triaxial loading, all unsaturated clay specimens with high initial total suctions are completely split into two parts by single shear planes and exhibit no evident barrel-shaped deformations. The shear plane of clay specimen under a low mean stress is very tortuous while it is relatively flat in the specimen under a high mean stress. This leads to a more evident dilation in the first case due to the stronger interlocking.
- A few cracks appear in all clay specimens after triaxial loading and the distribution of cracks seems related to the level of mean stresses. Many mesoscale pores (whose sizes are larger than 0.05 mm) are observed in all clay specimens. The void volume and void size in unsaturated remoulded clay decreases with the increase in mean stress. Most of the pores particularly those with large sizes away from the shear plane rotate towards the horizontal plane, which is perpendicular to the major principal stress direction. These horizontal-oriented pores seem to develop in the pre-consolidation stage (before the application of suctions).

## 2. Future perspectives

The research reported in this dissertation has resulted in a better understanding of the multiscale behaviour of both saturated and unsaturated remoulded clays. However, some aspects still need further investigations, and thus several research topics may be suggested for further work.

- Some new techniques are recommended for the microstructural investigation of clays. On the one hand, the resin impregnation technique combined with polishing procedures are highly recommended during the preparation of microscopic samples for both SEM observations and XR- $\mu$ CT scans. The application of this method allows preparing small intact samples with smooth surfaces and ensures the quality of

obtained micrographs. On the other hand, it is interesting to bring some high tech equipments in material science to the field of clay microstructural studies. These equipments include the focused ion beam - scanning electron microscopy (FIB-SEM) for 3D microscale characterisations and the electron backscatter diffraction (EBSD) for nanoscale or particle-scale characterisations.

- The conceptual modes of particle orientation and the microscopic mechanism of dilatancy phenomenon of saturated remoulded clays found in this research were all based on the limited experimental results of a kaolinite clay. The reliability and universality of these findings still need further verifications. To this end, additional experiments considering different cases of stress paths and overconsolidation ratios should be performed involving the same kaolinite material in future. Moreover, both macroscopic and microscopic experiments on other types of remoulded clays (e.g., remoulded specimens of natural clays) under identical conditions are also necessary for comparison purposes.
- The triaxial test groups with respect to unsaturated remoulded clays in this research, were not abundant due to time, energy and other constraints. This had led to some difficulties in comparing the experimental results of different suctions, mean stresses and soil types. In addition, several XR- $\mu$ CT scans were performed on unsaturated clay specimens; however, the microstructural characteristics were not well quantified. Therefore, further work can be focused on the quantification of microstructural characteristics of remoulded clays on various suction-stress paths and examine the link between shear strength behaviour and microstructural properties.
- Another interesting topic may be the development of microscopic constitutive models of remoulded clays. This research presented a multiscale investigation of remoulded clays under various loading conditions, which could offer micro and macro properties for constitutive modelling. Remoulded clay may be considered as an assembly of equal-sized spherical clay clusters. The intercluster forces including capillary force, van der waals force, electric double-layer force and contact force can be calculated by theoretical equations. On this basis, microstructural elastoplastic models may be developed following the method proposed by Chang and Hicher (2007) and Yin et al. (2011).

---

## References

---

### A:

---

AFNOR, NF P 94-074, 1994. Soils : investigation and testing. Shear strength tests with revolving triaxial test apparatus. Apparatus. Preparation of test specimens. UU test. CU test. CD test. French standard. (in French)

Al-Mukhtar M., Qi Y., Alcover J.F., Bergaya F., 1999. Oedometric and water-retention behaviour of highly compacted unsaturated smectites. *Canadian Geotechnical Journal*, 36(4): 675–684.

Alonso E.E., Gens A., Josa A., 1990. A constitutive model for partially saturated soils. *Géotechnique*, 40(3): 405–430.

Alshibli K.A., Cil M.B., 2017. Influence of particle morphology on the friction and dilatancy of sand. *Journal of Geotechnical and Geoenvironmental Engineering*, 144(3), doi: 10.1061/(ASCE)GT.1943-5606.0001841.

Anandarajah A., Kuganenthira N., Zhao D., 1996. Variation of fabric anisotropy of kaolinite in triaxial loading. *Journal of Geotechnical Engineering*, 122(8): 633–640.

ASTM D4404-10, Standard Test Method for Determination of Pore Volume and Pore Volume Distribution of Soil and Rock by Mercury Intrusion Porosimetry, ASTM International, West Conshohocken, PA, 2010.

---

### B:

---

Bai X., Smart R., 1997. Change in microstructure of kaolin in consolidation and undrained shear. *Geotechnique*, 47(5): 1009–1017.

Barton C.M., 1974. The micromorphological soil investigation work of Dr. Lafeber. In: Rutherford, G.K. (Ed.), *Soil Microscopy*. The Limestone Press, Kingston, Ontario, 1–19.

Been K., Jefferies M., 2004. Stress dilatancy in very loose sand. *Canadian Geotechnical Journal*, 41(5): 972–989.

Biarez J., Hicher P.Y., 1994. *Elementary Mechanics of Soils Behaviour. Saturated Remoulded Soils*. Rotterdam: A.A.Balkema.

Blatz J.A., Cui Y.J., Oldecop L., 2008. Vapour equilibrium and osmotic technique for suction control. In *Laboratory and Field Testing of Unsaturated Soils*. Springer, Dordrecht.

Blatz J.A., Graham J., Chandler N.A., 2002. Influence of suction on the strength and stiffness of compacted sand bentonite. *Canadian Geotechnical Journal*, 39(5): 1005–1015.

Bolton M.D., 1986. The strength and dilatancy of sands. *Géotechnique*, 36(1): 65–78.

Burton G.J., Pineda J.A., Sheng D., Airey D., 2015. Microstructural changes of an undisturbed, reconstituted and compacted high plasticity clay subjected to wetting and drying. *Engineering Geology*, 193: 363–373.

---

## **C:**

---

Cetin H., Söylemez M., 2004. Soil-particle and pore orientations during drained and undrained shear of a cohesive sandy silt clay soil. *Canadian geotechnical journal*, 41(6): 1127–1138.

Chi M.J., Zhao C.G., Li X.J., 2009. Stress-dilatancy mechanism of sands. *China Civil Engineering Journal*, 42(3): 99–104. (in Chinese)

Cotecchia F., Cafaro F., Guglielmi S., 2016. Microstructural changes in clays generated by compression explored by means of SEM and Image Processing. *Procedia Engineering*, 158: 57–62.

Cui Y.J., Delage P., 1996. Yielding and plastic behaviour of an unsaturated compacted silt. *Géotechnique*, 46(2): 291–311.

Czurda K.A., Hohmann M., 1997. Freezing effect on shear strength of clayey soils. *Applied clay science*, 12(1-2): 165–187.

---

## **D:**

---

Dai J.Q., Su Z.J., Zhao M.C., Xiang Y.H., 2017. True triaxial tests on stress-strain characteristics of soft clay considering the structural effects. *Chinese Journal of Rock Mechanics and Engineering*, 36(4): 997–1004. (in Chinese)

De Josselin de Jong G., 1976. Rowe's stress-dilatancy relation based on friction. *Géotechnique*, 26(3): 527–534.

Delage P., Cui Y.J., 2008. An evaluation of the osmotic method of controlling suction. *Geomechanics and Geoengineering: An International Journal*, 3(1): 1–11.

---

Delage P., Cui Y.J., Tang A.M., 2010. Clays in radioactive waste disposal. *Journal of Rock Mechanics and Geotechnical Engineering*, 2(2): 111–123.

Delage P., Lefebvre G., 1984. Study of the structure of a sensitive Champlain clay and of its evolution during consolidation. *Canadian Geotechnical Journal*, 21(1): 21–35.

Delage P., Pellerin F.M., 1984. Influence de la lyophilisation sur la structure d'une argile sensible du Québec. *Clay Minerals*, 19(2): 151–160. (in French)

Delage P., Suraj de Silva G.P.R., De Laure E., 1987, Un nouvel appareil triaxial pour les sols non saturés (A novel triaxial apparatus for unsaturated soils), *Proceedings of the 9th European Conference on Soil Mechanics and Foundation Engineering*, The Netherlands, Vol. 1, pp. 26–28.

Delage P., Vicol T., Suraj de Silva G.P.R., 1992. Suction controlled testing of non saturated soils with an osmotic consolidometer. In *7th International Conference on Expansive Soils*, pp.206–211.

Djéran-Maigre I., Tessier D., Grunberger D., Velde B., Vasseur G., 1998. Evolution of microstructures and of macroscopic properties of some clays during experimental compaction. *Marine and Petroleum Geology*, 15(2): 109–128.

---

## **E:**

---

Esposito III M.P., Andrus R.D., 2016. Peak shear strength and dilatancy of a pleistocene age sand. *Journal of Geotechnical and Geoenvironmental Engineering*, 143(1), doi: 10.1061/(ASCE)GT.1943-5606.0001582.

---

## **F:**

---

Fleureau J.M., Hadiwardoyo S., Correia A.G., 2003. Generalised effective stress analysis of strength and small strains behaviour of a silty sand, from dry to saturated state. *Soils and Foundations*, 43(4): 21–33.

Fredlund D.G, Rahardjo H., 1993. *Soil mechanics for unsaturated soils*. John Wiley & Sons.

Fredlund D.G., Morgenstern N.R., Widger R.A., 1978. The shear strength of unsaturated soils. *Canadian Geotechnical Journal*, 15(3): 313–321.

Fredlund M.D., Wilson G.W., Fredlund D.G., 2002, March. Representation and estimation of the shrinkage curve. In *Proc., 3rd Int. Conf. on Unsaturated Soils, UNSAT 2002*, pp.145-149.

---

**G:**

---

Gao Y., Sun D.A., Zhou A., 2015. Hydromechanical behaviour of unsaturated soil with different specimen preparations. *Canadian Geotechnical Journal*, 53(6): 909–917.

Gao Z., Zhao J., Yin Z.Y., 2016. Dilatancy relation for overconsolidated clay. *International Journal of Geomechanics*, 17(5), doi: 10.1061/(ASCE)GM.1943-5622.0000793.

Griffiths F.J., Joshi R.C., 1989. Change in pore size distribution due to consolidation of clays. Technical note. *Geotechnique*, 39(1): 159–167.

Gu C., Wang J., Cai Y., Sun L., Wang P., Dong Q., 2016. Deformation characteristics of overconsolidated clay sheared under constant and variable confining pressure. *Soils and Foundations*, 56(3): 427–439.

Guo P., Su X., 2007. Shear strength, interparticle locking, and dilatancy of granular materials. *Canadian Geotechnical Journal*, 44(5): 579–591.

---

**H:**

---

Hammad T., 2010. Comportement des sédiments marins de grande profondeur approche multiéchelle. Doctoral dissertation, Ecole Centrale Paris, France. (in French)

Hattab M., 2011. Critical state notion and microstructural considerations in clays. *Comptes Rendus Mécanique*, 339(11) : 719–726.

Hattab M., Bouziri-Adrouche S., Fleureau J.M., 2010. Évolution de la microtexture d'une matrice kaolinitique sur chemin triaxial axisymétrique. *Canadian Geotechnical Journal*, 47(1): 34–48. (in French)

Hattab M., Fleureau J.M., 2010. Experimental study of kaolin particle orientation mechanism. *Géotechnique*, 60(5): 323–331.

Hattab M., Fleureau J.M., 2011. Experimental analysis of kaolinite particle orientation during triaxial path. *International Journal for Numerical and Analytical Methods in Geomechanics*, 35(8): 947–968.

Hattab M., Hammad T., Fleureau J.M., Hicher P.Y., 2013. Behaviour of a sensitive marine sediment: microstructural investigation. *Géotechnique*, 63(1): 71–84.

Hattab M., Hammad T., Fleureau J.M., 2015. Internal friction angle variation in a

kaolin/montmorillonite clay mix and microstructural identification. *Géotechnique*, 65(1): 1–11.

Hattab M., Hicher P.Y., 2004. Dilating behaviour of overconsolidated clay. *Soils and Foundations*, 44(4): 27–40.

Henkel D.J., 1956. The effect of overconsolidation on the behaviour of clays during shear. *Geotechnique*, 6(4): 139–150.

Hicher P.Y., Chang C.S., 2007. A microstructural elastoplastic model for unsaturated granular materials. *International journal of solids and structures*, 44(7-8): 2304–2323.

Hicher P.Y., Wahyudi H., Tessier D., 2000. Microstructural analysis of inherent and induced anisotropy in clay. *Mechanics of Cohesive-frictional Materials*, 5(5): 341–371.

Hue D.T.M., Phie-Wej N., Giao P.H., 2010. Evaluation of the changes in stiff clay microstructure by SEM digital image processing. In *Proceedings of the International Symposium Hanoi Geoengineering*, pp.97-104.

---

**I:**

---

Ighil Ameer L., 2016. Etude expérimentale du phénomène de l'endommagement et de la fissuration d'une matrice poreuse. Doctoral dissertation, University of Lorraine, France. (in French)

Indarto, 1991. Comportement mécanique et compactage des matériaux de barrages. Doctoral dissertation, Ecole Centrale Paris, France. (in French)

Ingles O.G., Lafeber D., 1966. The influence of volume defects on the strength and strength isotropy of stabilized clays. *Engineering Geology*, 1(4): 305–310.

---

**J:**

---

Jefferies M., Been K., 2015. *Soil liquefaction: a critical state approach*. CRC press.

Jiang M., Zhang F., Hu H., Cui Y., Peng J., 2014. Structural characterization of natural loess and remolded loess under triaxial tests. *Engineering Geology*, 181: 249–260.

Jotisankasa A., Coop M., Ridley A., 2009. The mechanical behaviour of an unsaturated compacted silty clay. *Géotechnique*, 59(5): 415–428.

---

**K:**

---

Kato S., Kawai K., 2000. Deformation characteristics of a compacted clay in collapse under isotropic and triaxial stress state. *Soils and Foundations*, 40(5): 75–90.

Kochmanová N., Tanaka H., 2010. Role of microstructure in the mechanical behaviour of clay. In *Soil Behavior and Geo-Micromechanics*, pp.166–171.

Kokusho T., Hara T., Hiraoka R., 2004. Undrained shear strength of granular soils with different particle gradations. *Journal of Geotechnical and Geoenvironmental Engineering*, 130(6): 621–629.

Kong L., Huang H., Hicher P.Y., Zhang D., 2011. Microstructural analysis of Shanghai remolded clay during one-dimensional consolidation test. In *Geomechanics and Geotechnics: From Micro to Macro*.

---

**L:**

---

Laloui L., Peron H., Geiser F., Rifa A., Vulliet L., 2006. Advances in volume measurement in unsaturated soil triaxial tests. *Soils and foundations*, 46(3): 341–349.

Lancelot L., Shahrour I., Al Mahmoud M., 2006. Failure and dilatancy properties of sand at relatively low stresses. *Journal of Engineering Mechanics*, 132(12): 1396–1399.

Landis E.N., Keane D.T., 2010. X-ray microtomography. *Materials characterization*, 61(12): 1305–1316.

Li Z.S., Derfouf F.E.M., Benchouk A., Abou-Bekr N., Taibi S., Fleureau, J.M., 2018. Volume change behavior of two compacted clayey soils under hydraulic and mechanical loadings. *Journal of Geotechnical and Geoenvironmental Engineering*, 144(4), doi: 10.1061/(ASCE)GT.1943-5606.0001851.

Li X., Zhang L.M., 2009. Characterization of dual-structure pore-size distribution of soil. *Canadian Geotechnical Journal*, 46(2): 129–141.

Liu, X., Hammad, T., Saiyouri, N. and Hattab, M., 2012. Physical chemical analysis of marine sediment cementation from the Gulf of Guinea. *Comptes Rendus Geoscience*, 344(9), pp.461–470.

Liu S., Matsuoka H., 2003. Microscopic interpretation on a stress-dilatancy relationship of granular materials. *Soils and Foundations*, 43(3): 73-84.

Liu C., Shi B., Zhou J., Tang C., 2011. Quantification and characterization of microporosity by image

processing, geometrical measurement and statistical methods: Application on SEM images of clay materials. *Applied Clay Science*, 54(1): 97–106.

Lloret A., Villar M.V., Sanchez M., Gens A., Pintado X., Alonso E.E., 2003. Mechanical behaviour of heavily compacted bentonite under high suction changes. *Geotechnique*, 53(1): 27–40.

Lu N., Godt J.W., Wu D.T., 2010. A closed - form equation for effective stress in unsaturated soil. *Water Resources Research*, 46(5), doi:10.1029/2009WR008646.

Lu N., Kim T.H., Sture S., Likos W.J., 2009. Tensile strength of unsaturated sand. *Journal of engineering mechanics*, 135(12): 1410–1419.

Lu N., Likos W.J., 2004. *Unsaturated soil mechanics*. John Wiley & Sons.

Luong M.P., 1978. Characteristic state soil mechanics. *Comptes Rendus Hebdomadaires des Séances de l'Académie des Sciences Serie B*, 287(15): 305–307.

---

**M:**

---

Ma S.K., Huang M.S., Fan Q.Y., 2009. Unsaturated soil strength theory based on total stress strength indexes of saturated soil and its application. *Chinese Journal of Rock Mechanics and Engineering*, 28(3): 635–640. (in Chinese)

Mandelbrot B.B., Passoja D.E., Paullay A.J., 1984. Fractal character of fracture surfaces of metals. *Nature*, 308(5961): 721–722.

Martin R.T., Ladd C.C., 1975. Fabric of consolidated kaolinite. *Clays and Clay Minerals*, 23(1): 17–25.

McKyes E., Yong R.N., 1971. Three techniques for fabric viewing as applied to shear distortion of a clay. *Clays and Clay Minerals*, 19: 289–293.

Mofiz S.A., Islam M.N., 2010. Modeling and numerical analysis of expansive soil in stress path tests. In *GeoFlorida 2010: Advances in Analysis, Modeling & Design*, pp.747–756.

Monroy R., Zdravkovic L., Ridley A., 2010. Evolution of microstructure in compacted London Clay during wetting and loading. *Géotechnique*, 60(2): 105–119.

Morgenstern N.R., Tchalenko J.S., 1967a. The optical determination of preferred orientation in clays and its application to the study of microstructure in consolidated kaolin. I. *Proc. R. Soc. Lond. A*, 300(1461): 218–234.

Morgenstern N.R., Tchalenko J.S., 1967b. The optical determination of preferred orientation in clays and its application to the study of microstructure in consolidated kaolin. II. Proc. R. Soc. Lond. A, 300(1461): 235–250.

Morgenstern N.R., Tchalenko J.S., 1967c. Microscopic structures in kaolin subjected to direct shear. Geotechnique, 17(4): 309–328.

Mukherjee M., Sachan A., 2008. Evolution of dilatancy angle during shearing of kaolin clay with different microfibrils. In proceeding of 12th International Conference of International Association for Computer methods and Advances in Geomechanics (IACMAG), Goa, India, 1-6 October.

Mun W., McCartney J.S., 2015. Compression mechanisms of unsaturated clay under high stresses. Canadian Geotechnical Journal, 52(12): 2099–2112.

Mun W., McCartney J.S., 2016. Constitutive model for the undrained compression of unsaturated clay. Journal of Geotechnical and Geoenvironmental Engineering, 143(4), doi: 10.1061/(ASCE)GT.1943-5606.0001635.

Murphy C.P., Bullock P., Biswell K.J., 1977. The measurement and characterisation of voids in soil thin sections by image analysis. Part II. Applications. European Journal of Soil Science, 28(3): 509–518.

---

**N:**

---

Nagaraj T.S., 1964. Soil structure and strength characteristics of compacted clay. Geotechnique, 14(2): 103–114.

Newland P.L., Allely B.H., 1957. Volume changes in drained triaxial tests on granular materials. Geotechnique, 7(1): 17–34.

Ng C.W.W., Coe J.L., 2015. Hydraulic conductivity of clay mixed with nanomaterials. Canadian Geotechnical Journal, 52(6): 808–811.

Ng T.T., 2001. Fabric evolution of ellipsoidal arrays with different particle shapes. Journal of Engineering Mechanics, 127(10): 994–999.

Nuth M., Laloui L., 2008. Effective stress concept in unsaturated soils: clarification and validation of a unified framework. International journal for numerical and analytical methods in Geomechanics, 32(7): 771–801.

---

**O:**

---

Oh W.T., Garga V.K., Vanapalli S.K., 2008. Shear strength characteristics of statically compacted unsaturated kaolin. *Canadian Geotechnical Journal*, 45(7) : 910–922.

---

**P:**

---

Péron H., Herchel T., Laloui L., 2007. An improved volume measurement for determining soil water retention curves. *Geotechnical Testing Journal*, 30(1): 1–8.

Pillai R.J., Robinson R.G., Boominathan A., 2010. Effect of microfabric on undrained static and cyclic behavior of kaolin clay. *Journal of Geotechnical and Geoenvironmental Engineering*, 137(4): 421–429.

Pillai R.J., Robinson R.G., Boominathan A., 2014. Undrained and drained shearing behavior of kaolinite with different microfabrics. *International Journal of Geotechnical Engineering*, 8(1): 10–20.

Pires L.F., Cooper M., Cássaro F.A.M., Reichardt K., Bacchi O.O.S., Dias N.M.P., 2008. Micromorphological analysis to characterize structure modifications of soil samples submitted to wetting and drying cycles. *Catena*, 72(2): 297–304.

Powrie W., Ni Q., Harkness R.M., Zhang X., 2005. Numerical modelling of plane strain tests on sands using a particulate approach. *Géotechnique*, 55(4): 297–306.

---

**R:**

---

Ramiah B.K., Purushothamaraj P., 1971. Effect of initial structure on the residual strength of kaolinitic clay. *Soils and Foundations*, 11(4): 15–23.

Raynaud S., Vasseur G., Célérier B., Loggia D., Ghoreychi M., Mathon M.H., Mazerolle F., 2010. Experimental study of the relation between the permeability of kaolinite and its deformation at micro and macro scale. *International Journal of Rock Mechanics and Mining Sciences*, 47(4): 559–567.

Revuzhenko A.F., 2007. *Mechanics of granular media*. Springer Science & Business Media.

Reynolds O., 1885. On the dilatancy of media composed of rigid particles in contact, with experimental illustrations. *Philosophical Magazine*, 20(127): 469–481.

Rifai A., Laloui L., Vulliet L., 2002. Volume measurement in unsaturated triaxial test using liquid variation and image processing. In *Proc. of the 3rd international conference on unsaturated soils*,

Recife, Brazil, 2: 441–445.

Romero E., Villar M.V., Lloret A., 2005. Thermo-hydro-mechanical behaviour of two heavily overconsolidated clays. *Engineering Geology*, 81(3): 255–268.

Rothenburg L., Bathurst R.J., 1992. Micromechanical features of granular assemblies with planar elliptical particles. *Geotechnique*, 42(1): 79–95.

Rowe P.W., 1962. The stress-dilatancy relation for static equilibrium of an assembly of particles in contact. *Proceedings of the Royal Society of London. Series A, Mathematical and Physical Sciences*, pp.500–527.

Rueden C. T., Schindelin J., Hiner M. C. et al., 2017. ImageJ2: ImageJ for the next generation of scientific image data, *BMC Bioinformatics* 18:529, doi:10.1186/s12859-017-1934-z.

---

**S:**

---

Sachan A., 2007. Variation in geometric arrangement of particles in kaolinite clay due to shear deformation using SEM technique. *Current Science*, 93(4): 515–522.

Sachan A., 2013. Effect of intermediate microfabric on shear strength and strain localization response of Kaolin clay under compression and extension loading. *Geotechnical and Geological Engineering*, 31(1): 213–228.

Sachan A., Penumadu D., 2007. Effect of microfabric on shear behavior of kaolin clay. *Journal of Geotechnical and Geoenvironmental Engineering*, 133(3): 306–318.

Sachan A., Vikash G., Prashant A., 2013. Development of intermediate microfabric in kaolin clay and its consolidation behaviour. *Geotechnical and Geological Engineering*, 31(1): 23–34.

Sahagian D.L., Prousevitich A.A., 1998. 3D particle size distributions from 2D observations: stereology for natural applications. *Journal of Volcanology and Geothermal Research*, 84(3): 173–196.

Schanz T., Vermeer P.A., 1996. Angles of friction and dilatancy of sand. *Géotechnique*, 46(1): 145–152.

Schindelin J., Rueden C. T., Hiner M. C., et al., 2015. The ImageJ ecosystem: An open platform for biomedical image analysis, *Molecular Reproduction and Development*, PMID 26153368.

Shimizu M., 1982. Effect of overconsolidation on dilatancy of a cohesive soil. *Soils and Foundations*, 22(4): 121–135.

---

Simoni A., Housley G.T., 2006. The direct shear strength and dilatancy of sand–gravel mixtures. *Geotechnical & Geological Engineering*, 24(3), doi: 10.1007/s10706-004-5832-6.

Sridharan A., Rao S.N., Rao G.V., 1971. Shear strength characteristics of saturated montmorillonite and kaolinite clays. *Soils and Foundations*, 11(3): 1–22.

Sun H., Chen J.F., Ge X.R., 2004a. Deformation characteristics of silty clay subjected to triaxial loading, by computerised tomography. *Geotechnique*, 54(5): 307–314.

Sun D.A., Matsuoka H., Xu Y.F., 2004b. Collapse behavior of compacted clays in suction-controlled triaxial tests. *Geotechnical Testing Journal*, 27(4): 362–370.

---

## T:

---

Taibi S., 1994. Comportement mécanique et hydraulique des sols soumis à une pression interstitielle négative. Etude expérimentale et modélisation. Doctoral dissertation, Ecole centrale Paris, Paris. (in French)

Takizawa S., Kamai T., Matsukura Y., 2005. Fluid pathways in the shearing zones of kaolin subjected to direct shear tests. *Engineering Geology*, 78(1-2): 135–142.

Tang Y.Q., Zhou J., Hong J., Yang P., Wang J.X., 2012. Quantitative analysis of the microstructure of Shanghai muddy clay before and after freezing. *Bulletin of Engineering Geology and the Environment*, 71(2): 309–316.

Tarantino A., De Col E., 2008. Compaction behaviour of clay. *Géotechnique*, 58(3): 199–213.

---

## V:

---

Vallejo L.E., 1996. Fractal analysis of the fabric changes in a consolidating clay. *Engineering Geology*, 43(4): 281–290.

Van Genuchten M.T., 1980. A closed-form equation for predicting the hydraulic conductivity of unsaturated soils. *Soil science society of America journal*, 44(5): 892–898.

Varadarajan A., Sharma K.G., Venkatachalam K., Gupta A.K., 2003. Testing and modeling two rockfill materials. *Journal of Geotechnical and Geoenvironmental Engineering*, 129(3): 206–218.

Velde B.B., Meunier A., 2008. The origin of clay minerals in soils and weathered rocks. Springer Science & Business Media.

Verdugo R., Ishihara K., 1996. The steady state of sandy soils. *Soils and foundations*, 36(2): 81–91.

Vesga L.F., 2008. Equivalent effective stress and compressibility of unsaturated kaolinite clay subjected to drying. *Journal of geotechnical and geoenvironmental engineering*, 134(3): 366–378.

Viggiani G., Lenoir N., Bésuelle P., Di Michiel M., Marelli S., Desrues J., Kretschmer M., 2004. X-ray microtomography for studying localized deformation in fine-grained geomaterials under triaxial compression. *Comptes Rendus Mécanique*, 332(10): 819–826.

---

**W:**

---

Wan R.G., Guo P.J., 2001. Effect of microstructure on undrained behaviour of sands. *Canadian Geotechnical Journal*, 38(1): 16–28.

Ward-Harvey K., 2009. *Fundamental building materials*. Universal-Publishers.

Washburn E.W., 1921. Note on a method of determining the distribution of pore sizes in a porous material. *Proceedings of the National Academy of Sciences*, 7(4): 115–116.

Wei X., 2014. Etude micro-macro de la fissuration des argiles soumises à la dessiccation. Doctoral dissertation. Ecole Centrale Paris, France.

Wei X., Hattab M., Bompard P., Fleureau J.M., 2016. Highlighting some mechanisms of crack formation and propagation in clays on drying path. *Géotechnique*, 66(4): 287–300.

Wen X.G., Zhang X., Zhou J., Guan L.B., Xie X.Y., 2011. Changing mechanism of microstructure of intact soft clay considering anisotropy. *Rock and Soil Mechanics*, 32(1): 27–32. (in Chinese)

Wheeler S.J., Sivakumar V., 1995. An elasto-plastic critical state framework for unsaturated soil. *Géotechnique*, 45(1): 35–53.

Wiebe B., Graham J., Tang G.X., Dixon D., 1998. Influence of pressure, saturation, and temperature on the behaviour of unsaturated sand-bentonite. *Canadian Geotechnical Journal*, 35(2): 194–205.

---

**X:**

---

Xu Y.H., Pitot H.C., 2003. An improved stereologic method for three-dimensional estimation of particle size distribution from observations in two dimensions and its application. *Computer methods and programs in biomedicine*, 72(1): 1–20.

---

**Y:**

---

Ye G.L., Ye B., Zhang F., 2013. Strength and dilatancy of overconsolidated clays in drained true triaxial tests. *Journal of Geotechnical and Geoenvironmental Engineering*, 140(4), doi: 10.1061/(ASCE)GT.1943-5606.0001060.

Yin Z.Y., Hattab M., Hicher P.Y., 2011. Multiscale modeling of a sensitive marine clay. *International Journal for Numerical and Analytical Methods in Geomechanics*, 35(15): 1682–1702.

You Z., Lai Y., Zhang M., Liu E., 2017. Quantitative analysis for the effect of microstructure on the mechanical strength of frozen silty clay with different contents of sodium sulfate. *Environmental Earth Sciences*, 76(4), doi: 10.1007/s12665-017-6454-7.

Yu C.Y., Chow J.K., Wang Y.H., 2016. Pore-size changes and responses of kaolinite with different structures subject to consolidation and shearing. *Engineering Geology*, 202: 122–131.

---

**Z:**

---

Zhang Z.L., Cui Z.D., 2017. Analysis of microscopic pore structures of the silty clay before and after freezing–thawing under the subway vibration loading. *Environmental Earth Sciences*, 76(15), doi: 10.1007/s12665-017-6879-z.

Zhao D., 2017. Study on the creep behavior of clay under complex triaxial loading in relation to the microstructure. Doctoral dissertation, University of Lorraine, France.

Zhao D., Hattab M., Yin Z.Y., Hicher P.Y., 2018. Dilative behavior of kaolinite under drained creep condition. *Acta Geotechnica*, doi: 10.1007/s11440-018-0686-x.

Zou W.L., Han Z., Vanapalli S.K., Zhang J.F., Zhao, G.T., 2018. Predicting volumetric behavior of compacted clays during compression. *Applied Clay Science*, 156: 116–125.